



Norwegian University of  
Science and Technology

# The Rock Slope Instability at Tytefjell in Vindafjord, Rogaland

Hazard Assessment for Different Failure  
Scenarios

**Øyvind Bertinussen Rem**

Geology

Submission date: May 2016

Supervisor: Reginald Hermanns, IGB

Co-supervisor: Martina Böhme, NGU

Norwegian University of Science and Technology  
Department of Geology and Mineral Resources Engineering



## ABSTRACT

NGU is currently in the process of identifying, classifying and completing hazard and consequence analyses of all unstable rock slopes in Norway. In the context of this long term project, a hazard analysis of the Tytefjell unstable rock slope was completed, involving detailed structural field mapping and analysis of high-resolution digital terrain models. The Tytefjell site is located in Vindafjord, Rogaland County, on an east dipping slope composed of phyllite. It is believed that the presence of weak graphite decreases slope stability. No daylighting sliding structure was observed, therefore it is believed that the unstable area continues below sea level. However, it is not possible to delimit the instability with certainty, due to low resolution bathymetry data. Morphological features and deformation over a large area allows to classify the instability as a deep seated gravitational slope deformation (DSGSD) of several hundred million m<sup>3</sup>.

Structural mapping revealed five main joint sets (dipdir/dip): J1(119/87), J2(213/87), J3(354/89), J4(067/43) and J5(274/87). The mean orientation of the foliation is 000/22. Six failure scenarios were defined within the unstable slope based on delimiting cracks forming possible failure surfaces. Failure scenarios range in volume from  $>500 \times 10^6 \text{ m}^3$  for failure of the entire slope, to  $400 \times 10^3 \text{ m}^3$  for release of frontal blocks. The two largest scenarios are considered of very low likelihood when comparing to postglacial and historical events in Norway. The remaining assessed four scenarios lie within the moderate hazard class following the NGU hazard and risk classifications system. Runout and displacement wave modelling indicated a high likelihood of a displacement wave in the case of failure of scenario 6. Using the empirical VAW model, a maximum wave run-up at the eastside of the fjord of 6-7 meters was estimated.

Model results were compared to an empirical displacement wave relation compiled by NGU. Further investigations were made on how including additional parameters; run-up slope angle and water depth, influenced the uncertainty of the empirical relation. This was done by analysing run-up height observations and bathymetry data for six displacement wave events. No significant correlation between the additional parameters and run-up height was found. It is therefore not beneficial to include the new parameters into the existing empirical relation with the current dataset. Results from applying the existing empirical relation to the scenarios at Tytefjell correspond well with the results from the VAW model. However, more research is needed to replace the VAW model with an empirical relation in order to use such relations as a predictive tool.



## **SAMMENDRAG (NORWEGIAN SUMMARY)**

NGU er i gang med å identifisere, kartlegge, klassifisere og ferdigstille fare- og konsekvensanalyser for alle ustabile fjellpartier i Norge. Som en del av dette langsiktige prosjektet er det blitt utført fareklassifisering av det ustabile fjellpartiet Tytefjell ved hjelp av detaljert strukturgeologisk kartlegging og analyser av høyoppløste digitale terrengmodeller. Det ustabile fjellpartiet Tytefjell ligger langs Vindafjord i Rogaland i en østvendt skråning bestående av fyllitt. Det antas at tilstedeværelse av svake grafittlag senker skråningsstabiliteten i området. Ingen utgående glidestruktur ble observert og derfor er det sannsynlig at det ustabile fjellpartiet fortsetter under havnivå. På grunn av de lavoppløste batymetridataene er det ikke mulig å avgrense det ustabile området nøyaktig. Morfologiske strukturer og deformasjon over et stort område indikerer en dyptgående gravitativ skråningsdeformasjon (DSGSD) på flere hundre millioner m<sup>3</sup>.

Strukturkartlegging resulterte i fem hovedsprekkesett (fallretning/fall): J1(119/87), J2(213/87), J3(354/89), J4(067/43) og J5(274/87). Gjennomsnittlig orientering for foliasjonen er 000/22. Seks scenarioer ble definert i det ustabile fjellpartiet basert på avgrensede sprekker som danner mulige bruddflater. Scenarioene varierer i volum fra >500 x 10<sup>6</sup> m<sup>3</sup> for hele det ustabile partiet, til 400 x 10<sup>3</sup> m<sup>3</sup> for utglidning av blokker i fronten av skråningen. En kollaps av de to største scenarioene er vurdert til å være lite sannsynlig hvis man sammenligner med postglasiale og historiske skredhendelser i Norge. De fire undersøkte scenarioene havner innenfor den moderate fareklassen i NGUs system for fare- og risikoklassifisering. Utløpsmodellering viser at en kollaps av scenario 6 med høy sannsynlighet vil kunne forårsake en flodbølge. Oppskyllingshøyden ble estimert ved hjelp av VAW-modellen og resulterte i en estimert oppskylling på 6-7 meter på østsiden av fjorden.

Modellresultatene ble sammenlignet med en empirisk flodbølgerelasjon utviklet av NGU. Videre undersøkelser ble gjort for å undersøke hvordan flere parametere, som oppskyllingsvinkel og vandyp, påvirker usikkerhetene i den empiriske relasjonen. Dette ble gjort ved å analysere oppskyllingshøyder og batymetridata fra seks tidligere hendelser. Det ble ikke funnet signifikant korrelasjon mellom de nye parameterne og den eksisterende empiriske relasjonen. Det er derfor ikke fordelaktig å inkludere de nye parameterne i den empiriske relasjonen basert på gjeldende datagrunnlag. Anvendelse av den eksisterende empiriske relasjonen på scenarioene ved Tytefjell gav resultater som stemmer godt med estimatene fra VAW modellen. Det er imidlertid behov for mer forskning for å kunne erstatte VAW modellen med en empirisk relasjon for at denne skal kunne brukes til estimering av oppskyllingshøyder.



## ACKNOWLEDGEMENTS

This thesis is the final work of my Master of Science (M.Sc.) degree in Engineering geology at the Department of Geology and Mineral Resource Engineering at the Norwegian University of Science and Technology (NTNU). It is written in collaboration with the Geological survey of Norway (NGU). Reginald Hermanns (head of the Geohazard and Earth Observation team at NGU and professor at NTNU) and Martina Böhme (NGU), have been my supervisors.

I owe my deepest gratitude to my supervisors for guiding me through the work during the last year. Thank you for all the valuable feedback you have given me. You always found time for discussions and to answer my countless questions. I would also like to thank Thierry Oppikofer for teaching me how to use the software needed to perform this analysis. A special thanks goes to the entire Geohazard and Earth Observation team at NGU for accepting me into the team the last two summers. These two field seasons inspired me to learn more about large rock slope instabilities.

I would like to acknowledge Vegard U. Jakobsen for his contribution during the fieldwork last summer. Your knowledge and the discussions we had during the fieldwork made a valuable contribution to this work. I also want to thank Kaja Krogh; our collaboration in the early stages of this work helped me a lot. I would like to show my gratitude to Susanne for proofreading this thesis and supporting me through this last year. Finally, too all my fellow students, thanks for five fantastic years at NTNU!

This work would not have been possible without bathymetrical data received from:

Louise Hansen (NGU), Nicholas Roberts (Simon Fraser University) and Galderic Lastras (University of Barcelona).

The bathymetric data of the Aysén fjord where obtained through:

Acción Complementaria DETSUFA (CTM2010-09891-E MAR) of the Spanish RTD programme, and a Generalitat de Catalunya “Grup de Recerca Consolidat” grant (2009-SGR 1305).

Trondheim, May 2016

*Øyvind Rem*





# TABLE OF CONTENTS

ABSTRACT.....	III
SAMMENDRAG (NORWEGIAN SUMMARY) .....	V
ACKNOWLEDGEMENTS .....	VII
LIST OF FIGURES.....	XIII
LIST OF TABLES .....	XIV
ABBREVIATIONS.....	XV
<b>1. INTRODUCTION .....</b>	<b>1</b>
1.1 UNSTABLE ROCK SLOPES IN NORWAY .....	1
1.2 AIMS AND RESTRICTIONS OF THE STUDY.....	3
1.3 AVAILABLE DATA .....	4
1.4 LOCATION AND GEOLOGICAL CONDITIONS.....	5
1.4.1 <i>Geological conditions</i> .....	7
1.4.2 <i>Precipitation</i> .....	7
1.4.3 <i>Historical events</i> .....	8
<b>2. THEORY .....</b>	<b>11</b>
2.1 LARGE ROCK SLOPE INSTABILITIES .....	11
2.1.1 <i>Controlling factors</i> .....	11
2.1.2 <i>Landslide research</i> .....	11
2.1.3 <i>Classification and terminology</i> .....	12
2.1.4 <i>Deep seated gravitational slope deformation (DSGSD)</i> .....	13
2.2 SECONDARY EFFECTS .....	13
2.2.1 <i>Displacement waves</i> .....	14
2.2.2 <i>Modelling of displacement waves</i> .....	15
2.2.3 <i>Previous work to develop an empirical run-up relationship</i> .....	16
2.3 CASE STUDIES – DISPLACEMENT WAVES .....	20
2.3.1 <i>Aysén events, Chile</i> .....	20
2.3.2 <i>Chehalis Lake event, Canada</i> .....	21
2.3.3 <i>Tafjord event, Norway</i> .....	22
2.4 LiDAR SCANNING .....	23
2.5 NGU MAPPING APPROACH .....	24

2.6	HAZARD ASSESSMENT.....	25
2.6.1	<i>Defining failure scenarios.....</i>	25
2.6.2	<i>Hazard classification .....</i>	26
2.6.1	<i>Hazard classes.....</i>	27
2.6.2	<i>Consequence assessment.....</i>	28
2.7	INTERNAL FRICTION ANGLE OF GRAPHITIC PHYLLITES .....	28
<b>3.</b>	<b>METHODS.....</b>	<b>29</b>
3.1	GEOLOGICAL FIELDWORK .....	29
3.1.1	<i>Mapping of discontinuities.....</i>	29
3.2	STRUCTURAL ANALYSIS .....	29
3.2.1	<i>Field data.....</i>	29
3.2.2	<i>DEM analysis .....</i>	31
3.3	GEOLOGICAL STRENGTH INDEX (GSI) CLASSIFICATION SYSTEM .....	32
3.3.1	<i>GSI classification for metamorphic rocks .....</i>	33
3.3.2	<i>Applicability to rock mass failures.....</i>	33
3.4	APPLICATION OF THE HAZARD CLASSIFICATION SYSTEM.....	34
3.4.1	<i>Kinematic analysis.....</i>	35
3.4.2	<i>Creation of structural profiles .....</i>	37
3.5	APPLICATION OF THE CONSEQUENCE ASSESSMENT .....	38
3.5.1	<i>Volume estimations using the SLBL technique.....</i>	38
3.5.2	<i>Fahrböschung.....</i>	41
3.5.3	<i>Flow-R runout model.....</i>	41
3.5.4	<i>VAW model.....</i>	42
3.6	EMPIRICAL ANALYSIS OF DISPLACEMENT WAVE DATA .....	44
<b>4.</b>	<b>RESULTS .....</b>	<b>47</b>
4.1	RESULTS FROM FIELD INVESTIGATIONS .....	47
4.1.1	<i>Mapped geological conditions .....</i>	47
4.2	GEOMORPHOLOGICAL AND MORPHO-STRUCTURAL FEATURES .....	49
4.2.1	<i>Back scarp .....</i>	49
4.2.2	<i>Cracks and trenches .....</i>	53
4.2.3	<i>Erosion features.....</i>	55
4.2.4	<i>Rock fall area.....</i>	55
4.3	GEOLOGIC STRUCTURES .....	56

4.3.1	<i>Foliation</i> .....	56
4.3.2	<i>Joint sets</i> .....	58
4.3.3	<i>Shear zones</i> .....	63
4.3.4	<i>Structural domains</i> .....	63
4.3.5	<i>Rose diagrams</i> .....	68
4.3.6	<i>GSI estimations</i> .....	69
4.4	RESULTS OF KINEMATIC ANALYSIS .....	70
4.4.1	<i>Northwest domain</i> .....	72
4.4.2	<i>North-east domain</i> .....	73
4.4.3	<i>South domain</i> .....	74
4.4.4	<i>Examples of failure modes found in the field</i> .....	75
4.5	STRUCTURAL PROFILES.....	76
4.6	FAILURE SCENARIOS .....	84
4.6.1	<i>Scenario 1</i> .....	87
4.6.2	<i>Scenario 2</i> .....	87
4.6.3	<i>Scenario 3</i> .....	88
4.6.4	<i>Scenario 4</i> .....	88
4.6.5	<i>Scenario 5</i> .....	89
4.6.6	<i>Scenario 6</i> .....	91
4.6.7	<i>Minor scenarios</i> .....	92
4.7	RESULTS FROM HAZARD ASSESSMENT .....	93
4.8	RESULTS FROM VAW ANALYSIS .....	94
4.9	RESULTS FROM EMPIRICAL DISPLACEMENT WAVE ANALYSIS.....	98
4.9.1	<i>Results from 2D and 3D statistical analysis</i> .....	98
4.9.2	<i>Maps displaying the gathered data</i> .....	100
4.9.3	<i>Results from applying the existing empirical relation on the scenarios at Tytefjell</i> .....	101
<b>5.</b>	<b>DISCUSSION</b> .....	<b>103</b>
5.1	LIMITS OF THE UNSTABLE AREA .....	103
5.2	STRUCTURAL CONTROL ON THE OBSERVED DEFORMATION AT TYTEFJELL .....	105
5.2.1	<i>Comparison between mapped lineaments and discontinuities</i> .....	105
5.2.2	<i>The implication of GSI values on slope stability</i> .....	106
5.3	CLASSIFICATION OF THE UNSTABLE AREA.....	107
5.3.1	<i>DSGSD features at Tytefjell</i> .....	107
5.4	SIMPLIFIED STABILITY MODEL.....	108

5.4.1	<i>Implications of reduced friction angle due to graphite content</i> .....	108
5.4.2	<i>The use of structural profiles to reduce uncertainties of the kinematic model</i> .....	108
5.5	HAZARD AND RISK OF A FUTURE ROCK SLOPE FAILURE AT TYTEFJELL.....	109
5.6	APPLICABILITY OF THE EMPIRICAL DISPLACEMENT WAVE EQUATIONS .....	110
5.6.1	<i>Uncertainties and adjustments done to the used datasets</i> .....	111
<b>6.</b>	<b>CONCLUSIONS .....</b>	<b>113</b>
<b>7.</b>	<b>RECOMMENDATIONS.....</b>	<b>115</b>
7.1	RECOMMENDED FURTHER INVESTIGATIONS.....	115
7.2	RECOMMENDED MONITORING TECHNIQUES.....	116
<b>8.</b>	<b>REFERENCES .....</b>	<b>119</b>
	<b>APPENDIX.....</b>	
<b>A.</b>	<b>OUTCROPS WITH GRAPHITE .....</b>	
<b>B.</b>	<b>GSI ESTIMATES .....</b>	
<b>C.</b>	<b>STRUCTURAL ANALYSIS .....</b>	
<b>D.</b>	<b>RUN-UP SLOPE ANGLE ESTIMATION .....</b>	
<b>E.</b>	<b>VAW PARAMETERS .....</b>	
<b>F.</b>	<b>HAZARD ASSESSMENT (SCENARIO 3-6) .....</b>	
<b>G.</b>	<b>EMPIRICAL ANALYSIS OF DISPLACEMENT WAVE PARAMETERS.....</b>	
<b>H.</b>	<b>MAPS DISPLAYING WAVE HEIGHT AND RUN-UP SLOPE ANGLE OR WATER DEPTH FOR HISTORICAL ROCK SLOPE FAILURES WITH EXISTING BATHYMETRY .....</b>	

# LIST OF FIGURES

FIGURE 1.1.....	2	FIGURE 4.17.....	63
FIGURE 1.2.....	5	FIGURE 4.18.....	64
FIGURE 1.3.....	6	FIGURE 4.19.....	65
FIGURE 1.4.....	8	FIGURE 4.20.....	66
FIGURE 1.5.....	9	FIGURE 4.21.....	67
FIGURE 2.1.....	12	FIGURE 4.22.....	68
FIGURE 2.2.....	14	FIGURE 4.23.....	70
FIGURE 2.3.....	19	FIGURE 4.24.....	72
FIGURE 2.4.....	21	FIGURE 4.25.....	73
FIGURE 2.5.....	22	FIGURE 4.26.....	74
FIGURE 2.6.....	23	FIGURE 4.27.....	75
FIGURE 2.7.....	27	FIGURE 4.28.....	77
FIGURE 3.1.....	30	FIGURE 4.29.....	78
FIGURE 3.2.....	32	FIGURE 4.30.....	79
FIGURE 3.3.....	34	FIGURE 4.31.....	79
FIGURE 3.4.....	36	FIGURE 4.32.....	80
FIGURE 3.5.....	38	FIGURE 4.33.....	81
FIGURE 3.6.....	40	FIGURE 4.34.....	81
FIGURE 3.7.....	40	FIGURE 4.35.....	82
FIGURE 3.8.....	43	FIGURE 4.36.....	83
FIGURE 4.1.....	47	FIGURE 4.37.....	83
FIGURE 4.2.....	48	FIGURE 4.38.....	85
FIGURE 4.3.....	50	FIGURE 4.39.....	86
FIGURE 4.4.....	51	FIGURE 4.40.....	86
FIGURE 4.5.....	52	FIGURE 4.41.....	90
FIGURE 4.6.....	52	FIGURE 4.42.....	92
FIGURE 4.7.....	54	FIGURE 4.43.....	95
FIGURE 4.8.....	55	FIGURE 4.44.....	96
FIGURE 4.9.....	56	FIGURE 4.45.....	97
FIGURE 4.10.....	57	FIGURE 4.46.....	99
FIGURE 4.11.....	57	FIGURE 5.1.....	104
FIGURE 4.12.....	59	FIGURE 5.2.....	106
FIGURE 4.13.....	60	FIGURE 7.1.....	117
FIGURE 4.14.....	61	FIGURE 7.2.....	118
FIGURE 4.15.....	62		
FIGURE 4.16.....	62		

## LIST OF TABLES

TABLE 1.1 .....	4
TABLE 2.1 .....	14
TABLE 2.2 .....	15
TABLE 2.3 .....	17
TABLE 2.4 .....	18
TABLE 2.5 .....	28
TABLE 3.1 .....	44
TABLE 4.1 .....	56
TABLE 4.2 .....	58
TABLE 4.3 .....	58
TABLE 4.4 .....	69
TABLE 4.5 .....	71
TABLE 4.6 .....	76
TABLE 4.7 .....	77
TABLE 4.8 .....	87
TABLE 4.9 .....	88
TABLE 4.10 .....	88
TABLE 4.11 .....	89
TABLE 4.12 .....	89
TABLE 4.13 .....	91
TABLE 4.14 .....	93
TABLE 4.15 .....	101
TABLE 7.1 .....	116

## **ABBREVIATIONS**

<b>ALS</b>	Airborne Laser Scanning
<b>DEM</b>	Digital Elevation Model
<b>dGNSS</b>	Differential Global Navigation Satellite Systems
<b>DSGSD</b>	Deep Seated Gravitational Slope Deformation
<b>GSI</b>	Geological Strength Index
<b>InSAR</b>	Interferometric Synthetic Aperture Radar
<b>LiDAR</b>	Light Detection and Ranging
<b>NGU</b>	Geological Survey of Norway
<b>NTNU</b>	Norwegian University of Science and Technology
<b>NVE</b>	Norwegian Water Resources and Energy Directorate
<b>SLBL</b>	Slope Line Base Level
<b>TLS</b>	Terrestrial Laser Scanning
<b>VAW</b>	The Laboratory of Hydraulics, Hydrology and Glaciology, ETH Zürich





# 1. INTRODUCTION

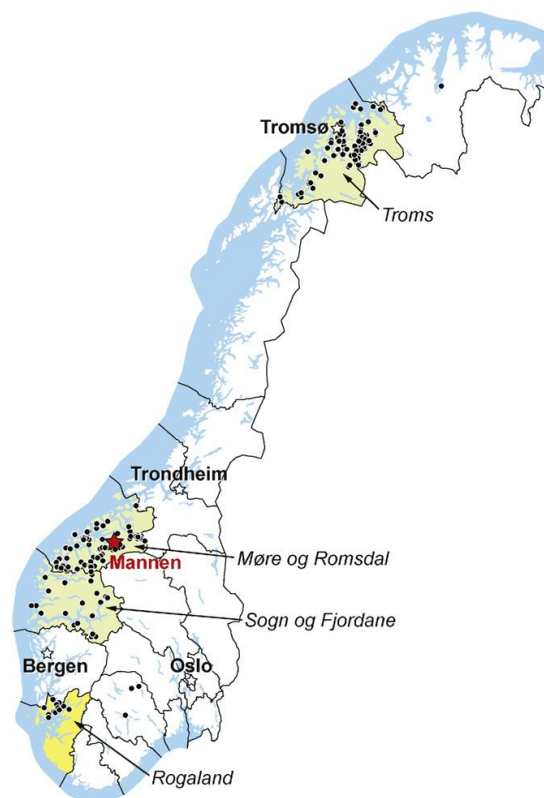
## 1.1 Unstable rock slopes in Norway

Catastrophic rock slope failures and related secondary effects are some of the biggest natural hazards in Norway. The long coastline with fjords stretching far into mountainous regions, combined with dense population in coastal areas, contributes to high likelihood for disastrous secondary effects from these events. Displacement waves which run up over the shoreline are often responsible for most of the damage after catastrophic failures (Harbitz, Pedersen, & Gjevik, 1993). In total, 33.000 historic landslides are registered throughout Norway, which have resulted in 4475 fatalities (Hermanns, Hansen, et al., 2012). In the last century alone, 174 people lost their lives as a result of displacement waves (Blikra, Arnold, Anda, Dehls, & Stalsberg, 2006). Due to increased tourism and high coastal population, future events might be even more disastrous, unless mitigation measures are taken (Harbitz et al., 2014).

In response to this obvious hazard, the Geological Survey of Norway (NGU) began systematic mapping of unstable rock slopes in 2005. The goal was to identify all rock slopes that could fail catastrophically and determine possible consequences (Hermanns, Oppikofer, Molina, Dehls, & Böhme, 2014). This activity is financed by the Norwegian Water Resources and Energy Directorate (NVE). Of the 19 counties in Norway, 17 are considered relevant for this mapping (figure 1.1). Over 300 potential future rock slope failures are identified so far (e.g. Blikra et al., 2006; Böhme, Dehls, et al., 2013; Böhme, Molina, Dehls, & Hermanns, 2015; Böhme, Saintot, Henderson, Henriksen, & Hermanns, 2011). Six of these are classified as high risk sites and recommended for permanent monitoring (Hermanns, Oppikofer, et al., 2013). The geographic distribution of unstable rock slopes clearly indicates clustering in specific zones, indicating a common cause. Mapping of historical events in the county of Møre og Romsdal reveals a distinct clustering in the inner fjord areas (Blikra, Longva, Harbitz, & Løvholt, 2005).

Information gathered at the different sites are stored in a database developed by NGU (Oppikofer et al., 2015). All potential unstable sites undergo a preliminary consequence analysis, in which sites with evident consequences (i.e. loss of life) are further investigated following directions given by Hermanns, Oppikofer, et al. (2012). The estimation of the hazard and risk level follows a strict classification system developed at NGU (Hermanns, Oppikofer, et al., 2014). The mapping approach was adapted to this classification system and allows resources to be focused on the sites with highest risk.

Investigations in the Rogaland County, Southwestern Norway, commenced in 2014. Systematic mapping has been initiated in three of the 26 municipalities. Displacement measurements started in 2015, and the first results will be available for analysis following the 2016 field campaign. Therefore, it is yet too early to identify any high-risk sites in this county. The rock slope at Tytefjell was investigated by NGU during the 2014 field campaign and classified as unstable. Three differential global navigation satellite system (dGNSS) rovers and one fixed point were installed and measured in 2015. Clear signs of deformation were observed, such as a prominent back scarp and several internal scarps and cracks. These indicate the site may fail catastrophically in the future. Detailed mapping of the Tytefjell unstable rock slope was undertaken as a part of this thesis.



**Figure 1.1:** Map displaying the known unstable rock slopes in Norway (black dots). Mapping is so far carried out in 4 of the 19 counties (Oppikofer et al., 2015). Tytefjell is located in Rogaland, southwestern Norway.

Chapter two of this master thesis introduces the prevailing climatic and geologic conditions at the site. Next, relevant theory is presented and the methodology used is discussed in Chapter three, including descriptions of the field work. The results from the field investigations, analysis and hazard assessment are presented in Chapter four, followed by a discussion in Chapter five. Chapter six presents a conclusion and summarizes the main findings. Chapter seven presents recommendations for further work and improvements for the monitoring network.

## 1.2 Aims and restrictions of the study

This master thesis aims to investigate the unstable rock slope at Tytefjell in order to perform a hazard assessment of different failure scenarios. Multiple methods and tools are applied, e.g. geological fieldwork, use of high resolution digital elevation models (DEMs) and runout modelling. The main workflow includes the following steps:

- Map in detail geological structures (e.g. foliation and joints) and geomorphological features (e.g. depression and scarps). This was done both in the field and by analysing high resolution DEMs. The bedrock lithologies within the unstable area are described.
- Map and define limits of the unstable area in order to determine volumes of the different failure scenarios.
- Perform a structural analysis to identify variations in the mapped geological structures and divide the unstable area into different structural domains. Carry out kinematic analyses for each of the structural domains to determine possible failure mechanisms.
- Classify the unstable rock slope according to the discussed terminology.
- Estimate the rock mass quality by applying the Geological Strength Index (GSI) classification system in the different structural domains within the landslide.
- Construct structural profiles in selected areas of the slope to reduce the uncertainties of the kinematic models.
- Define different failure scenarios within the landslide area based on observed deformation and limiting structures.
- Perform volume calculations for the different scenarios using the “Sloping Local Base Level” (SLBL) method and runout analysis for each scenario using the FlowR software.
- Assess displacement waves for the different scenarios using a model developed at the Laboratory of Hydraulics, Hydrology and Glaciology, ETH Zürich (VAW).
- Assess hazards for each failure scenario using standardized hazard and risk classification developed at NGU.
- Undertake empirical analysis of displacement wave parameters.
- Suggest a suitable monitoring technique for the further investigation of the unstable slope.

The risk analysis, which focuses exclusively on loss of life, is not included due to time restrictions and the amount of data required to perform this analysis. NGU will perform the risk analysis based on the results found in this thesis. However, some of the consequence assessment is done in relation with the displacement wave analysis. Stability calculations and numerical

modelling are not included due to the large size of the instability and time restrictions. Lack of structural data in the subsurface and information regarding the hydrological conditions, severely limits the use of such a model at Tytefjell. The results of this thesis provides useful information for evaluating and improving the current monitoring network at this unstable slope, and the results will be included in NGUs database.

### 1.3 Available data

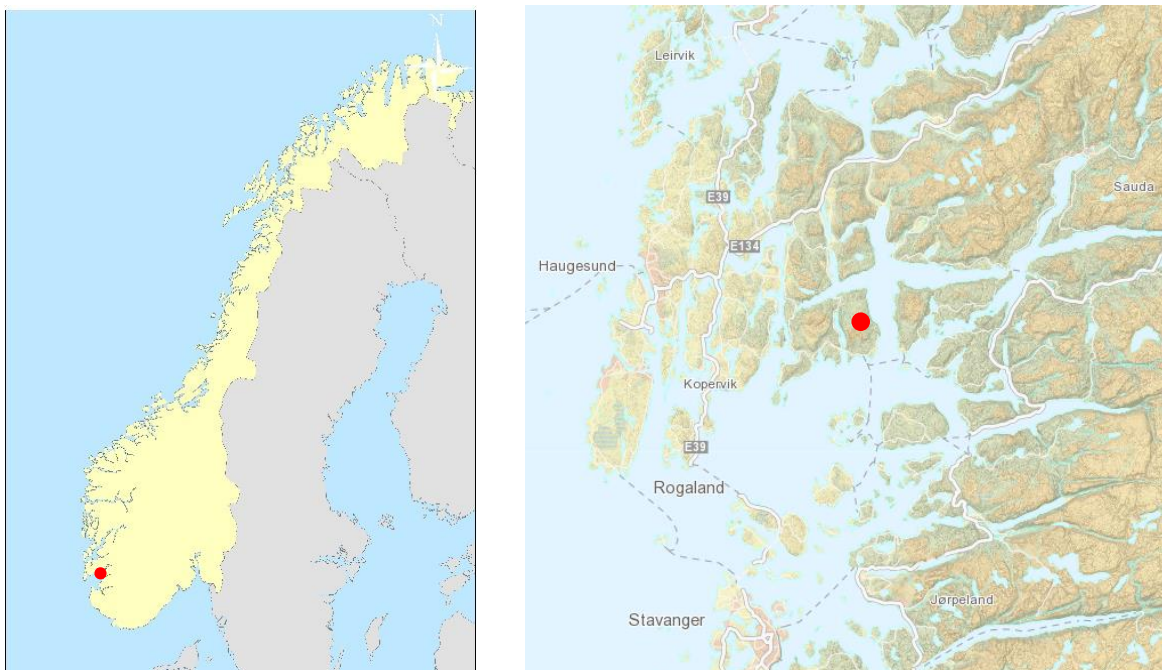
Results presented in this thesis are mostly based on data collected during the detailed mapping performed by the author and Vegard Utstøl Jakobsen from the Norwegian University of Science and Technology (NTNU), during two and a half weeks of field investigations in June 2015. In addition, detailed Light Detection and Radar (LiDAR) data and aerial photographs were made available by the NGU and the Norwegian mapping authority (Statens Kartverk). A summary of the available data is listed in table 1.1. This list also includes the data used in the empirical displacement wave analysis.

**Table 1.1:** Available data

<b>Available data</b>	<b>Source</b>
LiDAR data (1x1 m)	NGU
Aerial photographs	NGU
Topographical data	Norwegian mapping authority (Kartverket)
Geological map Vindafjord	Marker, Solli, and Slagstad (2013)
Location of existing dGNSS points	Trond Eiken, University of Oslo (UiO)
Global catalogue of displacement waves	Roberts, McKillop, Hermanns, Clague, and Oppikofer (2014)
Bathymetric data (Vindafjord)	NGU
Bathymetric data (Loen)	Louise Hansen (NGU)
Bathymetric data (Tafjord)	NGU
Bathymetric data (Chehalis lake)	Nicholas Roberts, Simon Fraser University (SFU)
Bathymetric profiles (Aysén Fjord)	Galderic Lastras, University of Barcelona (UB)
Run-up heights (Aysén Fjord)	Scheele et al. (2013)
Previous work: Empirical analysis of displacement wave data	Böhme (2013)

## 1.4 Location and geological conditions

The site of the Tytefjell unstable rock slope is located on the west side of Vindafjord in Rogaland County, in southwestern Norway (figure 1.2). It is located approximately seven kilometres north of the town of Nedstrand. This fjord is the southern branch of Krossfjorden, which consists of Vindafjord, Yrkefjord and Sandeidsfjord. Vindafjord is 500-700-meter-deep adjacent to the site. The study area is situated on a east facing mountain side where Tytefjell has its peak at 508 meters above sea level. The unstable slope extends 1.2 km in an east-west direction at its widest point, from just below the top of the slope at 500 m a.s.l, down to the fjord. The north-south extension is 2.5 km and the area above water level is around 3 km<sup>2</sup>.

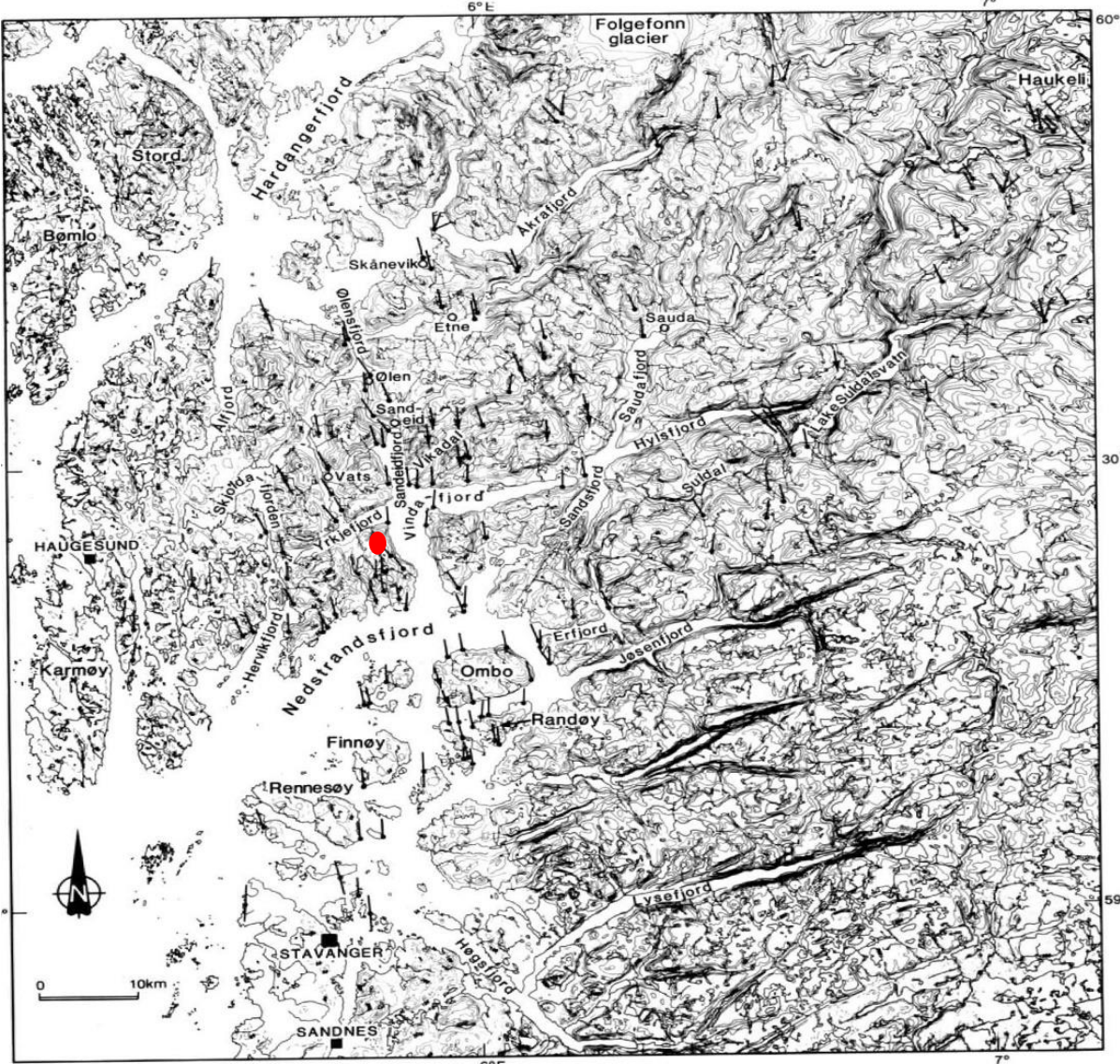


**Figure 1.2:** Figure showing the location of Tytefjell in the southwestern parts of Norway. The unstable slope is located approximately 50 kilometres southeast of Haugesund.

Other potential unstable areas have been discovered by NGU both north and south of Tytefjell in the same fjord region. NGU has also investigated the possibility for an unstable slope on the opposite side of the fjord. These have not yet been mapped in detail. The deformation structures along Vindafjord have been investigated before by NGU (Olesen et al., 2000). They concluded that the deformation visible at Tytefjell is the result of gravitational sliding along discontinuities dipping towards the fjord.

Series of weathered glacial striae along the Vindafjord reveals an old glacial movement towards the south (Anundsen, 1990). The same flow markers are found on the plateaus and in the valley sides (figure 1.3). In total, six different ice movements can be distinguished in this area.

Anundsen (1990) states that there exists a close connection between fault-systems and fjord patterns in the area. NNW-SSE and WSW-ENE are the two main fault directions, which fits well with the Vindafjord fjord system. This is also mentioned by Riis (1977). He describes a major weakness zone striking NNW-SSE west of Tytefjell running along Lysevatnet lake, crossing the Yrkjefjord and continuing northwards along Vatsfjord.



**Figure 1.3:** Glacial flow directions in the Vindafjord area. Black arrows indicate flow direction mainly towards the south. Red dot marks the study area. Modified from (Anundsen, 1990).

#### 1.4.1 Geological conditions

Geological mapping has been done twice in the area, first by Riis (1977) and later by Marker et al. (2013). Riis (1977) classified the rock at Tytefjell as mica schist, but states that the composition of these rocks are essentially the same as the phyllites he mapped further west. The distinction is made mostly on a small difference in grain size and due to a classification scheme that is used in his thesis. Riis (1977) states that these two lithologies are so similar within the area that it is extremely difficult to separate them in the field. The later mapping done in 2013 identified the area as phyllites, and this is the term used in this thesis.

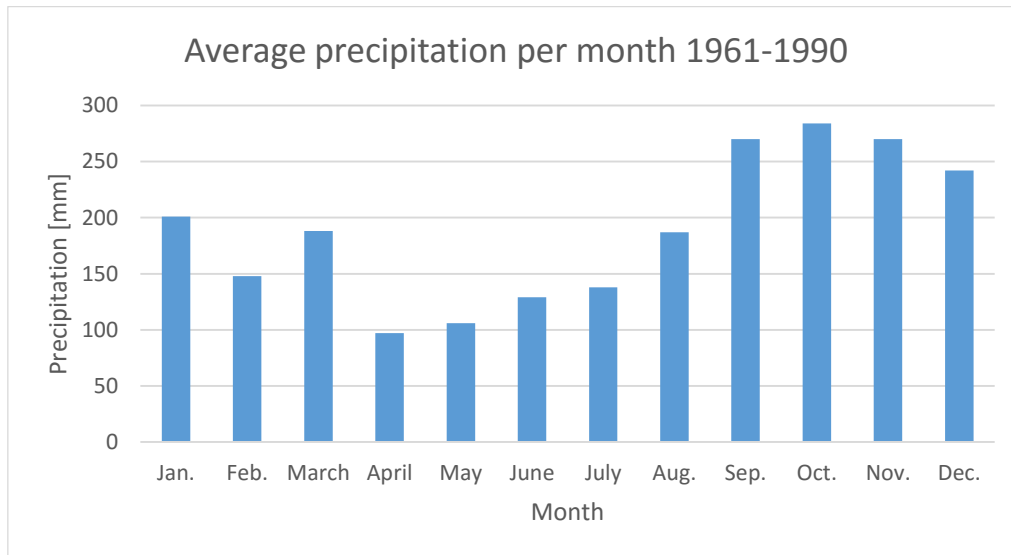
The phyllites at Tytefjell are a part of the Buadalsnappe (Sigmond, 1978). This nappe belongs to a group of rocks called the Ryfylke-schists. These rocks are assumed to be of Cambro-Silurian age and were overthrust during the Caledonian orogeny as part of the lower allochthon (Marker et al., 2013). Transport direction is towards SSE based on mapped lineations (Riis, 1977). It is possible to roughly divide the rocks in the Ryfylke area into bedrock, phyllites and overlying gneisses (Riis, 1977). According to Sørbye (1964), the Nedstrand area is situated in a NNW striking depression in the bedrock which extends all the way from Boknafjord to Hardangerfjord. This area contains a complete nappe-stack ranging from lower to upper allochthon and is similar to other nappes found elsewhere in Norway (Riis, 1977). These remnants of the Caledonian nappes contain rocks of different age and metamorphic grade (Birkeland, 1975). Other theories regarding the origin of the rocks in the southern parts of Norway have been developed more recently by Slagstad, Roberts, Marker, Røhr, and Schiellerup (2013). They argue, based on findings of subduction related features, that an accretionary orogeny is a better alternative to explain the evolution of this area.

Several other active rock slope instabilities composed of phyllites are known and comparable to the situation at Tytefjell. The Ruinon rockslide in Italy is composed of phyllites and is located in a glacial valley (Agliardi, Crosta, & Zanchi, 2001). Similarly, the active rock slope in Stampa, western Norway, is also composed of phyllites (Böhme, Hermanns, et al., 2013). Graphite is observed at this location, but the influence of the graphite bearing lithologies has not been investigated in detail.

#### 1.4.2 Precipitation

Tytefjell lies within the Vindafjord catchment area which covers an area of 55.23 km<sup>2</sup>. The average seepage is 94.5 million m<sup>3</sup>/year based on measurements done from 1961-1990 (NVE, 2015). The closest weather station from Tytefjell lies at Vats in Vindafjord municipality,

approximately 10 kilometres NW of the studied area. The precipitation data is interesting because it is possible to correlate earlier rock falls with heavy precipitation events. The average monthly precipitation in the area is 188 mm with peaks between September-November (Johnsen, 2015). Average precipitation for each month at this weather station is shown in figure 1.4.



**Figure 1.4:** Average precipitation at the measuring station Vats between 1961-1990, based on data received from Johnsen (2015).

The drainage system at Tytefjell is strongly influenced by the observed slope deformation. Anda (2013) found that if the drainage system was controlled by surface runoff, the water level of several lakes west of the landslide would be 6-7 meters higher. He also identified several springs, and creeks disappearing into the ground which provide further evidence of a sub-surface drainage network.

### 1.4.3 Historical events

Based on interviews with locals in the town of Nedstrand, south of the mapped area, there has been one significant rockfall event documented from the frontal limit of the northern sector of the unstable slope. This occurred in November 1999 when a bigger rockfall event created a displacement wave in the fjord directly below the northern sector. A boat lying by a fish farm 450 meters south of the impact area broke loose from the dock, and equipment was washed out in the fjord from another dock lying two meters above water level (figure 1.5). The fish farm itself did not sustain any damage. The event resulted in large amounts of driftwood that caused problems for the fish farm in the following days. Employees at the fish farm who experienced the event, estimated the wave to be less than five meters high. A smaller event occurred from



the same area two years later, in 2001. No damage was reported from this event. According to the employees at the fish farm, smaller rockfall events happen quite frequent especially in rainy periods. This applies to the entire south end of Vindafjord, also at the front of the other unstable slopes in the area.

### **Correlation with precipitation data**

Looking at historic precipitation data, November 1999 has one of the highest recorded values of precipitation at the weather station mentioned in chapter 1.4.2. 481 mm of precipitation was recorded this month, which is 211 mm more than the average for November and 293 mm above the monthly average (Johnsen, 2015).



**Figure 1.5:** Orthophoto showing the northeast sector of the unstable area. The fish farm is located approximately 450 meters south of the impact area. Location of the boat that broke loose and the damaged equipment are indicated. Length of the fish farm is 240 meters. Modified from Kartverket (2015).



## **2. THEORY**

### **2.1 Large rock slope instabilities**

Landslides can occur almost anywhere in the world. This widespread distribution is due to a wide range of controlling factors and triggering mechanisms (Highland & Bobrowsky, 2008). They are one of the most important known agents of topographic change and landscape evolution (Korup, 2012). Large landslides are known for having long runouts that can exceed several kilometres. The reason for this long runout is still debated, see (e.g. Davies & McSaveney, 2012; Hungr, 2006; McDougall, McKinnon, & Hungr, 2012). The phenomenon of long runouts was first discovered in the 19th century in Switzerland (Heim, 1932). Knowledge regarding the possible runout of landslides is important to be able to minimize hazard.

#### **2.1.1 Controlling factors**

According to Fell, Stapledon, and MacGregor (2012), the main controlling factors for landslides are topography, climate, seismicity, geology and geologic discontinuities. In addition, the glacial history can be of importance if the area in question has been glaciated in the past. Several publications conclude that pre-existing geological structures play an important role for large rock slope instabilities (e.g. Agliardi et al., 2001; Ambrosi & Crosta, 2006; Böhme et al., 2011; Brideau, Yan, & Stead, 2009). All known cases of rock slope failure in Norway have been controlled by discontinuities, as weak sedimentary rocks do not exist due to erosional glacial activity (Hermanns, Oppikofer, et al., 2012).

Numerous processes can contribute to and condition a slope towards failure, including (Stead & Eberhardt, 2013):

- Tectonics – folds and faults
- Geologic processes associated with rock genesis – intrusion and alteration
- Geomorphic processes – glacial erosion and rebound, fluvial down cutting
- Earthquakes
- Precipitation and snowmelt events

These processes result in fatigue of the rock slope and a long term accumulation of damage until a critical slope damage threshold is reached and failure occurs (Stead & Eberhardt, 2013).

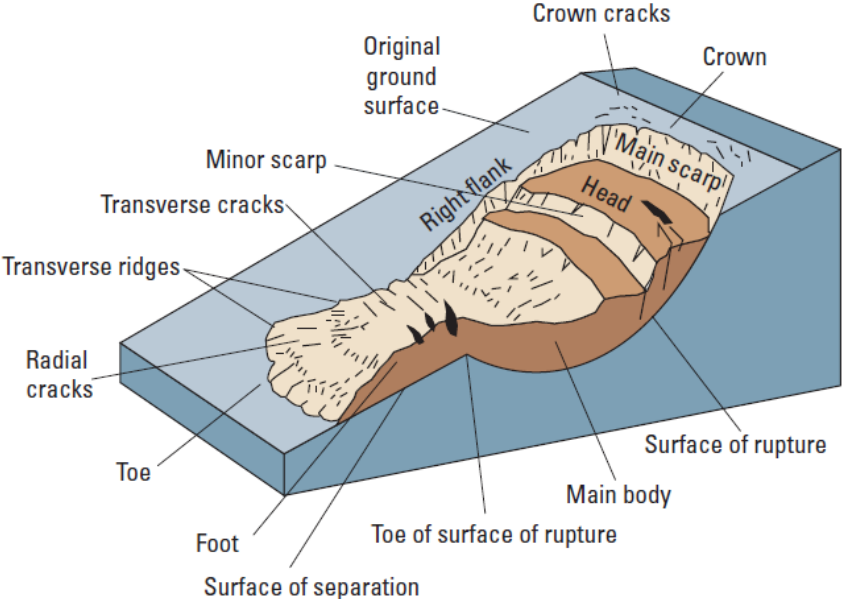
#### **2.1.2 Landslide research**

Areas subjected to slope deformation can provide important information regarding the actual cause of rock slope failures. In order to predict catastrophic events in the future, there is a need

for better understanding of such failures (Braathen, Blikra, Berg, & Karlsen, 2004). As defined by Hermanns and Longva (2012), catastrophic events are failures that involve substantial fragmentation of the rock mass during runout, and which impact a larger area than rockfall events. During the last few years, landslide research has progressed to include methods from several disciplines such as geomorphology, structural geology, engineering geology and remote sensing e.g. (Böhme, Hermanns, et al., 2013; Booth et al., 2014). This combination of different methods, notably geophysics and remote sensing contributes to unprecedented amounts of data available to study landslides (Stead & Eberhardt, 2013).

### 2.1.3 Classification and terminology

The most commonly used landslide classification system today was developed by Varnes (1978) and later updated and republished by Hungr, Leroueil, and Picarelli (2014). This classification system is based on the type of movement and materials involved. It does not provide a precise tool for describing large slope scale slope instabilities, but is more suitable for smaller failure scenarios (Jaboyedoff, Penna, Pedrazzini, Baroň, & Crosta, 2013). The same publication by Hungr also defined most of the landslide terminology used in scientific publications today, which is also followed in this thesis (figure 2.1). However, a classification system for the structures and fabrics produced by the landslide processes described in these publications does not yet exist (Jaboyedoff et al., 2013). The diversity of definitions and classification systems reflects the complexity associated with large landslides (Highland & Bobrowsky, 2008).



**Figure 2.1:** Landslide terminology (Varnes, 1978).

#### 2.1.4 Deep seated gravitational slope deformation (DSGSD)

DSGSDs are one type of large scale slope movement that has been extensively studied since the 1940's when this phenomenon was first described (Stini, 1941). It has been defined in different ways by several authors.

Agliardi et al. (2001) listed characteristic features typical for this type of slope deformation:

- Presence of characteristic morpho-structures such as scarps, counterscarps, trenches and double ridges.
- Size of the unstable area comparable to the whole slope.
- Low rate of displacement, often at, or below the detection limit of monitoring equipment.
- Presence of minor landslides within the unstable area in addition to collapse of the lower part of the slope.
- DSGSDs are often observed along deep glacial valleys in rock mass composed of foliated metamorphic rocks.
- Contraction of valley floor and bulging of the frontal sector of the unstable area, leading to highly fractured rock masses at the slope toe.

A rear scarp behind the hill crest is typical for some types of DSGSDs (Hutchinson, 1988). This type of deformation is not necessarily bounded by a continuous yielding surface and can often have poorly defined lateral boundaries (Agliardi, Crosta, & Frattini, 2012). Two or more rock slope failures situated side-by-side sharing parts of the same lateral boundary are common. Agliardi et al. (2012) states that at the scale of entire slopes, steeply dipping fractures appear to be particularly important in constraining the localization, geometry and surface expression of DSGSDs. All these diagnostic features are often masked by weathering and erosion. A database of DSGSDs in the European alps developed by Agliardi et al. (2012) including 904 separate slopes covering an area of 5472 km<sup>2</sup>, indicated that DSGSDs are most common in foliated metamorphic rocks with 12.7 % areal density.

## 2.2 Secondary effects

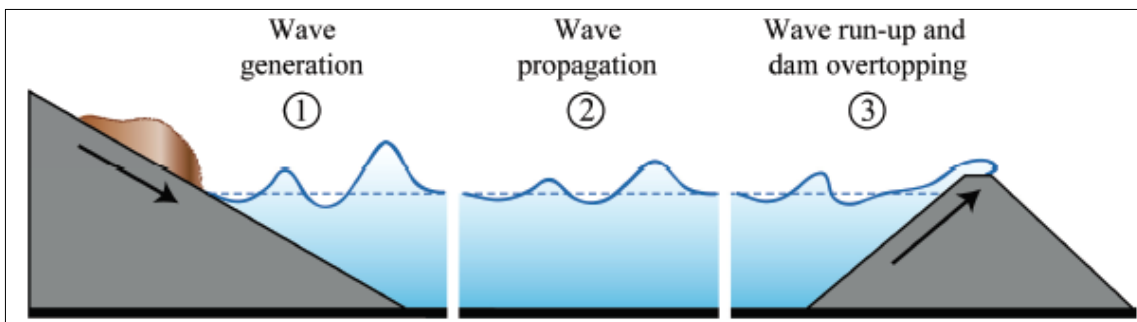
Secondary effects from large rock slope failures in Norway have caused devastating catastrophes with many fatalities (table 2.1). These effects include damming of valleys and subsequent dam burst with downstream flooding as well as landslide triggered displacement waves in fjords, lakes and reservoirs (Hermanns, Hansen, et al., 2012). Since a displacement wave is the most severe secondary effect from a failure at Tytefjell, this is described in more detail in the following sub-chapter.

**Table 2.1:** The ten most devastating mass movement events in Norwegian history. Sorted after fatalities. (Hermanns, Hansen, et al., 2012).

Type of event	Year	Fatalities
Landslide damming and dam burst	1345	500
Quick clay landslide	1893	116
Rock avalanche and displacement wave	1936	74
Rock avalanche and displacement wave	1905	61
Rock fall	1811	45
Rock avalanche and displacement wave	1934	40
Rock avalanche and displacement wave	1756	32
Snow avalanche	1868	32
Snow avalanche	1679	28
Snow avalanche	1679	27
Snow avalanche	1770	27

### 2.2.1 Displacement waves

Displacement waves are typically caused by landslides, rockfall, snow avalanches or glacial calving in oceans, bays, lakes or reservoirs (Heller, Hager, & Minor, 2009). They occur in a range of different environments including continental margins, ocean islands, fjords, natural and artificial dams and rivers (Hermanns, L’Heureux, & Blikra, 2013). Displacement waves should not be confused with the similar tsunami phenomenon. The term tsunami is Japanese and translates to “sudden wave in harbour” and is used to describe earthquake triggered waves (seismic waves) (Hermanns, L’Heureux, et al., 2013). Displacement wave is used here for waves triggered by subaerial mass movement. Figure 2.2 displays the three different faces of a displacement wave generated in a reservoir. The initial wave amplitude of displacement waves triggered by subaerial landslides can be up to hundreds of meters in contrast to the waves generated by subaqueous landslides that are in general in the order of a few meters (Hermanns, L’Heureux, et al., 2013)



**Figure 2.2:** The three different phases of displacement waves (Heller et al., 2009). This example shows a landslide going into a reservoir with subsequent dam overtopping. The three faces are also applicable to waves generated in fjords.

Displacement waves occurring in fjords, lakes and reservoirs can cause large oscillations resulting in a series of waves. These waves can last for hours and the first wave is not necessarily the largest (Harbitz et al., 2014). Tests have shown that highest run-up is obtained where the wave impacts the shore perpendicularly, typically in the heads of the fjord systems (Harbitz et al., 2014). Displacement and tsunami waves are known to have higher wavelengths than ordinary waves created by wind. Since fjords and lakes restrict the propagation of the waves, the energy concentrates and results in a higher run-up compared to tsunami waves hitting the shore line.

The run-up of a displacement wave starts when the wave comes into shallow water. As the velocity of the wave depends on water depth; shallower water results in lower wave velocity. The shoaling waves slow down, shorten in wavelength and grow in amplitude when approaching the shoreline (Ward, 2011). Displacement waves occupy more of the water column than ordinary beach waves, and thus their shoaling amplification is higher (Ward, 2011).

2.2.2 Modelling of displacement waves

According to Heller et al. (2009), five methods for predicting landslide generated displacement waves exist:

- (i) Generally applicable equations developed from model tests
- (ii) Prototype-specific model tests
- (iii) Numerical simulations
- (iv) Empirical equations derived from field data
- (v) Analytical investigations

These are compared in table 2.2 in terms of six different parameters and show that the highest quality results incur higher cost and time consumption. Heller et al. (2009) concludes that empirical methods are still not fully developed.

**Table 2.2:** Comparison of five methods for the prediction of displacement waves (Heller et al., 2009).

Criterion	Method (i)	Method (ii)	Method (iii)	Method (iv)	Method (v)
Quality of results	Estimation	Exact	Estimation - exact	Rough estimate	Rough estimate
Time requirement	Low	Very high	High - very high	Low	Low
Cost	Low	Very high	High - very high	Low	Low
User	Engineer	Engineer	Expert	Engineer	Engineer
Clarity	Medium	High	Low	Medium	Low
Effort for governing parameters	Medium	High	High	Medium	Medium

Several parameters have to be taken into account when modelling displacement waves using numerical models; volume of moving mass, morphology of the frontal area, water depth and sliding velocity (Hermanns, L'Heureux, et al., 2013). Sensitivity analyses show that the frontal area of the rockslide is more important than the volume when it comes to wave generation (Harbitz et al., 2014). Heller et al. (2009) states that the water depth and the angle of the run-up slope are believed to be governing factors for the wave run-up height. Equation 3.16 in Heller et al. (2009) which is applied in the VAW model, predicts greater run-up height with decreasing run-up slope angle. This equation is based on experimental data derived by Müller (1995) by testing run-up height for three different run-up slope angles: 18.4°, 45° and 90°.

Numerical modelling of displacement waves is a complex and often very expensive task. Empirical equations derived from field data have a low time requirement and low cost but give only rough estimates of the run-up heights (Heller et al., 2009). This is because the field data inputs and the governing parameters are often estimates, e.g. volume estimations from bathymetry data (Heller et al., 2009). Nevertheless, in certain situations, it can be very useful to get a quick estimate of run-up heights, using empirical equations.

### 2.2.3 Previous work to develop an empirical run-up relationship

Due to the high levels of cost and complexity of numerical simulations, researchers at NGU developed an empirical relationship between run-up height, distance to impact and impact volume (Böhme, 2013; Oppikofer et al., in press). Böhme used a worldwide inventory of landslide-triggered displacement waves compiled by Roberts et al. (2014), which contains general landslide parameters and details about the resulting displacement waves. These empirical relations are foreseen to form a first, quick tool to assess consequences from landslide-triggered displacement waves (Oppikofer et al., in press).

Adjustments were made to some of the historical volume estimations as described in the following to better represent the actual volume of material that entered the water for each event (Böhme, 2013). The volume of the Tafjord event is reported as 3 Mm<sup>3</sup> in most publications, however analyses done by Oppikofer (2009) suggested a more accurate volume of 2.7 Mm<sup>3</sup>. The Punta Cola landslide, which will be further discussed in section 2.3.1, was reported to have an initial volume of approximately 20.9 Mm<sup>3</sup>, although only around 14 Mm<sup>3</sup> entered the fjord (Oppikofer et al., 2012). In addition, bay effects were removed for four of the events, by omitting points where the general run-up trend deviated due to local bays (Lituya bay, Tafjord, Loen and Chehalis Lake). Averaging the run-up heights at nearby locations gave better fits for



the Tafjord event (Böhme, 2013). This was done where the distance between the run-up estimates were small.

The 10 displacement wave events with multiple registered run-up heights used in the analysis by Böhme (2013) is listed in table 2.3:

**Table 2.3:** Location, year and volume of the 10 events analysed by Böhme (2013). In addition, the publication describing each event is listed.

<b>Landslide event</b>	<b>Location</b>	<b>Year</b>	<b>Volume [Mm<sup>3</sup>]</b>	<b>Description</b>
Scilla	Italy	1783	5.4	Mazzanti and Bozzano (2011)
Loen lake	Norway	1905	0.35	Grimstad and Nesdal (1990)
Tafjord	Norway	1934	2.7	Blikra et al. (2005)
Loen lake	Norway	1936	1	Grimstad and Nesdal (1990)
Lituya bay	Alaska	1958	30.6	Fritz, Mohammed, and Yoo (2009)
Isla Mentiroso	Chile	2007	8	Scheele et al. (2013)
Chehalis lake	Canada	2007	1.5	Roberts et al. (2013)
Punta Cola	Chile	2007	14	Scheele et al. (2013)
Wu Gorge	China	2008	0.38	Huang et al. (2012)
Aratozawa	Japan	2008	1.5	Miyagi, Yamashina, Esaka, and Abe (2010)

Several analyses were conducted by Böhme (2013);

- Analysis of the 10 events listed in table 2.3 in 2D
- Analysis of all data in 3D
- Different 3D functions were tested with different input data

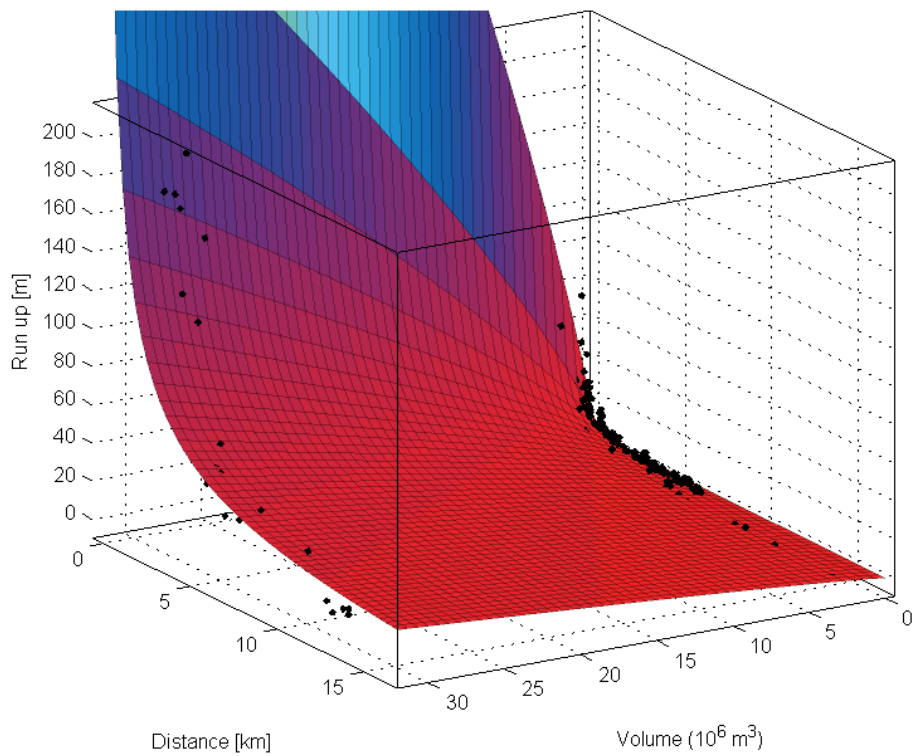
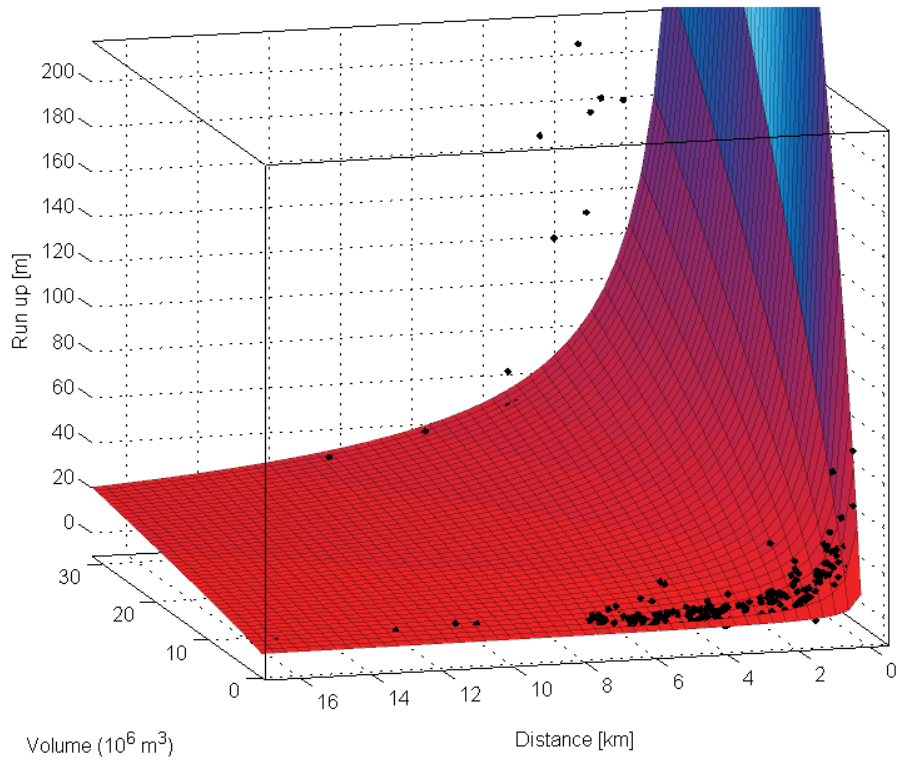
The 2D analysis performed by Böhme (2013) showed that a 2D power-law ( $f(x) = ax^b$ ), gave the best fit for all events when plotting run-out as a function of distance, where  $x$  is distance and  $a$  and  $b$  are constants. The goodness of fit was judged upon the coefficient of determination ( $R^2$ ). This quantity measures the proportion of the variability that is explained by the fitted model, where  $R^2=1$  indicates a perfect fit (Walpole, Myers, Myers, & Ye, 2012). Four of the events had poor fits ( $R^2<0.6$ ) (Böhme, 2013). This applies to the following events: Loen 1905, Punta Cola, Aratozawa and Scilla. The remaining six events with good fits ( $R^2>0.6$ ) were considered for further analysis.

Six different 3D functions with different constants were investigated, giving different fits (table 2.4). A 3D power law was used to calculate the fitted surface shown in figure 2.3 (Böhme, 2013). The best fits achieved with this equation gave only  $R^2\sim 0.5$ . Results from the 3D analysis revealed that approximately 200 of the registered measurements plotted above the fitted curve (out of total 453) for all the investigated equations, which means that the actual run-up is higher

than the calculated one for these points. The high uncertainties ( $\pm 10\text{-}15\text{m}$ ) are most likely due to local effects in bays and at the end of fjords, where wave heights get exaggerated (Oppikofer et al., in press). This was concluded to be too much to replace the currently used method (VAW) for empirical calculation of the run-up heights (Böhme, 2013). Additional parameters such as slide impact velocity, wave propagation angle from impact, water depth and run-up slope angle still need to be taken into account to reduce the uncertainties and to make this empirical relation a useful tool (Oppikofer et al., in press). The dataset prepared by Böhme (2013) is used and built on during the work performed in this thesis.

**Table 2.4:** The six different empirical relations tested by Böhme (2013).

Equation number	Formula D = distance [Km] V = volume [Mm <sup>3</sup> ]	Constants
1	$Run\ up = a * \left(\frac{V}{D}\right)^b$	a = 11.85 b = 0.4382
2		a = 11.91 b = 0.837
3		a = 13.17 b = 0.6433
4	$Run\ up = \left(\frac{V}{a+b * D^2}\right)$	a = 0.151981 b = 0.013847
5	$Run\ up = a * e^{(b*D+c*V^2)} + d$	a = 23.82 b = -0.3421 c = 0.002987 d = 0.8328
6	$Run\ up = a * b^V * D^c$	a = 9.546 b = 1.133 c = -1.101



**Figure 2.3:** Empirical power-law relationship between run-up height, volume and distance from impact developed by Böhme (2013), seen from two different view angles. The graphs show a relatively good fit, but has high uncertainties.

## 2.3 Case studies – Displacement waves

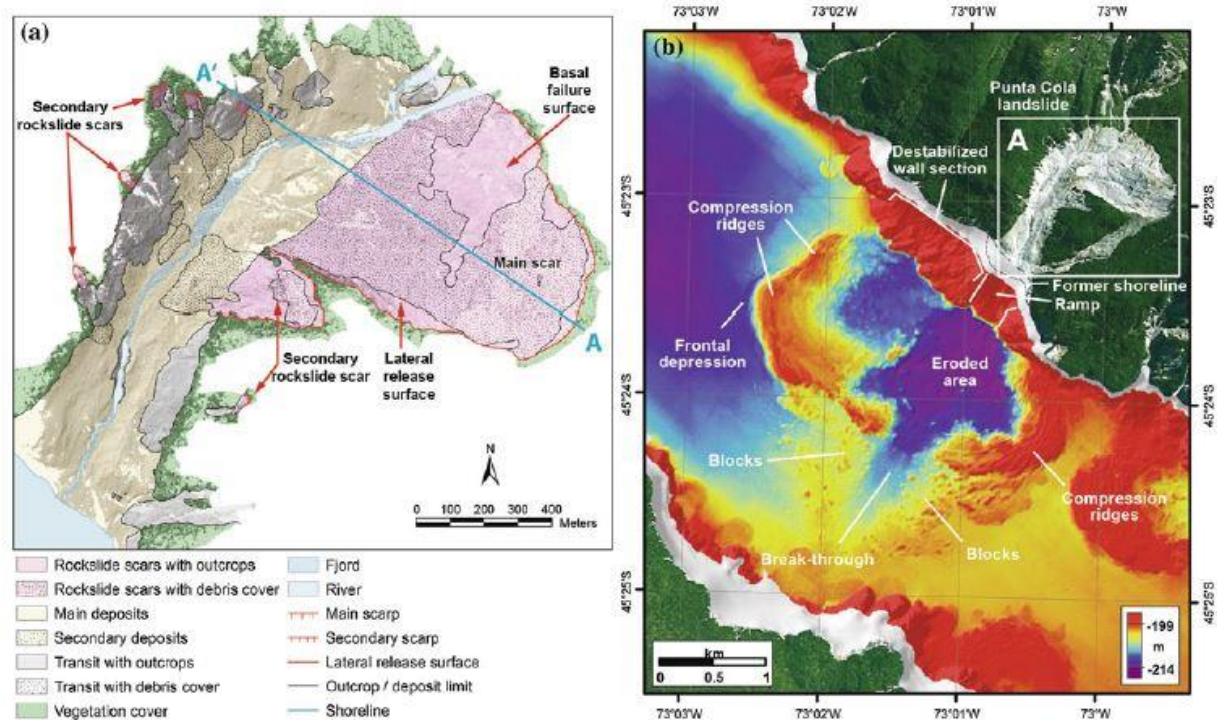
Insights gained from mapping and understanding earlier landslide events can be used to evaluate and quantify imminent hazard related to large rock avalanches and displacement waves (Blikra et al., 2005). The assessment of hazard and risk posed by displacement waves is still at an early stage. However significant advances have been made in this field the last decades (Hermanns, L'Heureux, et al., 2013).

Mass movements into standing bodies of water with subsequent displacement waves are an imminent danger also outside Norway. Two case-studies, from Chile and Canada are included to show how landslide mapping and displacement wave modelling can be used to understand the dynamics of such events. In addition, a case study from one of the best known displacement wave events in Norway (1934 Tafjord event) is presented to shed light on the massive forces involved in such events.

### 2.3.1 Aysén events, Chile

On the 21<sup>st</sup> of April 2007, over 500 landslides were triggered along the Aysén fjord by a moment magnitude ( $M_w$ ) 6,2 earthquake (Hermanns, Sepúlveda, et al., 2014). The largest landslide had a volume of 20.9 million  $m^3$  of rock and occurred in the Punta Cola valley, 1-1.75 km from the shore (figure 2.4). Entrainment of material caused the landslide to increase in volume before entering the fjord. This caused the failure of a 100-meter-wide section of the delta along the shoreline and submarine slope failure. In total, this mass movement deformed an area of 7.6  $km^2$  of the fjord bottom (Hermanns, Sepúlveda, et al., 2014).

The combined effect of the landslide and several other events in the same area generated a series of displacement waves within the fjord that caused ten fatalities and severe damage to the salmon industry. The Aysén event demonstrated the large impact subaerial landslides can have on the morphology of the fjord floor (Hermanns, Sepúlveda, et al., 2014). Modelling reproduced the observed run-up heights on nearby islands but differed by a factor of 2-3 in more distal areas. This might be explained by the sudden upward movement of the marine sediments due to the landslide impact, which was not included in the displacement wave model (Hermanns, Sepúlveda, et al., 2014).



**Figure 2.4:** (a) Overview over the Punta Cola rockslide. (b) Combined satellite imagery and bathymetric map of the Punta Cola landslide area (Hermanns, Sepúlveda, et al., 2014).

### 2.3.2 Chehalis Lake event, Canada

A 3 Mm<sup>3</sup> debris avalanche entered the Chehalis Lake, British Columbia, on the 4<sup>th</sup> of December 2007 (Roberts et al., 2013). The rock mass slid into a steep gully, then rapidly disintegrated into a debris avalanche which travelled 800 meters including an elevation drop of approximately 550 meters. The resulting displacement wave caused damage along the shoreline of the lake and also far down the Chehalis River (>15km) (Roberts et al., 2013). Known displacement wave events in this area are concentrated along rivers or lakes with steep slopes of unconsolidated sediments or in glacially carved valleys with steep bedrock slopes (Roberts et al., 2013).

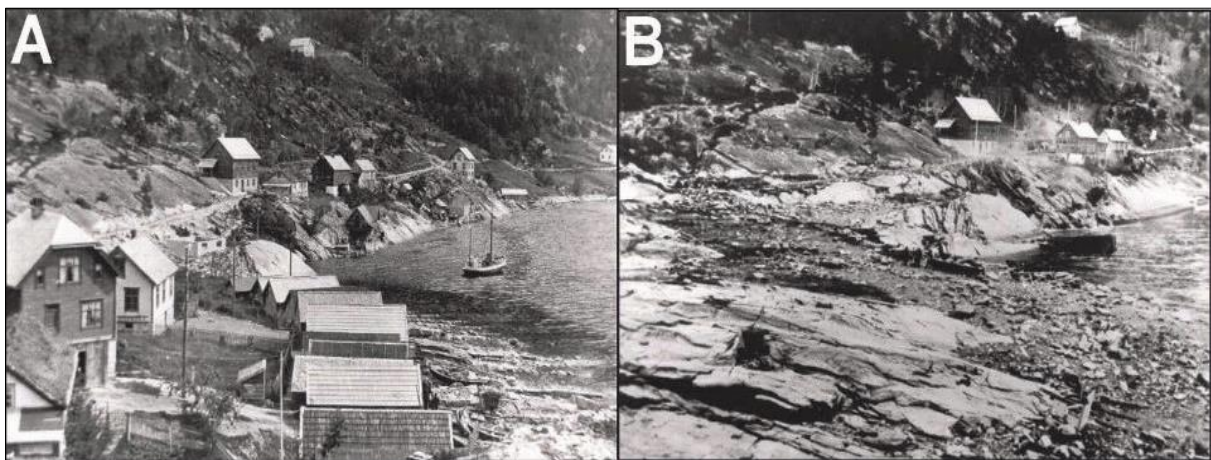
The authors mapped geomorphic impacts caused by the displacement wave which can provide information on wave energy, inundation, run-up, trajectory and energy. This information is also useful to identify the sites of past events, as vegetation trim lines may be visible for decades after the event (Roberts et al., 2013). The severity of the impact of the displacement wave, the elevation above and distance travelled from the lake shore decrease to the south away from the landslide, but increase near lake outlet. Most prominent geomorphic markers are recorded along the northern third of the lake, adjacent to and across from the landslide. The authors found an evident vegetation trim line in these areas. Woody debris remaining in trees was used as an

indicator for the wave inundation level, and debris wrapped around trees as indicator of wave direction.

The spatial distribution of displacement wave impact features suggests that wave energy and run up heights are influenced by a combination of distance to the landslide, bathymetry, shoreline orientation and distance from the shoreline (Roberts et al., 2013). Landslide generated waves result in a range of erosional, impact and depositional features that provide useful information on wave dynamics. This information can be used to improve wave models and thus contribute to more reliable hazard and risk assessments in the future (Roberts et al., 2013).

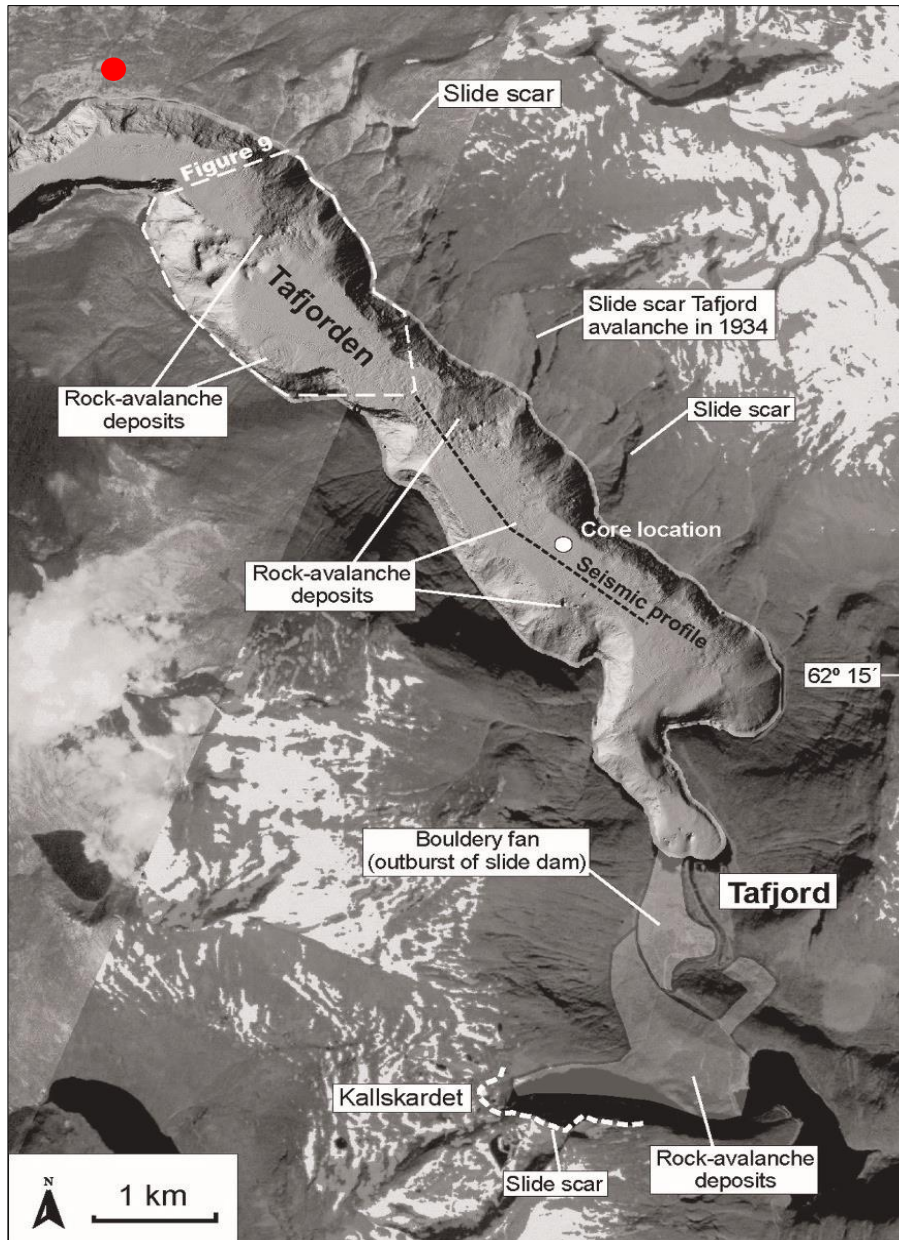
### 2.3.3 Tafjord event, Norway

The Tafjord landslide event occurred in April 1934 when 3 Mm<sup>3</sup> of rock fell into the fjord close to the village of Fjørå in Møre og Romsdal county (figure 2.5). The resulting displacement wave run-up reached a maximum of 62 meters above sea level causing the destruction of several villages adjacent to the fjord and killing 41 people (Blikra et al., 2005). This area also shows a high frequency of historic landslides. More than 10 rock avalanche deposits have been mapped in the fjord within seven kilometres from the Tafjord landslide (figure 2.6) (Blikra et al., 2005).



**Figure 2.5:** The village of Fjørå in Tafjord before **A** and after **B** the 1934 displacement wave (Furseth, 1985).

Pre-existing discontinuities play an important role on the stability of this area. The foliation dips steeply, to moderately, towards the fjord. Additional sub-vertical fractures parallel and perpendicular to the slope, delimited the failed block. The foliation was especially important for the 1934 event (Braathen et al., 2004). Back analysis of events such as this one, where run-up heights are known, can improve displacement wave models. Numerical simulations of displacement waves have, returned reasonable results. A back analysis of the 1934 event was performed by Harbitz et al. (1993), and showed good agreement with measured run-up heights.



**Figure 2.6:** Figure showing rock avalanche deposits and scars in Tafjord. The position of the 1934 event is shown. Red dot indicates the position of the village Fjóra shown in figure 2.5. Modified after Blikra et al. (2006).

## 2.4 LiDAR scanning

LiDAR is a remote sensing technique that has caused a revolution in landslide investigations. The generation of 3D terrain models is opening new methods of investigating landslides (Jaboyedoff et al., 2012). In this thesis, LiDAR data has played a crucial role in both the mapping and later investigations of the unstable slope at Tytefjell because of the opportunity to view the rock surface in great detail without vegetation cover.

Jaboyedoff et al. (2012) lists the applications of this method:

- Detection and characterization of mass movements.
- Hazard assessments and susceptibility mapping.
- Modelling.
- Monitoring.

LiDAR scans provide high resolution point clouds that can be converted to terrain models and hillshades. The density of the point clouds, and hence the resolution of the models, depends on the position of the sensor. Airborne Laser Scanning (ALS) gives a lower resolution (metric to desi metric) compared to millimetric to desi metric for Terrestrial Laser Scanning (TLS) (Jaboyedoff et al., 2012).

## **2.5 NGU mapping approach**

The overall goal of NGU's mapping activities is to identify all unstable rock slopes in Norway which could fail catastrophically. This mapping approach involves a combination of several steps and was developed to address the need for a standardized mapping approach and to serve as input for the hazard and risk classification developed by Hermanns, Oppikofer, et al. (2013). To ensure that resources are directed primarily towards high risk sites, sites with no consequences in case of failure are eliminated from further investigations early in the process. The level of detail of geologic information required will not be equal for sites with different risk levels. Outcomes of the hazard and risk analysis will thus be different according to the level of detail of geologic information (Hermanns, Oppikofer, et al., 2014). The level of detail required for hazard maps increases with increasing risk level. Inconsequential sites are present on hazard maps without a hazard class, while medium and high risk sites will show the assigned hazard classes (Hermanns, Oppikofer, et al., 2014). It is important to standardize the mapping approach so that results from the hazard and risk analysis are comparable and reproducible. The hazard maps created provide meaningful information for decisions about where to direct resources.

The approach was developed as an iterative process; starting with a simple assessment of remote sensing imagery to identify possible unstable sites, before investigations continue in the field. During field reconnaissance, sites with no real signs of deformation of large rock volumes are divided in three categories; (1) rockfall area, (2) not relevant or (3) potential unstable area (Hermanns, Oppikofer, et al., 2014). The final category needs to be followed up after several years to look for changes. All sites that are classified as a potentially unstable area undergo a



preliminary consequence analysis. This is the step in which sites with no buildings or life lines in the runout area are discarded from further investigations. Sites with evident hazard will be further investigated. Based on the geological mapping, two situations are possible; the geological conditions are well understood, or the simple geological mapping did not provide enough information. For the latter case, periodic displacement measurements and detailed geological mapping becomes necessary (Hermanns, Oppikofer, et al., 2014). NGU uses a wide variety of displacement monitoring techniques including; extensometers, dGNSS, Interferometric Synthetic Aperture Radar (InSAR), TLS and photogrammetry (Hermanns, Oppikofer, et al., 2014).

## **2.6 Hazard assessment**

Systematic mapping in three of Norway's 17 relevant counties has revealed more than 300 potential unstable slopes (Oppikofer et al., 2015). This high number of sites makes it essential to standardize both the mapping approach and the hazard and risk classification system especially for Norwegian conditions (Hermanns, Oppikofer, et al., 2012). A group of 18 Norwegian and five international experts participated in the discussion leading to this classification system. Due to the large cost of monitoring systems and periodic displacement measurements, an objective classification system was needed to assist the decisions regarding the follow up after the initial mapping. This includes types of monitoring, further investigations or mitigation measures (Hermanns, Oppikofer, et al., 2012).

*“The hazard analysis focuses on capturing unfavourable geological conditions, morphological features expressing slope deformations and changes within the slope that can give a hint of the stability state of the slope as well as on the area that will be impacted by direct impact of the rockslide or a related secondary effect”* (Hermanns, Oppikofer, et al., 2013, p. 246).

### **2.6.1 Defining failure scenarios**

NGUs hazard classification system is scenario based, which means that the process of hazard and risk need to be performed independently for all possible failure scenarios. This is necessary because the scenarios may have different failure probabilities and volume, thus having different consequences and risk (Hermanns, Oppikofer, et al., 2012). A realistic estimate of the scenario volumes is vital for the risk management in the hazard areas (Blikra & Kristensen, 2013). Since no detailed information on the historic repeated failures in Norway exist (e.g. The Loen events), the system base the scenarios on varying geological conditions and displacement rates (Hermanns, Oppikofer, et al., 2012).

According to Hermanns, Oppikofer, et al. (2012), different scenarios need to be analysed at slopes that show a combination of:

- Different deformation rates.
- Varying structural conditions.
- Internal scarps, cracks and depressions which dissect the unstable slope.

Due to the complexity of rock slope failures, the likelihood of failure cannot be given quantitatively. Therefore, the risk analysis is based on a qualitative hazard assessment and a quantitative consequence analysis. Timing of earthquakes cannot be predicted with today's knowledge, thus, the classification system focuses only on aseismic failures (Hermanns, Oppikofer, et al., 2012). The authors state that the system should be updated once more scientific knowledge becomes available.

### 2.6.2 Hazard classification

The hazard classification uses nine criteria as shown in figure 2.7 describing the present state of an unstable slope. These can be arranged in three main groups (Hermanns, Oppikofer, et al., 2012):

- The structural/morphologic development of the unstable slope.
- Displacement rates and other signs of activity.
- Earlier events on the same slope section.

For each criterion several conditions are possible and a score is assigned to each condition as showed in figure 2.7. The sum of these scores gives the total hazard score for that scenario. This score can range from 0 to 12 and it is assumed that the likelihood of failure increases with increasing hazard score (Hermanns, Oppikofer, et al., 2012).

It is often difficult to choose only one of the specified conditions. To account for these uncertainties, it is possible to assign probabilities for each condition (figure 2.7). In order to calculate the entire range of possible outcomes this automated step is organized in a decision tree as explained thoroughly in Hermanns, Oppikofer, et al. (2012). The advantage of the decision tree is that the outcome is a range of possible hazard classes instead of giving a single hazard score. A detailed description of the nine criteria used in the hazard analysis is available in Hermanns, Oppikofer, et al. (2012).

<b>1. Back-scarp</b>	<b>Score</b>
Not developed	0
Partly open over width of slide body (few cm to m)	0.5
Fully open over width of slide body (few cm to m)	1
<b>2. Potential sliding structures</b>	<b>Score</b>
No penetrative structures dip out of the slope	0
Penetrative structures dip on average < 20 degree or steeper than the slope	0.5
Penetrative structures dip on average > 20 degree and daylight with the slope	1
<b>3. Lateral release surfaces</b>	<b>Score</b>
Not developed	0
Partly developed on 1 side	0.25
Fully developed or free slope on 1 side or partly developed on 2 sides	0.5
Fully developed or free slope on 1 side and partly developed on 1 side	0.75
Fully developed or free slope on 2 sides	1
<b>4. Kinematic feasibility test</b>	<b>Score</b>
Kinematic feasibility test does not allow for planar sliding, wedge sliding or toppling	0
Failure is partly kinematically possible (movement direction is more than $\pm 30^\circ$ to slope orientation)	0.5
Failure is kinematically possible (movement direction is less than $\pm 30^\circ$ to slope orientation)	0.75
Failure is partly kinematically possible on persistent discontinuities (movement direction is more than $\pm 30^\circ$ to slope orientation)	0.75
Failure is kinematically possible on persistent discontinuities (movement direction is less than $\pm 30^\circ$ to slope orientation)	1
<b>5. Morphologic expression of the rupture surface</b>	<b>Score</b>
No indication on slope morphology	0
Slope morphology suggests formation of a rupture surface (bulging, concavity-convexity, springs)	0.5
Continuous rupture surface is suggested by slope morphology and can be mapped out	1
<b>6. Displacement rates</b>	<b>Score</b>
No significant movement	0
0.2 - 0.5 cm/year	1
0.5 - 1 cm/year	2
1 - 4 cm/year	3
4 - 10 cm/year	4
> 10 cm/year	5
<b>7. Acceleration (if velocity is &gt;0.5 cm/yr and &lt;10 cm/yr)</b>	<b>Score</b>
No acceleration or change in displacement rates	0
Increase in displacement rates	1
<b>8. Increase of rock fall activity</b>	<b>Score</b>
No increase of rock fall activity	0
Increase of rock fall activity	1
<b>9. Past events</b>	<b>Score</b>
No post-glacial events of similar size	0
One or several events older than 5000 years of similar size	0.5
One or several events younger than 5000 years of similar size	1

**Figure 2.7:** Nine criteria describing the present state of the unstable slope. For each criterion, several conditions are possible. Scores can be assigned to several of the conditions for one criterion to take consideration of the uncertainties (Hermanns, Oppikofer, et al., 2013).

### 2.6.1 Hazard classes

The possible hazard scores are divided into five hazard classes ranging from very low to very high hazard (table 2.5). Summing the probabilities of the hazard scores within the range of each hazard class gives the probability of that class.

**Table 2.5:** The five possible hazard classes resulting from the hazard assessment. The given ranges include the lower number, but excludes the highest. e.g. [7.2; 9.6] goes from 7.2-9.6 including 7.2, but excluding 9.6. Modified from Hermanns, Oppikofer, et al. (2012).

Hazard class	Hazard Scores
Very low	[0.0; 2.4]
Low	[2.4; 4.8]
Moderate	[4.8; 7.2]
High	[7.2; 9.6]
Very high	[9.6; 12.0]

## 2.6.2 Consequence assessment

The NGU consequence assessment involves four main steps with different levels of detail according to the approach for systematic mapping of unstable rock slopes (Oppikofer et al., in press). This methodology includes assessment of secondary effects such as displacement waves. This assessment differs based on risk level. A first approach involves application of empirical relations and empirical models such as VAW. Medium to high risk sites may require detailed numerical simulation (Oppikofer et al., in press). This can be performed using the Dpwaves and GloBouss models as applied by Harbitz et al. (2014). Further development of this consequence assessment will also include consideration of landslide dams (Oppikofer et al., in press). The assessed consequences are combined into a qualitative hazard assessment to classify the risk posed by an unstable slope.

## 2.7 Internal friction angle of graphitic phyllites

The internal friction angle of the rock determines the size of the friction cone in the stereonet and thus becomes an important parameter in kinematic analyses. Davies and McSaveney (2012) state that the internal friction angle of rocks usually lies between 30-35°. According to Wyllie and Mah (2005 p. 81), “*Fine grained rock with a high mica content aligned parallel to the surface, such as a phyllite, will tend to have a low friction angle...*”. They estimate the typical friction range of phyllites to lie between 20-27°. Graphite is well known for being a solid lubricant (e.g., Oohashi, Hirose, and Shimamoto (2013); Oohashi, Hirose, and Shimamoto (2011); Savage (1948)). Hoek and Brown (1980) estimate the internal friction angle of graphite to lie between 8-16°. Even lower estimates are proposed by Oohashi et al. (2011) where friction experiments at various slip rates were performed. They state that the friction coefficient of pure graphite lies around 0.1. This is equivalent to an internal friction angle of 5.7°. For any given shear strain and slip rate, a 5-20 volume % content of graphite leads to decreased friction coefficients, giving values similar to pure graphite with 30-50 volume % (Oohashi et al., 2013)

## **3. METHODS**

### **3.1 Geological fieldwork**

#### **3.1.1 Mapping of discontinuities**

Approximately 2100 orientation measurements of joints and foliation were collected during the field work. These were taken both inside and outside the unstable area at 123 measurement locations. All orientation data are measured as dip direction and dip angle. This was done using a standard Silva compass. Some small areas within the unstable slope lacked outcrops due to the dense vegetation. Apart from these areas, the entire slope was covered. A Panasonic Toughbook field computer was used for navigation purposes during the fieldwork to help identify cracks and outcrops using hillshades.

Crack orientations, including opening and depth, were measured at several locations. Infill and signs of activity were also recorded. Geomorphological features such as depressions and scarps were drawn directly into the field computer running ArcMap (ESRI, 2014). The main focus of the fieldwork was to map variations in the observed discontinuities throughout the area. Another main task was to map and confirm the limits of the unstable slope. Information was gathered based on the requirements for the hazard and risk classification system published by Hermanns, Oppikofer, et al. (2012).

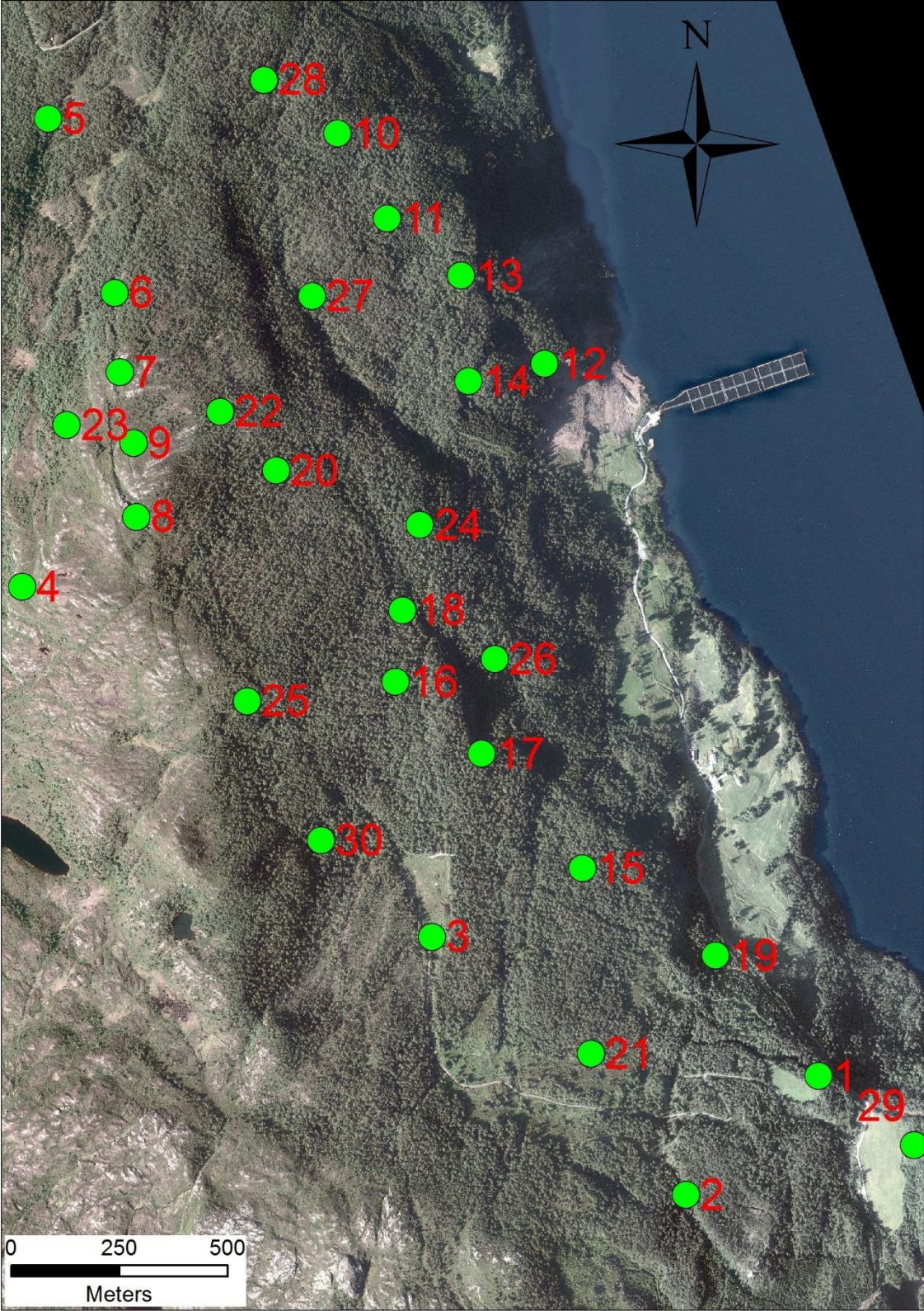
### **3.2 Structural analysis**

The structural analysis was undertaken using the Dips 6.0 software (Rocscience, 2013a). Orientation data were plotted using stereographic projection (lower hemisphere, equal angle, fisher distribution). All joint sets have a certain amount of variation, which results in a pole scatter when the data are plotted in a stereonet (Wyllie & Mah, 2005). According to Rocscience (2013b), a rule of thumb regarding contours is that concentrations greater than 6 % are considered very significant, 4-6 % represent a marginally significant cluster, and less than 4 % is not significant assuming the overall quantity of data is high. These recommendations were followed to evaluate the significance of the pole clusters.

#### **3.2.1 Field data**

In order to identify spatial variations in the mapped discontinuities, all of the 123 measurement locations were plotted on a map of the area. Based on the location, these were further grouped into 30 main locations (figure 3.1). These main locations are used as reference for observations described later in this thesis. One stereonet was plotted for each main location containing data from the initial 123 measurement points belonging to the corresponding group. This map is

shown in Appendix C and served as basis for dividing the unstable slope into structural domains.



**Figure 3.1:** Aerial photograph showing the 30 main locations. It also shows the dense forest covering most of the unstable area.

### 3.2.2 DEM analysis

The 1x1 meter resolution DEM received from NGU was converted into two hillshades using ArcMap. One with the sun light azimuth set to 315° and the other at 45°. Both had the sun set to an altitude corresponding to 45° above the horizon. These were used for digitizing open fractures and lineaments within each structural subdomain.

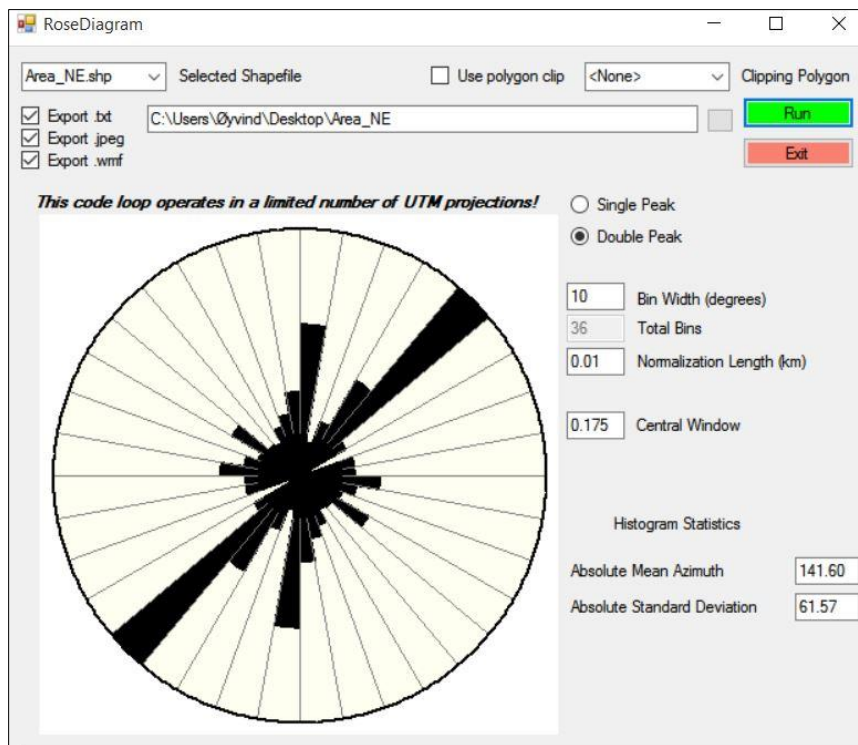
The software Rose (Redfield, 2015b), was used to create rose diagrams of the digitized lineaments (figure 3.2). Shapefiles created in ArcMap were imported into the software and converted into rose diagrams based on certain criteria. The bin width defines the width of each sector in the rose diagram and was set to 10° after recommendations by Nilsen and Brock (2011). The software weights the lineaments based on length so that longer lineaments have greater impact on the resulting rose diagram. A normalization length of 0.01 km was used for this analysis. This implies that the software divides each lineament into segments of 10 meters and adds the amount of segments with the same azimuth in the correct azimuth bin (Redfield, 2015a).

To determine if the mapped lineaments follow the joint sets measured in the field, resulting rose diagrams were compared to the corresponding stereoplot for area of the slope. This gives a good indication on how the pre-existing discontinuities influence the observed slope deformation in the area. Böhme, Hermanns, et al. (2013) also applied this method using the same software. They concluded that most of the pre-existing lineaments developed along the main discontinuity sets or a combination of two of them. The DEM covering Tytefjell was also used to identify major geomorphic features within the unstable area, surface area estimations, and to extract topographical profiles. Slope and aspect maps were created from the DEM to determine the exact average slope orientation.

#### **Comments on hillshade lineament mapping**

Recent studies have been performed to investigate the advantages and disadvantages with this type of digital lineament mapping. This method is quick, cost effective and a powerful tool to produce lineament maps, but is influenced by several biases (Scheiber et al., 2015). They found that scale, illumination azimuth of the hillshade and operator had significant influence on the results. Number of lineaments, orientation and length varied significantly based on these three parameters. The authors conclude that the reproducibility of such maps are poor, and that caution should be taken when producing lineament maps (Scheiber et al., 2015). To account for

these biases, the lineament mapping done in this thesis was performed using two different illumination azimuths and the human perception bias is kept in mind during the analysis.



**Figure 3.2:** Screenshot of the user interface in the software Rose that was used to generate rose diagrams. Values used for bin width, normalization length and central window is shown in the figure. Files were exported and edited in Adobe Illustrator.

### 3.3 Geological Strength Index (GSI) classification system

The GSI system has been developed to provide a quantitative method to relate field observation to rock mass quality. It is based on assessment of the structure and conditions of discontinuity surfaces in the rock mass (Marinos, Marinos, & Hoek, 2005). The original GSI system was introduced by Hoek (1994) and Hoek, Kaiser, and Bawden (1995). Later modifications of the GSI table have resulted in the most used version published by Marinos and Hoek (2000). The application of the system has also been extended to include weak and heterogeneous rock masses.

GSI classification is done based on visual examinations of field outcrops or in underground excavations. Lithology, structure and the condition of the discontinuities are evaluated. The visual appearance of outcrops has been influenced by surface relaxation, weathering and/or alteration, and this may influence the GSI classification (Marinos et al., 2005). Due to the dependence of the outcrop orientation relative to the joint sets, and the natural variation within the rock mass, it is not meaningful to assign one precise GSI value. A GSI classification is best



described by assigning a range of possible values due to the subjectivity of the user (Marinos et al., 2005). The rock mass strength depends on the properties of the intact rock and the freedom of these pieces to slide and rotate (Marinos & Hoek, 2000). GSI values below 25 are considered as very poor rock mass quality (Sonmez & Ulusay, 1999).

The structure of laminated/sheared rocks have also been incorporated into the GSI table. Since this category is located in the inferior part of the table, estimations done on metamorphic rocks will always end up in the same low range. Marinos and Hoek (2000 p. 10) states that “*The persisting schistosity planes and their usually “poor” surface conditions restrain the range of GSI values*”. This poses a problem for tunnel excavations, because the resulting tunnel support will be over-designed. Also, for slope stability applications, the rock mass quality could be significantly underestimated. Therefore, a new GSI table was been developed to give a more accurate GSI-value when dealing with metamorphic rocks. This modification was published by Truzman (2007) based on experiences from railroad tunnelling projects in Venezuela where 90% of the encountered rock mass was composed of graphitic phyllites and schists.

### 3.3.1 GSI classification for metamorphic rocks

Since the Tytefjell unstable area is composed of graphitic phyllites, this modified version of the GSI table was used for all field estimations (figure 3.3). As with the original table, this modified version includes six structures and five surface categories to choose from. The biggest modifications are visible in the structure column in the GSI table. Instead of decreasing the link between rock blocks, the presence of foliated rocks increases. The surface characteristics are modified to include the aperture between the foliation planes. In metamorphic rocks this is an important aspect to be considered in the rock mass classification (Truzman, 2009).

### 3.3.2 Applicability to rock mass failures

Studies have shown that specific rock failure mechanisms are related to rock mass classification such as the GSI. Brideau et al. (2009) showed that both the lithology and tectonic structure have great impact on the GSI value. Based on four case studies they delineated zones within the GSI table where particular failure mechanisms can be expected. It should be noted that the analysis in this publication is done based on the old version of the GSI table, not considering the issues with metamorphic rocks mentioned above.

The obtained GSI values were used to compare the rock mass damage throughout the unstable area to see if low GSI values coincides with the areas with most prominent deformation. GSI values were estimated at locations with good visible outcrops where the rock mass could be

inspected in detail. The condition of the rock mass was discussed in the field before a final decision was made. Aperture width was measured with a ruler where possible.


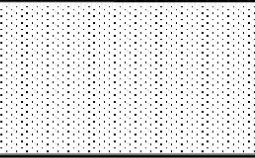










CHARACTERISTIC OF THE ROCK MASS TO ESTIMATE THE GEOLOGICAL STRENGTH INDEX (GSI)		SURFACE CONDITIONS				
<p>From the description of structure and surface conditions of the rock mass, select the appropriate interval of this chart. Estimate the average value of the Geological Strength Index (GSI) from the interval. Do not attempt to be too precise. Guiding a range of GSI from 35 to 42 is more realistic than stating that GSI = 38. It is also important to recognize that the Hoek-Brown criterion should only be applied to rock masses where the size of the individual blocks or pieces is small compared with size of the excavation under consideration. When individual block sizes are more than approximately one quarter of the excavation dimension, failure will generally be structurally controlled and the Hoek-Brown criterion should not be used.</p>		VERY GOOD Very rough, closed and fresh unweathered surfaces	GOOD Rough, slightly weathered, aperture < 1 mm, hard fillings	FAIR Slightly rough, moderately weathered, aperture 1-5 mm, hard and soft fillings	POOR Smooth, highly weathered, aperture > 5 mm, predominant soft fillings	VERY POOR Stickensided, highly weathered, surfaces, aperture > 5 mm, soft fillings
STRUCTURE		DECREASING SURFACE QUALITY				
NON-FOLIATED ROCK MASS	FOLIATED ROCK MASS	INCREASING PRESENCE OF FOLIATED ROCKS OR DECREASING INTERLOCKING OF ROCK PIECES				
 <p><b>INTACT OR MASSIVE</b> Intact or massive rocks in situ rock with few discontinuities widely spaced</p>		90			N/A	N/A
 <p><b>NON-FOLIATED/FRACTURED</b> rock mass little perturbed consisting of cubical blocks formed by three orthogonal systems of discontinuities, very well interlocked.</p>	 <p><b>LITTLE FOLIATED</b> rock mass partially fractured formed by three discontinuity systems. Massive intervals can have some thin layers of foliated rocks</p>	80	70	60		
 <p><b>NON-FOLIATED/WEAKLY FRACTURED</b> rock mass partially disturbed consistent of angular blocks interlocked, formed by four or more discontinuity sets</p>	 <p><b>MODERATELY FOLIATED</b> rock mass fractured formed by intervals of foliated or non-foliated rocks in similar proportions</p>		50	40		
 <p><b>NON-FOLIATED/DISTURBED</b> rock mass folded and/or faulted with angular blocks formed by many intersecting discontinuity system</p>	 <p><b>FOLIATED</b> rock mass some folded and/or faulted very fractured, foliated rocks prevail with occasionally non foliated rock intervals</p>	N/A		30		
 <p><b>NON-FOLIATED/WEAKLY INTERLOCKED</b> poorly interlocked, heavily broken rock mass with a mixture of angular and rounded rock pieces</p>	 <p><b>VERY FOLIATED</b> rock mass folded, highly fractured, formed only by foliated rocks. Can be present some faults</p>	N/A	N/A	20		
 <p><b>NON-FOLIATED/PULVERIZED</b> rock mass totally fractured and tectonic sheared, resulting in complete lack of blocks</p>	 <p><b>FAULTED/SHEARED</b> rock mass very folded and faulted, tectonically disturbed with aspect of breccia.</p>	N/A	N/A	N/A	10	

Figure 3.3: GSI classification system for metamorphic rocks (Truzman, 2007). The structure column for foliated rock mass was used during the fieldwork at Tytefjell.

### 3.4 Application of the hazard classification system

The hazard assessment was applied to the scenarios at Tytefjell following the methodology described by Hermanns, Oppikofer, et al. (2012) and Hermanns, Oppikofer, et al. (2013). Based on recommendations by (Hermanns, Oppikofer, et al., 2012), a high level of uncertainty was

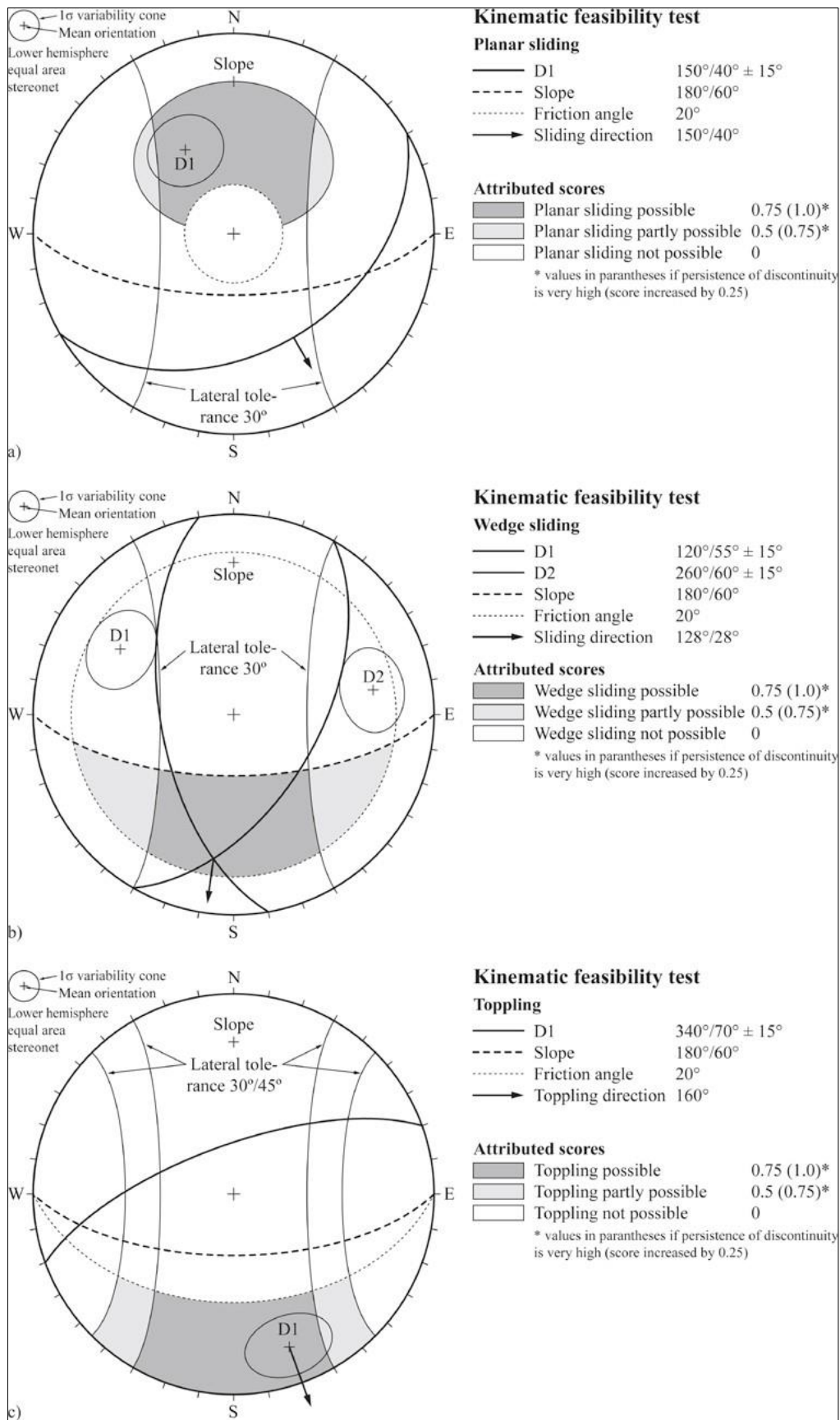
assigned to criteria where data is not yet available. This applies to the morphologic expression of the rupture surface, displacement measurements and the acceleration criteria. All nine criteria were assessed for scenario 3-6. Scenarios with a low likelihood of failure were not included in the hazard assessment.

### 3.4.1 Kinematic analysis

A kinematic feasibility test is a part of NGU's hazard assessment and investigates the possibility for different failure mechanics based on the orientation of mapped discontinuities with respect to the slope orientation. The kinematic analysis performed in this thesis was done using the software Dips 6.0 (Rocscience, 2013a), following recommendations given by Hermanns, Oppikofer, et al. (2012).

The input values regarding the slope orientation have great importance for the results of the kinematic analysis. The slope dip angle used should not be an average value over the entire slope, since this can severely limit the possible failure modes and thus lower the hazard score. If the slope has a steep scarp at the front, values from these areas should be used in the analysis (Oppikofer, 2015). This minimizes the risk of underestimating the failure possibilities. Slope aspect was determined by looking at aspect maps created in ArcMap. The kinematic analyses for Tytefjell were performed for both the mean and maximum slope angles to also assess the worst case scenario. Hermanns, Oppikofer, et al. (2012) recommended setting the friction angle used for kinematic analysis to  $20^\circ$  as a conservative value for all rock types. Since the Tytefjell unstable rock slope is made up of phyllites, a value of  $20^\circ$  is a reasonable estimate but because of graphite lenses found along the foliation, this value could be even lower.

Due to the possible range in the size and complexity of unstable rock slopes, often with varying slope orientations within the same unstable area, the lateral limits for planar and wedge failure are defined even more conservatively in this analysis ( $30^\circ$ ) than the  $20^\circ$  recommended in Wyllie and Mah (2005). The kinematic feasibility test which is used here assumes that planar or wedge sliding is feasible (score 0.75) if the difference between sliding direction and slope aspect is less than  $30^\circ$ , and partly feasible (score 0.5) if the difference is larger than  $30^\circ$ . Toppling was assumed possible if the difference between dip direction of discontinuities and slope aspect was smaller than  $30^\circ$  (score 0.75) and partly feasible if the difference was smaller than  $45^\circ$  (score 0.5) (Hermanns, Oppikofer, et al., 2012). Three failure modes were assessed: planar sliding, wedge sliding and toppling (figure 3.4). General geometrical conditions for failure apply for the three failure modes. These are described in detail by Wyllie and Mah (2005).



**Figure 3.4:** Kinematic feasibility test for a) planar sliding b) wedge sliding, and c) toppling failure. The scores given in brackets are used if the persistence of the discontinuity is very high (Hermanns, Oppikofer, et al., 2012).

### 3.4.2 Creation of structural profiles

More complex failure mechanisms such as biplanar, multiplanar and buckling failure are not easily assessed by using simple kinematic analysis techniques (Stead & Eberhardt, 2013). It is important not to over-simplify the kinematics of landslides just by looking at the kinematic analysis. Therefore, in order to reduce the uncertainty, five structural profiles were made to investigate the interaction between the discontinuities in more detail. The findings from these profiles are not taken into account in the hazard scores, but serve as additional information that can verify the findings from the kinematic analysis.

The profile orientations are shown in figure 4.18: profile two, three and five are oriented E-W and profile one and four are oriented parallel to the most likely direction of movement (striking 55°). Movement direction is set orthogonal to the internal scarps. dGNSS displacement measurements are necessary to determine the movement direction more precisely. The profiles contain measurements from only one structural domain, except profile three. This profile crosses both the two structural domains and contains the structures from both domains. Structures that strike almost parallel with the profiles were not included.

Bathymetric data were included in the profiles because no visible daylighting sliding surface was observed for the larger failure scenarios above sea level, suggesting that the sliding surface might daylight below sea level. These data were only available in a 50-meter grid that was converted into a 10-meter resolution DEM. The 1-meter resolution DEM was used to create the topographic profile above sea level and later combined with the bathymetric profile with lower resolution. This is evident when looking at the level of detail visible above and below sea level. The 3D analyst tool in ArcMap was used to create the structural profiles which were edited in Excel. Profiles were made so that the vertical and horizontal scale are the same. Since the strike of the discontinuities and structures included in the profiles are not perpendicular to the profile orientation, apparent dip was calculated. Apparent dip is defined as the angle on a plane between the horizontal and a direction other than the true dip (Groshong, 1999). The calculation was done using equation 1.

**Equation 1:** Equation used to calculate apparent dip (Groshong, 1999).

$$d_a = \arctan(\tan(d) \times \cos(\alpha))$$

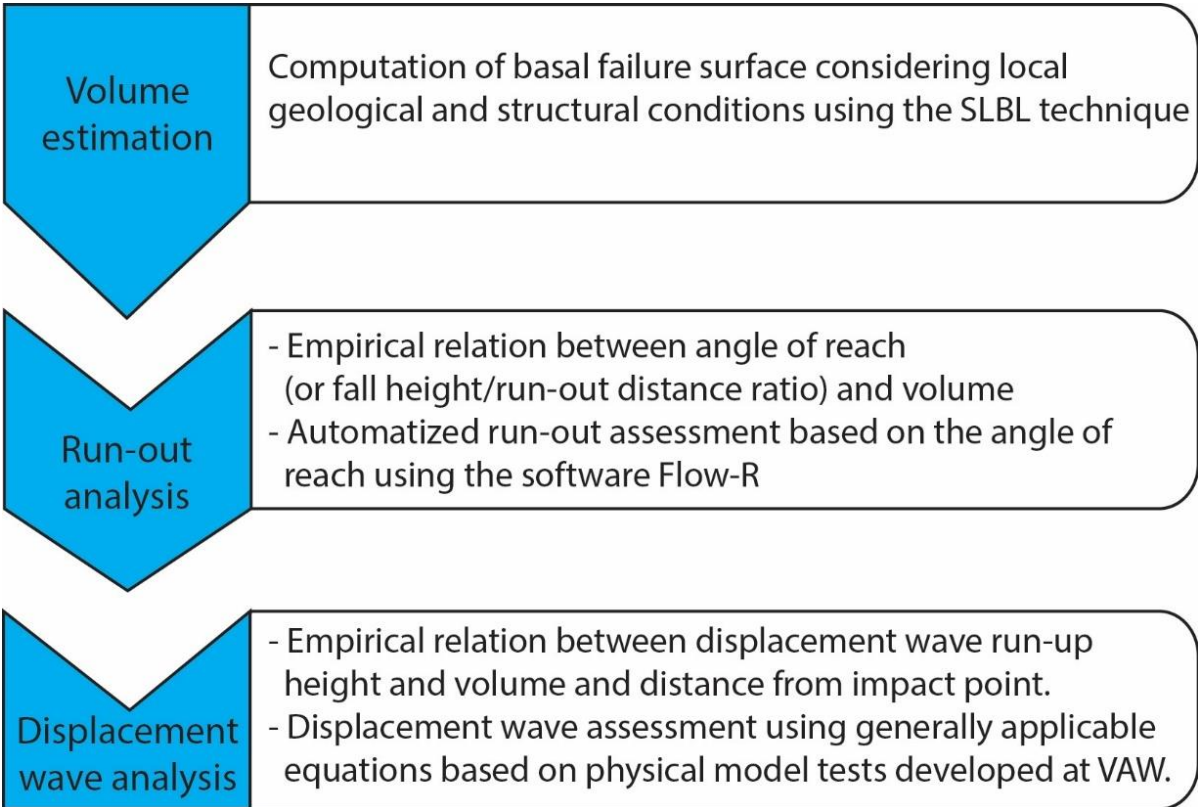
$d_a$  = Apparent Dip

$d$  = Dip

$\alpha$  = Horizontal angle between the true and the apparent dip

### 3.5 Application of the consequence assessment

Since this thesis aims to assess the secondary consequences of a failure at Tytefjell, NGU's workflow for consequence assessment was applied (figure 3.5). The analysis done in this thesis involved three main steps; volume estimation, run-out analysis and displacement wave analysis. The last part of the consequence and risk assessment described in Oppikofer et al. (in press), which focuses on loss of life only, will not be performed in this thesis due to temporal restrictions.



**Figure 3.5:** Workflow for the consequence assessment performed in this thesis. Modified from (Oppikofer et al., in press).

To implement both the SLBL, Flow-R and the VAW model, an ArcGIS toolbox developed by NGU was used to prepare all the input files for the different methods. This toolbox runs in ArcMap and lowers the workload by preparing all input files needed for the subsequent analysis. The initial files required to create the input files includes the DEM, and polygons outlining the different failure scenarios (Oppikofer et al., in press).

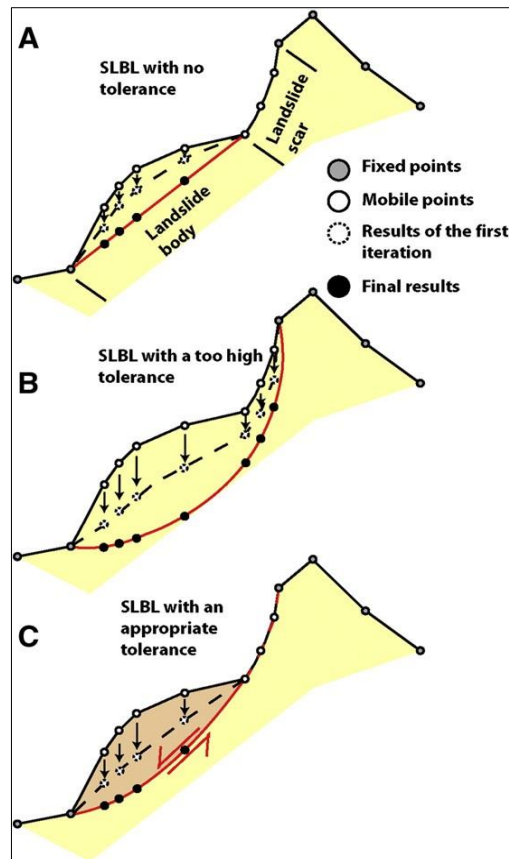
#### 3.5.1 Volume estimations using the SLBL technique

Defining the volume of unstable slopes is a key part of a consequence assessment. The volume has large impact on the runout length and possible secondary effects of the mass movement such as displacement waves and damming of valleys (Oppikofer et al., in press). However,

especially when dealing with large unstable areas, the volume estimation is difficult and involves large uncertainties. Knowledge about the exact 3D geometry of the failure surface is important for volume estimations, numerical simulations and the assessment of possible failure modes (Oppikofer, Jaboyedoff, Pedrazzini, Derron, & Blikra, 2011). The hazard analysis carried out today at NGU applies the SLBL method originally developed by Jaboyedoff, Baillifard, Couture, Locat, and Locat (2004) to compute possible basal sliding surfaces of large unstable rock slopes (Oppikofer et al., in press). Base level is defined as the lowest level that can be eroded by a stream (Strahler & Strahler, 2006). As landslide scars are found in sloping topography, a sloping local base level is used here. *“The basic idea of the approach involving the SLBL is to find, for a given relief at a given time, the volumes that are liable to be affected by gravitational movements”* (Jaboyedoff et al., 2004 p. 200-201).

An excel tool developed at NGU was used to calculate the curvature parameters for the basal rupture surface. This tool adapts the curvature parameters to the computed surface to local and geological structural conditions representing the probable basal sliding surface (Oppikofer et al., in press). Altitude differences between the back scarp and the assumed toe, in addition to the length of the scenario in question were given as inputs into the excel sheet. The scenario length was measured as the maximum length within the block limitations in the assumed direction of movement. Angles for the back scarp and toe-line were set based on field measurements and DEM analyses to restrict the computation of the failure surface. If these values did not allow for a surface to be created, the excel sheet gave a warning. In this case, standard values were used to get the most reliable results. The elevation difference between the DEM and the computed surface allows computation of the unstable volumes (Oppikofer et al., in press).

Three different surfaces are calculated by the NGU tool (figure 3.6): The shallowest ellipse is a straight line from the back scarp to the toe (A). The deepest is an ellipse that is vertical at the back scarp and horizontal at the toe (B). The last is the intermediate failure surface that fits the ellipse to the user defined angles (C). This represents the most likely failure surface and the resulting volume was used in the subsequent run-out and displacement wave analysis.



**Figure 3.6:** Estimating the depth of the failure surface using different tolerance levels. Figure C shows the geometry when the surface fits the scar curvature defined by the user (Travelletti, Demand, Jaboyedoff, & Marillier, 2010).

The actual SLBL calculation was done in the software CONEFALL developed by Jaboyedoff and Labiouse (2011) following a standard procedure given in Oppikofer et al. (2016). The CONEFALL software is based on a simple Coulomb frictional model. This resulted in a table of residuals i.e. altitude differences between the DEM and the computed failure surfaces. These values were reported into an excel sheet that computes the three volumes (figure 3.7).

#### Angle of reach and run-out length of rock avalanches

Scenario	Area [m <sup>2</sup> ]	Hmax [m]	Hmean [m]	Volume [Mm <sup>3</sup> ]	Angle of reach [°]	Run-out length [m]
Minimum SLBL surface	46600	72.4	23.5	1.10	25.5	2550
Intermediate SLBL surface	46600	261.9	113.9	5.31	20.4	3265
Maximum SLBL surface	46600	319.7	144.3	6.72	19.7	3388
From Zonal Statistics as Table tool				Based on Scheidegger (1973), Onofri & Candian (1979)		
Potential fall height	1215	from back-scarp down to valley bottom/fjord				

#### Legend:

User input fields
Computed fields

**Figure 3.7:** SLBL excel sheet used to calculate volumes for all three basal rupture surfaces (Oppikofer et al., 2016). The excel sheet also computes angles of reach and the Fahrböschung runout length.



### 3.5.2 Fahrböschung

A first step runout assessment was done using the empirical relationship between fall height/runout-distance vs. volume developed by Scheidegger (1973). This is acceptable as the Scheidegger relation serves as an envelope for Norwegian cases (Hermanns, Oppikofer, et al., 2012). Potential fall height, and minimum altitude of the valley bottom, lake or fjord was given as input in the Excel tool developed by (Oppikofer et al., in press). The angle of reach is provided by the Scheidegger (1973) relationship based on the computed volumes. This is used together with the fall height and to compute the runout distance (figure 3.7) (Oppikofer et al., in press). ArcMap was used to display this calculated runout length to determine whether a water body or infrastructure lies within the runout area. However, this relationship has shown to be conservative for Norwegian rock avalanches and more than 90% of Norwegian events have shorter run-outs than predicted (Oppikofer et al., in press).

### 3.5.3 Flow-R runout model

Run-out analyses presented in this thesis were performed using the Flow-R software. It is difficult to perform a hazard assessment at a regional scale using process-based modelling due to the complex nature of unstable rock slopes, variability of local controlling factors and the uncertainty of the input parameters (Horton, Jaboyedoff, Rudaz, & Zimmermann, 2013). Such a model needs to be able to consider a simplified approach that can facilitate hazard zonation with minimum data requirements. The Flow-R model has been developed by Horton et al. (2013) to meet these requirements. Flow-R was originally developed to model debris flows but has been adapted by Oppikofer et al. (in press) to be used for rock-avalanches.

Main advantages with the Flow-R model are the low data requirements. The source area delineation, angle of reach and a DEM are the only input needed to perform the calculation. Implementation was done in two distinctive steps; identification of source areas by means of morphological and user defined criteria and propagation of the material from the source area using frictional laws and flow direction algorithms. The spreading algorithms controls the path and spreading, while friction laws determine the runout distance. Details regarding the model calculations and algorithms can be found in Horton et al. (2013).

### 3.5.4 VAW model

The laboratory of hydraulics, hydrology and glaciology (VAW) at ETH Zürich have carried out a number of research projects on displacement waves. They have developed a practical computation procedure applying applicable semi-empirical equations (Heller et al., 2009). Such equations are developed from the evaluation of tests carried out on the basis of systematic and independent variation of all important governing parameters (Heller et al., 2009). This method allows investigations into the effect of impulse waves on shores and dams. Heller et al. (2009) specifies that the method can only be used approximately for complex reservoir geometries. Uncertainties for the equations related to the run-up are ~60 %, which do not include the uncertainties connected to the slide parameters and fjord geometry (Oppikofer et al., in press). Therefore, the presented results should only be considered as estimates.

The following input parameters were given as input for the calculations (Oppikofer et al., in press):

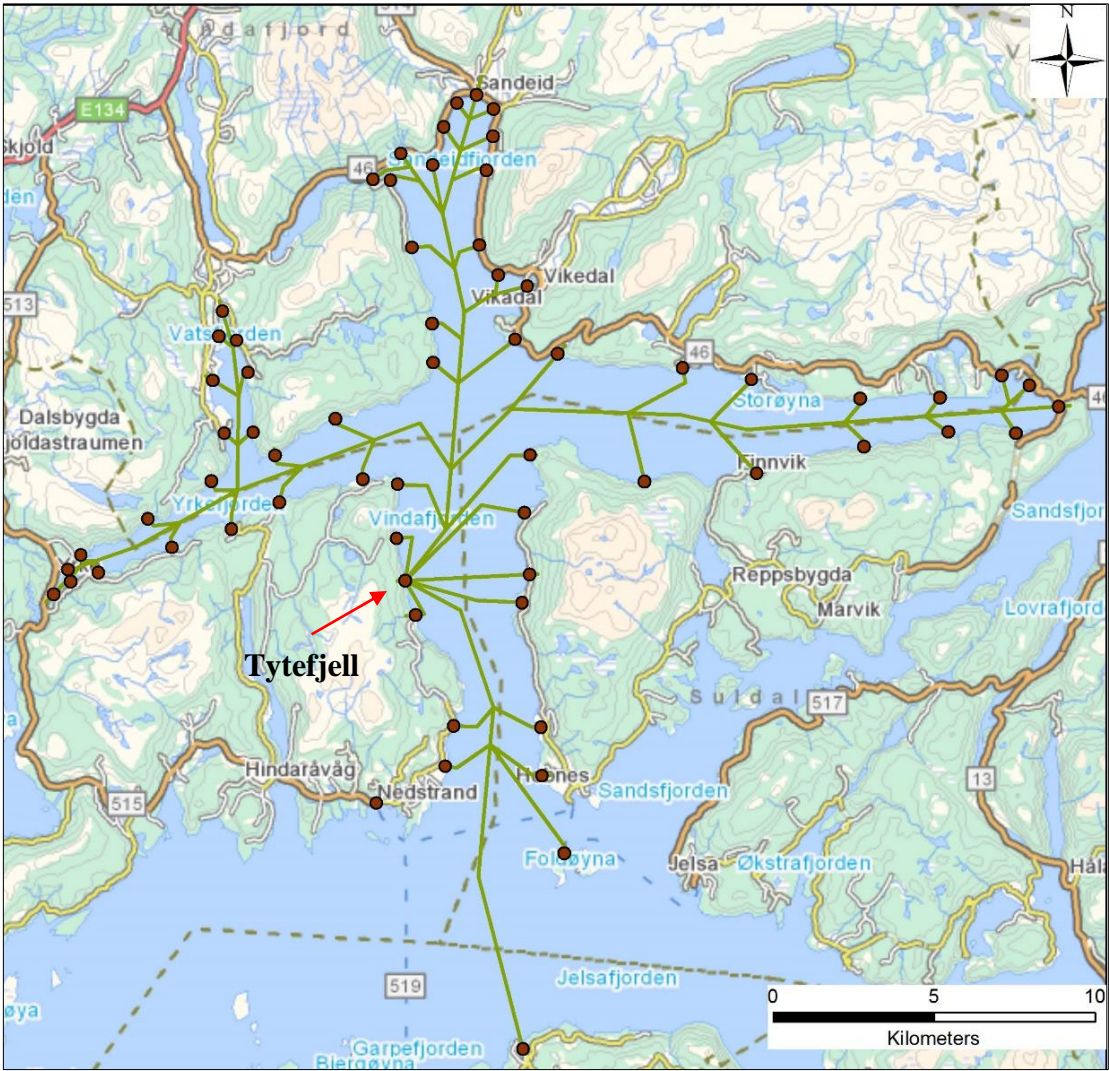
- The initial slide volume, slide density and the bulk slide porosity.
- The slide width and length at impact determined from the runout model.
- The height difference and length of the impact slope to determine the slide impact angle.
- Still water depth below the unstable slope.
- Surface elevation and mean slide thickness at the centre of gravity of the unstable mass and the distance from the centre of gravity to impact.
- Wave run-up angle.

Some default values are defined by NGU: The initial slide density was set to  $2700 \text{ kg/m}^3$  and the bulk slide porosity is set to a standard value of 37 % (Oppikofer et al., 2016). The run-up slope angles used in the model was measured perpendicular to the shoreline following the procedure shown in Appendix D. Details on the model calculations can be found in Heller et al. (2009). The slightly adjusted method used by NGU is described in Oppikofer et al. (2016) and (Oppikofer et al., in press).

The VAW analysis was performed by selecting points around Vindafjord where run-up estimates were needed due to existence of settlements and infrastructure. Bathymetric profiles were drawn, connecting the unstable area with the different run-up points. Each profile was divided into segments that include information on length, wave propagation angle, fjord width and water depth. These profiles were later imported into an Excel sheet developed by NGU based on VAW that calculates the estimated run-up height at each point. The user defined input values need to lie within certain limits to satisfy all the criteria in the VAW model, e.g. the run-

up slope angle has to lie between  $18.4^\circ$  and  $90^\circ$ . This is because the experiments that serve as a basis for the model were only tested for run-up angles greater than  $18.4^\circ$  (Müller, 1995). If not fulfilled, the uncertainties of the calculated run-up heights are higher.

Affected areas are obtained by interpolating the computed run-up heights between the points over the study area and intersecting the run-up heights with a digital elevation model (Oppikofer et al., in press). The displacement wave profiles and the selected run-up points are shown in figure 3.8. The fjord geometry south of the village Nedstrand is considered too complex to model the displacement wave. Run-up heights are nevertheless believed to be negligible in these areas when modelling smaller, more realistic scenarios. The intermediate volumes for each scenario from the SLBL analysis were used for the VAW modelling. The parameters used for the modelled scenarios are presented in Appendix E.



**Figure 3.8:** Displacement wave profiles (green lines) and selected run-up points (red dots) in the fjords surrounding the unstable area at Tytefjell.

### 3.6 Empirical analysis of displacement wave data

The VAW analysis described in chapter 3.5.4 is time consuming and requires a substantial amount of data and input parameters. Therefore, NGU have tried to develop an empirical tool that gives a quick estimate of displacement wave run-up with a low number of input parameters (Oppikofer et al., in press). As a continuation of this project, data on run-up slope angle and water depth were gathered for six displacement wave events with recorded run-up heights. The dataset prepared by Böhme (2013) is used and built upon in the work presented in this thesis. As mentioned in chapter 3.5.4, numerous parameters influence the run-up height of a displacement wave. Some of these parameters are difficult to quantify if the unstable area has not been investigated in detail before failure. Therefore, the analysis in this thesis focused on parameters that are possible to quantify within acceptable uncertainties.

Bathymetrical data has been gathered from several sources covering the events listed in table 3.1, including the three case studies described in chapter 2.3 (Loen 1905, Loen 1936, Punta Cola, Isla Mentiroso, Chehalis lake and Tafjord). This provides an opportunity firstly, to gain an overview of the basin geometry, and also to experiment with including additional parameters in the empirical model to lower the uncertainties. Two additional parameters were extracted for the events where bathymetric data were available:

- Angle of the run-up slope
- Water depth directly in front of run-up slope

Both parameters were measured as done in the VAW analysis (Heller et al., 2009). These are believed to be two of the many governing parameters for tsunami run-up height (Heller et al., 2009). Several other parameters could have been included in such a model, but many are difficult to quantify precisely e.g. the morphology of the frontal area of the sliding mass.

**Table 3.1:** Source of bathymetry data for the investigated displacement wave events.

<b>Landslide event</b>	<b>Location</b>	<b>Source of bathymetric data</b>
Loen lake	Norway	Louise Hansen (NGU)
Tafjord	Norway	NGU
Loen lake	Norway	Louise Hansen (NGU)
Isla Mentiroso	Chile	Galderic Lastras, University of Barcelona
Chehalis lake	Canada	Nicholas Roberts, Simon Fraser University
Punta Cola	Chile	Galderic Lastras, University of Barcelona

In total, run-up angle and water depth were measured for a total of 182 points with run-up estimates. The amount of points was limited by the availability of bathymetry data. The water depth was measured directly in front of the run-up slope. The run-up slope angle was measured

as an average of the angle along the run-up slope (Appendix D). All measurements were taken perpendicular to the shoreline, as for the VAW analysis. For two of the events with multiple run-up measurements, several closely spaced run-up measurements were averaged (Loen 1936 and Chehalis lake) just as in the original analysis by Böhme (2013). An average distance and run-up height were calculated and used in the analysis for these locations. This was done because the density of run-up estimates made it difficult to estimate separate run-up angles. The only event where further run-up points were added to the dataset used by Böhme (2013) was for the Aysén fjord event. These additional points were extracted from Scheele et al. (2013). Uncertainties of the used data are discussed in chapter 5.6.1.

Each parameter was plotted against run-up height in 2D to determine if the data allowed fitting of a function. In addition, all collected data were plotted in a 3D scatterplot to identify general trends in the data. Several maps displaying the different parameters were produced to get an overview over the basin geometry's influence on run-up height (Appendix H). These maps visualize the variation of run-up heights and run-up angle along the different basins. The original empirical relation developed by Böhme (2013) was applied to the two smallest failure scenarios at Tytefjell and the computed run-up heights were compared to the VAW model results.

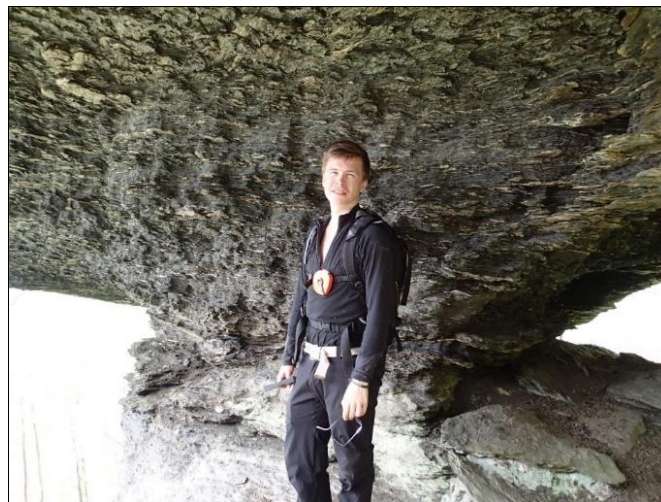


## 4. RESULTS

### 4.1 Results from field investigations

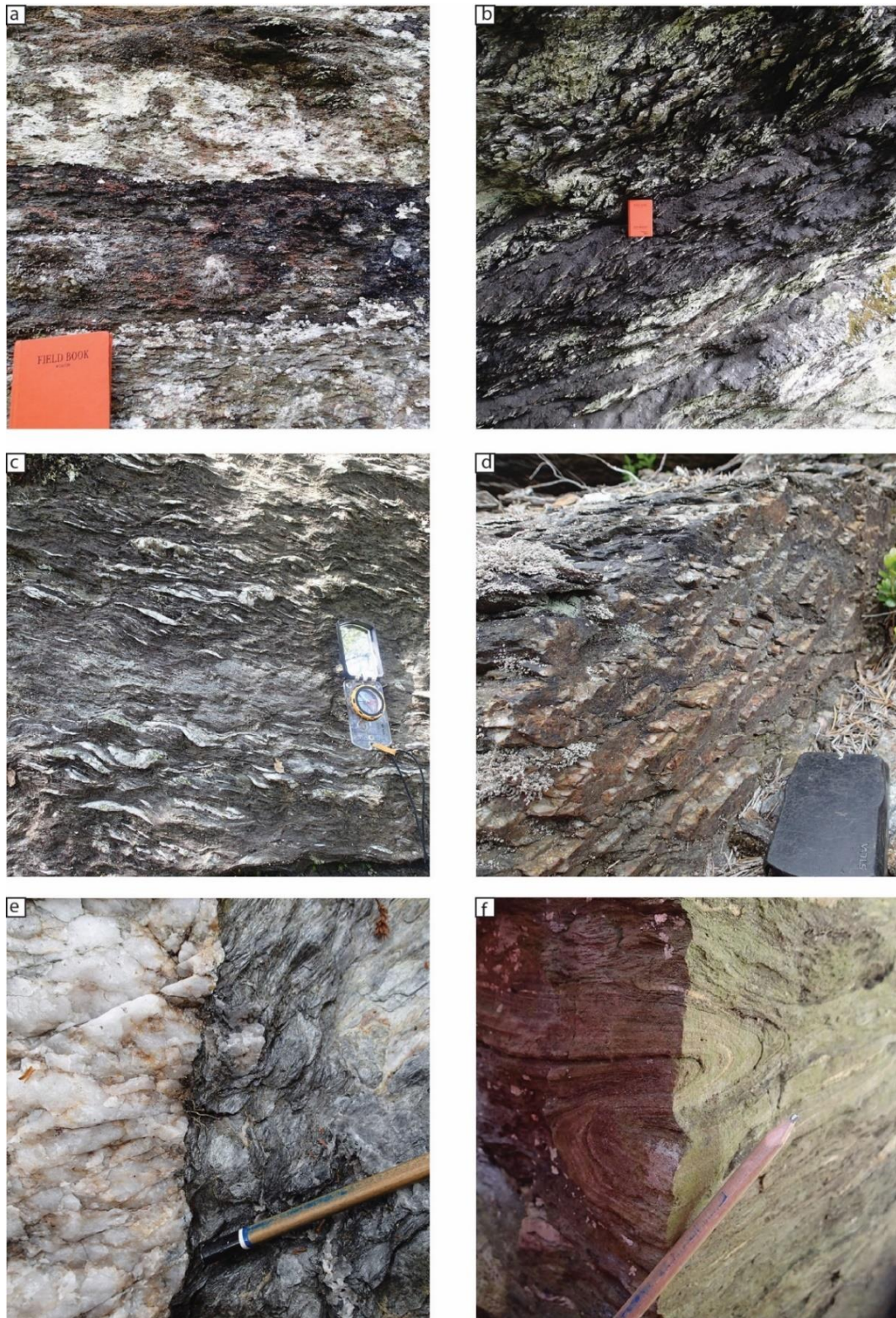
#### 4.1.1 Mapped geological conditions

Most of the unstable area at Tytefjell is composed of graphitic phyllites. Graphite rich lenses with a thickness of up to one meter were found along the foliation over the entire mapped area (appendix A). Traces of graphite was also found by Riis (1977) in most of his samples. Graphite rich dust have accumulated under overhanging cliffs at several locations. This graphite dust is easily removed by rain, and thus the amount of graphite might be higher than what is observed in the field. Rock strength appears to decrease with increasing graphite content. The graphite rich areas crumble easily and it is possible to break the rock by hand. Multiple examples of extensive weathering of the graphite were observed in the field. Crumbling and downfall of graphitic rocks has created overhangs at several locations. At one outcrop, this process had created a mushroom shape with a 5x5x3 meter block resting on a thin pillar (figure 4.1).



**Figure 4.1:** Intensively weathered graphitic phyllite resulting in a block resting on a thin residual pillar.

The graphite gives the phyllite a dark colour (figure 4.2a and b). Elsewhere, a grey shiny colour dominates, with occasional greenish colours present. The phyllites show intense small scale folding over the entire study area (figure 4.2c and f). The phyllite tends to break up in thin sheets. Quartz lenses were often found parallel to the foliation and constitute between 5-10 % of the rock mass, which influences the GSI. These lenses were often found protruding out of outcrops compared to the phyllite (figure 4.2d). As mapped by Riis (1977), a small amount of quartzite was also found in the northern part of the study area during this fieldwork (figure 4.2e). The limits of this lithology was not mapped in detail. However, it was only present in the northern parts of the study area, just west of location 10 in figure 3.1.



**Figure 4.2:** Photos of the rock mass within the unstable area at Tytefjell A: **A:** 20cm thick graphite rich layer easily recognizable by the darker colour. Marked strength contrast between the layers. **B:** Interlayering of graphite and quartz bands. The field book measures 19x12cm. **C:** Picture showing the intense small scale folding. Compass for scale. **D:** Folded quartz lenses sticking out of outcrop, compass for scale. This amount of quartz is not representative for the entire study area. **E:** Shiny grey phyllite to the right, quartzite to the left. **F:** Isoclinal small scale folding. Photo shows a corner, with shade on the left face.

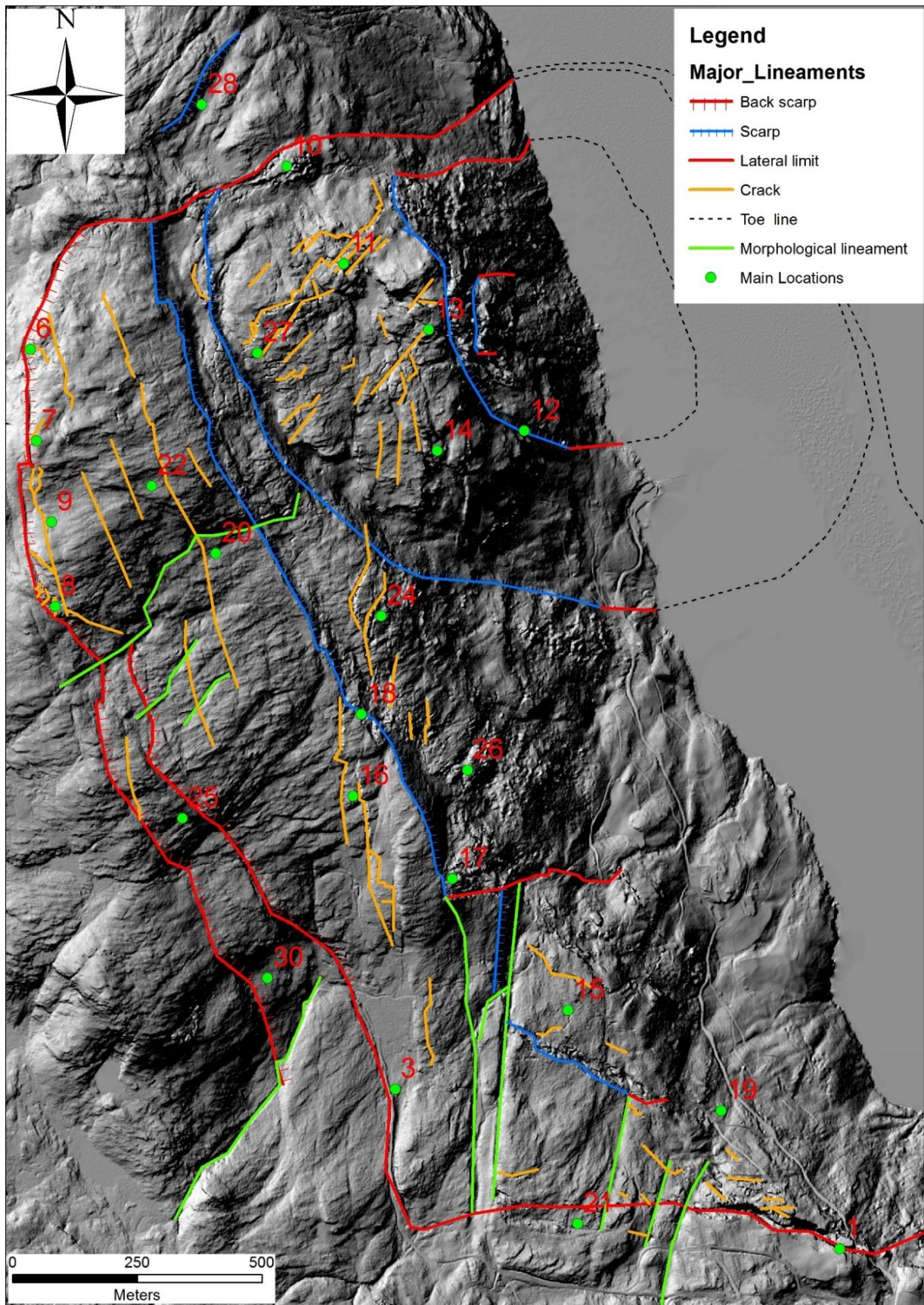


## **4.2 Geomorphological and morpho-structural features**

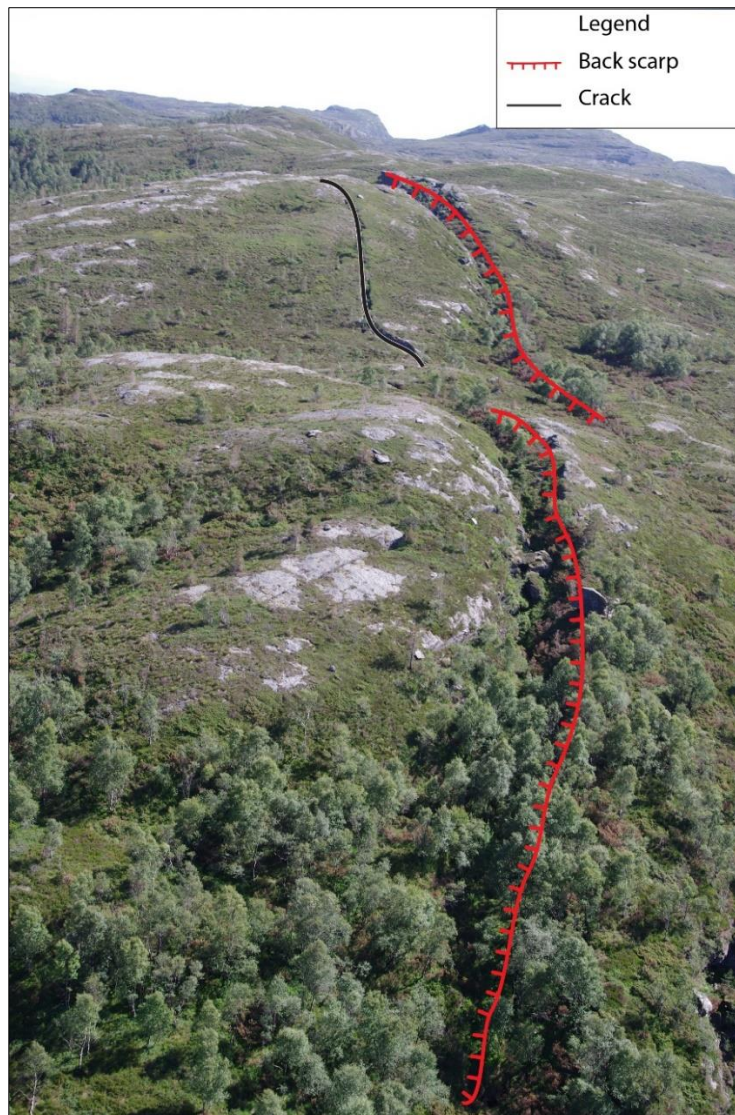
A map showing the major lineaments is presented in figure 4.3 and will be explained in the following paragraphs. This map focuses on the limits of the unstable area and the most prominent internal scarps and cracks identified in the field and on the hillshades.

### **4.2.1 Back scarp**

The back scarp is clearly visible in the field at approximately 500 meters a.s.l. The open, most visible part stretches approximately 700 meters north from location 8. As seen in figure 4.4, the back scarp is not continuous but is composed of two scarps joined by a 25-meter step close to location 7. One of the two back scarps ends south of location 7 but continues south as a vertical transverse crack. This crack continues parallel with the other back scarp before disappearing north of location 8 (figure 4.3). South of location 8, the back scarp becomes more difficult to identify in the field. Two major lineaments are visible south of this location, but no open fractures were observed in this area during fieldwork. Nevertheless, these lineaments are observable as depressions in the terrain and are interpreted to be a less developed southward continuation of the back scarp. The westernmost back scarp continues towards SE but ends against a depression south of location 30. No continuation of this feature was observed. The second major lineament continues south from location 8 and becomes less evident close to location 3 (figure 4.3). This is interpreted as the start of the southern lateral limit. Discussions dealing with the limits of the unstable area can be found in chapter 5.1.

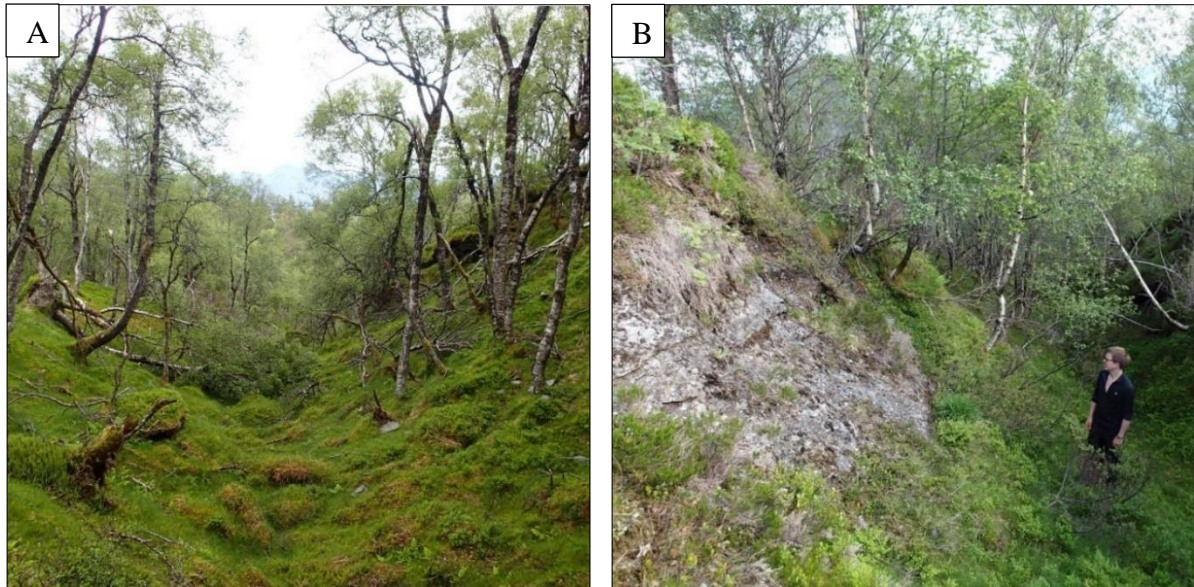


**Figure 4.3:** Lineament map showing the interpreted limits of the unstable area and the most prominent morphological features. Main locations are marked with green dots.



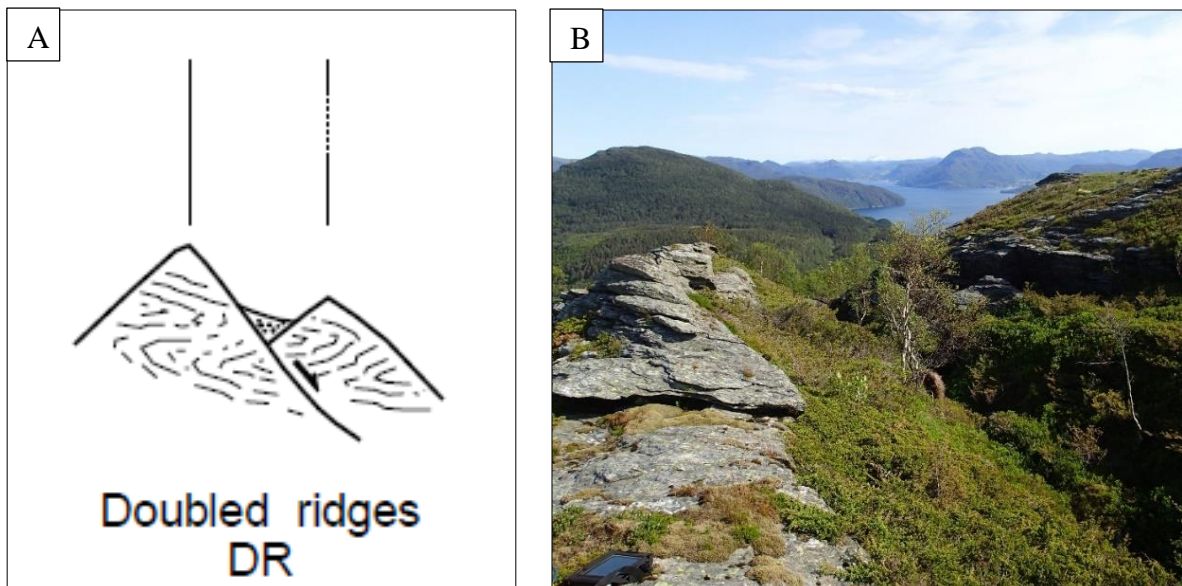
**Figure 4.4:** Photo of the back scarp taken from a helicopter looking SSW. The increasingly dense vegetation towards N is easily observable. The transverse crack is indicated in black. The two parts of the observable back scarp is separated by 25 meters.

Towards the north, where the back scarp turns in a NNE direction, it develops into a deep vegetated depression (figure 4.5a). Further north, this depression turns almost 90° towards the east. This kink is defined as the start of the northern lateral limit. North of location 7, the back scarp is partly covered with vegetation (figure 4.5b). A pronounced 1-3-meter-high counterscarp is found along the entire back scarp.



**Figure 4.5:** **A:** Picture taken north of location 6 showing how the back scarp has changed from an open scarp to a vegetated depression. The picture is taken looking north; the unstable part is on the right side of the picture. **B:** Picture taken looking north showing the back scarp at location 7. This is also the area where the back scarp becomes more vegetated towards the north. Person for scale.

Following the definition given by Agliardi et al. (2001), the structures at location 7 and 8 can be defined as double ridges. The back scarp and the associated counterscarp make up two N-S striking ridges (figure 4.6).



**Figure 4.6:** **A:** Photo that shows a double ridge as defined by Agliardi et al. (2001). **B:** Picture taken looking NNE at the top of the slope (location 7) showing the double ridge at Tytefjell where a clear scarp and counterscarp is visible. This back scarp is located behind the hill crest with the unstable part to the right.

### **Internal scarps**

In the northern sector of the slope, rock deformation increases towards the east along three pronounced lineaments, and results in areas with higher degree of fracturing closer to the fjord. These lineaments are internal scarps with observable offset of blocks sliding down along a discontinuity. The first and the more developed scarp starts at the northern lateral limit (east of location 6) and continues southwards for 1.4 kilometres with the same strike as the transverse cracks observed in the NW regions of the slope (figure 4.3). The scarp is oriented  $065^{\circ}/50^{\circ}$  on average. After 1.4 km the scarp jumps 110 meters eastward and continues further south, gradually developing into a depression. The degree of deformation is more pronounced on the eastern side of this scarp, when comparing the amount of observable cracks visible on the hillshades. A possible continuation of the largest internal scarp was observed north of the interpreted limit of the instability. This scarp is situated west of location 28 (figure 4.3).

A second parallel scarp was found 100 meters east of the one described in the paragraph above. This scarp does not extend as far south, but turns east towards the fjord after approximately 840 meters. A smaller scarp is observable on the slope map above the rockfall area. This scarp is curved with a general strike of NW-SE and extends approximately 500 meter along the fjord. During investigation of the rockfall area, a 10-meter-high vertical wall was observed directly east of location 13. This is interpreted to be the scarp observable on the lineament map. Several counterscarps are found association with the internal scarps. Height varies from 1-20 meters. The largest one is found close to location 27 (figure 4.3).

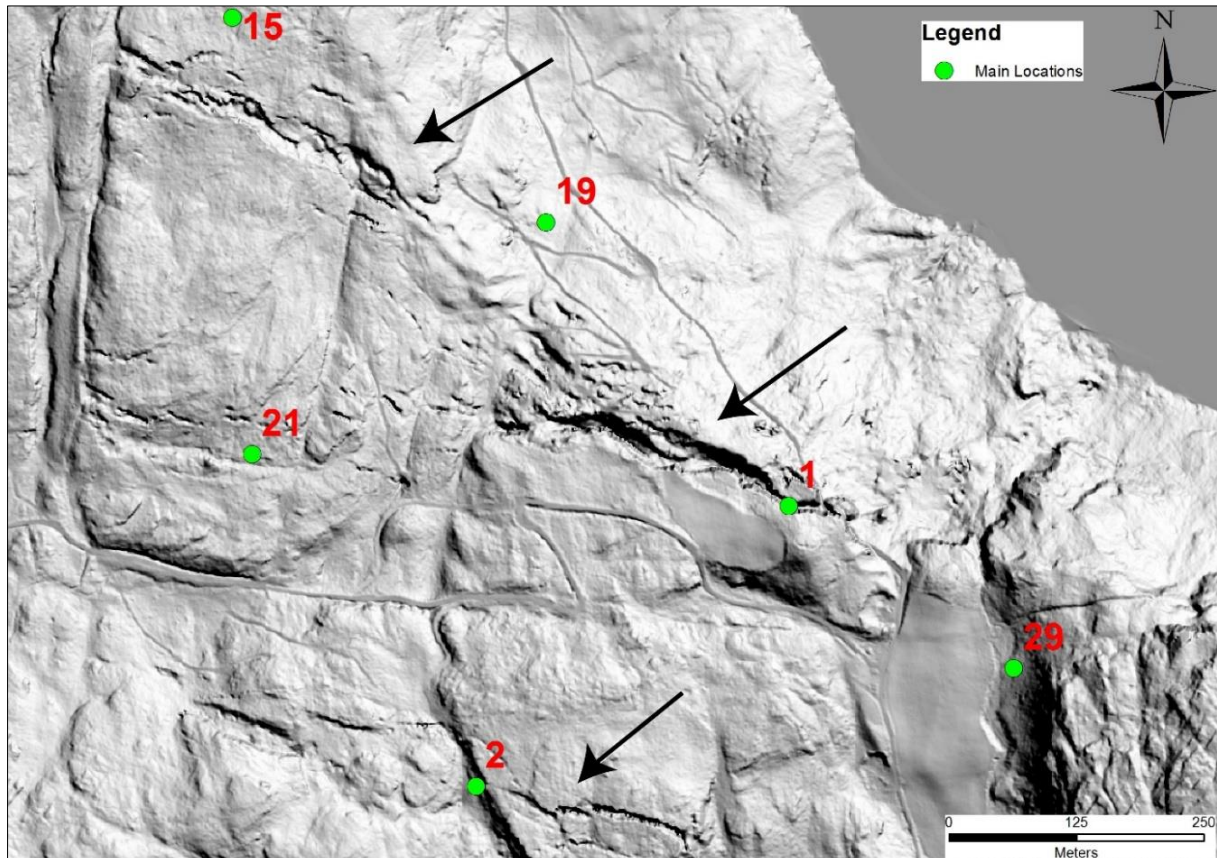
#### **4.2.2 Cracks and trenches**

Numerous cracks with different orientations are observed on the entire slope. Opening, depth, infill and orientation were recorded. Most of the major cracks found throughout the area follow discontinuities (chapter 4.3.2). The areas surrounding location 12, 13, 24 and 26 in figure 4.3 are completely broken up to a degree that make it difficult to get a general overview of all the cracks. No detailed investigations were done in this area because of the large amount of rotated blocks and difficult terrain. The large amount of blocks is visible on the hillshade in figure 4.3.

Towards the southern end of the instability, three large fracture systems are easily observable in the field and on the hillshades (figure 4.7). The system furthest to the south is interpreted to be located outside the unstable area. The second big fracture system was found at location 1. This big canyon is 10-15-meter-deep and up to 20 meters wide. It extends approximately 325 meters in WNW-ESE direction. Field observations showed that this canyon gets wider towards

the west, before dying out east of location 21. It is defined to be a part of the southern lateral limit of the entire instability, although some minor deformation occurs south of it.

The third fracture system is found south of location 15 and is oriented NW-SE. It approximately 350 meters long and up to 50 meters wide. This fracture system is composed of multiple fractures with large blocks in between. It ends towards the west against a 25-meter-wide N-S striking depression (figure 4.7).



**Figure 4.7:** Figure showing a section of the southernmost area of the instability. The one close to location 1 is set as the southern lateral limit. Three prominent fracture systems are marked with black arrows.

Several NNW-SSE oriented transversal cracks are observed east of location 9 both in the field and on the hillshades (figure 4.3). These are oriented parallel to the internal scarps. Closer to the fjord at location 27, several prominent NE-SW oriented cracks are observed.

### Depressions

Several prominent depressions were observed during fieldwork. These might be less developed cracks or cracks covered with vegetation and thus be important for the overall stability of the slope. Most of the depressions are found in the southern area of the slope and are oriented N-S or NNE-SSW. Three prominent NNE striking depressions were observed crossing the southern

lateral limit east of location 21. Right north of location 20, a NE striking depression is easily visible on the hillshade. This feature is also continuing westwards, out of the unstable area (figure 4.3).

#### 4.2.3 Erosion features

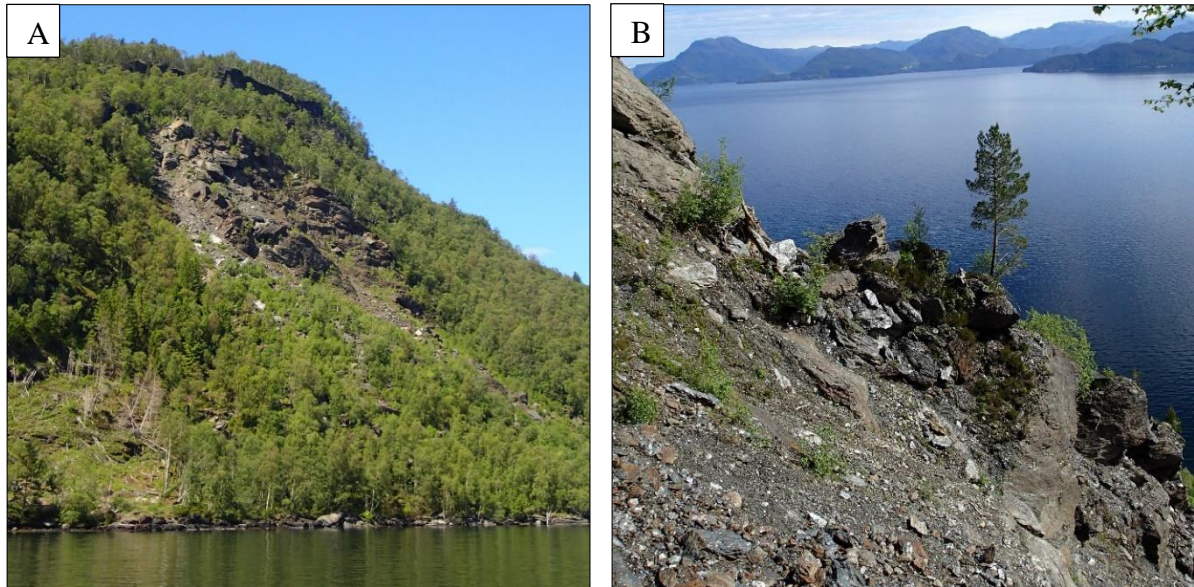
A completely rounded surface was observed above the deforested area in the NE part of the unstable slope (figure 4.8). This corner was observed on a 10-meter-high outcrop and is interpreted to be carved by glaciers. The carved side of the outcrops is aligned parallel with the fjord and fits with glacial flow directions described by Anundsen (1990).



**Figure 4.8:** Completely rounded, 10-meter-high outcrop above the deforested section south of the rock fall area. Picture taken towards south. Person for scale.

#### 4.2.4 Rock fall area

As described in chapter 1.4.3, several rockfall events were recorded from the frontal area of the NE sector of the slope. This is the area with the most advanced stage of deformation on the entire slope, and is therefore not covered by vegetation. The area measures 150-meters in width, and 200-meters in length (figure 4.9a). Several loose blocks are still lying on the slope (figure 4.9b). The fact that the vegetation has not been able to recover shows that this area is very active.



**Figure 4.9:** **A:** Picture taken from the fish farm looking NW showing the active rockfall release area indicated in figure 1.5. The areal extent is 150x200 meters. **B:** Picture taken within the rockfall area, looking north. Unstable blocks are still present on the slope.

### 4.3 Geologic structures

All orientation data of discontinuities in this thesis are given as dip direction/dip angle in degrees. The variability of the discontinuity data is reported as one standard deviation ( $\sigma$ ).

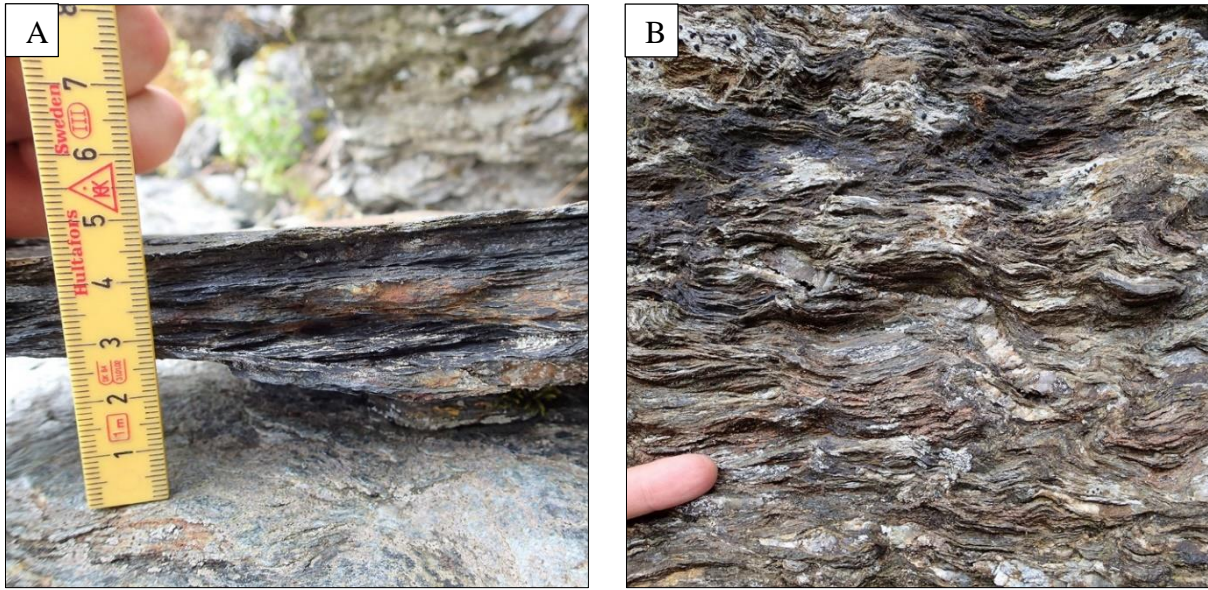
#### 4.3.1 Foliation

Given the lithology of the unstable area, well-developed foliation was found at all measurement locations. Due to intense small scale folding, the foliation measurements varied significantly over short distances (figure 4.10). It was therefore important to take a significant number of measurements to calculate the mean orientation and its variability. The foliation scatters between N and E dipping with an average orientation of 360/22±14 (table 4.1). It was not possible to identify the persistence in the field; however, it is believed to be high. This is consistent with Riis (1977) which also found intense small scale folding.

**Table 4.1:** Table giving the orientation of the foliation in each sub-domain in addition to a total average orientation. All are statistically significant with an contour range of 2-10 in dips (Rocscience, 2013a). The uncertainty number is describing the opening of the variability cone in degrees and thus combines the uncertainty for both the dip direction and the dip.

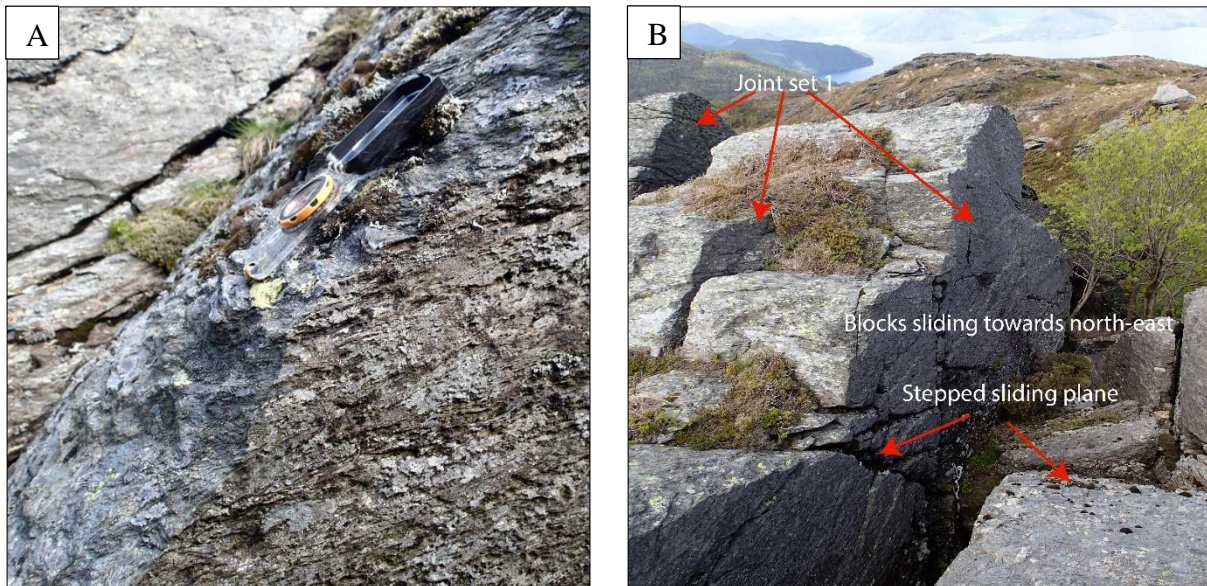
Domain	DipDir/Dip
NW	360/24±12
NE	351/22±12
S	011/21±13
Mean	360/22±14





**Figure 4.10:** **A:** Picture showing the foliation in a sample found in the rockfall area at the front of the NE sector. **B:** Undulating foliation. Picture taken close to location 7. Finger for scale.

A discontinuity composed of multiple, stepped foliation planes was found at several locations. This structure did not have a continuous orientation, but rather the dip direction varied between NE-NW (figure 4.11). Blocks sliding along this plane was observed close to location 8 and several other locations in the NE and south domain.



**Figure 4.11:** **A:** Plane composed of multiple daylighting foliation planes in a step-like fashion observed at location 8. The plane is clearly steeper than the sub-horizontal foliation visible in the picture. Compass for scale. Orientation of this plane:  $030^{\circ}/36^{\circ}$ . **B:** Overview over location 8 where multiple blocks is sliding towards NW along the stepped plane in figure A. The persistent joints seen on the picture belongs to joint set 1.

### 4.3.2 Joint sets

In total, based on the measured data, five statistically significant joint sets were identified within the unstable area. The mean orientations displayed in table 4.2 were determined by using the Dips software.

**Table 4.2:** Overview of mean joint orientations within the different structural domains and mean orientation over all domains. All joint sets are statistically significant with an contour range of 2-10 in DIPS (Rocscience, 2013a), except those outlined in black, where the contour range was increased to 1-10 to make them significant. All measurements are given as DipDir/Dip in degrees.

<b>Domain</b>	<b>Joint 1</b>	<b>Joint 2</b>	<b>Joint 3</b>	<b>Joint 4</b>	<b>Joint 5</b>
<b>NW</b>	289/90±12	-	-	067/36±12	-
<b>NE</b>	124/86±9	223/86±12	<b>002/85±16</b>	<b>062/43±12</b>	-
<b>S</b>	123/84±12	205/88±12	167/83±6	<b>072/50±17</b>	274/87±13
<b>Mean</b>	119/87±11	213/87±13	354/89±12	067/43±12	274/87±13

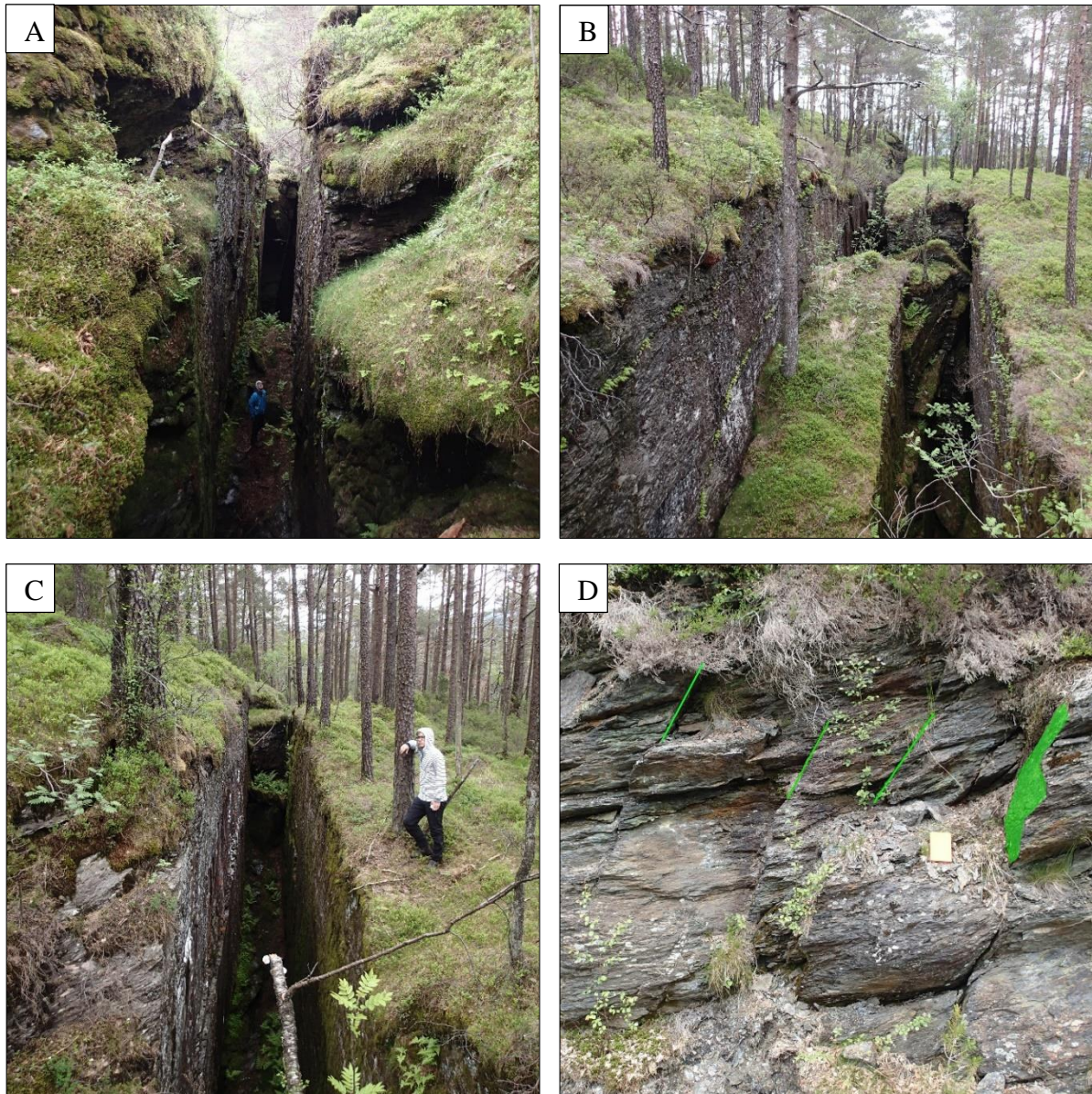
A strong variation in joint spacing was observed. Therefore, no specific value is given for any of the joint sets. Persistence was difficult to determine because of the sub-vertical dip of the discontinuities. Estimated values are given in table 4.3.

**Table 4.3:** Spacing and persistence for all the 6 major discontinuities found in the study area.

<b>Set</b>	<b>Spacing</b>	<b>Persistence</b>
<b>Foliation</b>	<1 cm	-
<b>Joint 1</b>	0.5-10	>100 m
<b>Joint 2</b>	1-25	>20 m
<b>Joint 3</b>	2-10	>50 m
<b>Joint 4</b>	1-5	-
<b>Joint 5</b>	5-15	>50 m

## Joint set 1

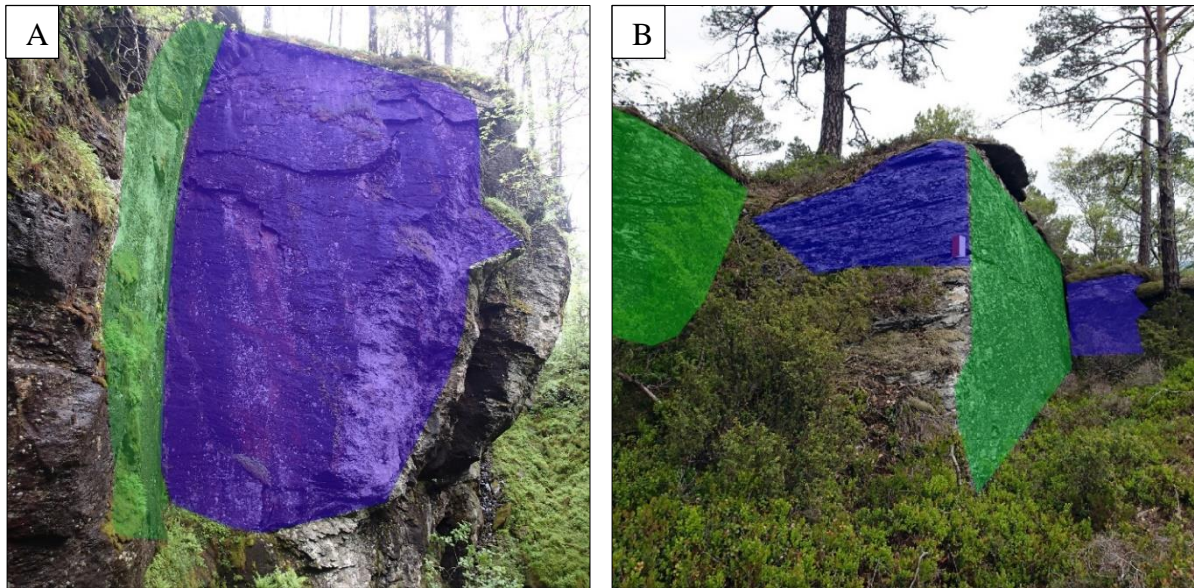
Joint set 1 was found at locations spread all over the unstable area and is believed to be the most persistent discontinuity. Table 4.2 shows that the joint set has a stable orientation across the slope. Multiple cracks follow this joint set, often in combination with one additional joint. The surface is found to be very smooth over long distances. A persistence of up to 100 meters was observed. Pictures of cracks following J1 are shown in figure 4.12.



**Figure 4.12:** Pictures showing cracks following J1. **A:** Large crack following J1, where the smooth surface is clearly visible. Person in the crack for scale. Photo taken looking south. **B:** Persistent crack following J1. The left crack has persistence of >100 meters. Rectangular block fallen in between the two J1 discontinuities. Spacing 5m. Close to location 11. **C:** Persistent crack following J1 close to location 27. Smooth vertical surfaces on both sides. The crack is two meters wide and six meters deep. Vegetated bottom. Photo taken at location 11 looking NE. **D:** Picture showing the J1 spacing (green colour indicates J1), here found to be approximately 0.5 meters. Photo taken at location 21 looking SE, notebook for scale.

## Joint set 2

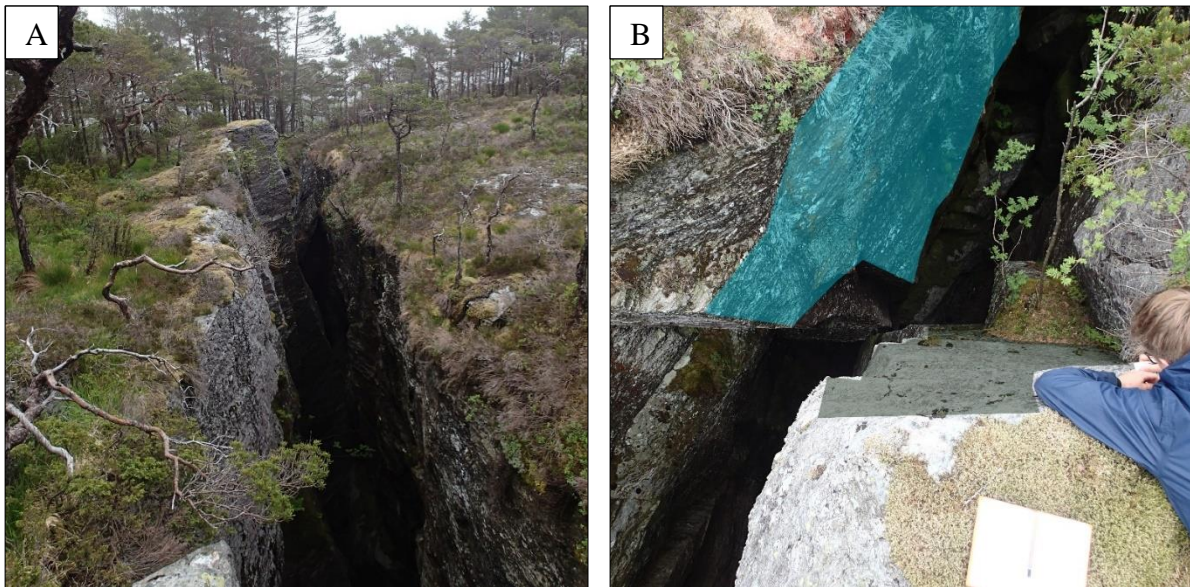
Joint set 2 was also found over the entire slope, except the NW sector surrounding the back scarp. It was often found together with J1, forming steps from one joint to the other (figure 4.13). The persistence varies between 1-25 meters. The orientation varies more than for J1, but is still quite stable. Steps between J1 and J2 are found over almost the entire study area. This joint set is dipping sub-vertically into the slope. A rougher surface than J1 is observed.



**Figure 4.13:** Steps between J1 (green) and J2 (blue) at two different locations. **A:** Photo taken towards WSW at location 1 inside the big canyon showing a 25-30-meter-high wall forming a standing wedge between J1 and J2. **B:** Looking north close to location 21. Clear steps between J1 and J2 vertical joint sets. Notebook for scale.

### Joint set 3

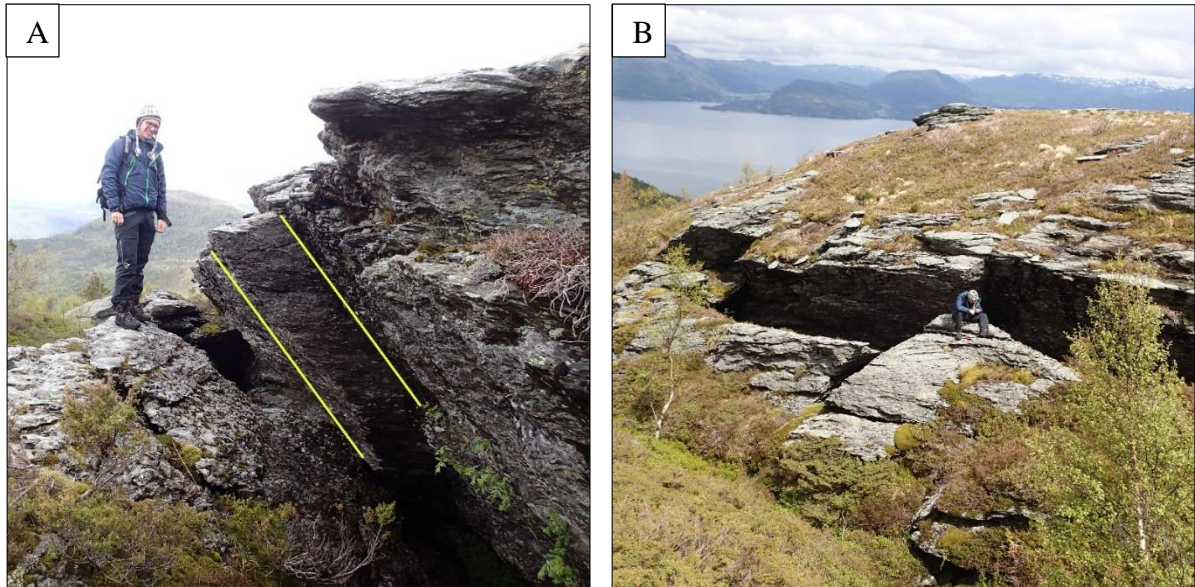
This joint set was not found over the entire unstable area; no traces were found in the western parts of the slope. One of the largest cracks found during the fieldwork developed along this joint set (figure 4.14). The spacing is found to vary between 2-10 meters. Persistence is not observed directly, but it is at least up to 50 meters based on length of cracks following this discontinuity.



**Figure 4.14:** Pictures taken of a large crack east of location 2. **A:** Structure partly follows J3 striking E-W. The crack is up to 10-meters-wide and at least 40 meters deep. It gets deeper towards the east. This photo shows a vertical displacement of 2-3 meters. Picture taken towards ESE. **B:** Looking down into the same structure. This big crack follows J3 (turquoise) and is cut by J5 indicated in black.

### Joint set 4

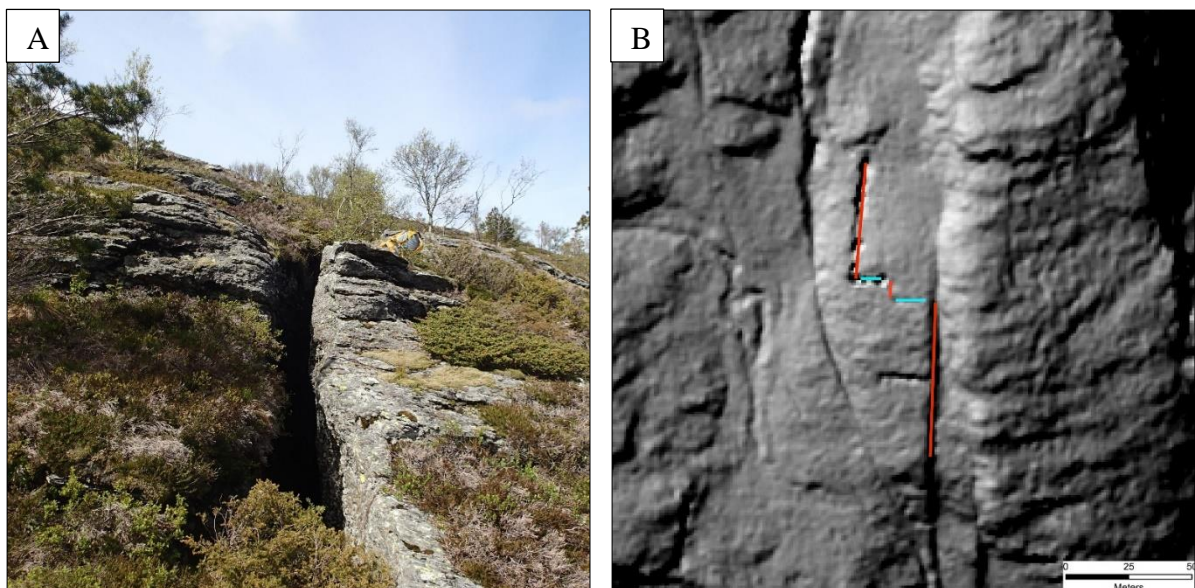
This set is found in all regions of the unstable area. It is a critical structure for the stability of the slope since it is the only structure dipping directly towards the fjord with a relatively shallow angle. The average orientation of this joint set is found to be 067/43, with a small variation across the slope. J4 is observed along the entire visible part of the back scarp in the NW domain. Blocks topple down into the back crack following this discontinuity (figure 4.15).



**Figure 4.15:** Pictures showing J4 along the back scarp close to location 7. **A:** Yellow lines mark J4 which dips towards the fjord. Spacing is around 0.5 meters. Blocks are toppling into the back scarp along this discontinuity. Photo taken looking north. **B:** J4 dipping towards the fjord along the back scarp. Blocks that have toppled along the discontinuity into the back scarp are visible. Photo taken towards NE. Sitting person for scale.

### Joint set 5

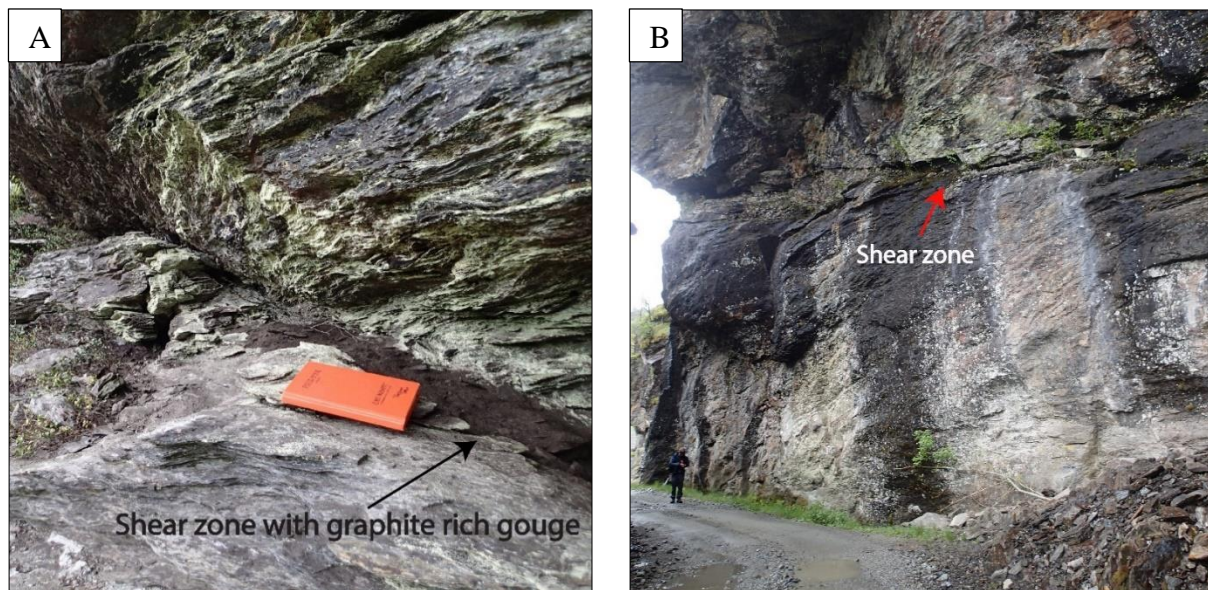
This joint set strikes approximately N-S and matches well with some of the large structures observed on the hillshade (figure 4.16b). It is only observed in the southern parts of the unstable area. This joint set was observed crosscutting J3 at several locations.



**Figure 4.16:** **A:** Photo taken towards NW that shows a NNW-SSE oriented crack following J5. Approximately 1-meter-wide and eight meter deep. Close to location 8. **B:** Map view over the area directly south of location 16. Red lines represent J5 and turquoise colour represent J3. This shows that the persistence of J5 can exceed 50 meter.

### 4.3.3 Shear zones

Two pronounced shear zones were observed within the unstable area. At location 6 (figure 4.3), an obvious cataclastic zone of deformation was observed on the eastern side of the back scarp. The average orientation of this 10 cm thick band was measured to be  $082^{\circ}/36^{\circ}$ . Graphite rich, dark coloured gouge was observed in the band of deformation (figure 4.17a). The persistence of the structure is uncertain. At the entrance of the big canyon at location 1, a large shear zone was observed in the wall above the road (figure 4.17b). A 50-meter continuation of this shear zone was mapped towards NE.



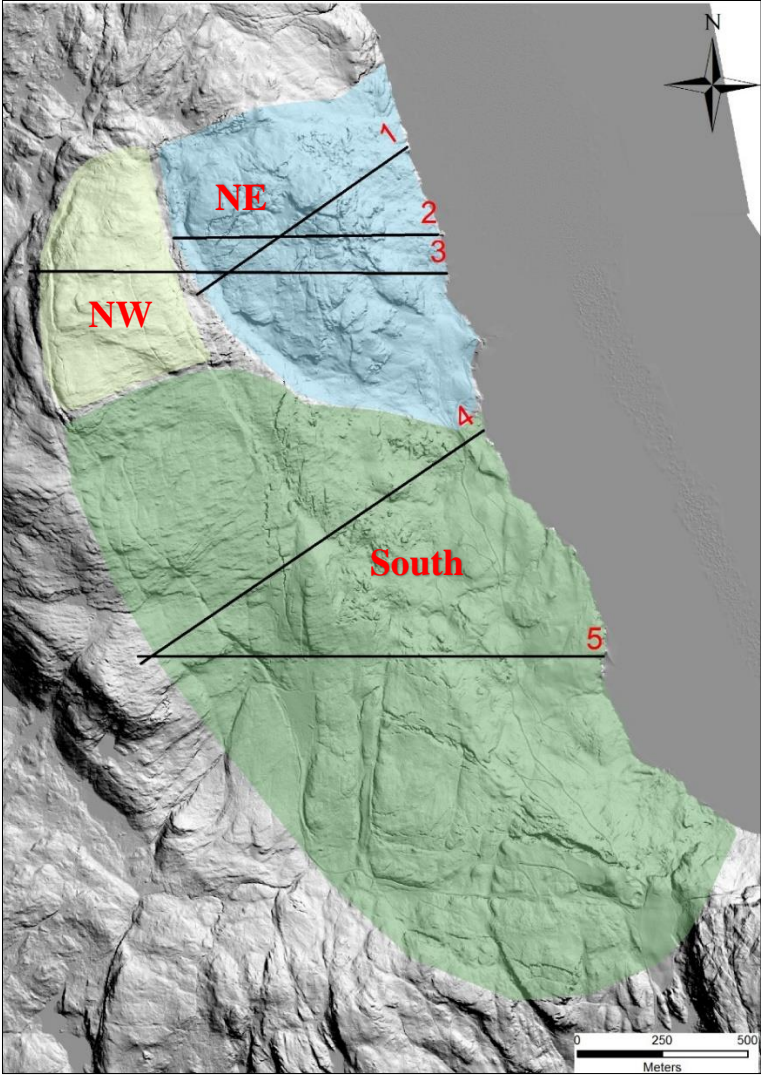
**Figure 4.17:** **A:** Evident shear zone close to location 6. Band of deformation is oriented  $082^{\circ}/36^{\circ}$  on average. Field book for scale. **B:** Big structure interpreted to be a shear zone at location 1. This structure was not possible to measure. Graphite dust was observed along this plane dipping towards NE. Person for scale.

### 4.3.4 Structural domains

The 123 measurements locations distributed over the entire slope were grouped into 30 main locations based on their location and measured structures. Resulting stereonet were used to divide the unstable area into three structural subdomains (figure 4.18). A figure including all of the 30 stereonet is shown in Appendix C. Three of the 30 stereonet are located north of the assumed limit of the instability. These are not included in any of the three domains. This applies to main location numbers 5, 10 and 28 in figure 3.1.

This division into three domains was done because of the spatially variable structural orientations across the slope (table 4.2). Some of the mapped joint sets are only observed in certain regions of the slope. The NW domain lacked observations of J2, J3 and J5. The NE

domain lacks J5. The southern domain shows some variation in joint orientation within the domain, but no clear trend is visible that allows for a further division. J1 and J4 are found in all three domains, however they vary significantly between the domains. All three domains contain a significant amount of measurements of all the mapped discontinuities in order to get a good representation of the structures. Since the structures vary between the structural domains, the feasible failure modes may differ between them.

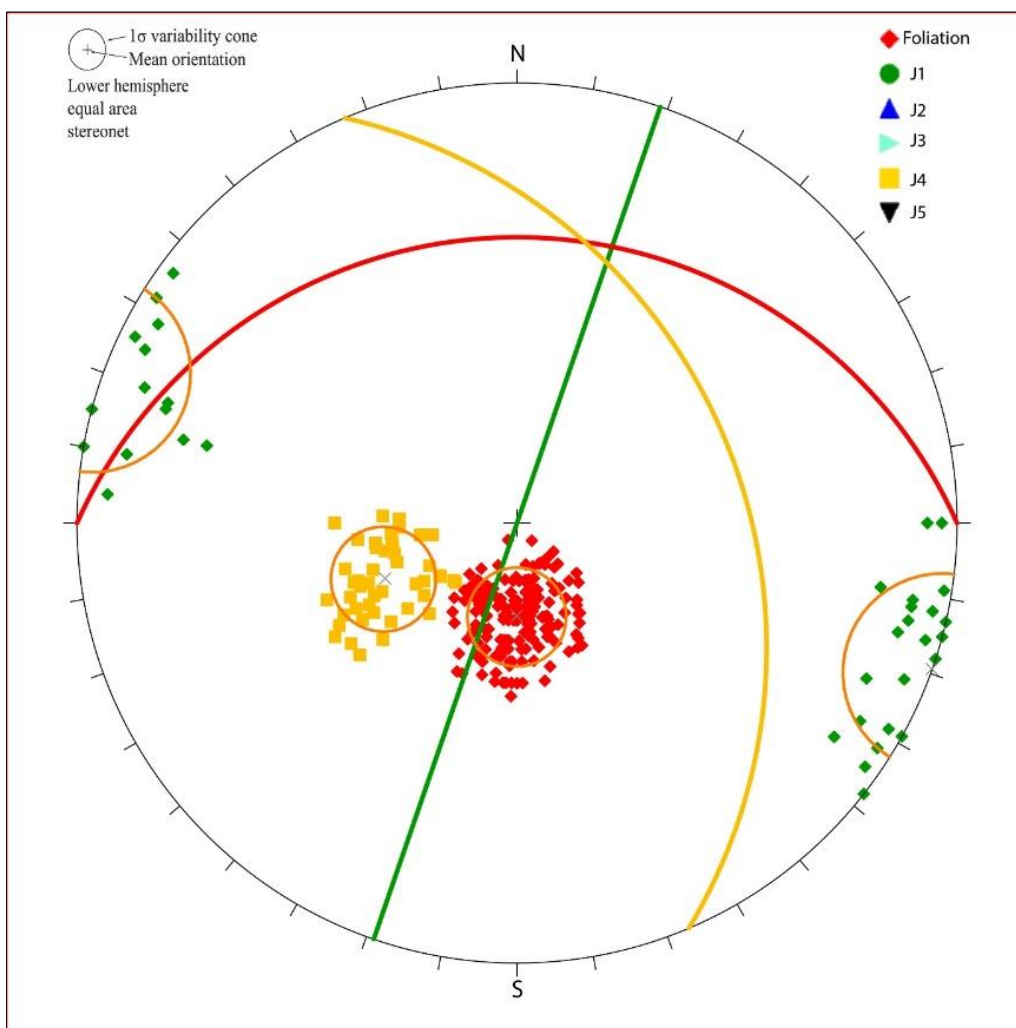


**Figure 4.18:** Hillshade showing the three structural domains. North-West domain in yellow, North-East domain in blue and the South domain in green. Profile lines 1-5 shown in black. These profile lines do extend into the fjord, but the low resolution of the bathymetry is not suitable to include in such a figure.



### North West domain

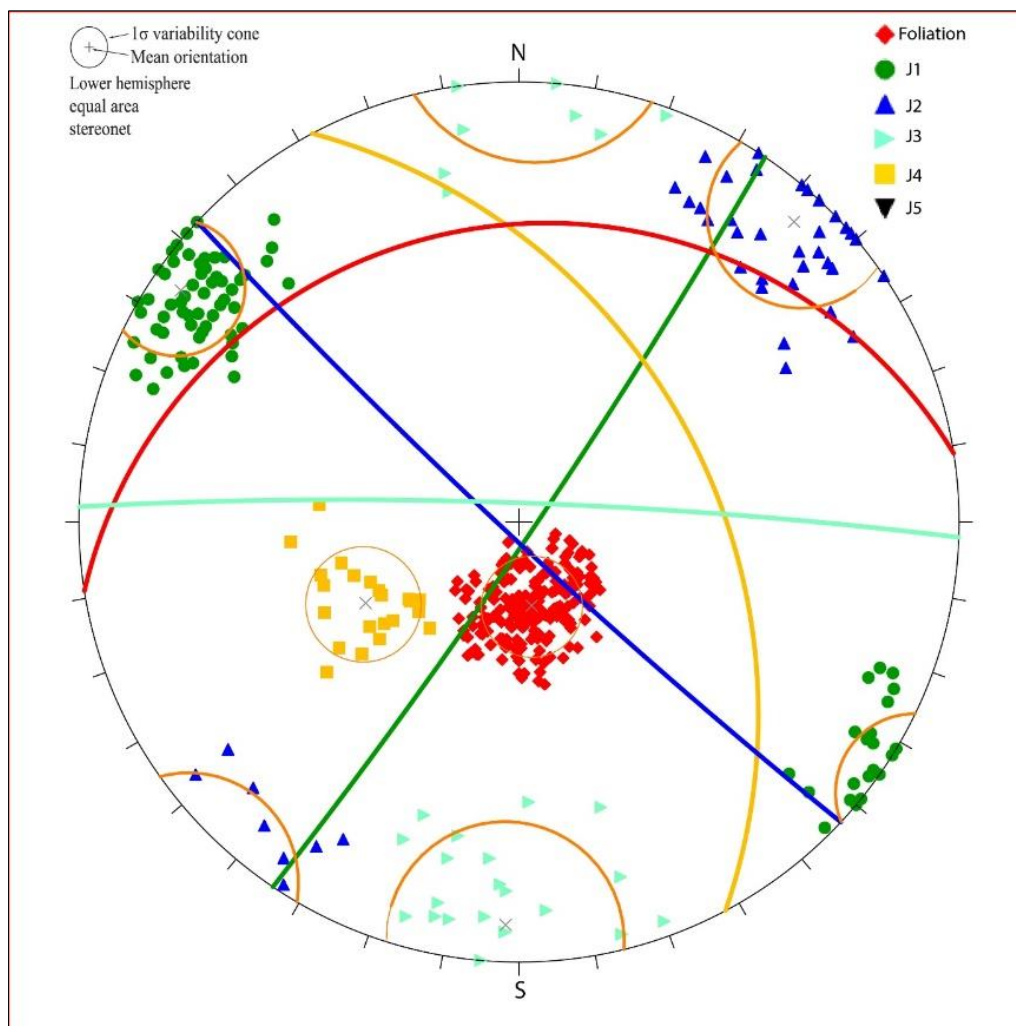
The North-West domain stretches from the back scarp eastwards towards the first secondary scarp observable on the hillshade. Most of the visible back scarp is situated within this domain. Three significant discontinuities were found (figure 4.19). The foliation, with an orientation of  $360/24 \pm 12$ , J1 with an orientation of  $289/90 \pm 12$  and J4 oriented  $067/36 \pm 12$  (figure 4.19). This is the only domain where J2 and J3 were not found. J4 is most prominent in this region of the unstable slope. J1 and the foliation are stable at all measurement locations. J4 changes slightly from NW to W dipping further north in the domain. Due to few good outcrops, some parts of this domain were not mapped in detail.



**Figure 4.19:** Stereoplot showing the mapped structures in the North-West domain.

## North East domain

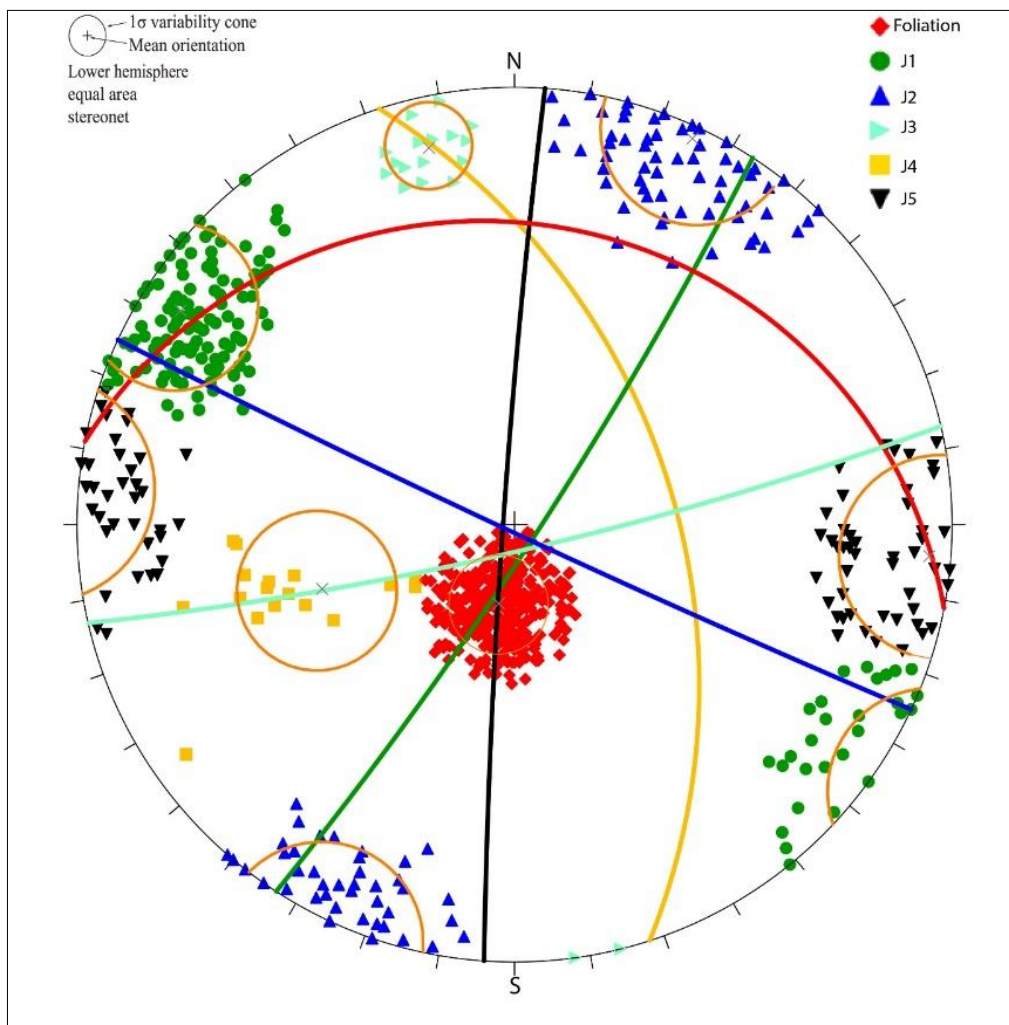
This domain was delimited based on differences in the observed structures and degree of deformation. As seen on the hillshade in blue colour, the NE domain displays the most advanced stage of deformation (figure 4.18). The east and south borders of this domain are made up of one of the internal scarps described in chapter 4.2.1. The active rockfall area is located in the steep areas towards the fjord at the eastern limit of this domain. All joint sets except J5 were found within this domain (figure 4.20). The foliation has an average orientation of  $351/22 \pm 12$  which trends more to the NNW when compared to the same structure in the NW domain. NE dipping foliation was recorded at one location close to the fjord. A possible explanation for this is the increasing deformation and the possible rotation of blocks. Contour ranges had to be changed in order to make J4 and J3 statistically significant (table 4.2). J1 and J2 show very stable orientation within the entire domain.



**Figure 4.20:** Stereoplot showing the mapped structures in the North-East domain.

## South domain

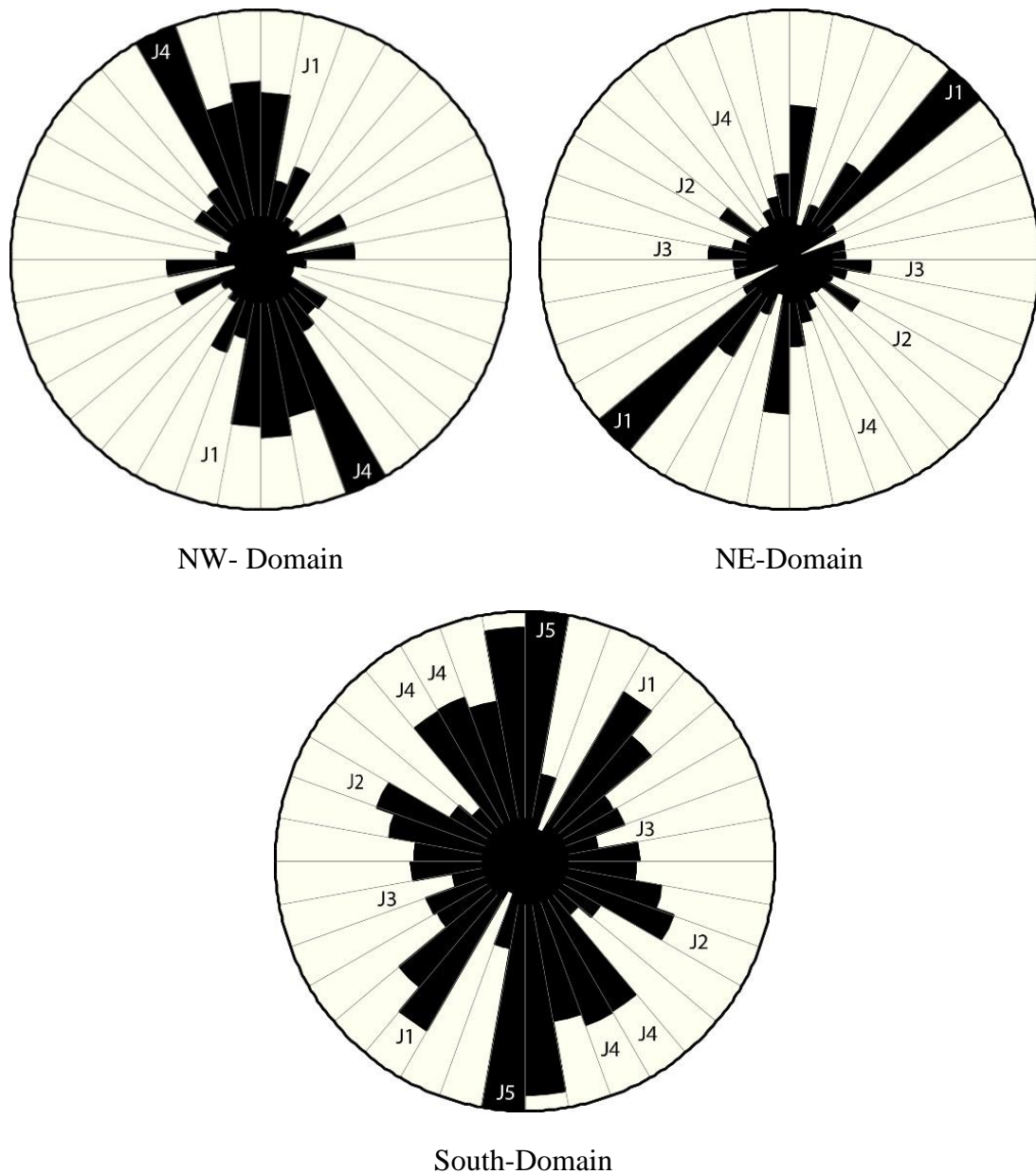
Some variation within the joint orientations and the foliation are visible within this domain, but no clear trend is visible. The foliation scatters between NE dipping to NW dipping with an average orientation of  $011/21 \pm 13$ . All joints are observed in this domain and it is the only domain where J5 was found (figure 4.21). J4 is only found at two locations, resulting in few measurements and the scatter seen in figure 4.21. This is also the reason why the contour range had to be changed to make J4 statistically significant (table 4.2). The border with the NW domain is drawn based on the lack of J2 observations in the NW domain. This is by far the biggest structural domain and stretches 1.5 km along the fjord. Thus, the amount of structural measurements and observations are greater compared to the two other domains.



**Figure 4.21:** Stereoplot showing the mapped structures in the South domain.

### 4.3.5 Rose diagrams

Figure 4.22 presented in this subchapter is a result from the procedure described in chapter 3.2.2. Rose diagrams are presented for each of the structural domains and are compared with the stereonets to test if the digitized lineaments and open cracks correspond to the mapped discontinuities. Looking at the diagrams, a reasonable fit between the lineaments and the joint sets are obvious.



**Figure 4.22:** Rose diagrams for all three domains. Bin width is set to 10 degrees. A reasonable fit between the mapped joint sets and the digitized lineaments is visible in all three structural sub-domains.

#### 4.3.6 GSI estimations

The GSI classification system was implemented to see if the GSI correspond with areas with increased deformation. In total, 32 GSI estimates were done, scattered over the entire study area. All GSI values were estimated as a range, since this is more precise than giving a single value due to natural variations in the rock mass.

Only two structural properties from the GSI table (figure 3.3) were used during the fieldwork, this is due to the lack of variation in lithology and the general poor condition of the rock mass:

- Foliated rock mass: phyllites are more abundant than massive or non-foliated rocks. E.g.: fractured graphitic phyllites with some quartz veins.
- Very foliated rock mass: folded rock mass with many fractures composed only of foliated rocks. Some faults may be present.

Recorded GSI values within the study area range from 15-50 but are concentrated between 15-35. This fits well with the recommended GSI values for phyllites given in Marinós and Hoek (2000). Examples of outcrops with GSI estimates are shown in figure 4.23.

The GSI ranges indicates a weak trend with lower GSI values eastwards and thus towards the fjord (Appendix B). In the NE domain, observed values average around 20-30. This trend is observed in both the NE and the southern domain. Along the back scarp and southwards, higher values are observed (table 4.4). In these areas, GSI values of 25-40 are average (Appendix B). This is in good agreement with the higher degree of deformation in the eastern parts of the slope.

**Table 4.4:** Minimum and maximum GSI estimates for all three structural subdomains.

<b>Domain</b>	<b>Average range</b>	<b>Maximum</b>	<b>Minimum</b>
<b>NW</b>	25-35	50	15
<b>NE</b>	20-30	40	15
<b>S</b>	25-35	48	20



**Figure 4.23:** Examples of outcrops where GSI was estimated. **A:** Outcrop close to location 16 with graphite. GSI range: 15-25 **B:** Outcrop at location 1 showing weathered phyllites with a GSI range of 25-35 **C:** Outcrop south of location 30. GSI range: 42-48.

#### 4.4 Results of kinematic analysis

This chapter presents results of the kinematic analysis of the three domains defined in chapter 4.3.4. All values for friction angles and lateral limits used in the kinematic analysis are described in chapter 3.4.1. Mapped discontinuities within each structural subdomain were combined into one mean plot by combining all the measurement locations within that domain. Slope orientations were estimated using the Zonal statistics tool in ArcMap 10.2 (ESRI, 2014). Because of the low value of internal friction for graphite (see chapter 2.7), it was decided to run one analysis with a friction angle of 10 degrees in addition to the recommended value of 20° to

check how much this influenced the results. Figures were not produced for this analysis, however, results are discussed. Values for slope orientation and friction angles for the different subdomains are summarized in table 4.5.

**Table 4.5:** Summary of the mean values used in the kinematic analysis for the three structural subdomains.

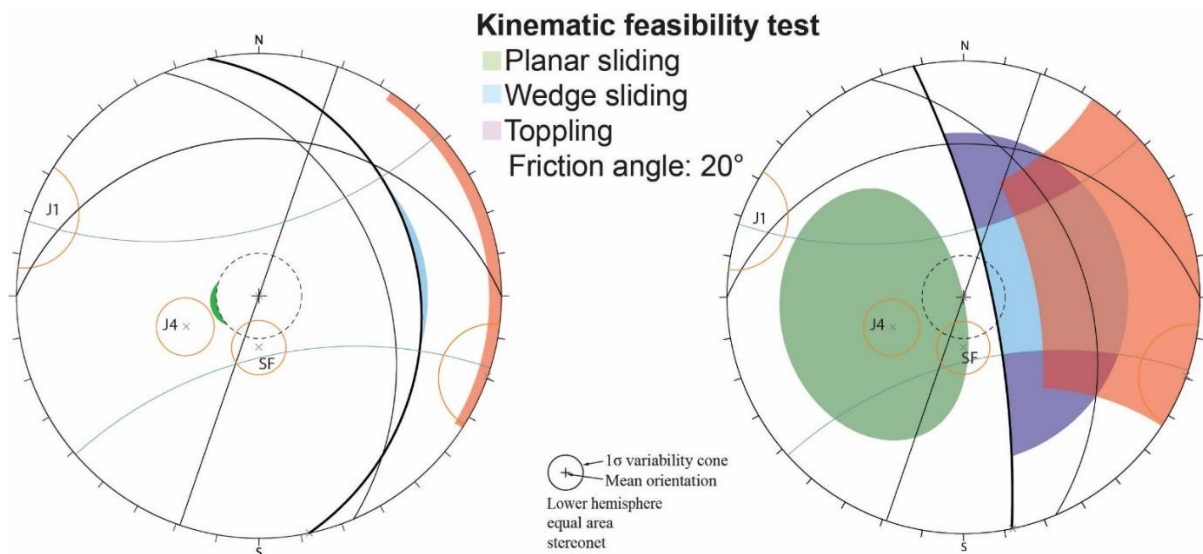
Subdomain	Slope orientation			Friction angle
	Dip direction	Dip		
		Mean	Max	
NW	78°	23°	76°	10°-20°
NE	84°	35°	79°	10°-20°
S	77°	27°	70°	10°-20°

Slope orientation for the NW domain was determined by taking the average orientation of a polygon over the slope map covering the NW and the NE domains. This was done in order to include the steep scarp close to the fjord. This maximized the possible failure modes and prevented the analysis from underestimating the hazard. In the NE domain, the flatter part of the domain was neglected when determining the average slope orientation. The southern domain slope does not have the same steep scarp at the front, therefore the orientation of the southern domain is determined from a polygon covering the entire domain.

In the kinematic analysis, green colour represents the critical area for planar sliding, blue represents wedge sliding and red represents toppling. The darker area in the blue sections symbolize the area outside lateral limits of 30°, since this results in a lower hazard score. This is also the case for the green and the red areas, but here the line representing the 30° limit is used to determine the hazard score. The colour of the critical wedge area is changed outside the 30° lateral limit because it partially overlaps with the toppling area. Joints are represented as thin black lines, while the thick black line represents the slope orientation. Yellow circles represent 1σ variability cones of the joint clusters. All figures were made using a friction angle of 20°.

The analysis was done both for the mean and max slope dip angles. Figures shown in the sub-chapters below are made after the procedure described in figure 3.4. The left figure represents the mean slope values. Due to a very shallow average slope dip, the resulting critical areas are very small. This illustrates the problem discussed in chapter 3.4.1 when determining the slope orientation for the analysis. Therefore, the hazard score was determined based on the max slope angles chosen from the steep frontal areas.

#### 4.4.1 Northwest domain



**Figure 4.24:** Kinematic analysis for the NW-Domain. Mean dip angle to the left, max to the right.

#### Max slope orientation

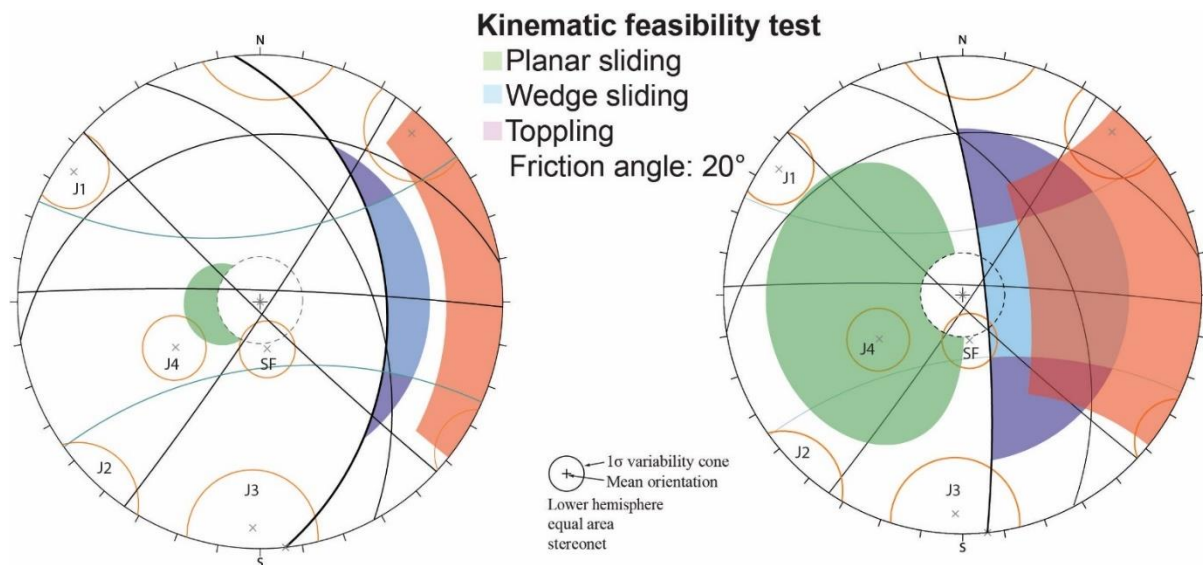
As seen in figure 4.24, planar sliding is kinematically feasible in the steepest part of the slope along J4 and the foliation. Lowering the friction angle to 10 degrees makes planar sliding along the foliation more feasible. Parts of the foliation variability cone falls inside the 20° friction cone which indicates that the friction angle can act as a limiting factor. Wedge failure is partly feasible along the intersection line between the foliation and J1. This intersection line plunges shallower than the average slope and thus have the possibility to daylight at the steepest part of the slope. Toppling is feasible along J1, but the mean orientation of this joint set lies right on the 30° limit, causing the variability cone to plot within both areas.

#### Mean slope orientation

The critical areas are a lot smaller when using the mean slope orientations. This severely limits the feasible failure modes. Looking at the figure to the left, the only feasible failure type is toppling along J1. Since most of the variability cone falls outside the 30° limit, this toppling is classified as partly feasible.



#### 4.4.2 North-east domain



**Figure 4.25:** Kinematic analysis for the NE-domain. Mean dip angle to the left, max to the right.

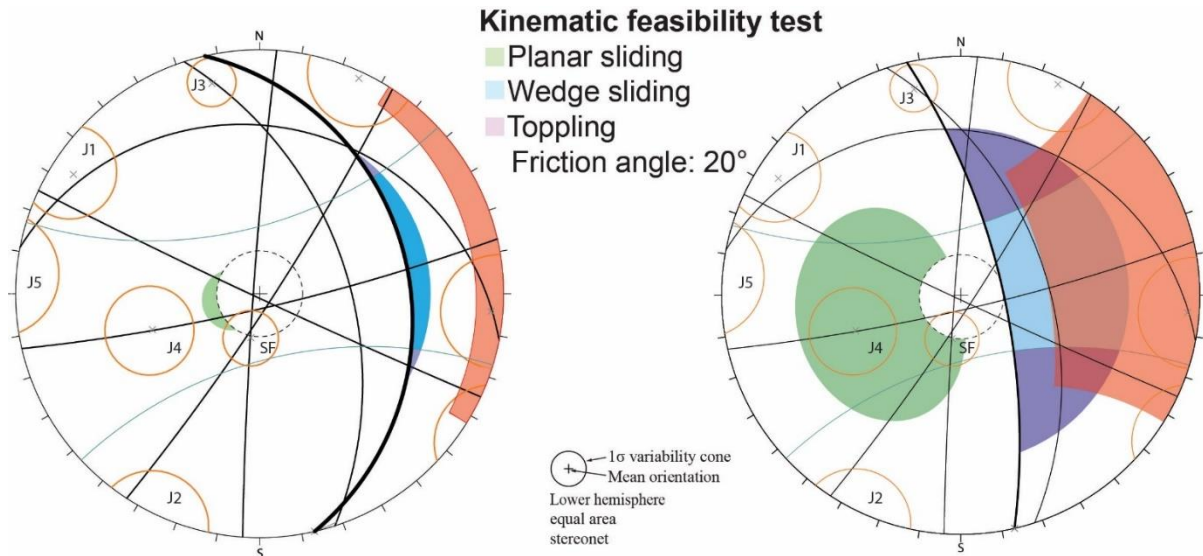
#### Max slope orientation

In the NE-domain, planar failure is feasible along J4. In this case, J1 and J2 can act as lateral release surfaces. Planar sliding is seen as less likely along the foliation in this area due to a large part of the variability cone lying outside the critical area. When lowering the friction angle to  $10^\circ$ , wedge sliding also becomes partly feasible along the intersection of J1 and the foliation. The intersection line plunges shallower than the slope and is therefore daylighting. Toppling failure is partly feasible along J1 and J2 (figure 4.25).

#### Mean slope orientation

Planar sliding is feasible along J4, however, most of the pole concentration plots outside the variability cone. Nevertheless, it is the only structural subdomain where this is feasible. More interestingly, wedge sliding along J1 and the foliation also becomes partly feasible for the mean slope orientation when lowering the friction angle to  $10^\circ$ . This intersection line daylights the slope. Toppling failure is partly feasible along J1 and J2.

#### 4.4.3 South domain



**Figure 4.26:** Kinematic analysis for the South-domain. Mean dip angle to the left, max to the right.

#### Max slope orientation

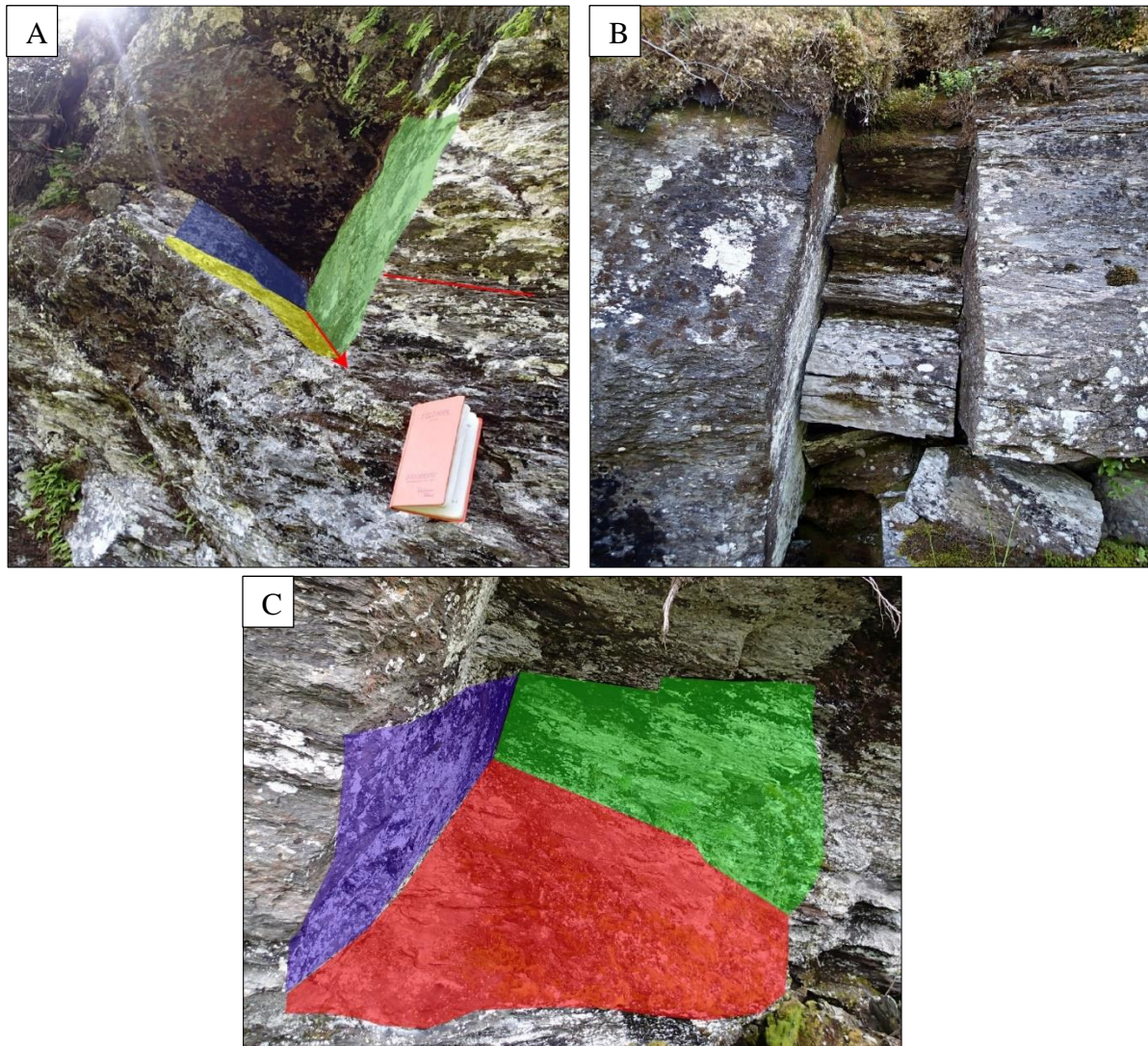
Planar failure is feasible along both J4 and the foliation. Wedge failure is partly feasible along the intersection line between J1 and the foliation if the friction angle is lowered to 10°. This is also the case for the intersection between J5 and the foliation. The intersection lines between the discontinuities forming these wedges lies right at the edge of the critical area when using a friction angle of 20°. Toppling is feasible along J5 and partly feasible along J1 and J2 (figure 4.26).

#### Mean slope orientation

For the mean orientation, toppling is feasible along J5 and partly feasible along J2 and J1. Wedge failure along J1 and the foliation is partly feasible if the friction angle is lowered. The intersection line is just shallow enough to daylight the slope.

#### 4.4.4 Examples of failure modes found in the field

Several examples of different failure modes were found in small scale outcrops within the southern domain (figure 4.27). This was mostly minor planar slides along the foliation and one evident wedge failure. These small scale features may give clues about what is possible on a larger scale.



**Figure 4.27:** Pictures showing different examples of failure mechanisms found in the southern domain. **A:** Example showing a small wedge failure found in the field 130 meters north of location 21. This wedge is composed of three discontinuities, J1 marked in green, J2 marked in blue and an irregular plane cutting the foliation just as in Figure 4.11. marked in yellow. The intersection lineation marked by a red arrow plunges  $45^{\circ} \rightarrow 033^{\circ}$ . The red line above the field book marks the dip of the foliation, this is clearly shallower than the dip of the yellow plane. **B:** Photo taken 80 meters SE of location 19 looking SW, showing two vertical discontinuities belonging to J1. The gap between the joints are around 1 meter. Blocks have been sliding out of the wall along multiple foliation planes using J1 as lateral release surfaces on both sides. Average orientation for the plane dipping out of the outcrop is  $047/24$ . **C:** Picture taken towards NW showing a planar failure along the foliation with two joint sets as lateral release surfaces. These features were not possible to measure. North of location 16.

## 4.5 Structural profiles

In total five structural profiles were made covering different parts of the unstable slope (figure 4.18). Two figures with different discontinuities were constructed for each of the five different profile orientations. One with mean structure orientations plotted as given in table 4.6 and one containing only those structures interpreted to be critical for the stability. All profiles are cut at 400 meters below sea level. The foliation is included in all profiles even if it is striking almost parallel with the profile orientation. This was done because this structure was found all over the unstable area and shows high degree of variability between measurement locations. All structures were drawn with the same spacing and infinite persistence. Colours assigned to the different discontinuities are the same as in chapter 4.4. Since these profiles do not show the actual spacing of the joint sets, the placement of each line impacts the apparent stability situation. Uncertainties are visualised by marking the deepest areas without observations in addition to the area below sea level in grey. The observation points are indicated on the structural profiles by black dots.

**Table 4.6:** Table showing mean dip angles for all profiles containing all structures. All dip values are given as apparent dip calculated using Equation 1.

Profile	Domains	Profile strike	J1 [a dip]	J2 [a dip]	J3 [a dip]	J4 [a dip]	J5 [a dip]	Foliation [a dip]
1	NE	55°	79°	86°	81°	42°	x	10°
2	NE	90°	85°	84°	22°	39°	x	3°
3	NW and NE	90°	90°/85°	x/84°	x/22°	33°/39°	x	0°/3°
4	South	55°	74°	87°	71°	48°	86°	15°
5	South	90°	82°	85°	61°	48°	86°	4°

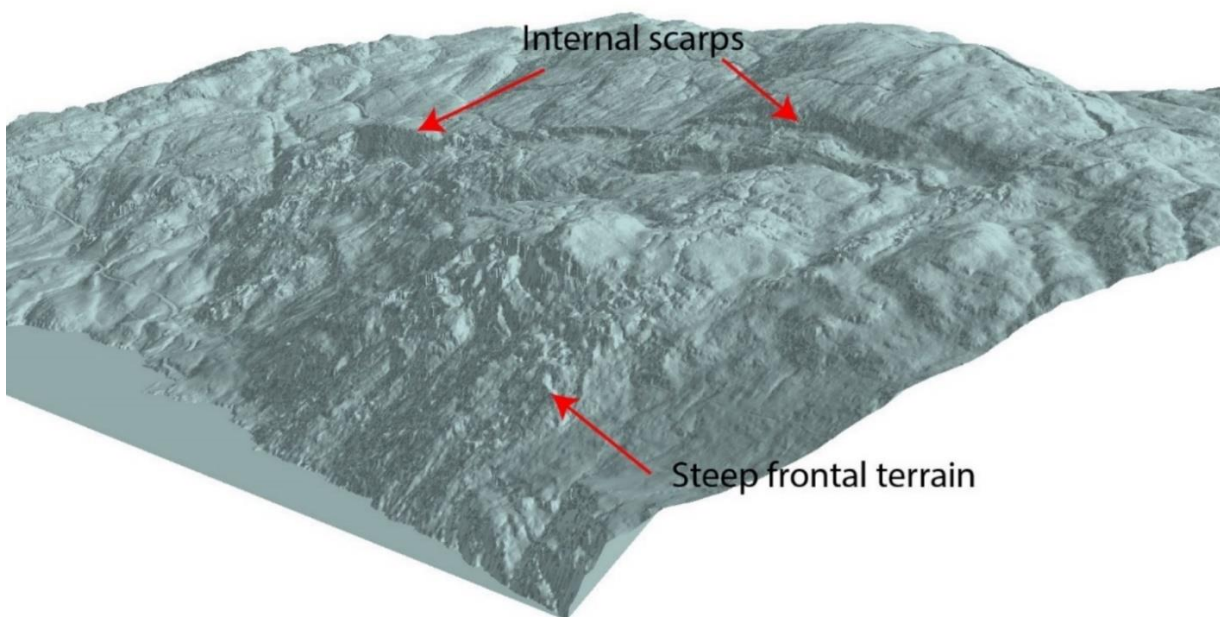
Since J1, J2, J3 and J5 are sub-vertical, their variation is not critical for the stability. Minimum values for J4 and maximum values for the foliation were determined in the stereonet for each domain and converted to apparent dip (table 4.7). These are the structures that are considered most critical. A significant worsening of the stability is observable in the profiles oriented 55° compared to the ones oriented 90°.

**Table 4.7:** Table showing the values used in the critical profiles. Dip values are given as apparent dip.

Profile	Domains	Profile strike	J4 [a dip] min	Foliation [a dip] max
1	NE	55°	34°	16°
2	NE	90°	31°	5°
3	NW and NE	90°	23°/31°	0°/5°
4	South	55°	35°	22°
5	South	90°	35°	6°

### Profile 1

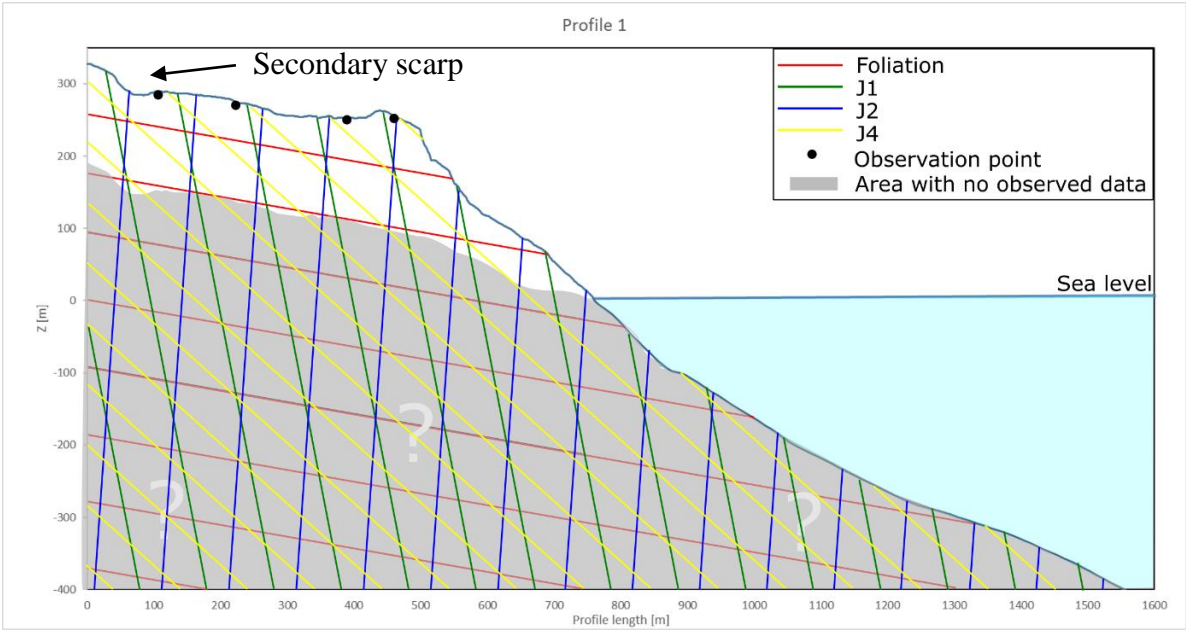
Profile 1 strikes 55° across the NE domain. No detailed investigations were done in the steepest part of the profile towards the fjord due to difficult terrain (figure 4.28).



**Figure 4.28:** Screenshot of a 3D model created based on the 1x1m DEM showing the steep frontal terrain and the internal scarps in the NE sector of the slope. The steepness of the frontal areas made investigations of these areas difficult. View is towards SW.

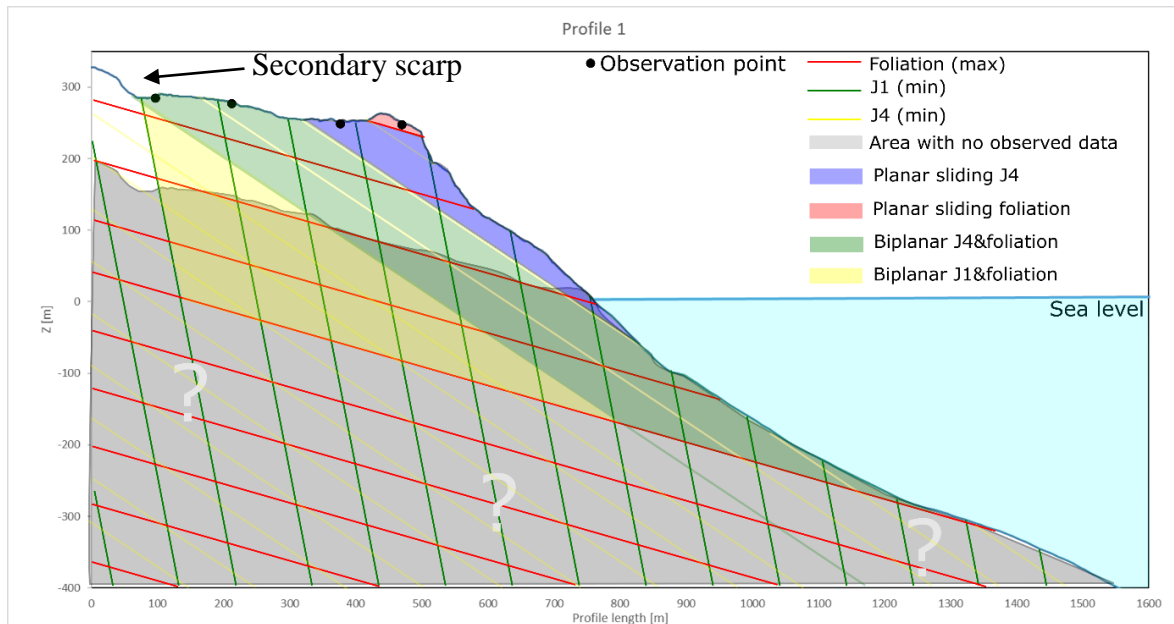
J3 is excluded from this profile due to a similar apparent dip as J1. This was also the structure found at fewest locations within the domain. J4 does not daylight in the slope when using average dip values (figure 4.29). It only daylights in the almost vertical section at the front of the slope. The shallow foliation daylights over the entire slope face, dipping at 10°. J1 and J2 are possible release surfaces.

The steep topography at the front continues below sea level before flattening out towards the fjord bottom at 700 meters below sea level. Due to the steep topography below sea level, the structures can daylight also here. The scarp that is set as the limit for the NE domain is recognisable on the left side of the profile as a 20-meter-high step. This step is also visible on the 3D model (figure 4.28).



**Figure 4.29:** Profile 1 crossing the NE domain with the mean dip values of the discontinuities. Orientation of the structures in the grey area is estimated based on observations elsewhere. Profile strikes 55°.

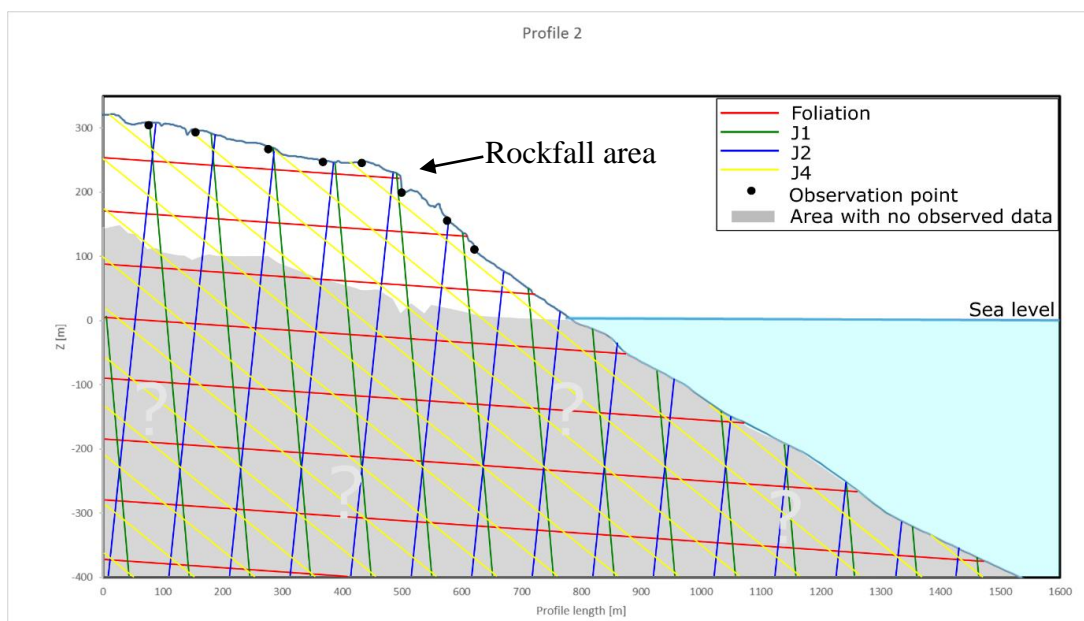
The profile shown in figure 4.30 is drawn with the structures that are believed to be most critical for the stability. Due to the steeper foliation, the stability situation is worse than in figure 4.29. When using the minimum dip value for J4, planar sliding is feasible along this structure. Planar sliding is also feasible along the steeper foliation dipping 16°. The green area in the figure is selected so that it matches the scarp indicated on the figure. This area indicates a volume made unstable by a bi-planar feature following J4 and the foliation. The yellow colour indicates the largest possible unstable area along J1 and the foliation. Both of these instabilities may daylight below sea level.



**Figure 4.30:** Profile 1 drawn with only the structures critical for the stability. Profile strikes 55°.

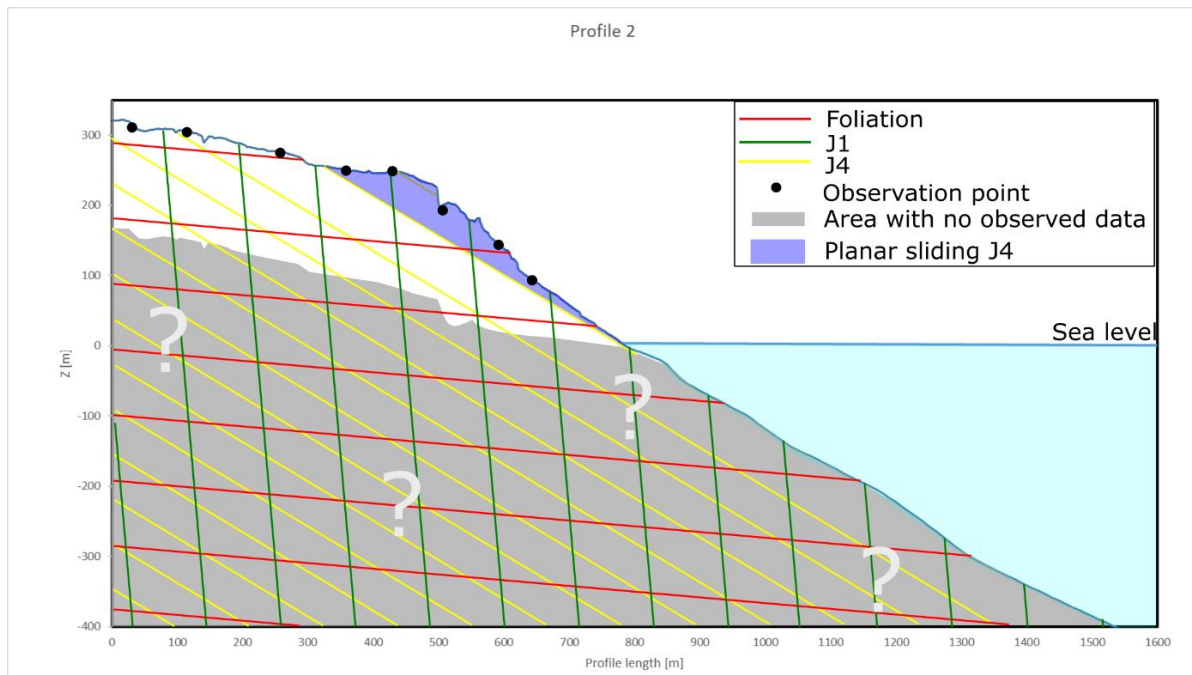
### Profile 2

This profile is oriented E-W across the NE domain. J3 is not drawn because it strikes almost parallel with the profile. This joint set can act as a lateral release surface. J4 does not daylight when using the mean dip value (figure 4.31). As in profile 1, the foliation daylights, but because of the shallow dip, it will not cause any stability problems. This limits the possible failures looking at figure 4.31. A bi-planar failure is not feasible because J4 is not daylighting. The topography underwater is shallower than in profile 1, thus restricting extension of any possible unstable areas underwater.



**Figure 4.31:** Profile 2 crossing the NE domain with the mean dip values. Profile strikes 90°.

When using the minimum dip angle for J4, a small area at the front has the possibility to become unstable (figure 4.32). The feasible planar sliding along J4 is indicated in blue colour. The foliation is not steep enough to allow sliding.

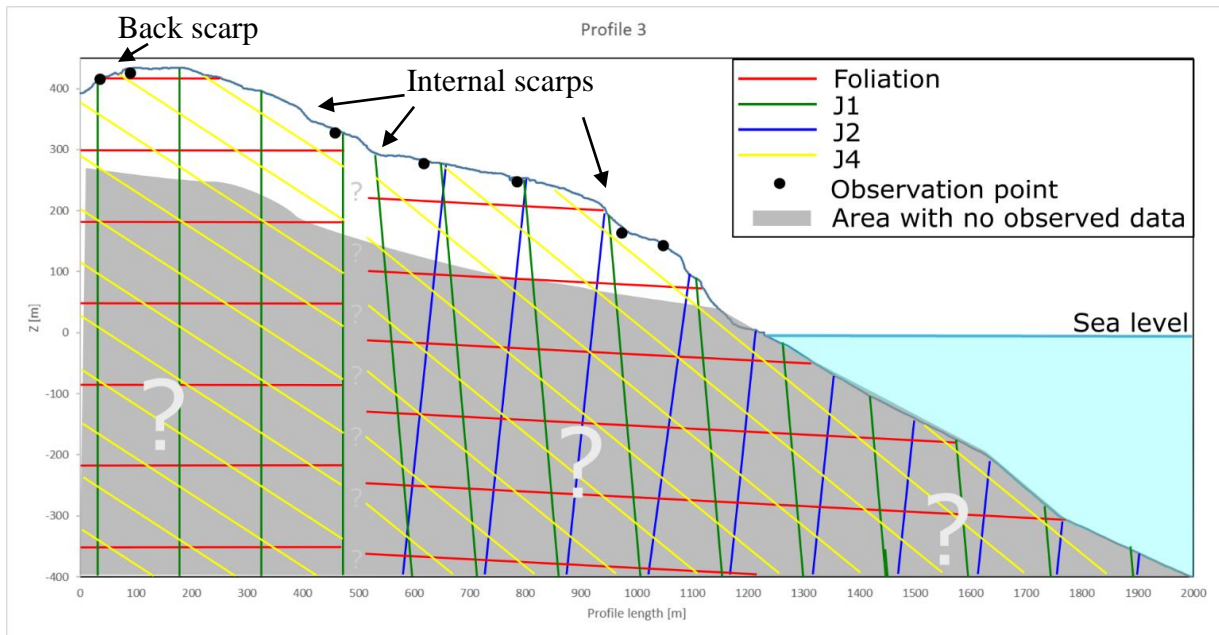


**Figure 4.32:** Profile 2 with the critical discontinuities. Profile strikes 90°.

### Profile 3

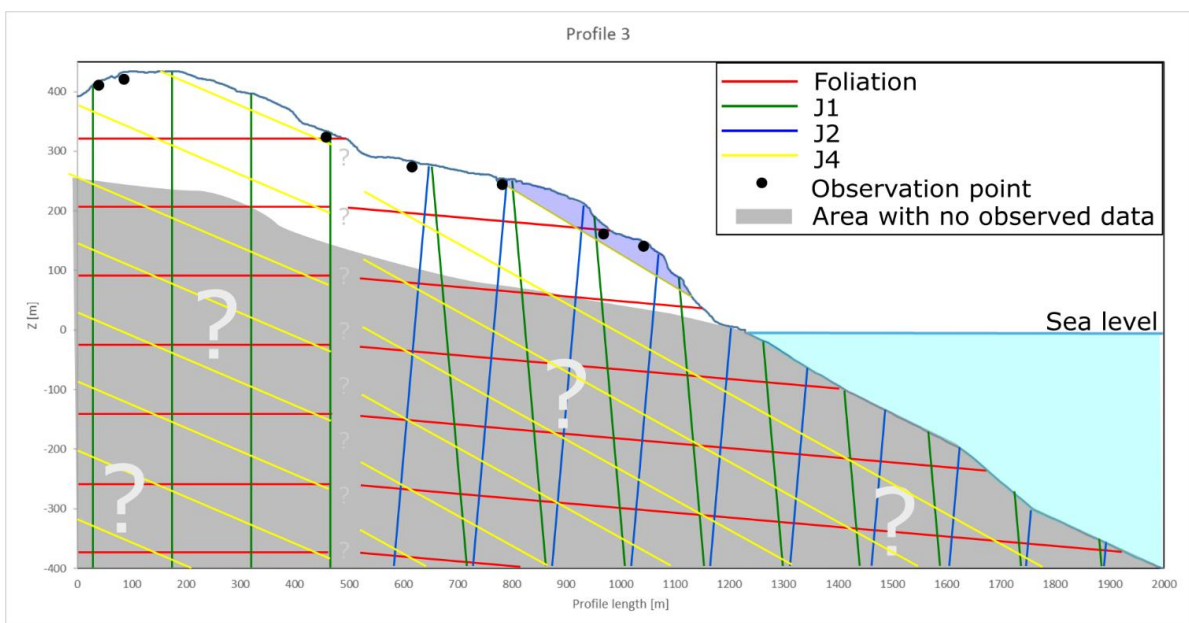
Profile 3 is the only profile spanning over two different domains. It is oriented E-W and includes structures both from the NW and the NE domain. Since the structures are different, they are separated by a gap indicating that the transition between these structures is unknown. This profile stretches from the back scarp all the way down to the fjord (figure 4.33). The fact that the back scarp is situated behind the hill crest is still visible in the profile. Both of the two scarps at the edge of the more deformed area are recognisable in this profile. In addition, the scarp close to the fjord is indicated. The area without observations in the NW domain is due to missing outcrops. No evident stability problems are possible when using the mean orientations.





**Figure 4.33:** Profile 3 crossing the NW and NE domains with the mean dip values. Profile strikes 90°.

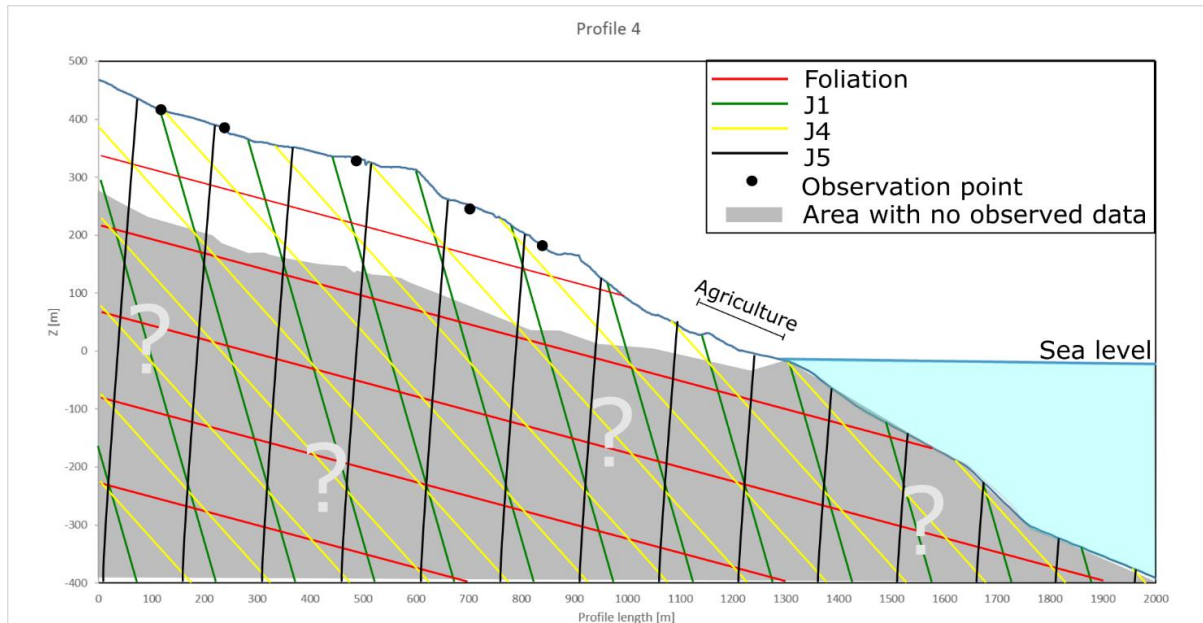
Figure 4.34 shows the same profile using the critical structures. The foliation daylight over the entire profile, but is too shallow to cause stability problems. J4 is too steep to daylight except in the steepest areas at the front. A planar instability is feasible along J4. No stability problems are feasible below sea level with this profile orientation.



**Figure 4.34:** Profile 3 crossing the NW and NE domains with only the critical structures. Profile strikes 90°.

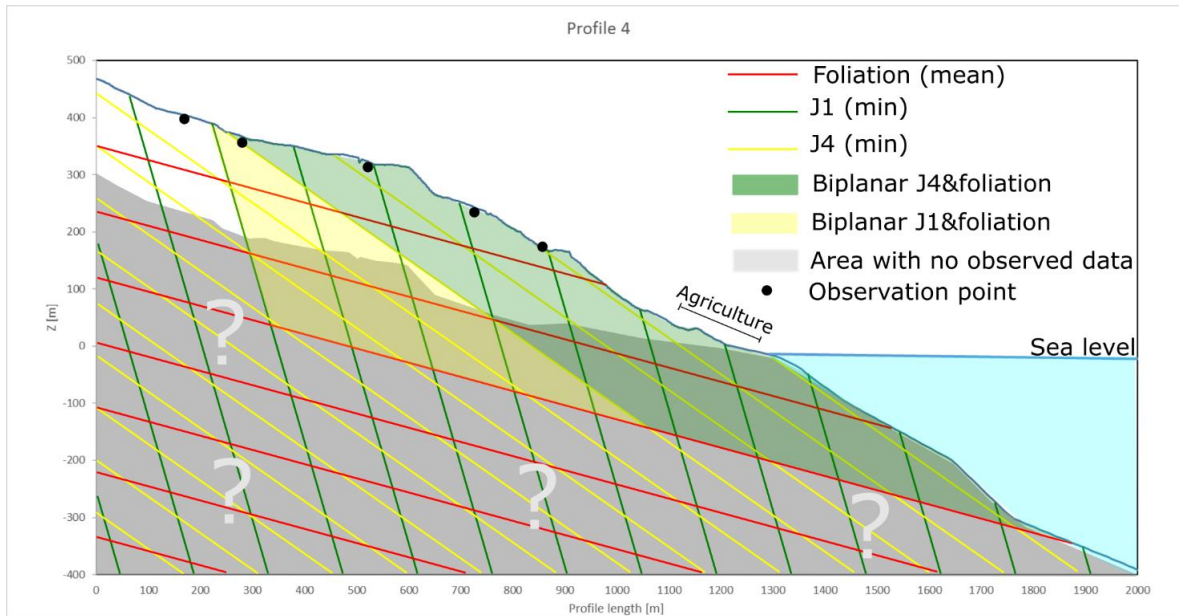
## Profile 4

This profile strikes  $55^\circ$  and stretches across the entire southern domain. J2 and J3 are not drawn due to similar dip values as those of J5 and J1, respectively. This is the profile with the steepest dipping foliation ( $15^\circ$ ), and it is therefore well above the lowest estimate for the friction angle. That makes bi-planar sliding along the foliation along with either J1, J2, J4 or J5 feasible (figure 4.35). J3 can in this case, act as lateral release surfaces on both sides. The lack of observation points close to the fjord is due to agricultural land without outcrops.



**Figure 4.35:** Profile 4 crossing the south domain showing the mean values. Profile strikes  $55^\circ$ .

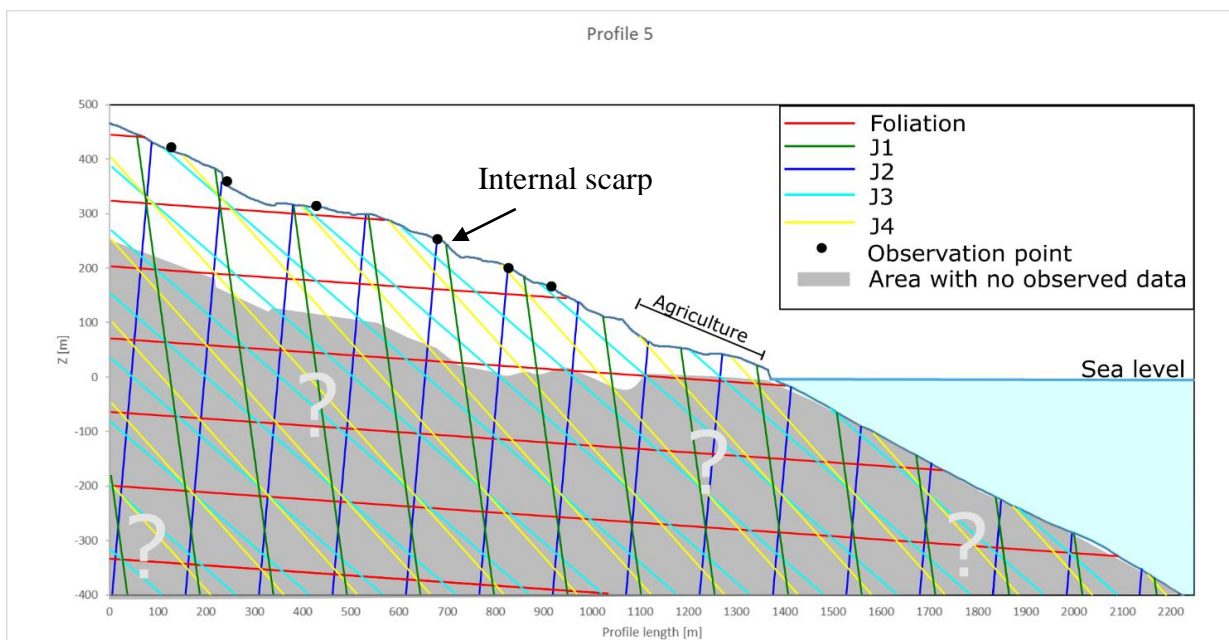
The maximum angle for the foliation in this domain is too steep to daylight. Therefore, the mean value is used also in the critical profile (figure 4.36). The feasible bi-planar sliding along J4 and the foliation is shown in green colour. Yellow colour shows the bi-planar feature along J1 and the foliation. The structures do not allow for planar sliding along a single discontinuity using this profile orientation



**Figure 4.36:** Profile 4 drawn showing only the structures critical for the stability. Profile strikes 55°.

### Profile 5

J5 is excluded from this profile due to almost identical apparent dip as J2. J3 and J4 do not daylight above or below sea level when using the mean dip values. The kinematic analysis for this domain clearly indicates planar sliding along J4 as a possibility. This is not visible in the profile below. Using the mean values does not indicate any severe stability problems (figure 4.37). This is also the case using the critical values. Therefore, the profile including the critical structures is not shown here.



**Figure 4.37:** Profile 5 crossing the south domain showing the mean values. Profile strikes 90°.

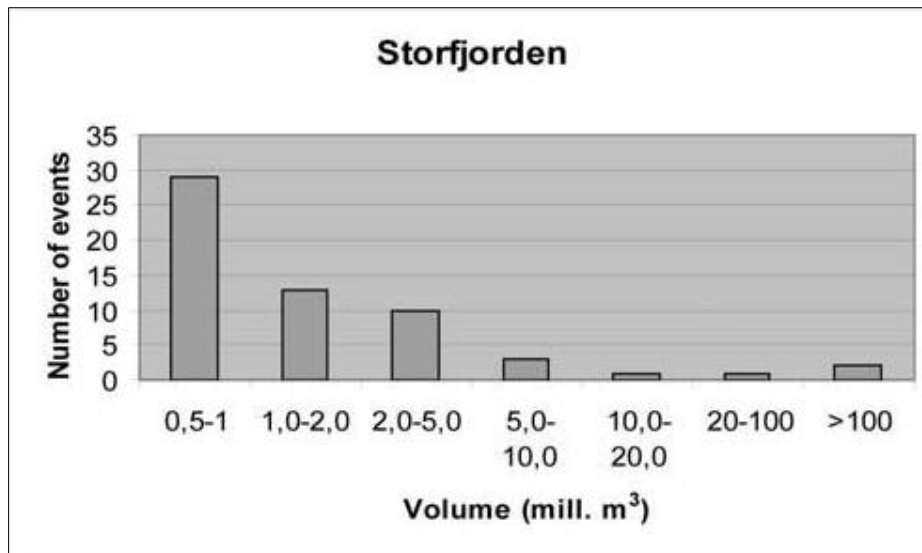
## 4.6 Failure scenarios

Based on recommendations in Hermanns, Oppikofer, et al. (2012), six failure scenarios have been defined within the unstable slope. Series of open, limiting cracks and scarps are used to define the six scenarios (figure 4.39 and figure 4.40 ). The scenarios range from blocks in the frontal area to the largest scenario which incorporates the entire instability. They are numbered from 1-6 where scenario 1 is the largest case scenario. Each smaller scenario is included within the largest scenarios.

Due to the low resolution of the bathymetric data, extrapolation of the structures in the structural profiles and changes in slope angle below sea level are used to determine the toe line of each scenario that might continue under water. These assumptions result in large uncertainties that are further discussed in chapter 5.5. The difference in resolution between the hillshade used to investigate the area above sea level and the bathymetry is illustrated in Appendix F.

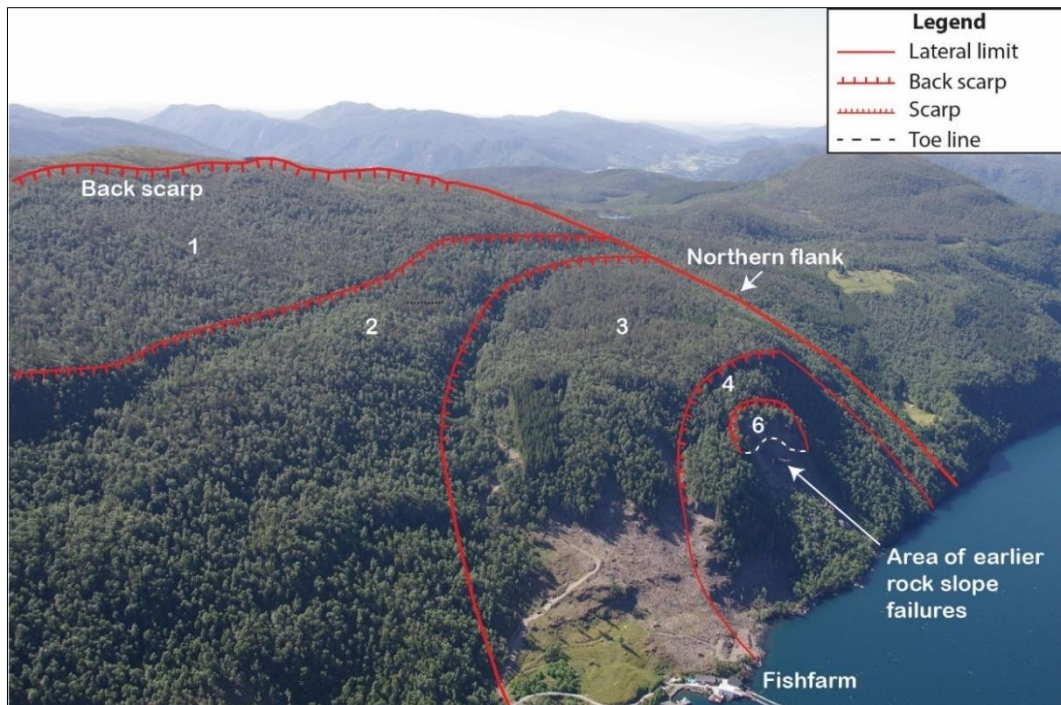
The geological model for the bigger scenarios fits best with daylighting structures below sea level since these have not been observed on the slope. Not all of the scenarios are analysed in detail due to the large size and volume: the biggest recorded rockslide in Norway is the Tjellefonna rockslide that occurred in 1756. This event had an estimated volume of 9-10 million  $\text{m}^3$  (Sandøy, 2012). Historic records show that large rock slope failures rarely exceed 10 million  $\text{m}^3$  (figure 4.38). No failure larger than  $5 \times 10^6 \text{ m}^3$  has been recorded in the Storfjord region within the last 9000 years (Böhme, Oppikofer, et al., 2015). Larger failures have been restricted to rock slope failures directly following deglaciation (Böhme, Oppikofer, et al., 2015; Hermanns & Longva, 2012).

Failure scenarios 1-4 at Tytefjell have mean volumes ranging from  $78.4 \times 10^6 \text{ m}^3$  -  $524 \times 10^6 \text{ m}^3$  and are therefore much greater than the size of Holocene events in Storfjord and historic events in Norway. The two biggest scenarios cross several structural domains, and no penetrative structures stretching across the entire slope that could allow these bigger scenarios to fail in one event were found during fieldwork. Scenario one and two are therefore not realistic without a large amount of extensive pre-failure deformation.

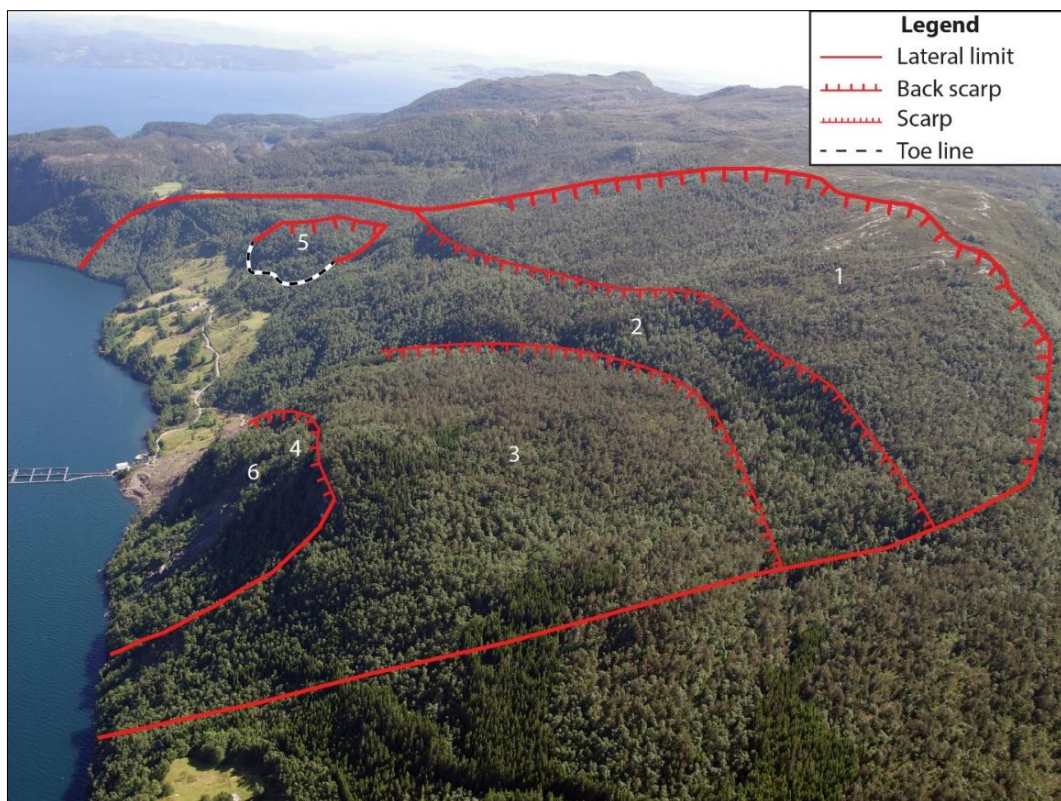


**Figure 4.38:** Diagram showing the number and volume of recorded rock-avalanche events in the entire Storfjord (Møre og Romsdal county). The distribution of events show that failures volumes rarely exceeds 10 million m<sup>3</sup>. This is one of the most active areas in terms of rock slope failures in Norway (Blikra et al., 2005).

The toolbox developed at NGU for the hazard analysis is not capable of completing runout analyses when the unstable area has one part above, and one part below sea level. Therefore, runout analysis is only performed for the two scenarios which have a toe line above water level (scenario 5 and 6). This analysis is normally done to determine if the runout of an unstable area might reach a standing body of water with resulting risk of displacement waves. Due to the fact that the larger scenarios are partly submerged, the chance of them causing a displacement wave is certain. The runout model for scenario 5 and 6 was run using a down-sampled 5x5 meter DEM because the Flow-R model is not developed for 1x1 meter resolution DEMs.



**Figure 4.39:** Aerial photograph taken towards NNW, showing the NE part of the unstable slope at Tytefjell with lineaments showing five of the six failure scenarios. Each smaller scenario is included within the bigger scenarios. The scenarios are marked with numbers.



**Figure 4.40:** Aerial photograph taken towards SSW of the unstable slope at Tytefjell. Failure scenario 5 is marked at the southern end of the unstable area. Each smaller scenario is included in the bigger scenarios. The flat agriculture area below scenario 5 is visible.

#### 4.6.1 Scenario 1

This is the largest scenario including the entire instability. The extent of this scenario is likely to continue below sea level, since no daylighting sliding structure is observed on the slope. Scenario 1 is limited by the back scarp at 500 meters a.s.l and the lateral limits as indicated on figure 4.40. Both the back scarp and the lateral limits are partly developed. The toe line of this instability is drawn on the bathymetry based on changes in slope angle in an area 300 meters below sea level. Here, the slope angle gets shallower, indicating a possible daylighting sliding plane. This is a rough estimate, but it is not possible to determine the extent of this scenario more precisely with the data available today.

Scenario 1 has volumes ranging from  $171 \times 10^6 \text{ m}^3$  to  $723 \times 10^6 \text{ m}^3$ , where the highest estimate is way bigger than the biggest recorded landslide in Norwegian history, which is described by Sandøy (2012). The area of the scenario, volume and other relevant parameters are listed in table 4.8. No hazard assessment was performed for this scenario as it is unlikely that this will ever fail in a single event.

**Table 4.8:** Parameters for scenario 1 which is the worst case scenario. It is not possible to determine the basal angle at the toe of this scenario because it is below sea level, therefore the angle that gave the best fit was chosen. The angle of the back scarp is measured on the slope map.

<b>Scenario 1</b>	
<b>Area [m<sup>2</sup>]</b>	3468800
<b>Angle at back scarp [°]</b>	56
<b>Basal angle at toe [°]</b>	10
<b>H<sub>max</sub> (m.a.s.l)</b>	494
<b>H<sub>min</sub> (m.b.s.l)</b>	-317
<b>Volume Min [m<sup>3</sup>]</b>	$171 \times 10^6$
<b>Volume Mean [m<sup>3</sup>]</b>	$524 \times 10^6$
<b>Volume Max [m<sup>3</sup>]</b>	$723 \times 10^6$

#### 4.6.2 Scenario 2

This scenario is limited to the west by the most prominent internal scarp running from the northern lateral limit and southwards to location 17 (figure 4.3 and figure 4.39). This scarp stretches almost the entire length of the scenario, but turns into a depression towards the south before connecting with the southern lateral limit. The back scarp is thus only partly developed. The northern lateral limit is the same as for scenario 1. The toe line is set at the same location as scenario 1 due to the change in slope angle observed below sea level on the profiles. Again, being below sea level, prevents judging the morphologic expression of this toe line. It is not

likely that this scenario will fail in one single event for the same reasons as scenario 1. Key parameters are listed in table 4.9.

**Table 4.9:** Parameters for scenario 2. It is not possible to determine the basal angle at the toe of this scenario because it is below sea level, therefore the angle that gave the best fit was chosen. The back scarp angle was measured on the slope map.

<b>Scenario 2</b>	
<b>Area [m<sup>2</sup>]</b>	2801000
<b>Angle at back scarp [°]</b>	55
<b>Basal angle at toe [°]</b>	10
<b>H<sub>max</sub> (m.a.s.l)</b>	376
<b>H<sub>min</sub> (m.b.s.l)</b>	-317
<b>Volume Min [m<sup>3</sup>]</b>	91 x10 <sup>6</sup>
<b>Volume Mean [m<sup>3</sup>]</b>	398 x10 <sup>6</sup>
<b>Volume Max [m<sup>3</sup>]</b>	524 x10 <sup>6</sup>

#### 4.6.3 Scenario 3

Scenario 3 is composed of the entire NE domain with an internal scarp as the limiting structure (figure 4.39). This scarp stretches southwards from the northern lateral limit before turning east after 570 meter and continues eastward down to the fjord. The northern lateral limit is characterized as partly developed. The visible part of the southern lateral limit is fully developed. An evident change in slope angle observed 300 meters below sea level is set as the toe line. Runout analysis are not performed for this scenario because of the underwater component. Key parameters are listed in table 4.10.

**Table 4.10:** Parameters for scenario 3. It is not possible to determine the basal angle at the toe of this scenario because it is below sea level, therefore the angle that gave the best fit was chosen. The back scarp angle was measured on the slope map.

<b>Scenario 3</b>	
<b>Area [m<sup>2</sup>]</b>	1070900
<b>Angle at back scarp [°]</b>	55
<b>Basal angle at toe [°]</b>	20
<b>H<sub>max</sub> (m.a.s.l)</b>	494
<b>H<sub>min</sub> (m.b.s.l)</b>	-317
<b>Volume Min [m<sup>3</sup>]</b>	28.7 x10 <sup>6</sup>
<b>Volume Mean [m<sup>3</sup>]</b>	78.4 x10 <sup>6</sup>
<b>Volume Max [m<sup>3</sup>]</b>	138.15 x10 <sup>6</sup>

#### 4.6.4 Scenario 4

This scenario encompasses the entire frontal area of the NE domain including the active rockfall area (figure 4.39). An almost 270-meter-long N-S trending vertical crack is interpreted to be the back crack for this scenario. The southern lateral limit is made up of a NE-SW trending



depression continuing from the back scarp down to the fjord. The northern lateral limit is more difficult to determine due to the sediment cover on the slope. No clear lateral limit could be identified in this region. The limit is set at the end of the sediment cover since these will most likely be a part of a potential failure. This ensures the magnitude is not underestimated. It is also possible with smaller failures with a lateral limit crossing these sediments down towards the fjord. The toe line is set 100 meters below sea level due to a sudden change in slope angle. Both lateral limits are characterized as partly developed. Key parameters are listed in table 4.11.

**Table 4.11:** Parameters for scenario 4. It is not possible to determine the basal angle at the toe of this scenario because it is below sea level, therefore the angle that gave the best fit was chosen. The back scarp angle was measured on the slope map and in the field.

<b>Scenario 4</b>	
<b>Area [m<sup>2</sup>]</b>	257200
<b>Angle at back scarp [°]</b>	85
<b>Basal angle at toe [°]</b>	20
<b>H<sub>max</sub> (m.a.s.l)</b>	226
<b>H<sub>min</sub> (m.b.s.l)</b>	-106
<b>Volume Min [m<sup>3</sup>]</b>	1.62 x10 <sup>6</sup>
<b>Volume Mean [m<sup>3</sup>]</b>	10.41 x10 <sup>6</sup>
<b>Volume Max [m<sup>3</sup>]</b>	16.51 x10 <sup>6</sup>

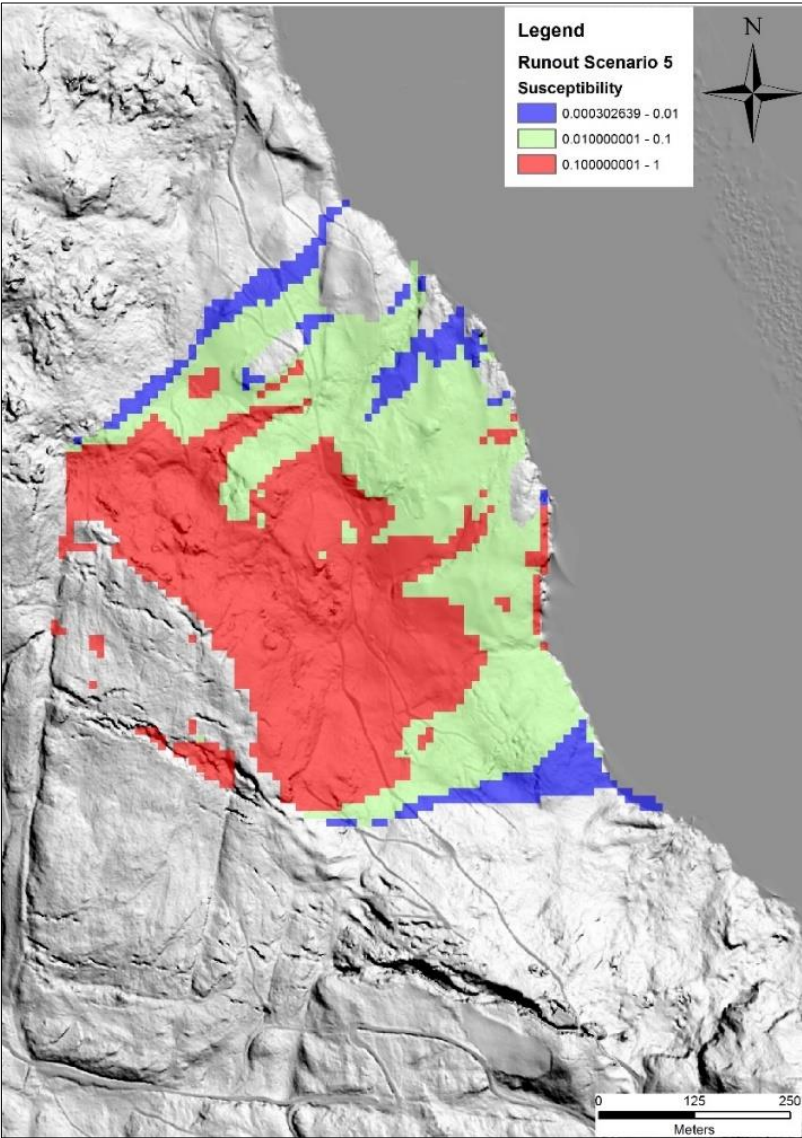
#### 4.6.5 Scenario 5

This scenario is located within the southern domain and is limited by one of the NW-SE striking fracture systems mentioned in chapter 4.2. The eastern limit is made up by a N-S striking depression. The toe line is uncertain because it was not observed in the field due to a lack of outcrops in the agricultural area below this scenario. The back scarp is partly developed. The southern lateral limit is fully developed along the northernmost fracture system seen in figure 4.7. The northern lateral limit is partly developed. Key parameters are listed in table 4.12.

**Table 4.12:** Parameters for scenario 5. The angle of the back-scarp was extracted from the slope map. Since no observations were done close to the toe line, the standard value of 20° were used.

<b>Scenario 5</b>	
<b>Area [m<sup>2</sup>]</b>	118900
<b>Angle at back scarp [°]</b>	50
<b>Basal angle at toe [°]</b>	20
<b>H<sub>max</sub> (m.a.s.l)</b>	250
<b>H<sub>min</sub> (m.a.s.l)</b>	114
<b>Volume Min [m<sup>3</sup>]</b>	1.68 x10 <sup>6</sup>
<b>Volume Mean [m<sup>3</sup>]</b>	3.85 x10 <sup>6</sup>
<b>Volume Max [m<sup>3</sup>]</b>	5.35 x10 <sup>6</sup>

The Scheidegger runout lengths ranges from 561-673 meters for the three different volumes. The intermediate volume that is used in the Flow-R model has a Scheidegger runout of 639 meters which is just enough to reach the fjord. This agrees with the Flow-R runout modelling showing that the runout from this scenario has a low probability to reach the shoreline due to the shallow angle of the slope below the scenario (figure 4.41). Most of the material will most likely be deposited before reaching the water. This has implications for the displacement wave analysis for this scenario (chapter 4.8). A farm consisting of four buildings is situated in the runout area with highest probability right below the scenario. This needs to be taken into account in the future risk analysis.



**Figure 4.41:** Computed runout area for scenario 5 (Flow-R). The simulations show a low probability for scenario 5 to reach the water due to the shallow angle of the runout slope. The green area indicates the area where the probability is less than 10 %. The narrow runout path furthest to the north was discarded because of the low probability.

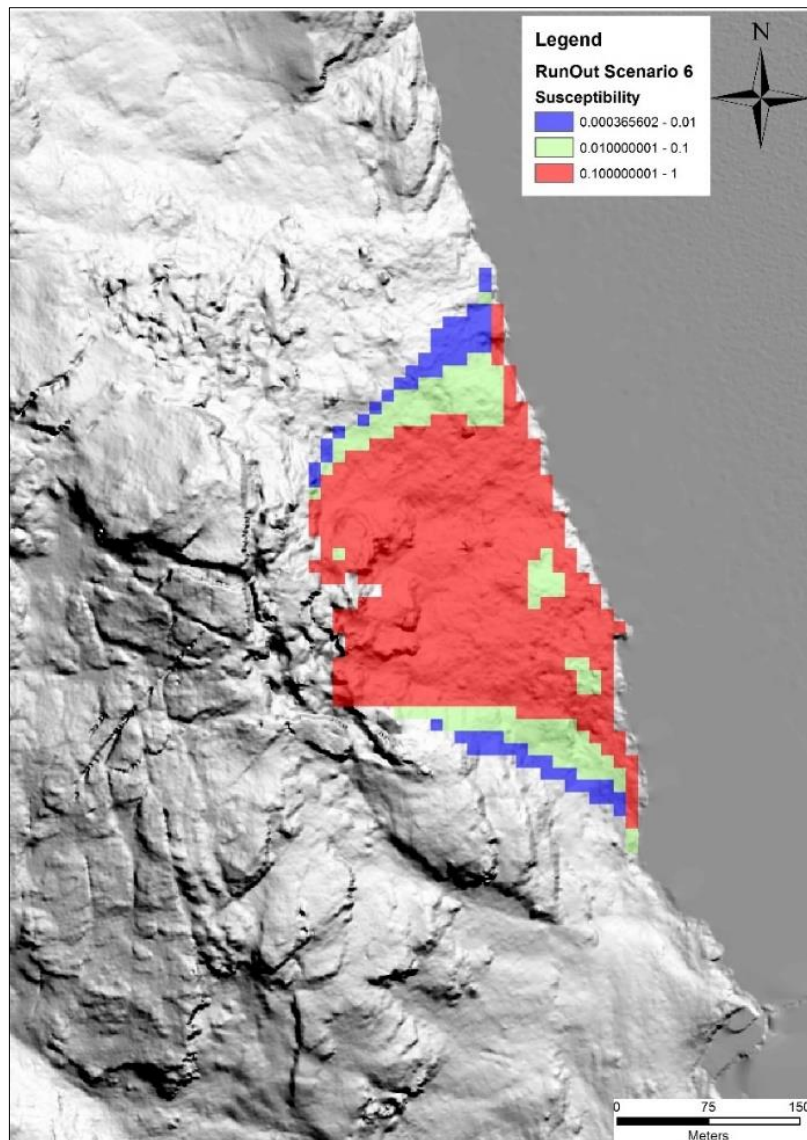
#### 4.6.6 Scenario 6

This is the smallest defined scenario composed of blocks located in the frontal area of the NE domain. The blocks are limited by a 150-meter-long N-S trending fracture. This crack is visible when looking at structural profile number two. The toe line is defined based on aerial photographs and the hillshades. The total area of this scenario is 12402 m<sup>2</sup>, and the volume estimates range between 0.1x10<sup>6</sup> - 0.51x10<sup>6</sup> m<sup>3</sup>. Key parameters are listed in table 4.13.

**Table 4.13:** Parameters for scenario 6. The basal angle at the toe of this scenario was not observed during fieldwork and therefore the angle that gave the best fit was chosen. The back scarp angle was measured on the slope map and in the field.

<b>Scenario 6</b>	
<b>Area [m<sup>2</sup>]</b>	12500
<b>Angle at back scarp [°]</b>	90
<b>Basal angle at toe [°]</b>	25
<b>H<sub>max</sub> (m.a.s.l)</b>	183
<b>H<sub>min</sub> (m.a.s.l)</b>	79
<b>Volume Min [m<sup>3</sup>]</b>	0.1x10 <sup>6</sup>
<b>Volume Mean [m<sup>3</sup>]</b>	0.4x10 <sup>6</sup>
<b>Volume Max [m<sup>3</sup>]</b>	0.51x10 <sup>6</sup>

The calculated Scheidegger runout lengths ranges from 305 meters for the minimum volume and 341 meter for the maximum volume which means that this scenario will reach the water if it fails. This is also confirmed looking at the Flow-R analysis (figure 4.42).



**Figure 4.42:** Computed runout area for scenario 6 (Flow-R). The computation shows a high probability for a failure reaching the fjord.

#### 4.6.7 Minor scenarios

Minor failures comparable to those recorded the last 20 years (chapter 1.4.3) are likely to occur from the most active areas of the slope situated in the NE domain. These are believed to be failures with volumes below 10000 m<sup>3</sup>. Frequent rock falls are reported by locals from this active area. Thus, the hazard of such small scenarios are large, but the consequences are low.

## 4.7 Results from hazard assessment

Results presented in this chapter are a preliminary hazard assessment based on the data collected for this thesis only. A more detailed hazard assessment has to be performed by NGU after the 2016 field campaign when displacement measurements become available.

The nine criteria described in Hermanns, Oppikofer, et al. (2012) were used for the hazard assessment of the scenarios. Two publications that are applying this method were used as guidance during this process: (Böhme, Dehls, et al., 2013; Böhme, Molina, et al., 2015). Results from the dGNSS displacement measurements are not available until after the 2016 field campaign. The nine criteria and the observations used for giving the corresponding scores for all scenarios are presented in Appendix F. Scenario 1 and 2 are not included in the hazard analysis since they are not seen as realistic. A summary of the resulting hazard scores can be seen in Table 4.14.

**Table 4.14:** Summary of the hazard scores and hazard classes for the four smallest scenarios. Hazard classes is determined based on the mean hazard scores. Details on each criterion are listed in Appendix F.

Scenario	Mean volume [m <sup>3</sup> ]	Max hazard score	Mean hazard score	Hazard class
3	78.4 x 10 <sup>6</sup>	9.25	5.53	Moderate
4	10.41 x 10 <sup>6</sup>	9.25	5.53	Moderate
5	3.85 x 10 <sup>6</sup>	9.5	5.78	Moderate
6	0.4 x 10 <sup>6</sup>	8.8	5.7	Moderate

All the assessed scenarios fall into the moderate hazard class when looking at the mean hazard scores ranging from 5.53-5.78. Due to high uncertainties when assessing several of the criteria, the hazard scores might be too high. Further investigations, mainly displacement measurements, in the unstable area will lower the uncertainties and can result in lower hazard scores for the four scenarios.

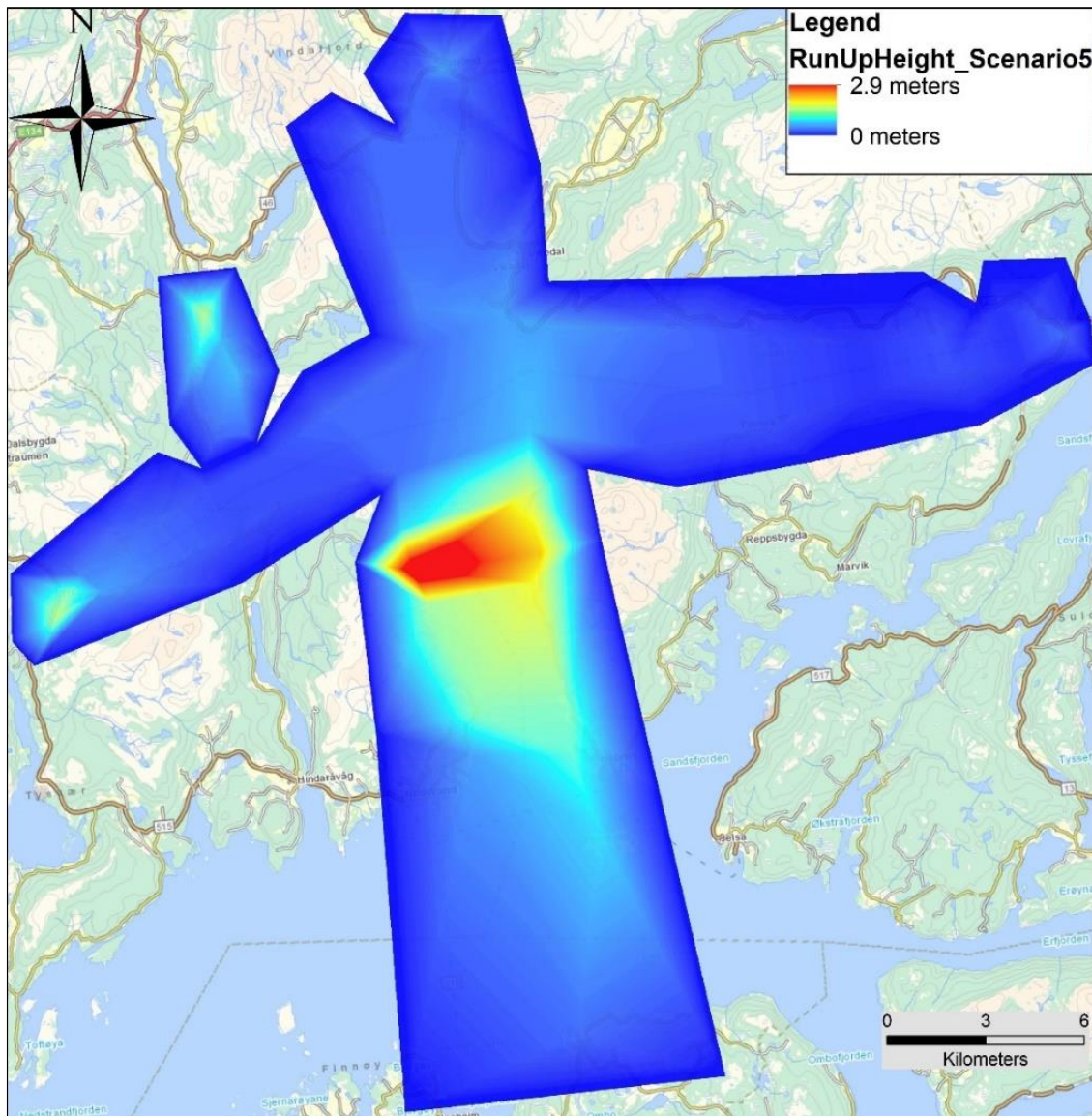
## 4.8 Results from VAW analysis

The VAW analysis was performed using a procedure that combines ArcMap and Excel. Only the two smallest scenarios were analysed since the parameter estimation for the VAW analysis requires data resulting from the Flow-R modelling. Since the Flow-R model is not adapted for modelling the scenarios with a component below sea level, such data is not available for scenario 3-6. In addition, the VAW model is not adapted for modelling displacement waves from landslides with an underwater component.

The results of the run-up model are presented as an interpolation between the run-up points creating a polygon of the run-up area covering the Vindafjord system. These interpolations are displayed as maps for each modelled scenario (figure 4.43 and figure 4.44). As the fjord geometry of Vindafjord is complex, these results should only be seen as rough estimates. All input parameters along with the resulting run-up heights for the modelled scenarios are listed in appendix E.

### Displacement wave run-up for Scenario 5

As mentioned in chapter 0, based on the Flow-R modelling, most of the material from a scenario 5 failure will most likely be deposited before reaching the shoreline. This has implications for the VAW model since it is not realistic to do the calculations using the entire volume obtained from the SLBL analysis. To take this into consideration, the model was run with a reduced volume of 1155000 m<sup>3</sup> (30% of the original volume). This resulted in an error in the VAW calculations where no material reached the water, therefore, the original volume of 3.85x10<sup>6</sup> m<sup>3</sup> was still used in the VAW modelling of scenario 5. The analysis performed with the original volume indicated a slide impact velocity of 1 m/s. This results in low run-up heights, mostly below one meter in distal areas (figure 4.43). When combining this with the fact that only a part of the failure volume is likely to enter the water, the displacement wave hazard from this scenario is negligible. The model shows that the highest waves occur close to the impact zone and on the other side of the fjord with a maximum run-up of 2.9 meters.

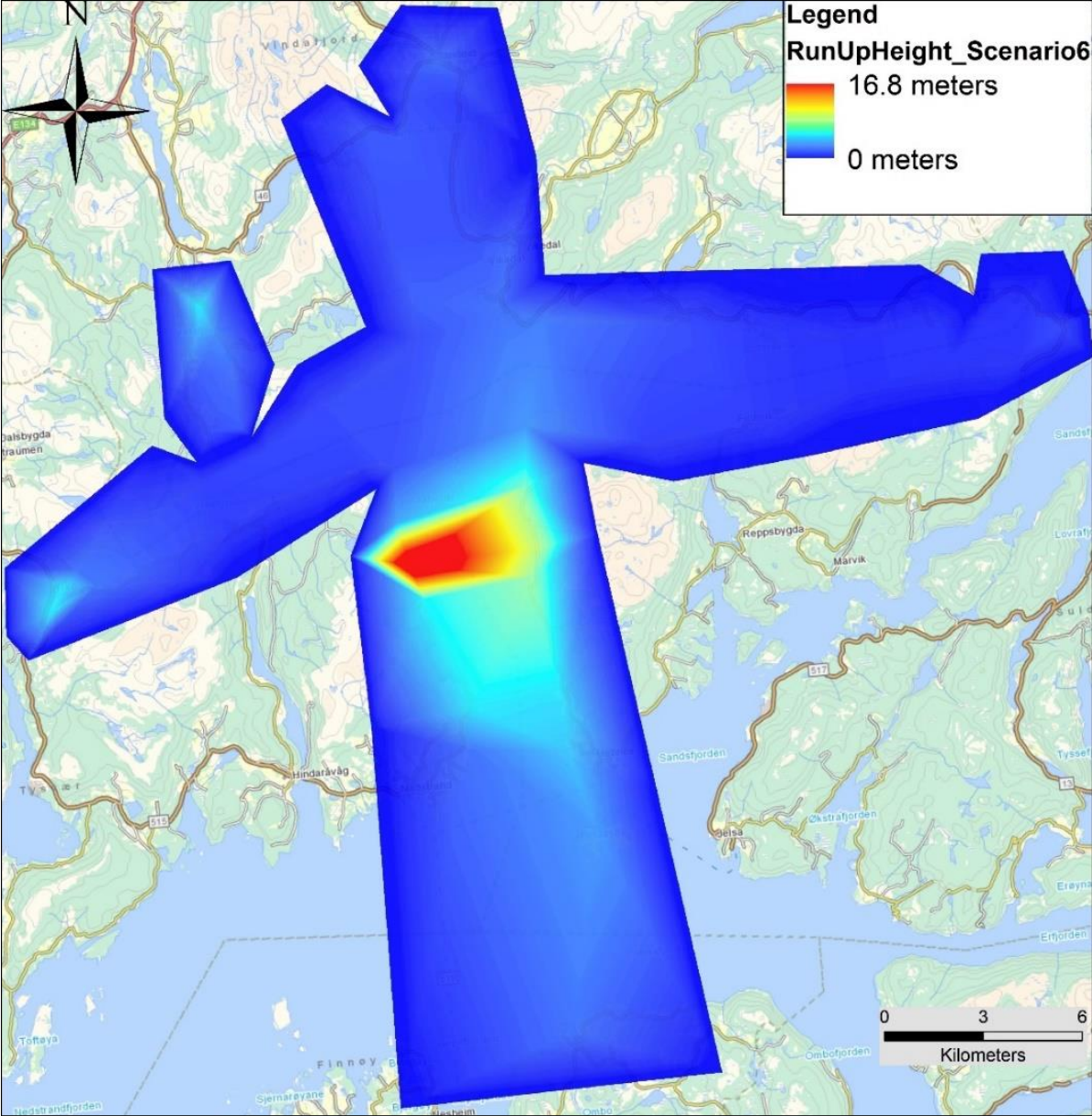


**Figure 4.43:** Results from the VAW analysis showing the run-up heights for scenario 5. Maximum run-up 2.9 meters.

### Displacement wave run-up for Scenario 6

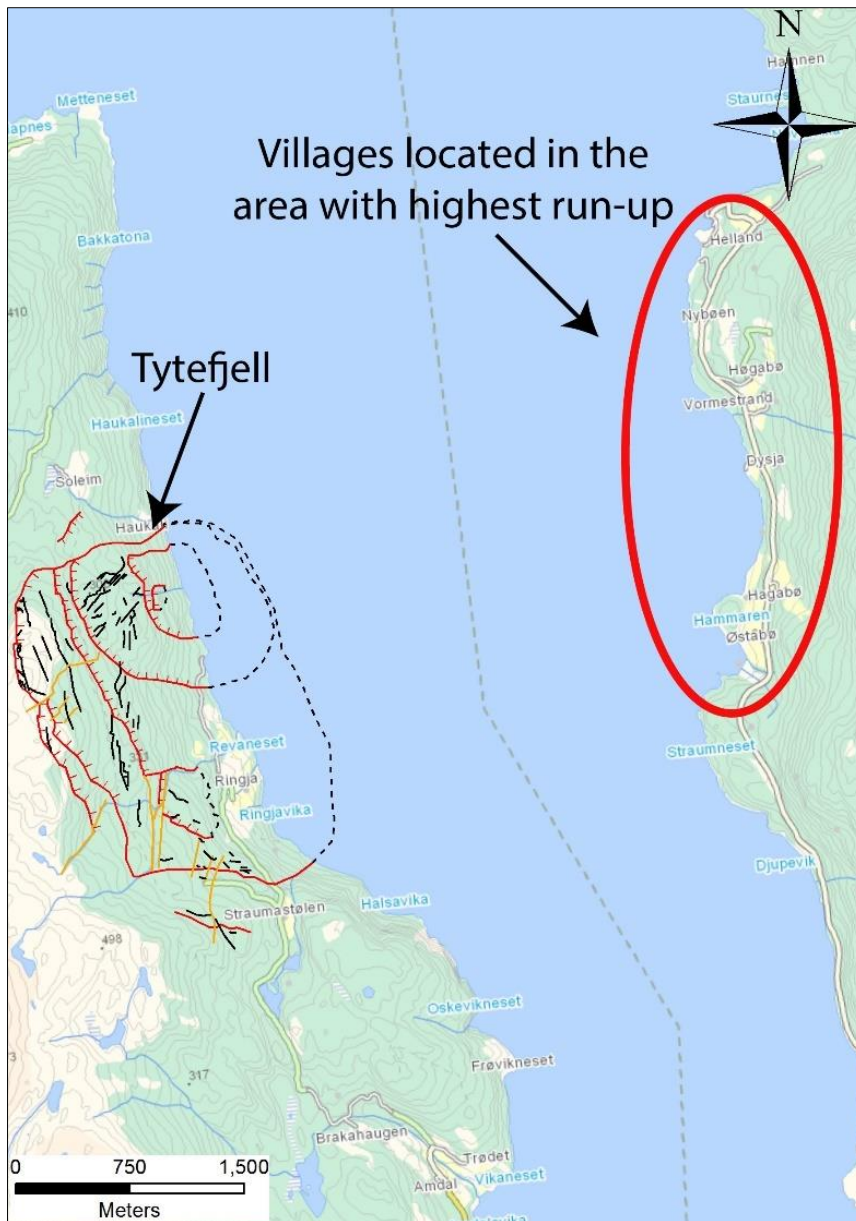
The runout model for scenario 6 showed that it is likely that the entire volume reaches the fjord over a width of approximately 260 meters. The slide impact velocity is estimated to be 19.6 m/s, which is higher than for scenario 5. Looking at figure 4.44, the highest run-up occurs at the opposite side of the fjord from the slide impact (6.7 meters) and at the end of the fjords. This is expected according to theory. A significantly higher run-up height is observed in the western fjord branch compared to the eastern one. The western fjord branch is characterized by a shallow water depth of less than 15-30 meters at the ends. This is also the case for the NNW striking Vatsfjord where the fjord depth decreases to less than three meters before reaching the end. Waves entering this fjord branch will most likely break before reaching the end, reducing

the actual run-up in this area. The buildings closest to the fjord in the small villages on the east side of Vindafjord (Hagabø, Vormestrand and Helland), mostly boathouses, will probably be hit by a displacement wave resulting from a scenario 6 failure (figure 4.45). A more detailed risk analysis has to be performed by NGU in the future.



**Figure 4.44:** Results from the VAW analysis showing the run-up heights for scenario 6. Maximum run-up 16.8 meters.





**Figure 4.45:** Villages located on the eastside of Vindafjord. This is the area with the highest expected run-up.

## 4.9 Results from empirical displacement wave analysis

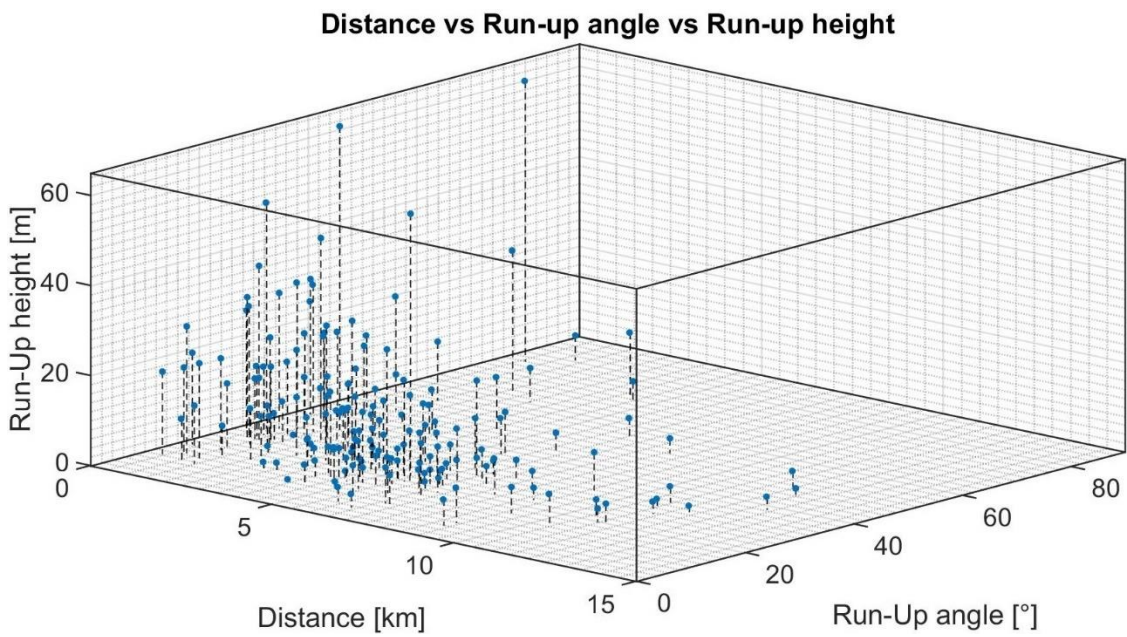
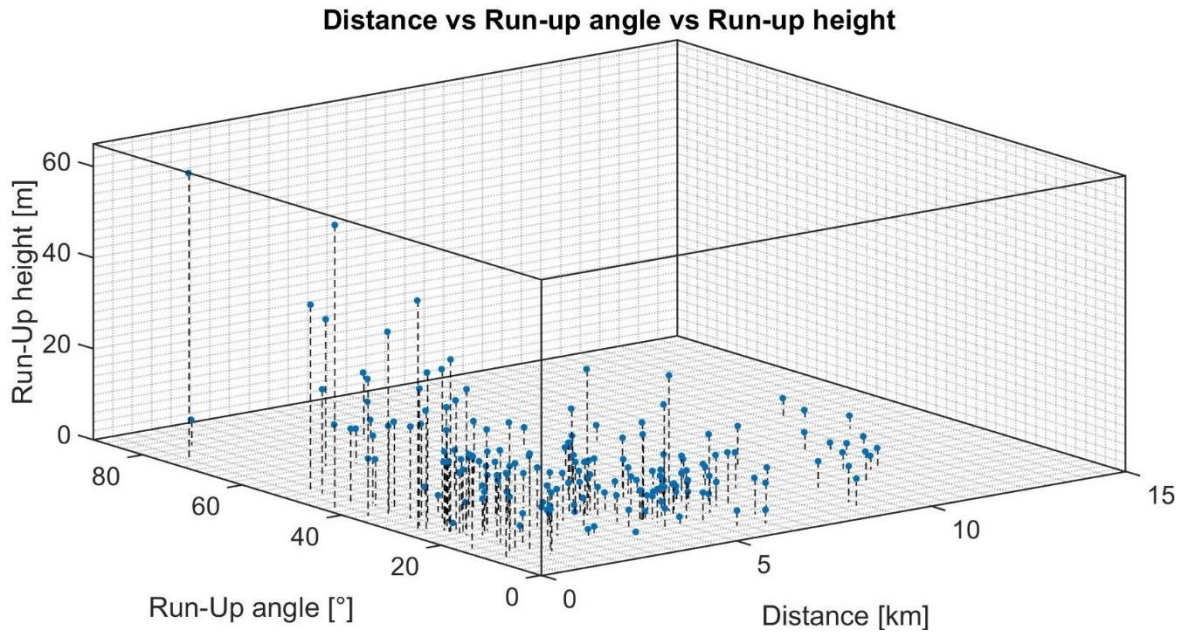
The following work was done as a continuation of the NGU project to develop an empirical relation for run-up height estimation. The analysis focused on events with available bathymetry only.

- Data on run-up slope angle and water depth were gathered for six displacement wave events with recorded run-up heights (table 3.1).
- All 182 data points with run-up angle and water depth was analysed using MATLAB.
- 2D and 3D statistical analysis was performed on the collected data.
- Maps were produced displaying the findings of the analysis.
- The empirical relation developed by Böhme (2013) was applied to the scenarios at Tytefjell and the results was compared to the results from the VAW model.

### 4.9.1 Results from 2D and 3D statistical analysis

Distance, run-up angle and water depth were plotted against run-up height in 2D scatterplots to investigate if these data displayed any trend. Of the events with available bathymetry, Chehalis lake, Isla Mentirosa and Loen 1936 show a distance vs run-up distribution with a reasonable fit. Since more run-up points were added along the Aysén fjord this was also possible to achieve for the combined Isla Mentirosa and Punta Cola datasets, see Appendix G. All data were fitted with a simple power law. The Punta Cola dataset is included in the Appendix to illustrate an event with a poor fit.

Water depth does not seem to have a consistent influence on the run-up height. The same water depth can result in a range of different run-up heights. Small variation in water depth in the investigated basins resulted in a very homogenous depth dataset. Run-up height as a function of run-up slope angle does not show any consistent trend. A steeper run-up angle does not necessary result in higher run-up. Since the influence of the run-up slope angle will vary depending on distance, the dataset was divided into three distance-groups. The data was divided based on visual inspection of a 3D plot displaying run-up, distance and run-up angle: 0-2 km, 2-4 km and 4-7 km. Even then, the results did not show any consistent trend. The 3D plot displaying all collected data shows a weak trend towards higher run-up with steeper run-up slope angle (figure 4.46).



**Figure 4.46:** Two different view angles of all the 182 data points. The plots display distance from impact, run-up slope angle and run-up height.

#### 4.9.2 Maps displaying the gathered data

Four maps covering five of the investigated events were created by plotting the gathered information at the different points with run-up estimates (Appendix H). The Loen 1905 event was omitted due to too few data points. For the maps including the run-up angle and run-up height, the run-up angle is represented as circles. The results are presented separately for each event in the following sections.

##### **Tafjord 1934**

Run-up measurements were plotted along the entire inner part of Storfjord covering the villages that suffered most damage, Fjøra and Tafjord. The map shows that the run-up is more dependent on distance and fjord geometry than of run-up angle. The colour changes from dark red towards green further away from the landslide (Appendix H). Similar run-up slope angles at approximately the same distance, result in different run-up heights. When the wave changes direction due to the kink in the fjord seen in the NW region of the map, the run-up height lowers drastically. The greatest run-up height is observed on the opposite side of the landslide along the fjord, except for the point closest to the impact point.

##### **Loen 1936**

Data points are distributed along the entire lake except for the southern tip, due to lack of available bathymetry data. The run-up heights are decreasing away from the landslide impact before increasing again close to the northern end of the lake (Appendix H). Higher run-up at the end of lakes and fjords have also been described by Harbitz et al. (2014). Close to the impact, several data points with similar run-up height have widely different run-up slope angles. This illustrates the lack of correlation in the data. The Loen lake has similar basin geometry as the inner parts of Storfjord near the village of Tafjord. In the Loen case, higher run-up is registered on the opposite side of the landslide along the entire lake.

##### **Chehalis lake 2007**

Chehalis lake is the event with most data points (Appendix H). They are distributed along the entire lake, except the southernmost tip. The data show that the run-up height has a strong dependence on distance, since the run-up heights get lower towards the southern end of the lake, away from the impact. Directly on the opposite of the impact, it is clear that the run-up angle does not have consistent influence on the run-up height. Several data points with similar run-up angle show different run-up heights in this area. In addition, a map displaying the water

depth and run-up height is included in appendix H. This clearly shows that the water depth is similar along the entire lake, but run-up heights vary significantly.

### Isla Mentirosa & Punta cola 2007

The data from these two events were plotted together in the same map (Appendix H) since it is difficult to differentiate between the effects of the landslide events that contributed to the run-up at different locations. These run-up data also show a good correlation with distance. Highest run-up is seen right in front of each of the landslide events, decreasing with distance. Run-up angle does not seem to influence the run-up height consistently.

#### 4.9.3 Results from applying the existing empirical relation on the scenarios at Tytefjell

The computed run-up heights from the VAW model were compared to the results using the existing empirical relation. All six equations tested by Böhme (2013) were applied to scenario 5 and 6 at Tytefjell to check the applicability compared to the VAW model (table 4.15). All six equations developed by Böhme (2013) were tested by comparing the average difference between VAW run-up heights and the run-up heights computed with the equations.

**Table 4.15:** The six different empirical relations tested by Böhme (2013), with the corresponding differences from the VAW model for scenario 5 and 6.

Equation number	Formula D = distance [Km] V = volume [Mm <sup>3</sup> ]	Constants	Average difference from the VAW model [m]	
			Scenario 5	Scenario 6
1	$Run\ up = a * \left(\frac{V}{D}\right)^b$	a = 11.85 b = 0.4382	7.52	1.45
2		a = 11.91 b = 0.837	5.78	0.98
3		a = 13.17 b = 0.6433	7.22	0.84
4	$Run\ up = \left(\frac{V}{a+b * D^2}\right)$	a = 0.151981 b = 0.013847	3.11	1.45
5	$Run\ up = a * e^{(b*D+c*V^2)} + d$	a = 23.82 b = -0.3421 c = 0.002987 d = 0.8328	2.09	1.43
6	$Run\ up = a * b^V * D^c$	a = 9.546 b = 1.133 c = -1.101	1.25	1.07

### **Scenario 5**

This scenario has negligible run-up heights due to parts of the failure volume most likely being deposited before reaching the water. Since the VAW model was run using the initial volume of  $3.85 \text{ Mm}^3$  this was also used in the equations. As evident from Table 4.15, equation 6 gave the lowest average difference in computed run-up heights when compared to the VAW model. Equation 6 predicts higher run-up heights at 55 out of 60 points when compared to the VAW model. The average difference from the VAW model varies significantly between the six equations (1.25-7.52 meters), all of them predicting in generally higher run-up heights than the VAW model.

### **Scenario 6**

This scenario has a higher average run-up height than scenario 5, due to the entire volume reaching the water. The best fit with the VAW model is achieved using equation 3 with an average difference of 0.84 meters. 40 of the points have lower run-up estimates than the VAW model and 20 have higher, which means that this equation has the possibility to underestimate the hazard of a future displacement wave. The general fit between the VAW model and the different equations is better for scenario 6 than for scenario 5. The highest average difference for scenario 6 is 1.45 meters.

## 5. DISCUSSION

### 5.1 Limits of the unstable area

The interpreted limits of the unstable area are shown in figure 4.39 and figure 4.40. The limits are based on field observations, aerial photographs and the lineaments digitized on the two high resolution hillshades. In addition, overview photographs taken from a helicopter were used to identify the limits discussed here.

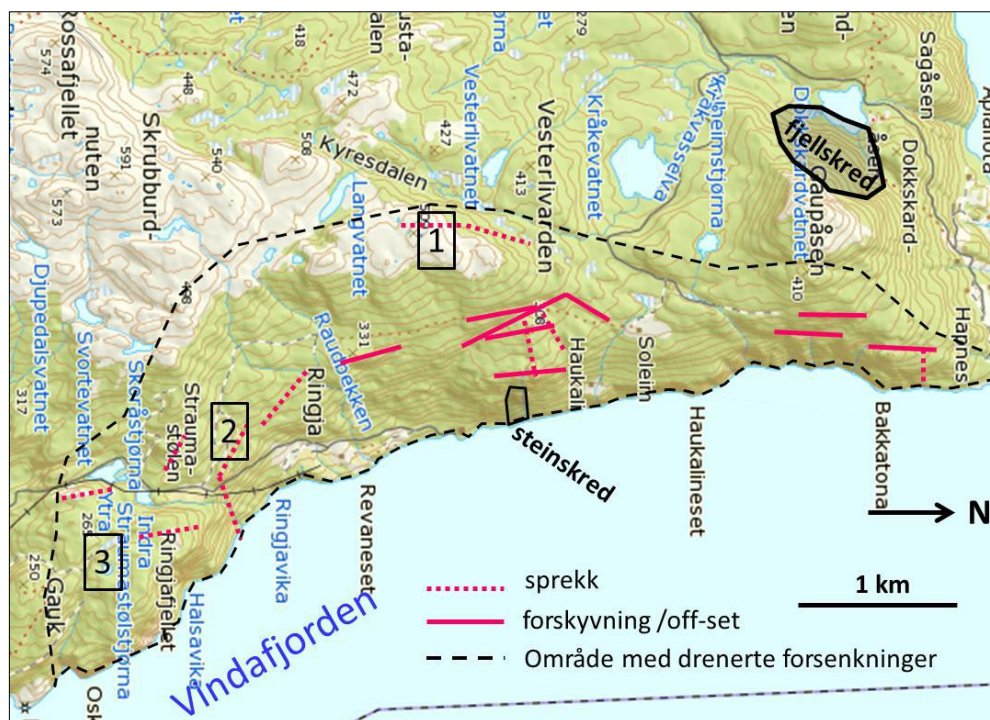
The back scarp is defined as the western limit of the instability. This is set due to the lack of observable deformation west of this scarp. This limit is easily recognisable in the terrain (figure 4.4). The southward continuation of this crack is connected with more uncertainties. The depression continuing southwards from the back scarp at location 8 has been traced in the terrain and is thus interpreted to be a less developed continuation of the back scarp (Figure 4.3). Looking at the slope and aspect maps it becomes clear that the southernmost part of the back scarp in the NW domain follows J4. The back scarp has almost the exact same orientation as the average for J4 in this domain (table 4.2). Further north, where the back scarp turns NNE-SSW the orientation coincides with measurements of J1 in the area.

No observation of a continuous deformation zone south of the defined lateral limit was found in the field. Three major SE-NW striking fracture systems are visible at the southern end of the instability (figure 4.7). The most developed fracture system is crossing location 1 and propagates westward but becomes less developed close to location 21, just west of the southern termination of the back scarp (figure 4.3). Field observations suggests that this fracture system consists of steps between J1 and J2. This is interpreted as the southern lateral limit because it has the most advanced stage of deformation and better connects with the deformation observed further west. It is important to note that the southern lateral limit has some uncertainty since there is observable deformation in the terrain further south (close to location 2). The big fracture system observed south of the interpreted limit is not interpreted to be directly connected to the unstable area because the vertical displacement showed in figure 4.14 indicates movement towards SSW.

The northern lateral limit is set along the observable line of deformation striking NE starting at the northern end of the visible back scarp (figure 4.3 and figure 4.4). North of this limit, no observable deformation that can be related to the unstable area was observed. J3 strikes parallel to this limit and is interpreted to be the active structure along this limit. It is only the areas closest to the fjord that do not have obvious deformation visible on the hillshades. This area

was difficult to map due to steep topography and dense vegetation. The toe line of the instability has large uncertainties since no daylighting sliding plane was observed. This might suggest that the instability continues under water. An area with shallower slope angle 300 meters below sea level was set as the toe line. However, this could be only an artefact of the coarse resolution of bathymetric data. This is therefore the most accurate interpretation possible with the current available data.

It must be pointed out that the western side of Vindafjord has at least three separate rock slope instabilities. Anda (2013) did not separate between these three instabilities but grouped them as one large area where cracks control the drainage system. This clearly shows that this particular area is conditioned for large scale gravitational deformation. The cracks and scarps indicated on the figure below largely agree with the cracks observed in the field. During the work presented in this thesis, no connecting features were identified supporting the interpretation that the entire area indicated in figure 5.1 is one single unstable slope. It is more likely to be several smaller unstable areas, including the Tytefjell site. Anda (2013) also indicated that the instability might continue below sea level.



**Figure 5.1:** Figure showing the western side of Vindafjord (Anda, 2013). The dotted black line indicated the extent of the deformation. Solid red lines indicated scarps with observable offset, and the dotted lines indicated cracks. The shaded area labelled fjellskred in the top right corner indicates an old rockslide.



## 5.2 Structural control on the observed deformation at Tytefjell

### 5.2.1 Comparison between mapped lineaments and discontinuities

In the rose diagram for the NW-domain, one can clearly see that J4 fits well with the most prominent fracture orientation (figure 4.22), which agrees with the assumption that parts of the back scarp follow J4. This is also the domain where J4 is found at most measurement locations. J1, which is the other joint set found in this domain, does not fit as well with the digitized fractures. Blocks topple towards the west into the back scarp along joint set 4 (figure 4.15).

In the NE domain, the situation is different where J1 is dominating the fracture orientations. J2 and J3 are also present, but not to the same extent as J1. When looking at Appendix C, all stereonet within the NE domain contain J1 with approximately the same orientation, which indicate that this joint set is highly developed in this area of the slope. This fits very well with the NE-SW striking open cracks following J1 in this domain (figure 4.12). Three of them are clearly visible on the hillshades. The southern domain, which is the biggest and with the most structural measurements, shows a very good correlation with mapped joint orientations. J1, J2, J4 and J5 dominate the fracture directions. The big canyon close to location 1 follows J1 and J2.

In all three rose diagrams, there exists peaks that do not correspond to a specific joint set. This can be explained by the natural variation of joint sets, since it is the average orientation that is used in this analysis. It is also important to have in mind when looking at data like this that the lineaments are mapped on an inclined slope. This implies that a feature with the same strike will have a varying appearance depending on the slope angle, which in turn causes variation in the rose diagrams. When looking at the results found by Böhme, Hermanns, et al. (2013) using the same technique, they also had peaks in their rose diagram that did not correspond directly to a discontinuity set. To summarize, a reasonably good correlation is found between digitized lineaments and the discontinuity sets mapped in the field. This suggests that most of the visible lineaments and open cracks developed along the main joint sets, or a combination of two of them. Boulders with smooth planar edges were observed close to location 19 (figure 4.3). These are probably released along joints and thus show that the pre-existing discontinuities influence the deformation (figure 5.2). The gravitational slope deformation observed in this area is thus strongly influenced by these pre-existing discontinuities as observed at several other large rock slope instabilities (Agliardi et al., 2001; Ambrosi & Crosta, 2006).



**Figure 5.2:** Picture taken towards north close to location 19 showing large boulder with planar smooth edges. Most likely released along joints.

### 5.2.2 The implication of GSI values on slope stability

Based on the publication by Brideau et al. (2009), the estimated GSI values at Tytefjell correspond to zone E and D in their classification system. Zone D is described as a transition between environments where structural elements controlling the failure and the strength of the rock mass is the dominant factor. Zone E corresponds to disintegrated mass that approaches soil-like behaviour. Descriptions of rocks corresponding to zone E do not fit very well with the observations at Tytefjell. Zone D, where structural control has a large impact on the stability fits better with the observed situation. The lower range of values might plot in zone E due to the fact that the zones are defined based on the old version of the GSI table, not taking into consideration the issues with metamorphic rocks. Zone D accommodates the fact that the slope deformation at Tytefjell is strongly influenced by pre-existing discontinuities.

A weak trend showing lower GSI ranges towards the east was observed when plotting the GSI data. This agrees with the more pronounced deformation observed in these areas. Appendix A also shows a clustering of graphite observations towards the east which have large implications on the GSI due to the lower strength of the graphite. When estimating GSI values in ranges, trends might be harder to identify. Graphitic phyllites will always end up in the lower part of the GSI table, resulting in a small room for systematic variation when the entire slope has the same lithology.

### 5.3 Classification of the unstable area

As mentioned in the theory section (chapter 2.1.3), the existing classification systems are not applicable to the large scale deformation observed at Tytefjell. The large size of the unstable area suggests that several failure mechanisms can have an influence on the stability. It is therefore not beneficial to apply the classification system published by Hungr et al. (2014).

#### 5.3.1 DSGSD features at Tytefjell

Several features observed at Tytefjell are congruent with the features listed in chapter 2.1.4 and provide justification that the deformation at Tytefjell can be classified as a DSGSD:

- Large size (3 km<sup>2</sup>). This might be even bigger if including the area below sea level. The instability stretches from behind the slope crest to the bottom of the slope.
- Situated in foliated metamorphic rocks in a glacially carved fjord.
- A double ridge is observed along the back scarp at 500 m a.s.l.
- The back scarp is situated west of the slope crest.
- Several scarps, counterscarps and trenches are observed within the unstable area.
- Presence of smaller instabilities within the main unstable slope (e.g. scenario 3 and 4).
- Active rockfall area at the front of the NE sector of the slope.
- More pronounced deformation towards the slope toe, with numerous vertical cracks and trenches.
- Several vertical joint sets are mapped on the slope and seem to be important in constraining the localization and the surface expression of this unstable area. This is mentioned to be typical for DSGSDs by Agliardi et al. (2012).

Some additional future observations may strengthen this interpretation. Higher resolution bathymetry may reveal slope bulging under water. The displacement measurements will most likely show a low present day displacement rate which fits well with DSGSD theory.

The kinematic analysis shows that smaller sections of the slope may fail along certain discontinuities as either planar, wedge or toppling failure. However, there is no single penetrative structure that allows the entire unstable slope to activate that structure. It is therefore obvious that extensive internal damage is needed to allow the deformation observed at Tytefjell. It is therefore justified to classify the unstable slope at Tytefjell as a DSGSD.

## 5.4 Simplified stability model

Based on the kinematic analysis and the structural profiles, it is possible to assess a preliminary stability model. As discussed earlier, the pre-existing discontinuities play a major role in the deformation of the rock mass at Tytefjell. No single feature that allows for movement of the entire unstable area was identified. The kinematic analysis indicates that the pre-existing discontinuities allow different failure mechanisms to be kinematically feasible for minor slope sections, which is in agreement with the findings in the structural profiles. These are bi-planar failures along J1 and J4 or planar failures along J4. Most of these instabilities are interpreted to continue under water, which introduces large uncertainties due to low resolution bathymetry.

### 5.4.1 Implications of reduced friction angle due to graphite content

As mentioned in chapter 4.1.1, graphite was observed along the foliation at several locations and is believed to reduce the friction along the foliation planes (Oohashi et al., 2013). Areas with high degree of deformation coincide well with more graphite rich areas (Appendix A). Locations where graphite is observed tend to cluster in the most deformed areas east of the internal scarps. This suggests that the graphite content weakens the rock mass making weathering and deformation processes more effective. A marked strength difference between the graphite rich phyllite and normal phyllite was observed in the field. Looking at the kinematic analysis, lowering the friction angle to  $10^\circ$  makes wedge failure between J1 and the foliation more feasible. This is also the case for the structural profiles, where a friction angle of  $10^\circ$  makes planar failures along the foliation and J4 more feasible.

### 5.4.2 The use of structural profiles to reduce uncertainties of the kinematic model

In all three structural domains, planar sliding is indicated as feasible along J4 when looking at the steepest part of the slope. As seen in the profiles, this will only include minor volumes in the frontal areas when using the minimum dip-value for J4. Bi-planar failures along J1 and the foliation are feasible in profile 1 and 4, both oriented  $55^\circ$ . The steep topography below sea level visible in the profiles, also allows for possible daylighting structures. However, in the profiles, the resolution of the bathymetric data is not high enough to use for detailed analysis. More detailed bathymetric data are required to determine the following:

- 1) whether rock slope deformation extends below sea level
- 2) where daylighting structures occur, and
- 3) the total area of deformation.

## 5.5 Hazard and risk of a future rock slope failure at Tytefjell

Applying the hazard classification system developed by NGU revealed that all the assessed failure scenarios at Tytefjell fall into the moderate hazard class when looking at the mean hazard scores (chapter 4.7). The maximum possible hazard scores lie within the high hazard class. As mentioned earlier, it is believed that future investigations such as displacement measurements and more accurate volume estimations will be able to drastically reduce the uncertainties of the presented hazard analysis and most likely lower the hazard scores for all the four assessed scenarios. A more detailed hazard assessment has to be performed by NGU after the 2016 field campaign when displacement measurements becomes available.

Acquiring high resolution bathymetry will give the opportunity to precisely evaluate the underwater continuation of the instability. This will also lower the uncertainties of the volume calculations and the runout models. The displacement measurements will remove the uncertainties of the movement criteria in the hazard analysis and most likely reduce the hazard scores significantly. The acceleration criteria will not be possible to evaluate until several displacement measurements are performed. Improving the monitoring network will provide more data in the most critical regions to the NE of the unstable slope. It is believed that scenarios 3-5 will end up in the low hazard class when all the necessary information is analysed. Scenario 6 is still estimated to fall in the moderate hazard class after reducing the uncertainties.

The performed VAW analyses gives some indications regarding the risk of a future failure at Tytefjell. These run-up heights should only be seen as rough estimates due to the large uncertainties of the failure volumes and the complex fjord geometry. Nevertheless, the VAW analysis for scenario 5 shows that only a small part of the unstable volume will enter the water due to a relatively flat area directly below the deforming area. This results in a negligible displacement wave, and the risk of a future failure is only concerning the farms situated below the failure scenario. Scenario 6 is more likely to cause a larger displacement wave since the entire volume is predicted to enter the fjord with a relative high velocity (19.6 m/s). The displacement wave will only be a significant hazard directly on the opposite side of the fjord since the other predicted run-up heights are, following our model, below one meter.

The larger scenarios with volumes exceeding 100 million m<sup>3</sup> would cause devastating displacement waves and run-up heights along the entire fjord system, also south of Vindafjord, but these are not seen as realistic without a large deformation related to high velocity prior to

failure. Future dGNSS measurements will provide information that will help to determine which of the scenarios is most realistic in terms of a possible failure.

## **5.6 Applicability of the empirical displacement wave equations**

The analyses done in this thesis regarding the displacement wave parameters tried to lower the uncertainties in the relationship developed by Böhme (2013), by adding more parameters. Oppikofer et al. (in press) stated that adding additional parameters such as the run-up slope angle and water depth might reduce the uncertainties. The findings presented in this thesis lead to the conclusion that it does not improve the model output to include the new parameters (run-up slope angle and water depth) into the existing empirical relation based on the current datasets. This is due to a lack of fit with the existing data. It is possible that the fit could have been improved by adding data from other displacement wave events, however, bathymetric data needs to be collected after the future events to improve the model.

The 3D scatterplot showing the relation reveals a very weak trend towards higher run-up height with steeper run-up slope angles (figure 4.46). This does not correspond with the equations published by Müller (1995) which are applied in the VAW model and predicts higher run-up with lower run-up angle. A visual inspection of the datasets used to create the fitted surface shown in figure 2.3 was done to check if differences in run-up angle or water depth could explain some of the outliers plotting above the fitted curve. The data was sorted based on distance from impact and data points at the same distance were compared. This inspection shows large discrepancies, and the new datasets are not able to consistently explain the points plotting above the fitted curve in figure 2.3.

Calculated run-up heights using the empirical relation corresponds well with the results from the VAW model (table 4.15). When judging the applicability of the empirical relations, the more advanced VAW model that is used by NGU today is set as a benchmark. 60 run-up points were calculated using both methods and the average difference between the two were compared between the six different equations. The equation giving the best fit did not match between scenario 5 and 6. Both equations gave an average difference around 1 meter. Equation six had the lowest average difference for scenario 5 and predicts higher run-up heights than the VAW model for 55 of the 60 points (table 4.15). This is favourable since the hazard is not underestimated. Scenario 5 is probably not the best for testing such a relation, since most of the calculated run-up heights are below one meter. Equation three gave the best fit for scenario 6 and predicts lower run-up compared with the VAW model for 40 of the 60 points but has a

slightly lower average difference. To summarise: The equations giving the lowest average difference from the VAW model did not match for the two scenarios (table 4.15). This indicates that the empirical relation requires more research before being permanently implemented in the hazard and risk classification. The fact that the average difference for all six equation applied to scenario 6 is below 1.45 meters is promising. However, it is not recommended to replace the current VAW model with an empirical relation. This requires more extensive testing to lower the uncertainties, which is further discussed in chapter 7.1.

Heller et al. (2009) concludes that empirical methods are not yet fully developed. This might be because empirical relations are not able to include site specific parameters and are unable to predict the run-up at certain locations. Several other parameters concerning waves and wave propagation could have been included in this relationship e.g. frontal geometry of the sliding mass, shoreline orientation and detailed basin geometry. A common feature with these parameters is that they are difficult to quantify, and are therefore not suitable in such empirical equations. Vindafjord is such an example, highlighting that complex fjord geometry makes the use of empirical relations difficult and numerical solutions might be better suited for such locations.

#### 5.6.1 Uncertainties and adjustments done to the used datasets

Some adjustments were done to the volumes and the distance from impact for the different landslide events. For Loen, Tafjord and Chehalis lake, closely spaced locations were grouped together to ease the process of estimating run-up angles. The change of run-up angle will anyway be negligible over such short distances.

The bathymetric data for the Loen lake does not cover the southernmost two kilometres of the lake. Therefore, information about water depth and run-up slope angle for at least 20 run-up points in this region of the lake could not be extracted. The bathymetric data from the Aysén fjord was not investigated by the author, but several topographic profiles were retrieved covering the points of interest. Data from the Aysén fjord is special, since it is not possible to quantify how the two landslides contributed individually to the run-up (Punta Cola or Isla Mentirosa). This generates uncertainties regarding the distances to each run-up point. Wave interference is likely to have influenced the run-up heights at several of the locations. The bathymetric data for Chehalis lake does not cover the southernmost 500 meters of the lake resulting in no data from this region.





## 6. CONCLUSIONS

A structural analysis and a hazard assessment have been performed for the unstable area Tytefjell in Vindafjord, Norway. The main findings can be summarized as follows:

- Limits of the unstable area have been defined by use of geomorphological mapping and by studying DEMs. The western limit is defined with a high degree of certainty due to the evident back scarp. The toe line of the instability is hard to define as no daylighting sliding structure was observed on the slope, which suggests that the instability continues under water. Low resolution bathymetry introduces high uncertainties regarding the toe line. The northern lateral limit is defined based on the lack of observable deformation further north. The southern limit is set along a major NE-SW striking fracture system which shows the most advanced stage of deformation. Thus, the total area of the unstable slope on land is estimated to be 3km<sup>2</sup>.
- The structural analysis led to the characterization of five joint sets based on 2100 orientation measurements: (dipdir/dip): J1(119/87), J2(213/87), J3(354/89), J4(067/43) and J5(274/87). The mean orientation of foliation was measured to be 000/22. Variation in these mapped structures across the slope resulted in three separate structural subdomains. A kinematic analysis was performed and revealed feasibility for failure in the three structural subdomains. The analysis shows a worsening of the stability situation if the friction angle is lowered. Doing so is in accordance with the graphite content. However, no single feature that allows for complete failure of the entire slope was found. Structural profiles show that the feasible failure modes found in the kinematic analysis only apply to smaller sections of the slope. All analyses indicate that the gravitational slope deformation is strongly influenced by inherited structures. Based on a good correlation between digitized open fractures and the joint sets it is concluded that fractures mostly form along the joint sets or a combination of two of them.
- Considering that no single structure was observed that allows for complete failure, it is inferred that extensive internal damage is needed to produce the deformation seen at Tytefjell today. Due to the large size and other characteristic features such as scarps, counterscarps, double ridges, several sub-vertical joints, smaller unstable areas present within the slope in addition to the fact that the back scarp is located behind the hill crest, Tytefjell is classified as a DSGSD.

The hazard assessment was performed according to the guidelines given by NGU for six failure scenarios at Tytefjell ranging from (6) blocks in the frontal area, to (1) the entire slope. A collapse of the larger scenarios involving several million m<sup>3</sup> is considered of very low likelihood, since no penetrative structures stretching across the entire slope that could allow these bigger scenarios to fail in one event were found during fieldwork.

- The hazard assessment revealed that the remaining four scenarios plot in the moderate hazard class. It is believed that by lowering the uncertainties connected to the hazard assessment by incorporating displacement measurements and more accurate volume estimates, scenarios 3-5 will drop into the low hazard class. The smallest scenario will most likely remain in the moderate hazard class.
- In order to reduce the uncertainties of the hazard classification within this thesis a monitoring system was suggested containing locations for additional dGNSS points. It is recommended to use a total station to monitor the deformation in the NE sector of the slope.
- The runout (FlowR) and the displacement wave (VAW) analysis showed that only a minor part of a scenario 5 failure will reach the water and thus result in negligible run-up heights of a displacement wave. One farm is situated within the runout area of this scenario. The entire volume of scenario 6 has a high probability reaching the water and of causing a displacement wave. Estimated run-up on the eastern side of the fjord is approximately 6-7 meters.
- NGU developed an empirical relation between displacement wave run-up, landslide volume and distance from impact. As a continuation of this project, data on run-up slope angle and water depth were gathered for six displacement wave events with recorded run-up heights. No significant correlation between these new parameters and the run-up height was found. It is therefore not beneficial to include the new parameters into the existing empirical relation with the current dataset. Results from applying the existing empirical relation to the scenarios at Tytefjell correspond well with the results from the VAW model. However, more research aiming to include more parameters into the relation is needed to replace the VAW model with an empirical relation.

## **7. RECOMMENDATIONS**

This chapter presents recommendations regarding further investigations to reduce uncertainties for the analyses performed in this thesis, especially the volume estimations and the hazard assessment. An adequate monitoring system that covers the most active areas of the slope is needed to reduce these uncertainties.

### **7.1 Recommended further investigations**

The most important uncertainty to be investigated further is the position of the toe line. For this, high resolution bathymetry data is required. In addition, this data will make it possible to determine if any earlier failures from the area have occurred.

The dGNSS displacement measurements need to be interpreted when they are collected during August 2016. This data will make it possible to decide on the recommended follow up and measurement intervals. A program for dGNSS measurements should be implemented depending on the rate of movement. More than one year of measurements are needed to investigate and precisely determine movement trends and direction. Acceleration is not possible to evaluate based on one single measurement. Other monitoring systems should also be applied in parts of the slope that is not covered by any displacement measurements today, see chapter 7.2.

Further investigations of the possible link between graphite bearing lithologies and the rock slope instability at Tytefjell are recommended to get a better understanding of the observed deformation. To get a better overview over the graphite content, it is possible to use geophysical resistivity measurements. Graphite is characterized by a low range of resistivity values. Such surveys have been conducted by for example Marescot, Monnet, and Chapellier (2008). A combination of several geophysical resistivity techniques needs to be combined to separate the graphite from other low-resistivity features.

The work on the empirical relation should continue by acquiring bathymetric data covering additional displacement wave events. This will give a larger dataset and the possibility to obtain a better fit for more parameters to be tested. This will strengthen the empirical relation by taking more run-up features into account without including parameters that are difficult to quantify.

## 7.2 Recommended monitoring techniques

The current monitoring network of dGNSS points is shown in figure 7.2. This monitoring network will not be able to catch the deformation in the most active regions in the NE, since all the three rovers are placed in the upper regions of the slope. It is therefore recommended to place rovers also in the NE area of the slope. Due to dense forest, this might not be the most efficient monitoring method to catch the deformation in these areas, since the dGNSS antennas needs an unimpeded view of the satellites. Installation might involve removal of small patches of forest. Installation of wire extensometers might be an alternative to monitor the deformation at the most prominent cracks in the NE sector.

The monitoring technique that is considered most suitable to monitor the NE parts of the slope is a total station, even if this instrument is not able to measure rotation. This instrument has the opportunity to monitor several cracks at the time with accuracy around  $\pm 0.6$  mm at 60 meters (Eberhardt & Stead, 2011). The vegetation in the area is not dense enough to cause major problems for the visibility to the prisms (figure 7.1), meaning that several prisms can be measured from the same point without having to remove large amounts of forest. The recommended positions for additional monitoring points are indicated in figure 7.2 and explained in table 7.1.

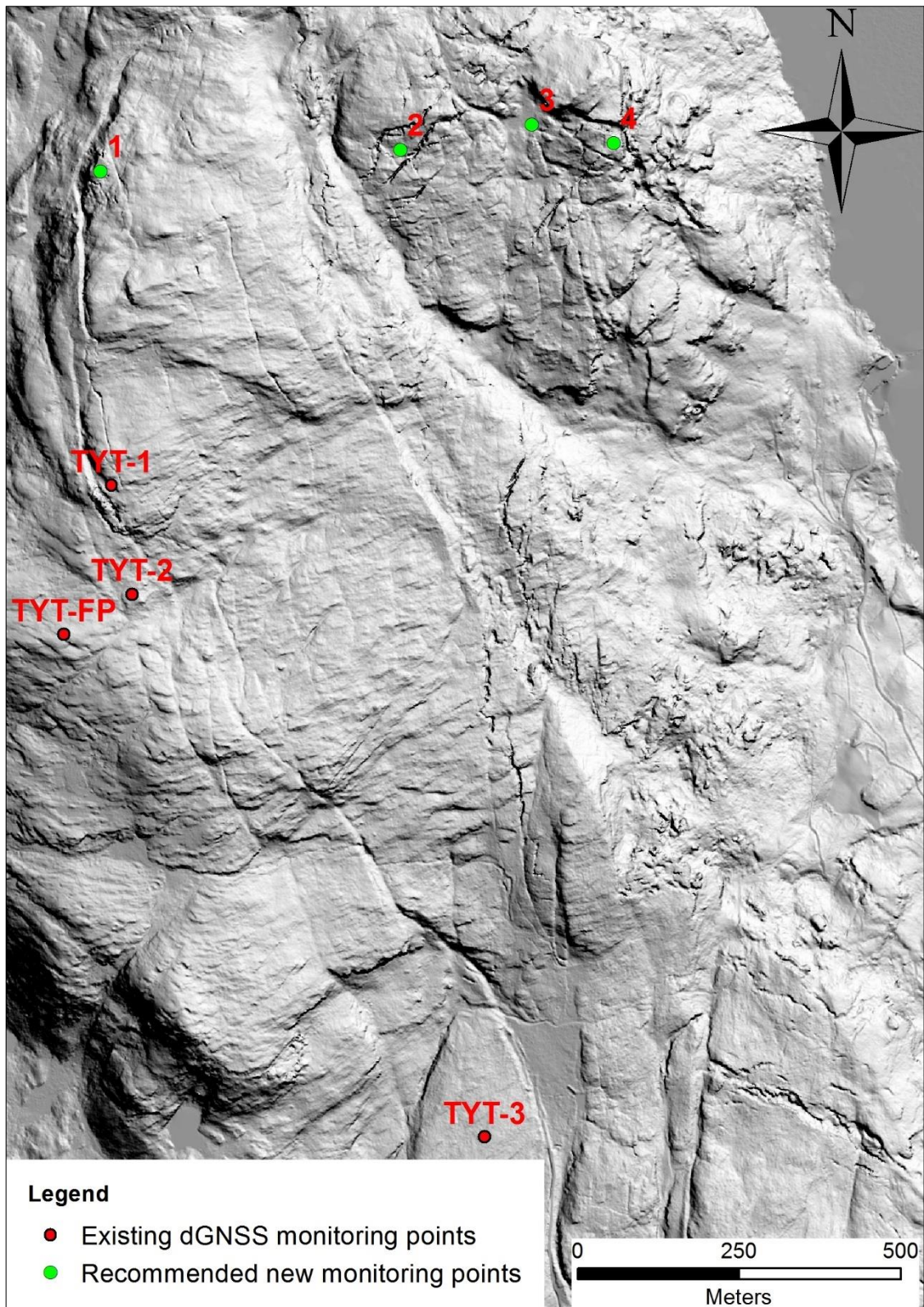
**Table 7.1:** Comments on the recommended new monitoring points shown in figure 7.2.

Point number	Recommended technique	Comments
1	dGNSS	This point is suitable for installation of an additional dGNSS bolt since its completely free of vegetation and situated along the most developed part of the back scarp.
2	Total station	These two points are selected as possible positions for a total station based on the current knowledge about the unstable site. Point two is suitable since it is possible to monitor the two major cracks on each side of the location in addition to the major scarp that delimits the NE domain. Point three is located in an open pine-forest and thus provides good visibility towards major cracks and a large rock outcrop located just north of the point.
3	Total station	
4	dGNSS or total station	Point four is situated on the edge where the slope gets steeper and will provide information about the most active area of the slope. It is possible to install a dGNSS bolt at this location, however, some forest has to be removed to get an unimpeded view of the satellites.

The most active parts of the slope have no suitable landing area for a helicopter, resulting in more workhours if the monitoring system involves several measuring points in the NE domain. The points closer to the back scarp will require less time for investigation, since suitable landings spots are available. It is important to have information on the displacement pattern before designing a monitoring network (Blikra & Kristensen, 2013). Better knowledge and a substantial reduction of the uncertainties for some of the scenarios are needed before any decision of implementing permanent monitoring can be made.



**Figure 7.1:** Photo illustrating the average amount of vegetation in the NE domain.



**Figure 7.2:** Location of the existing dGNSS monitoring network. Three rover points are installed in addition to one fixed point marked TYT-FP. In addition, 4 additional monitoring points are suggested to capture the deformation in the most deformed area and along the head-scarp. See text for details.

## 8. REFERENCES

- Agliardi, F., Crosta, G. B., & Frattini, P. (2012). Slow rock-slope deformation. In J. Clague & D. Stead (Eds.), *Landslides: Types, Mechanisms and Modeling* (pp. 207-221). Cambridge: Cambridge University Press.
- Agliardi, F., Crosta, G. B., & Zanchi, A. (2001). Structural constraints on deep-seated slope deformation kinematics. *Engineering Geology*, 59, 83-102. doi:10.1016/S0013-7952(00)00066-1
- Ambrosi, C., & Crosta, G. B. (2006). Large sackung along major tectonic features in the Central Italian Alps. *Engineering Geology*, 83(1), 183-200. doi:10.1016/j.enggeo.2005.06.031
- Anda, E. (2013). *Potensielle ustabile fjellpartier i Rogaland*. Unpublished report. NGU.
- Anundsen, K. (1990). Evidence of ice movement over southwest Norway indicating an ice dome over the coastal district of west Norway. *Quaternary Science Reviews*, 9(1), 99-116. doi:10.1016/0277-3791(90)90007-W
- Birkeland, T. (1975). Western Karmøy, an integral part of the Precambrian basement of south Norway. *Norsk Geologisk Tidsskrift*, 55, 213-241.
- Blikra, L. H., Arnold, N., Anda, E., Dehls, J. F., & Stalsberg, K. (2006). Rock slope failures in Norwegian fjord areas: examples, spatial distribution and temporal pattern. In S. G. Evans, G. S. Mungnozza, A. Strom, & R. Hermanns (Eds.), *Landslides from Massive Rock Slope Failure* (pp. 475-496). Netherlands: Springer
- Blikra, L. H., & Kristensen, L. (2013). Monitoring Concepts and Requirements for Large Rockslides in Norway. In C. Margottini, P. Canuti, & K. Sassa (Eds.), *Landslide Science and Practice* (pp. 193-200). Berlin: Springer.
- Blikra, L. H., Longva, O., Harbitz, C. B., & Løvholt, F. (2005). Quantification of rockavalanche and tsunami hazard in Storfjorden, western Norway. In K. Senneset, K. Flaate, & J. O. Larsen (Eds.), *Landslides and Avalanches ICFL 2005 Norway*. London: Taylor & Francis Group.
- Booth, A. M., Dehls, J., Eiken, T., Fischer, L., Hermanns, R. L., & Oppikofer, T. (2014). Integrating diverse geologic and geodetic observations to determine failure mechanisms and deformation rates across a large bedrock landslide complex: the Osmundneset landslide, Sogn og Fjordane, Norway. *Landslides*, 12(4), 745-756. doi:10.1007/s10346-014-0504-y
- Böhme, M. (2013). *Test to develop an empirical relation in between run up height of a tsunami with respect to distance from impact and impact volume*. Internal report. Geological Survey of Norway. Trondheim, Norway.
- Böhme, M., Dehls, J., Hermanns, R. L., Oppikofer, T., Redfield, T., Rønning, J.S.,... Kristensen, L. (2013). *The unstable phyllitic rocks in Stampa – Flåm, western Norway: Compilation, scenarios, risk and recommendations. (Report nr 35/2013)*. Retrieved from Norwegian Water Resources and Energy Directorate: [http://webby.nve.no/publikasjoner/rapport/2013/rapport2013\\_35.pdf](http://webby.nve.no/publikasjoner/rapport/2013/rapport2013_35.pdf)

- Böhme, M., Hermanns, R. L., Oppikofer, T., Fischer, L., Bunkholt, H., Eiken, T.,... Nilsen, B. (2013). Analyzing complex rock slope deformation at Stampa, western Norway, by integrating geomorphology, kinematics and numerical modeling. *Engineering Geology*, 154, 116-130. doi:10.1016/j.enggeo.2012.11.016
- Böhme, M., Molina, F. Y., Dehls, J., & Hermanns, R. L. (2015). *Fare- og risikoklassifisering av det ustabile fjellpartiet Storhaugen blokk i Manndalen, Troms* (Report nr 2015.050). Retrieved from NGU, Trondheim: [http://www.ngu.no/upload/Publikasjoner/Rapporter/2015/2015\\_050.pdf](http://www.ngu.no/upload/Publikasjoner/Rapporter/2015/2015_050.pdf)
- Böhme, M., Oppikofer, T., Longva, O., Jaboyedoff, M., Hermanns, R. L., & Derron, M. H. (2015). Analyses of past and present rock slope instabilities in a fjord valley: Implications for hazard estimations. *Geomorphology*, 248, 464-474. doi:10.1016/j.geomorph.2015.06.045
- Böhme, M., Saintot, A., Henderson, I., Henriksen, H., & Hermanns, R. L. (2011). Rock slope instabilities in Sogn and Fjordane County, Norway: a detailed structural and geomorphological analysis. *Geological Society, London, Special Publications*, 351(1), 97-111. doi:10.1144/SP351.5
- Braathen, A., Blikra, L. H., Berg, S. S., & Karlsen, F. (2004). Rock-slope failures of Norway, type, geometry deformation mechanisms and stability. *Norsk Geologisk Tidsskrift*, 84(1), 67-88. Retrieved from: <http://www.alvarbraathen.com/wp-content/uploads/2013/2012/Braathen-et-al-2004-Rockslope-failures-of-Norway.pdf>.
- Brideau, M.-A., Yan, M., & Stead, D. (2009). The role of tectonic damage and brittle rock fracture in the development of large rock slope failures. *Geomorphology*, 103(1), 30-49. doi:10.1016/j.geomorph.2008.04.010
- Davies, T., & McSaveney, M. (2012). Mobility of long-runout rock avalanches. In J. Clague & D. Stead (Eds.), *Landslides. Types, Mechanisms and Modeling* (pp. 50-58). Cambridge: Cambridge University Press.
- Eberhardt, E., & Stead, D. (2011). Geotechnical instrumentation. In P. Darling (Ed.), *SME Mining Engineering Handbook* (3 ed., pp. 551-571). Englewood, CO: Society for Mining, Metallurgy & Exploration.
- ESRI. (2014). ArcMap 10.2 [Computer software]. Retrieved from <http://resources.arcgis.com/en/help/main/10.2/>
- Fell, R., Stapledon, D., & MacGregor, P. (2012). Landslides and geologic environments. In J. Clague & D. Stead (Eds.), *Landslides. Types, Mechanisms and Modeling* (pp. 134-143). Cambridge: Cambridge University Press.
- Fritz, H. M., Mohammed, F., & Yoo, J. (2009). Lituya Bay Landslide Impact Generated Mega-Tsunami 50th Anniversary. *Pure and Applied Geophysics*, 166(1), 153-175. doi:10.1007/s00024-008-0435-4
- Furseth, A. (1985). *Dommedagsfjellet - Tafford 1934*. Oslo: Gyldendal Norsk Forlag.
- Grimstad, E., & Nesdal, S. (1990). The Loen rockslides - a historical review. *Publikasjon-Norges Geotekniske Institutt*, 182, 1-6.
- Groshong, R. H. (1999). *3-D structural geology - A practical guide to Quantitative Surface and Subsurface Map Interpretations* (2nd ed.). Berlin: Springer.



- Harbitz, C. B., Glimsdal, S., Løvholt, F., Kvelde, V., Pedersen, G. K., & Jensen, A. (2014). Rockslide tsunamis in complex fjords: From an unstable rock slope at Åkerneset to tsunami risk in western Norway. *Coastal Engineering*, 88, 101-122. doi:10.1016/j.coastaleng.2014.02.003
- Harbitz, C. B., Pedersen, G., & Gjevik, B. (1993). Numerical simulations of large water waves due to landslides. *Journal of Hydraulic Engineering*, 119(12), 1325-1342.
- Heim, A. (1932). *Bergsturz und menschenleben*. Zurich, Switzerland: Fretz & Wasmuth.
- Heller, V., Hager, W. H., & Minor, H. E. (2009). *Landslide generated impulse waves in reservoirs: Basics and computation. Mitteilungen 211*. Retrieved from ETH Zürich: [http://people.ee.ethz.ch/~vawweb/vaw\\_mitteilungen/211/211\\_g.pdf](http://people.ee.ethz.ch/~vawweb/vaw_mitteilungen/211/211_g.pdf)
- Hermanns, R. L., Hansen, L., Sletten, K., Böhme, M., Bunkholt, H., Dehls, J.,... Høgaas, F. (2012). Systematic geological mapping for landslide understanding in the Norwegian context. In E. Eberhardt, C. Froese, K. Turner, & S. Leroueil (Eds.), *Landslide and engineered slopes: protecting society through improved understanding*. (pp. 265-271). London: Taylor & Francis Group.
- Hermanns, R. L., L'Heureux, J. S., & Blikra, L. H. (2013). Landslide triggered tsunami, displacement wave. In P. Bobrowsky (Ed.), *Encyclopedia of Natural Hazards* (pp. 611-615). Netherlands: Springer
- Hermanns, R. L., & Longva, O. (2012). Rapid rock-slope failures. In J. Clague & D. Stead (Eds.), *Landslides: types, mechanisms and modeling*. (pp. 59-70). Cambridge: Cambridge University Press.
- Hermanns, R. L., Oppikofer, T., Anda, E., Blikra, L. H., Böhme, M., Bunkholt, H.,... Fischer, L. (2012). *Recommended hazard and risk classification system for large unstable rock slopes in Norway*. Retrieved from [http://www.ngu.no/upload/Publikasjoner/Rapporter/2012/2012\\_029.pdf](http://www.ngu.no/upload/Publikasjoner/Rapporter/2012/2012_029.pdf)
- Hermanns, R. L., Oppikofer, T., Anda, E., Blikra, L. H., Böhme, M., Bunkholt, H.,... Molina, F. Y. (2013). Hazard and Risk Classification for Large Unstable Rock Slopes in Norway. *Italian journal of engineering geology and environment, Book Series 6*, 245-254. doi:10.4408/IJEGE.2013-06.B-22
- Hermanns, R. L., Oppikofer, T., Molina, F. Y., Dehls, J., & Böhme, M. (2014). Approach for Systematic Rockslide Mapping of Unstable Rock Slopes in Norway. In K. Sassa, P. Canuti, & Y. Yin (Eds.), *Landslide Science for a Safer Geoenvironment* (pp. 129-134). Switzerland: Springer International Publishing.
- Hermanns, R. L., Sepúlveda, S. A., Lastras, G., Amblas, D., Canals, M., Azpiroz, M., ... Frigola, J. (2014). Earthquake-Triggered Subaerial Landslides that Caused Large Scale Fjord Sediment Deformation: Combined Subaerial and Submarine Studies of the 2007 Aysén Fjord Event, Chile. In G. Lollino, A. Manconi, J. Locat, Y. Hang, & M. C. Artigas (Eds.), *Engineering Geology for Society and Territory. Marine and Coastal Processes* (Vol. 4, pp. 67-70). Switzerland: Springer.
- Highland, L. M., & Bobrowsky, P. T. (2008). *The landslide handbook - A guide to understanding landslides*. Reston, Virginia, USA: U.S Geological Survey Circular 1325
- Hoek, E. (1994). Strength of rock and rock masses. *ISRM News Journal*, 2(2), 4-16.

- Hoek, E., & Brown, E. T. (1980). *Underground excavations in rock*. London: Institute of Mining and Metallurgy.
- Hoek, E., Kaiser, P. K., & Bawden, W. F. (1995). *Support of underground excavations in hard rock*. Rotterdam: CRC Press.
- Horton, P., Jaboyedoff, M., Rudaz, B., & Zimmermann, M. (2013). Flow-R, a model for susceptibility mapping of debris flows and other gravitational hazards at a regional scale. *Natural Hazards and Earth System Science*, 13(4), 869-885. doi:10.5194/nhess-13-869-2013
- Huang, B., Yin, Y., Liu, G., Wang, S., Chen, X., & Huo, Z. (2012). Analysis of waves generated by Gongjiafang landslide in Wu Gorge, three Gorges reservoir, on November 23, 2008. *Landslides*, 9(3), 395-405. doi:10.1007/s10346-012-0331-y
- Hungr, O. (2006). Rock avalanche occurrence, process and modeling. In S. Evans, G. Mugnozza, A. Strom, & R. Hermanns (Eds.), *Landslides from Massive Rock Slope Failure* (Vol. 49, pp. 243-266). Netherlands: Springer.
- Hungr, O., Leroueil, S., & Picarelli, L. (2014). The Varnes classification of landslide types, an update. *Landslides*, 11(2), 167-194. doi:10.1007/s10346-013-0436-y
- Hutchinson, J. N. (1988, 10–15 July). *General report: morphological and geotechnical parameters of landslides in relation to geology and hydrogeology: Proc 5th International Symposium on Landslides, Lausanne*. Paper presented at the International Journal of Rock Mechanics and Mining Sciences & Geomechanics Abstracts.
- Jaboyedoff, M., Baillifard, F., Couture, R., Locat, J., & Locat, P. (2004). Toward preliminary hazard assessment using DEM topographic analysis and simple mechanical modeling by means of sloping local base level. In W. A. Lacerda, M. Ehrlich, S. A. B. Fontoura, & A. S. F. Sayao (Eds.), *Landslides: Evaluation and Stabilization* (Vol. 2, pp. 199-205). London: Taylor & Francis Group.
- Jaboyedoff, M., & Labiouse, V. (2011). Technical Note: Preliminary estimation of rockfall runout zones. *Natural Hazards and Earth System Science*, 11(3), 819-828. doi:10.5194/nhess-11-819-2011
- Jaboyedoff, M., Oppikofer, T., Abellan, A., Derron, M.-H., Loye, A., Metzger, R., & Pedrazzini, A. (2012). Use of LIDAR in landslide investigations: a review. *Natural Hazards*, 61(1), 5-28. doi:10.1007/s11069-010-9634-2
- Jaboyedoff, M., Penna, I., Pedrazzini, S., Baroň, I., & Crosta, G. B. (2013). An introductory review on gravitational-deformation induced structures, fabrics and modeling. *Tectonophysics*, 605, 1-12. doi:10.1016/j.tecto.2013.06.027
- Johnsen, J. E. (2015). *Norwegian Meteorological Institute: Precipitation data for the weather station Nedre Vats*. Retrieved from: <http://eklima.met.no/eklimapub/servlet/ReportInfo?action=stationinfo&s=46910&la=no&co=NO>
- Kartverket. (2015). Norge i bilder. Retrieved from <http://norgebilder.no/?zoom=3&lat=7210000&lon=795000&srs=EPSG:32632>
- Korup, O. (2012). Landslides in the Earth system. In J. J. Clague & D. Stead (Eds.), *Landslides: Types, Mechanisms and Modeling* (pp. 10-24). New York: Cambridge University Press.

- Marescot, L., Monnet, R., & Chapellier, D. (2008). Resistivity and induced polarization surveys for slope instability studies in the Swiss Alps. *Engineering Geology*, 98(1–2), 18-28. doi:10.1016/j.enggeo.2008.01.010
- Marinos, P., & Hoek, E. (2000). *GSI: a geologically friendly tool for rock mass strength estimation*. Paper presented at the ISRM International Symposium.
- Marinos, V., Marinos, P., & Hoek, E. (2005). The geological strength index: applications and limitations. *Bulletin of Engineering Geology and the Environment*, 64(1), 55-65. doi:10.1007/s10064-004-0270-5
- Marker, M., Solli, A., & Slagstad, T. [Cartographer]. (2013). Bergrunnsgeologisk kart Vindafjord 1213-1, M 1:50000
- Mazzanti, P., & Bozzano, F. (2011). Revisiting the February 6th 1783 Scilla (Calabria, Italy) landslide and tsunami by numerical simulation. *Marine Geophysical Research*, 32(1), 273-286. doi:10.1007/s11001-011-9117-1
- McDougall, S., McKinnon, M., & Hungr, O. (2012). Developments in landslide runout prediction. In J. Clague & D. Stead (Eds.), *Landslides: Types, Mechanisms and Modeling* (pp. 187-195). Cambridge: Cambridge University Press.
- Miyagi, T., Yamashina, S., Esaka, F., & Abe, S. (2010). Massive landslide triggered by 2008 Iwate-Miyagi inland earthquake in the Aratozawa Dam area, Tohoku, Japan. *Landslides*, 8(1), 99-108. doi:10.1007/s10346-010-0226-8
- Müller, D. R. (1995). *Auflaufen and Überschwappen von Impulswellen an Talsperren*. (PhD thesis), ETH, Versuchsanstalt für Wasserbau, Hydrologie und Glaziologie (VAW), Zürich. (Mitteilungen 137)
- Nilsen, B., & Brock, E. (2011). *Ingeniørgeologi-Berg Grunnkurskompendium*. NTNU, Trondheim: Institutt for geologi og bergteknikk.
- NVE. (2015). *The National Catchment Database: REGINE*. Retrieved from: <http://www.nve.no/en/Water/NVEs-geographic-databases/The-National-Catchment-Database-REGINE/>
- Olesen, O., Dehls, J., Bungum, H., Riis, F., Hicks, E., Lindholm, C.,... Longva, O. (2000). *Neotectonics in Norway, final report*. Retrieved from NGU (Report nr 2000.002): [http://www.ngu.no/upload/Publikasjoner/Rapporter/2000/2000\\_002.pdf](http://www.ngu.no/upload/Publikasjoner/Rapporter/2000/2000_002.pdf)
- Oohashi, K., Hirose, T., & Shimamoto, T. (2011). Shear-induced graphitization of carbonaceous materials during seismic fault motion: Experiments and possible implications for fault mechanics. *Journal of Structural Geology*, 33(6), 1122-1134. doi:10.1016/j.jsg.2011.01.007
- Oohashi, K., Hirose, T., & Shimamoto, T. (2013). Graphite as a lubricating agent in fault zones: An insight from low- to high-velocity friction experiments on a mixed graphite-quartz gouge. *Journal of Geophysical Research: Solid Earth*, 118(5), 2067-2084. doi:10.1002/jgrb.50175
- Oppikofer, T. (2009). *Detection, analysis and monitoring of slope movements by high-resolution digital elevation models*. (PhD thesis), University of Lausanne, Lausanne, Switzerland.
- Oppikofer, T. (2015, 13.10.2015). [Personal Communication].

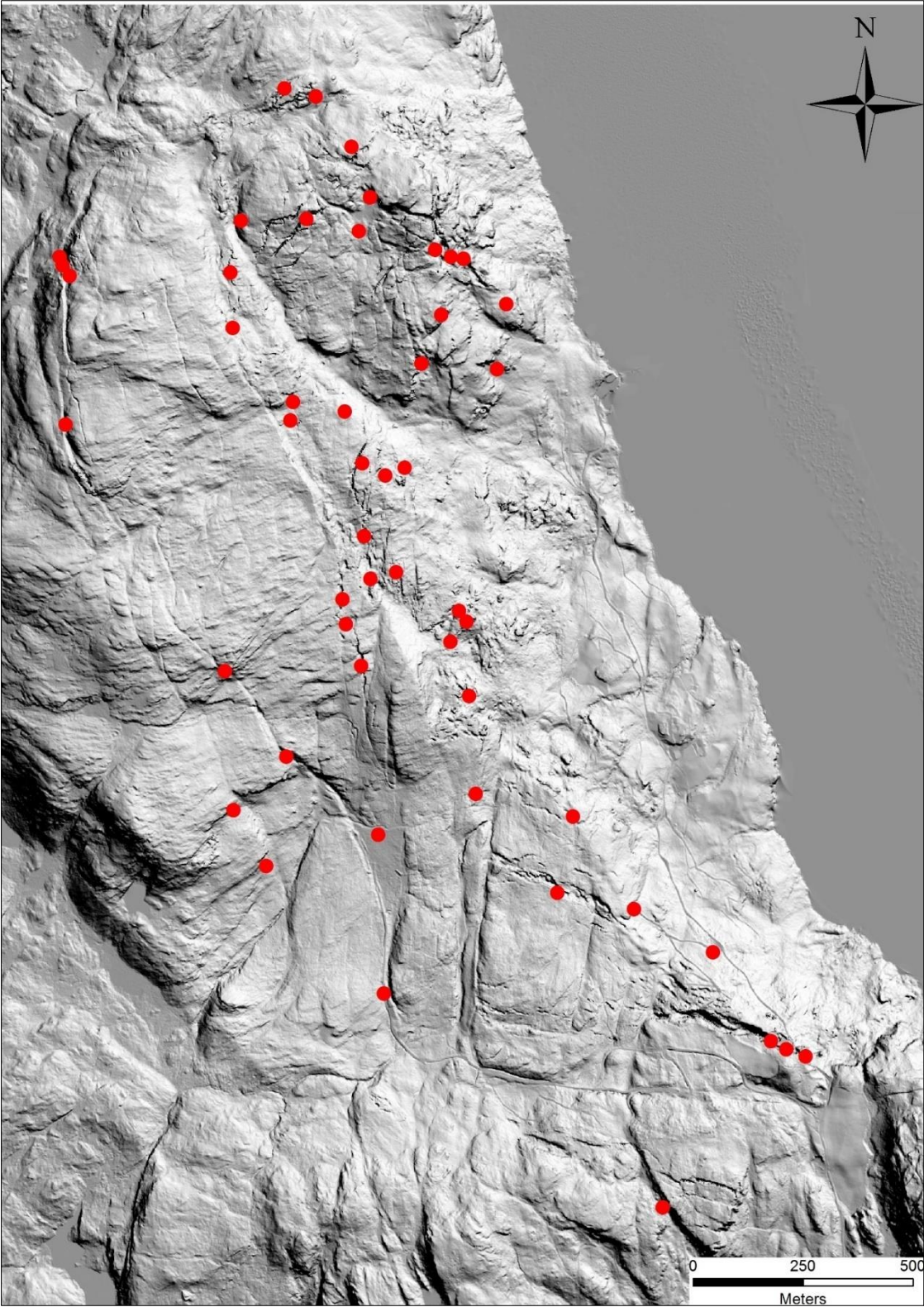
- Oppikofer, T., Hermanns, R. L., Redfield, T. F., Sepúlveda, S. A., Duhart, P., & Bascuñán, I. (2012). Morphologic description of the Punta Cola rock avalanche and associated minor rockslides caused by the 21 april 2007 Aysén earthquake (Patagonia, southern Chile). *Revista de la Asociación Geológica Argentina*, 69(3), 339-353. Retrieved from: <http://ppct.caicyt.gov.ar/index.php/raga/article/view/1535>.
- Oppikofer, T., Hermanns, R. L., Sandøy, G., Böhme, M., Jaboyedoff, M., Horton, P., ..Fuchs, H. (in press). *Quantification of casualties from potential rock-slope failures in Norway*. Paper presented at the 12th International Symposium on Landslides, Napoli, Italy.
- Oppikofer, T., Hermanns, R. L., Sandøy, G., Roberts, N., Böhme, M., & Yugsi, F. (2016). *Workflow for consequence assessment*. Unpublished report. Geological Survey of Norway. Trondheim, Norway.
- Oppikofer, T., Jaboyedoff, M., Pedrazzini, A., Derron, M. C., & Blikra, L. H. (2011). Detailed DEM analysis of a rockslide scar to characterize the basal sliding surface of active rockslides. *Journal of Geophysical Research: Earth Surface*, 116(F2), 1-22. doi:10.1029/2010JF001807
- Oppikofer, T., Nordahl, B., Bunkholt, H., Nicolaisen, M., Jarna, A., Iversen, S.,... Molina, F. Y. (2015). Database and online map service on unstable rock slopes in Norway - From data perpetuation to public information. *Geomorphology*, 249, 69-81. doi:10.1016/j.geomorph.2015.08.005
- Redfield, T. F. (2015a, 29.10.15). [Personal communication].
- Redfield, T. F. (2015b). Rose [Computer Software]. Trondheim.
- Riis, F. (1977). *En petrografisk-strukturgeologisk undersøkelse av Nedstrand-området, Ryfylke*. Unpublished master thesis. University of Oslo. Oslo.
- Roberts, N. J., McKillop, R., Hermanns, R. L., Clague, J., & Oppikofer, T. (2014). Preliminary global catalogue of displacement waves from subaerial landslides. In K. Sassa, P. Canuti, & Y. Yin (Eds.), *Landslide Science for a Safer Geoenvironment* (Vol. 3, pp. 687-692). Switzerland: Springer International Publishing.
- Roberts, N. J., McKillop, R. J., Lawrence, M. S., Psutka, J. F., Clague, J. J., Brideau, M.-A., & Ward, B. C. (2013). Impacts of the 2007 Landslide-Generated Tsunami in Chehalis Lake, Canada. In C. Margottini, P. Canuti, & K. Sassa (Eds.), *Landslide Science and Practice* (pp. 133-140). Berlin: Springer
- Rocscience. (2013a). Dips 6.0 [Computer software]. Retrieved from <https://rocscience.com/rocscience/products/dips>
- Rocscience. (2013b). Kinematic Analysis - Toppling, Planar Sliding, Wedge Sliding. *Dips 6.0 tutorial*. Retrieved from [https://rocscience.com/help/dips/webhelp/pdf\\_files/tutorials/Tutorial\\_04\\_Toppling\\_Planar\\_and\\_Wedge\\_Sliding.pdf](https://rocscience.com/help/dips/webhelp/pdf_files/tutorials/Tutorial_04_Toppling_Planar_and_Wedge_Sliding.pdf)
- Sandøy, G. (2012). *Back-analysis of the 1756 Tjellefonna rockslide, Langfjorden*. (Master thesis), Norwegian University of Science and Technology, Trondheim.
- Savage, R. H. (1948). Graphite lubrication. *Journal of applied physics*, 19(1), 1-10. doi:10.1063/1.1697867

- Scheele, L., Yugsi, F., Oppikofer, T., Hermanns, R., Kveldevisk, V., & Glimsdal, S. (2013). Tsunami modeling and prediction: modeling of the Aysén fjord rock slide tsunami. (ICG report 3013-10-1, NGI report 20061073-02-R), 1-19.
- Scheiber, T., Fredin, O., Viola, G., Jarna, A., Gasser, D., & Łapińska-Viola, R. (2015). Manual extraction of bedrock lineaments from high-resolution LiDAR data: methodological bias and human perception. *GFF*, 137(4), 1-11. doi:10.1080/11035897.2015.1085434
- Scheidegger, A. E. (1973). On the prediction of the reach and velocity of catastrophic landslides. *Rock mechanics*, 5(4), 231-236. doi:10.1007/BF01301796
- Sigmond, E. M. O. (1978). *Beskrivelse til det berggrunnegeologiske kartbladet Sauda 1: 250 000: (med fargetrykt kart)*. Trondheim: Universitetsforlaget.
- Slagstad, T., Roberts, N. M., Marker, M., Røhr, T. S., & Schiellerup, H. (2013). A non-collisional, accretionary Sveconorwegian orogen. *Terra Nova*, 25(1), 30-37.
- Sonmez, H., & Ulusay, H. (1999). Modifications to the geological strength index (GSI) and their applicability to stability of slopes. *International Journal of Rock Mechanics and Mining Sciences*, 36(6), 743-760. doi:10.1016/S0148-9062(99)00043-1
- Stead, D., & Eberhardt, E. (2013). Understanding the mechanics of large landslides. *Italian Journal of Engineering Geology and Environment. Book Series 6*, 85-112. doi:10.4408/IJEGE.2013-06.B-07
- Stini, J. (1941). Unsere Täler wachsen zu. *Geologie und Bauwesen*, 13(3), 71-79.
- Strahler, A. H., & Strahler, A. N. (2006). *Introducing physical geography* (4th ed.). Hoboken: John Wiley and Sons.
- Sørbye, R. C. (1964). Anthophyllite-cordierite-gneisses in the basal rock complex of the Haugesund Peninsula, Western Norway. *Norsk Geologisk Tidsskrift*, 44, 323-340.
- Travelletti, J., Demand, J., Jaboyedoff, M., & Marillier, F. (2010). Mass movement characterization using a reflexion and refraction seismic survey with the sloping local base level concept. *Geomorphology*, 116(1), 1-10. doi:10.1016/j.geomorph.2009.10.006
- Truzman, M. (2007). *Statistical Summary of Rock Mass Characterization for Tunnels of the Caracas-Tuy Medio Railroad Project*. Paper presented at the XIII Panamerican Conference on Soil Mechanics and Geotechnical Engineering.
- Truzman, M. (2009). *Metamorphic Rock Mass Characterization Using the Geological Strength Index (GSI)*. Paper presented at the 43rd US Rock Mechanics Symposium & 4th US-Canada Rock Mechanics Symposium.
- Varnes, D. J. (1978). Slope movement types and processes. In R. L. Schuster & R. J. Krizek (Eds.), *Landslides, analysis and control, special report* (pp. 11-33). National Academy of Sciences, Washington DC: Transportation research board
- Walpole, R. E., Myers, R. H., Myers, S. L., & Ye, K. (2012). *Probability and Statistics for Engineers and Scientists* (9 ed.). New York: Pears education inc.
- Ward, S. N. (2011). Tsunami. In H. K. Gupta (Ed.), *Encyclopedia of Solid Earth Geophysics* (pp. 1473-1493). Netherlands: Springer.
- Wyllie, D. C., & Mah, C. W. (2005). *Rock slope engineering, civil and mining* (4th ed.). New York: Spon Press.



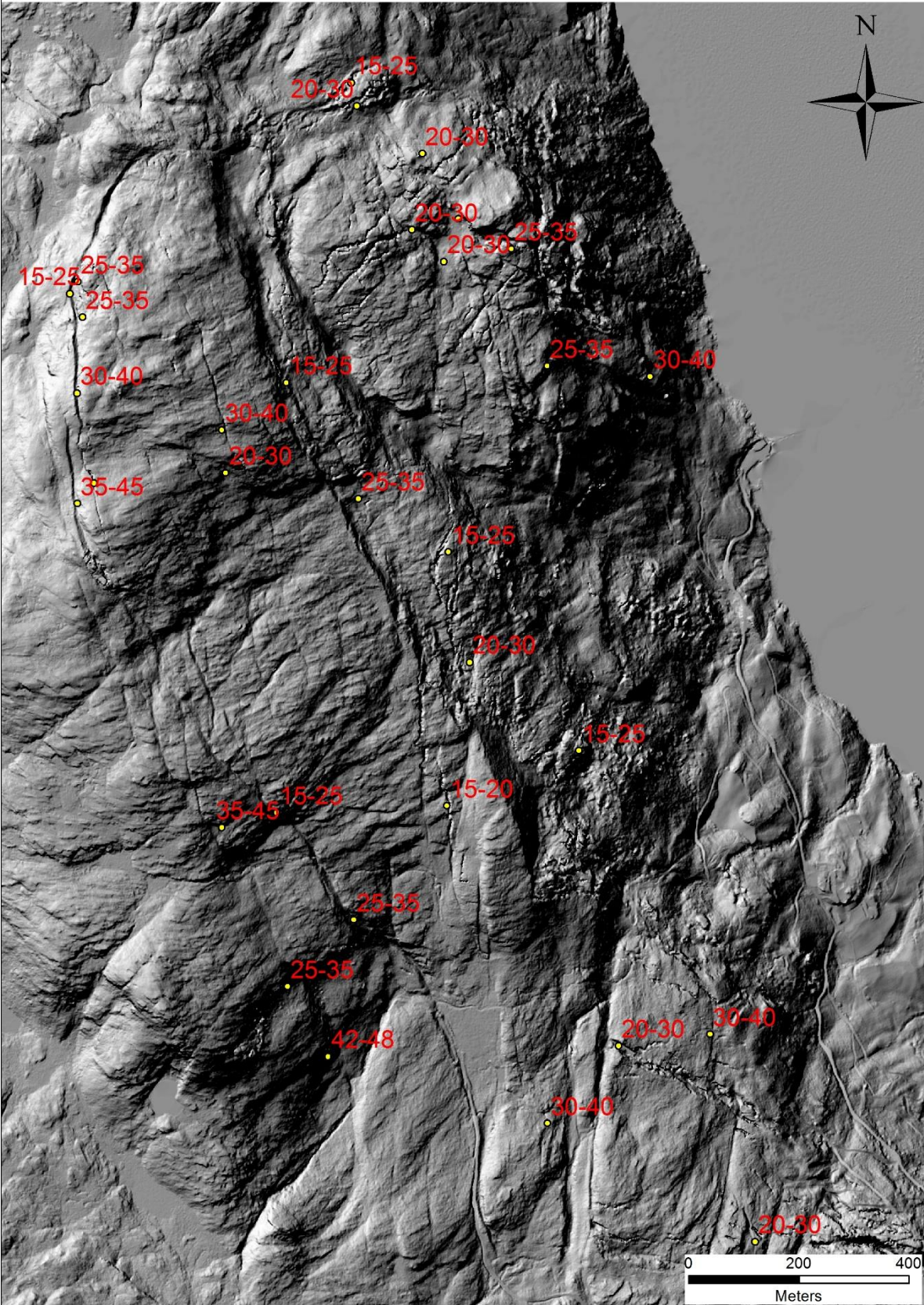
**APPENDIX**

**A. Outcrops with graphite**



**Figure 8.1:** Outcrops with observed graphite.

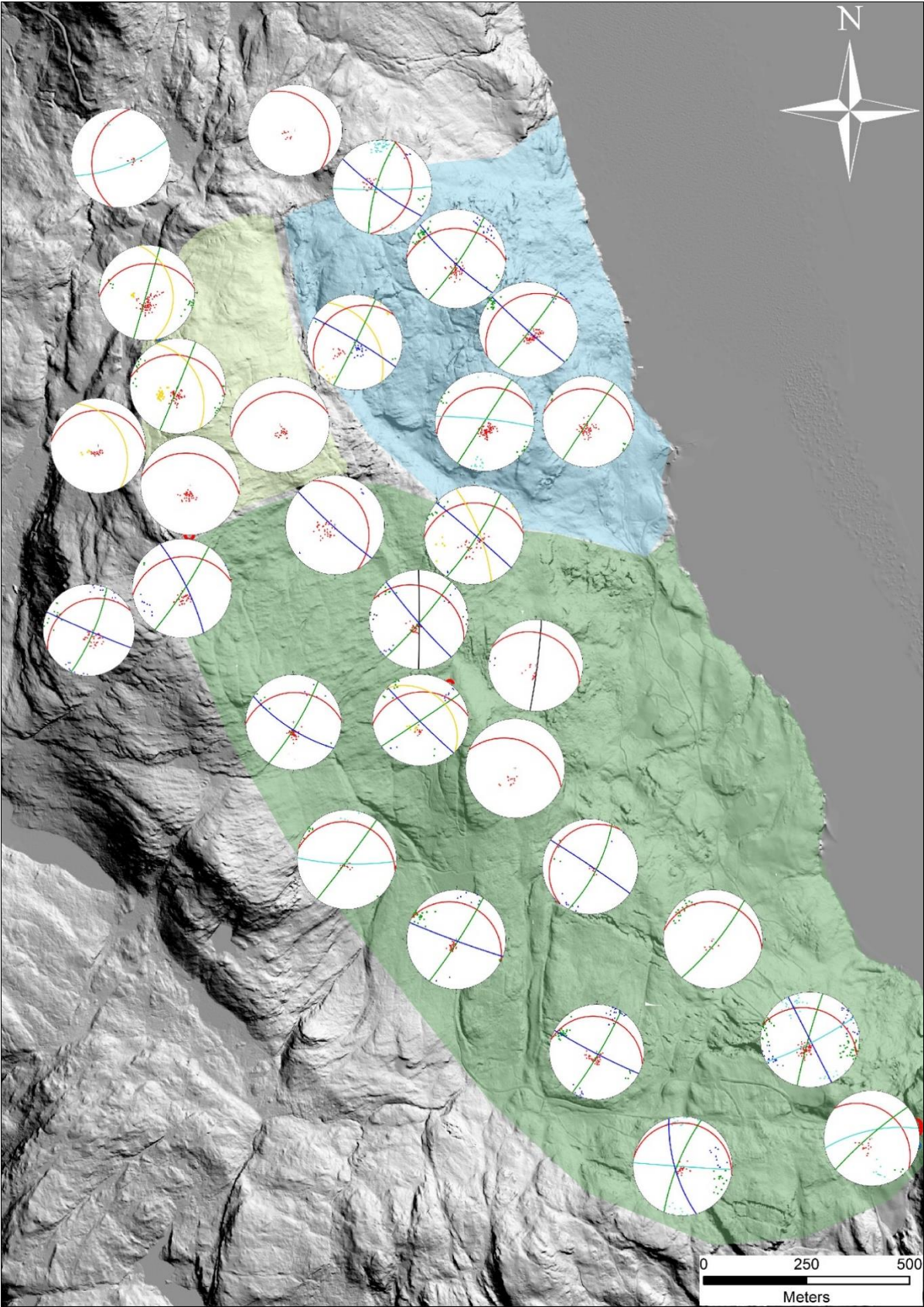
**B. GSI estimates**



**Figure 8.2:** Overview showing all GSI estimates.

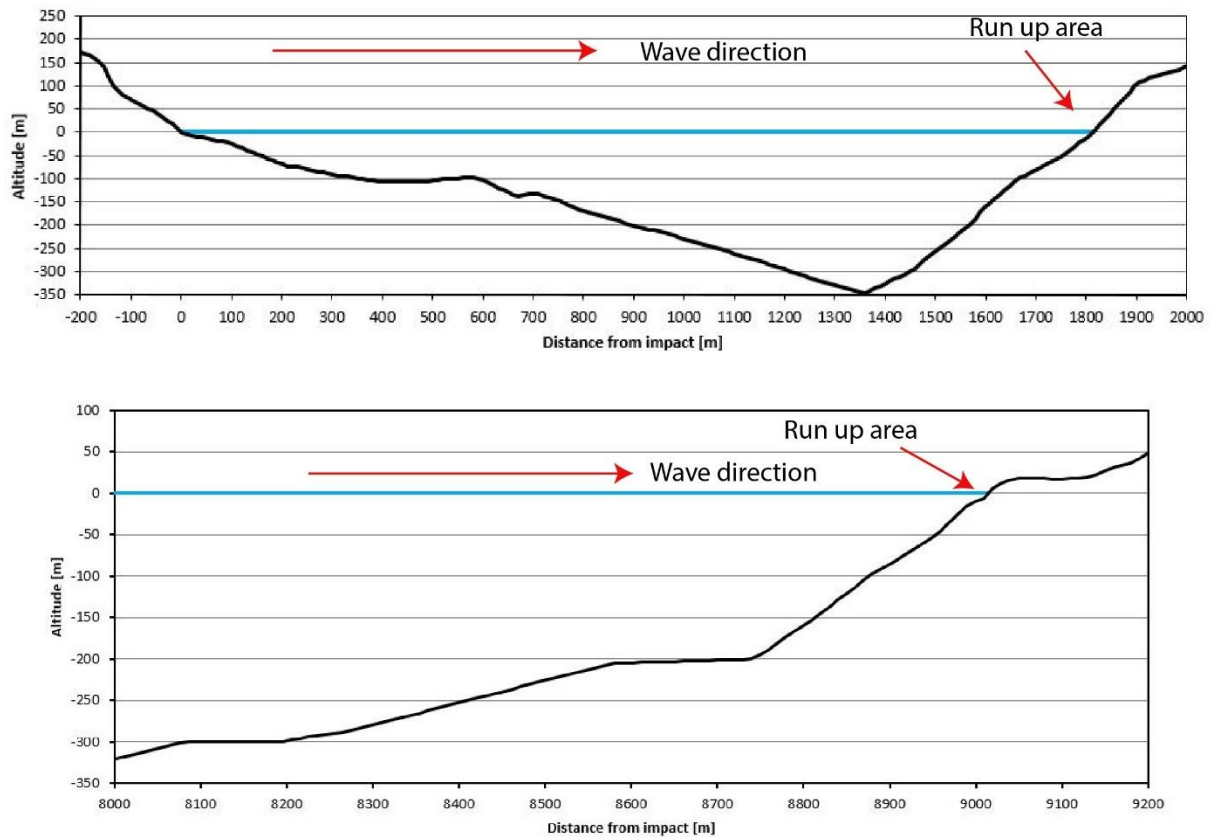


### C. Structural analysis



**Figure 8.3:** Hillshade showing a stereonet for all main locations with the three structural domains indicated with different colours.

## D. Run-up slope angle estimation



**Figure 8.4:** Figure showing how the run-up slope angles was defined both for the VAW analysis and the empirical analysis. All angles were measured perpendicular to the shoreline since this maximizes run-up. **Top:** If the run-up area consists of a smooth slope, the average angle was used as run-up angle. **Bottom:** If the run-up slope angle increased towards the shoreline, the inclination of the area closest to the run-up was chosen.

## E. VAW parameters

### Slide impact parameters

Parameter		Value	Unit	Minimum	Maximum
Initial slide volume	$V_g$	3850000	m <sup>3</sup>		
Initial slide density	$\rho_g$	2700	kg/m <sup>3</sup>	960	2750
Bulk slide porosity	$n$	37	%	30.7	43.3
Bulk slide volume	$V_s$	6111111	m <sup>3</sup>		
Bulk slide density	$\rho_s$	1701	kg/m <sup>3</sup>	590	1720
Slide width at impact	$b$	496	m		
Slide length at impact	$l$	635	m		
Slide thickness	$s$	37	m		
Height difference of impact slope	$\Delta Z_{slope}$	199	m		
Length of impact slope	$\Delta X_{slope}$	538	m		
Slide impact angle	$\alpha$	30	°	30	90
Still water depth	$h$	200	m		
Surface elevation at centre of gravity	$Z_{sc}$	210.2	m		
Weighted mean slide thickness	$s_{sc}$	61.8	m		
Altitude of centre of gravity	$\Delta Z_{sc}$	179.3	m		
Distance from centre of gravity to impact	$\Delta X_{sc}$	458.0	m		
Dynamic bed friction angle	$\delta$	21.4	°		
Slide impact velocity	$V_s$	1	m/s		
Froude number	$F$	0.0305	-	0.86	6.83
Relative slide width	$B$	2.4800	-	0.74	3.33
Relative slide thickness	$S$	0.1853	-	0.09	1.64
Relative slide volume	$\Psi$	0.3080	-	0.05	5.94
Relative slide mass	$M$	0.5239	-	0.11	10.02
Impulse product parameter	$P$	0.0106	-	0.17	8.13
Maximum wave height	$H_M$	2.9	m		
Location of max. wave height	$x_M$	113	m		
Solitary wave celerity	$c_M$	45	m/s		
Wave period at max. height	$T_M$	4.2	s		
Wave length at max. height	$L_M$	186	m		

**Figure 8.5:** Parameters used in the VAW analysis for scenario 5. Slide impact velocity was 1 m/s. This analysis was run using the initial intermediate volume of  $3.85 \times 10^6$  m<sup>3</sup>.

## Slide impact parameters

Parameter		Value	Unit	Minimum	Maximum
Initial slide volume	$V_g$	400000	m <sup>3</sup>		
Initial slide density	$\rho_g$	2700	kg/m <sup>3</sup>	960	2750
Bulk slide porosity	$n$	37	%	30.7	43.3
Bulk slide volume	$V_s$	634921	m <sup>3</sup>		
Bulk slide density	$\rho_s$	1701	kg/m <sup>3</sup>	590	1720
Slide width at impact	$b$	260	m		
Slide length at impact	$l$	195	m		
Slide thickness	$s$	24	m		
Height difference of impact slope	$\Delta Z_{slope}$	270	m		
Length of impact slope	$\Delta X_{slope}$	440	m		
Slide impact angle	$\alpha$	32	°	30	90
Still water depth	$h$	110	m		
Surface elevation at centre of gravity	$Z_{sc}$	141.4	m		
Weighted mean slide thickness	$s_{sc}$	48.5	m		
Altitude of centre of gravity	$\Delta Z_{sc}$	117.1	m		
Distance from centre of gravity to impact	$\Delta X_{sc}$	175.0	m		
Dynamic bed friction angle	$\delta$	29.2	°		
Slide impact velocity	$V_s$	19.6	m/s		
Froude number	$F$	0.5952	-	0.86	6.83
Relative slide width	$B$	2.3636	-	0.74	3.33
Relative slide thickness	$S$	0.2174	-	0.09	1.64
Relative slide volume	$\Psi$	0.2018	-	0.05	5.94
Relative slide mass	$M$	0.3433	-	0.11	10.02
Impulse product parameter	$P$	0.2005	-	0.17	8.13
Maximum wave height	$H_M$	16.9	m		
Location of max. wave height	$X_M$	271	m		
Solitary wave celerity	$C_M$	35	m/s		
Wave period at max. height	$T_M$	13.5	s		
Wave length at max. height	$L_M$	470	m		

**Figure 8.6:** Parameters used in the VAW analysis for scenario 6. Slide impact velocity was 19.6 m/s. This analysis was run using the initial intermediate volume of  $400 \times 10^3 \text{ m}^3$ .

F. Hazard assessment (Scenario 3-6)

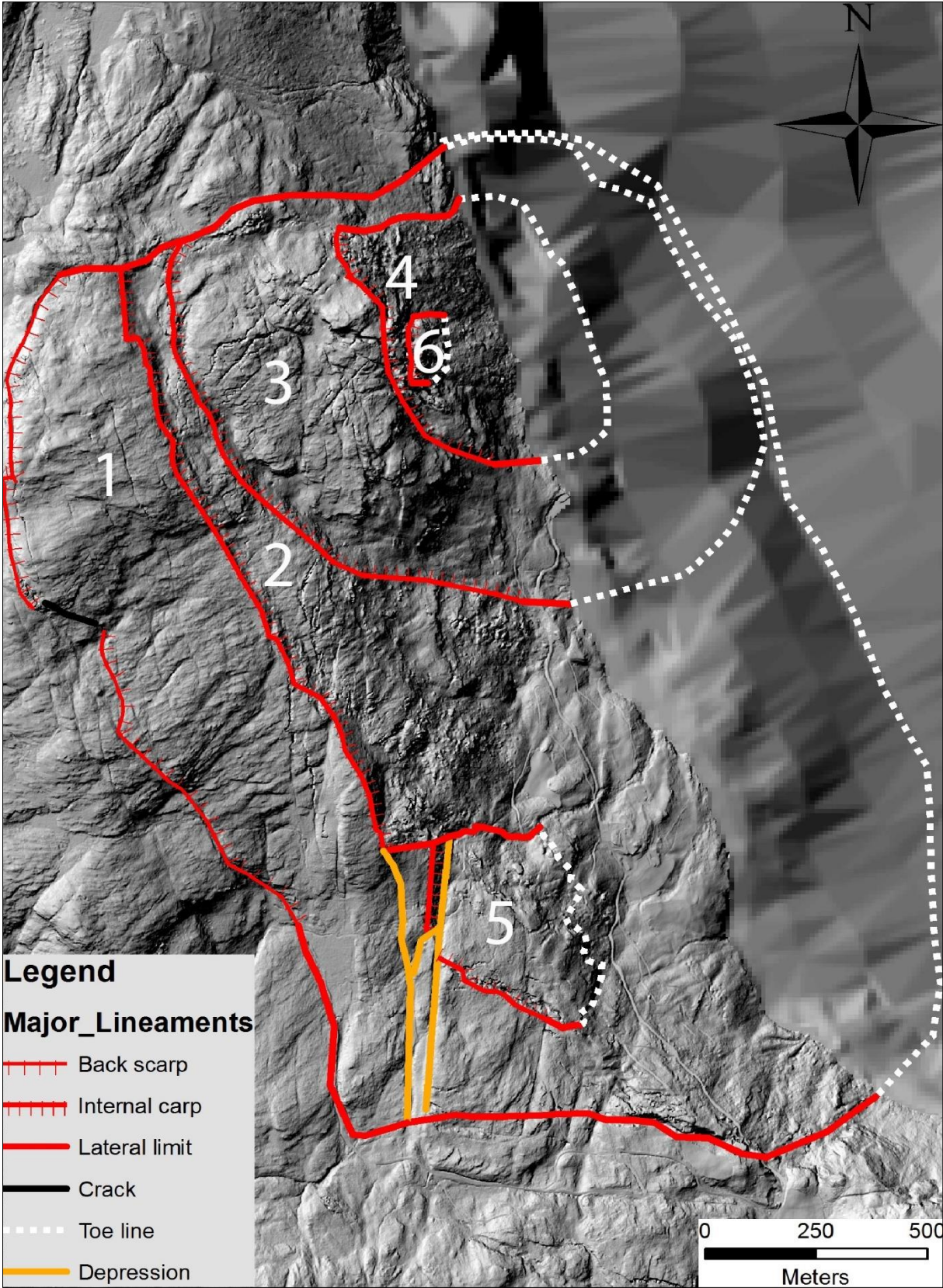


Figure 8.7: Hillshade displaying the six failure scenarios. The prominent change in resolution between the hillshade and the bathymetric data is evident.

Hazard assessment of large unstable rock slopes in Norway								
Site name:	Tytefjell	Scenario:	3	Made by	Øyvind Rem	Date:	06/05/2016	
<b>Hazard classes</b>	<b>Probability</b>	<b>Cumulative prob.</b>	<b>Hazard score</b>		<b>Fitted normal distribution</b>			
Very low	0.0 %	0.0 %	Minimum	3.25	Mean $\mu$	5.3		
Low	40.0 %	40.0 %	Maximum	9.25	St. dev. $\sigma$	1.5		
Medium	42.1 %	82.1 %	Mode	4.25	Mean - $2\sigma$	2.3		
High	17.9 %	100.0 %	Mean	5.53	Mean + $2\sigma$	8.3		
Very high	0.0 %	100.0 %	5th percentile	3.50	Corr. coeff.	0.9984		
			95% percentile	7.73	K-S-test (max.)	6.5 %		
<b>1. Back-scarp</b>							<b>Score</b>	<b>Norm. prob.</b>
Not developed							0	0.0 %
Partly open over width of slide body (few cm to m)							0.5	100.0 %
Fully open over width of slide body (few cm to m)							1	0.0 %
Comment: Back scarp partly developed.								
<b>2. Potential sliding structures</b>							<b>Score</b>	<b>Norm. prob.</b>
No penetrative structures dip out of the slope							0	0.0 %
Penetrative structures dip on average < 20 degree or steeper than the slope							0.5	100.0 %
Penetrative structures dip on average > 20 degree and daylight with the slope							1	0.0 %
Comment: Foliation dips parallel with slope angle. J4 dips out of slope but is not daylighting.								
<b>3. Lateral release surfaces</b>							<b>Score</b>	<b>Norm. prob.</b>
Not developed							0	0.0 %
Partly developed on 1 side							0.25	0.0 %
Fully developed or free slope on 1 side or partly developed on 2 sides							0.5	100.0 %
Fully developed or free slope on 1 side and partly developed on 1 side							0.75	0.0 %
Fully developed or free slope on 2 sides							1	0.0 %
Comment: Both lateral limits are partly developed								
<b>4. Kinematic feasibility test</b>							<b>Score</b>	<b>Norm. prob.</b>
Kinematic feasibility test does not allow for planar sliding, wedge sliding or toppling							0	0.0 %
Failure is partly kinematically possible (movement direction is more than $\pm 30^\circ$ to slope orientation)							0.5	0.0 %
Failure is kinematically possible (movement direction is less than $\pm 30^\circ$ to slope orientation)							0.75	100.0 %
Failure is partly kinematically possible on persistent discontinuities (movement direction is more than $\pm 30^\circ$ to slope orientation)							0.75	0.0 %
Failure is kinematically possible on persistent discontinuities (movement direction is less than $\pm 30^\circ$ to slope orientation)							1	0.0 %
Comment: Back scarp is following J4. Planar sliding is feasible along this set within in the 30 degree limit.								
<b>5. Morphologic expression of the rupture surface</b>							<b>Score</b>	<b>Norm. prob.</b>
No indication on slope morphology							0	50.0 %
Slope morphology suggests formation of a rupture surface (bulging, concavity-convexity, springs)							0.5	25.0 %
Continuous rupture surface is suggested by slope morphology and can be mapped out							1	25.0 %
Comment: Rupture surface might daylight below sea level. Not possible to determine with todays bathymetry.								
<b>6. Displacement rates</b>							<b>Score</b>	<b>Norm. prob.</b>
No significant movement							0	30.0 %
0.2 - 0.5 cm/year							1	30.0 %
0.5 - 1 cm/year							2	30.0 %
1 - 4 cm/year							3	10.0 %
4 - 10 cm/year							4	0.0 %
> 10 cm/year							5	0.0 %
Comment: No displacement measurements are ready until August 2016. It is believed that the unstable area moves less than 4cm/year.								
<b>7. Acceleration (if velocity is &gt;0.5 cm/yr and &lt;10 cm/yr)</b>							<b>Score</b>	<b>Norm. prob.</b>
No acceleration or change in displacement rates							0	50.0 %
Increase in displacement rates							1	50.0 %
Comment: This criterion is not possible to evaluate without displacement measurements. According to the instructions, equal probabilities are given to all conditions of this criteria.								
<b>8. Increase of rock fall activity</b>							<b>Score</b>	<b>Norm. prob.</b>
No increase of rock fall activity							0	0.0 %
Increase of rock fall activity							1	100.0 %
Comment: Several rockfall event from the frontal limit is recorded the last 20 years. Frequent rockfall from the frontal limit is observed by locals during rainfall.								
<b>9. Past events</b>							<b>Score</b>	<b>Norm. prob.</b>
No post-glacial events of similar size							0	33.3 %
One or several events older than 5000 years of similar size							0.5	33.3 %
One or several events younger than 5000 years of similar size							1	33.3 %
Comment: Uncertain if there exist earlier event with size compared to this scenario in the vicinity of the unstable area.								

**Figure 8.8:** Complete hazard assessment of scenario 3 (figure 4.39 and figure 4.40).

Hazard assessment of large unstable rock slopes in Norway							
Site name:	Tytefjell	Scenario:	4	Made by:	Øyvind Rem	Date:	06/05/2016
<b>Hazard classes</b>	<b>Probability</b>	<b>Cumulative prob.</b>	<b>Hazard score</b>		<b>Fitted normal distribution</b>		
Very low	0.0 %	0.0 %	Minimum	3.25	Mean $\mu$	5.3	
Low	40.0 %	40.0 %	Maximum	9.25	St. dev. $\sigma$	1.5	
Medium	42.1 %	82.1 %	Mode	4.25	Mean - $2\sigma$	2.3	
High	17.9 %	100.0 %	Mean	5.53	Mean + $2\sigma$	8.3	
Very high	0.0 %	100.0 %	5th percentile	3.50	Corr. coeff.	0.9984	
			95% percentile	7.73	K-S-test (max.)	6.5 %	
<b>1. Back-scarp</b>					<b>Score</b>	<b>Norm. prob.</b>	
Not developed					0	0.0 %	
Partly open over width of slide body (few cm to m)					0.5	100.0 %	
Fully open over width of slide body (few cm to m)					1	0.0 %	
Comment: Back scarp partly developed.							
<b>2. Potential sliding structures</b>					<b>Score</b>	<b>Norm. prob.</b>	
No penetrative structures dip out of the slope					0	0.0 %	
Penetrative structures dip on average < 20 degree or steeper than the slope					0.5	100.0 %	
Penetrative structures dip on average > 20 degree and daylight with the slope					1	0.0 %	
Comment: Foliation dips parallell with slope. J4 dips out of slope, but is not penetrative.							
<b>3. Lateral release surfaces</b>					<b>Score</b>	<b>Norm. prob.</b>	
Not developed					0	0.0 %	
Partly developed on 1 side					0.25	0.0 %	
Fully developed or free slope on 1 side or partly developed on 2 sides					0.5	100.0 %	
Fully developed or free slope on 1 side and partly developed on 1 side					0.75	0.0 %	
Fully developed or free slope on 2 sides					1	0.0 %	
Comment: Southern flank is partly developed above waterlevel, uncertain continuation below sea level. Northern flank partly developed.							
<b>4. Kinematic feasibility test</b>					<b>Score</b>	<b>Norm. prob.</b>	
Kinematic feasibility test does not allow for planar sliding, wedge sliding or toppling					0	0.0 %	
Failure is partly kinematically possible (movement direction is more than $\pm 30^\circ$ to slope orientation)					0.5	0.0 %	
Failure is kinematically possible (movement direction is less than $\pm 30^\circ$ to slope orientation)					0.75	100.0 %	
Failure is partly kinematically possible on persistent discontinuities (movement direction is more than $\pm 30^\circ$ to slope orientation)					0.75	0.0 %	
Failure is kinematically possible on persistent discontinuities (movement direction is less than $\pm 30^\circ$ to slope orientation)					1	0.0 %	
Comment: Planar sliding is feasible along J4 within the 30 degree limit. Wedge failure along J1 and the foliation partly feasible if friction angle is lowered.							
<b>5. Morphologic expression of the rupture surface</b>					<b>Score</b>	<b>Norm. prob.</b>	
No indication on slope morphology					0	50.0 %	
Slope morphology suggests formation of a rupture surface (bulging, concavity-convexity, springs)					0.5	25.0 %	
Continuous rupture surface is suggested by slope morphology and can be mapped out					1	25.0 %	
Comment: Rupture surface might daylight below sea level. Not possible to determine with todays bathymetry.							
<b>6. Displacement rates</b>					<b>Score</b>	<b>Norm. prob.</b>	
No significant movement					0	30.0 %	
0.2 - 0.5 cm/year					1	30.0 %	
0.5 - 1 cm/year					2	30.0 %	
1 - 4 cm/year					3	10.0 %	
4 - 10 cm/year					4	0.0 %	
> 10 cm/year					5	0.0 %	
Comment: No displacement measurements are ready until August 2016. It is believed that the unstable area moves less than 4cm/year.							
<b>7. Acceleration (if velocity is &gt;0.5 cm/yr and &lt;10 cm/yr)</b>					<b>Score</b>	<b>Norm. prob.</b>	
No acceleration or change in displacement rates					0	50.0 %	
Increase in displacement rates					1	50.0 %	
Comment: This criterion is not possible to evaluate without displacement measurements. According to the instructions, equal probabilities are given to all conditions of this criteria.							
<b>8. Increase of rock fall activity</b>					<b>Score</b>	<b>Norm. prob.</b>	
No increase of rock fall activity					0	0.0 %	
Increase of rock fall activity					1	100.0 %	
Comment: Several rockfall event from the frontal limit is recorded the last 20 years. Frequent rockfall from the frontal limit is observed by locals during rainfall.							
<b>9. Past events</b>					<b>Score</b>	<b>Norm. prob.</b>	
No post-glacial events of similar size					0	33.3 %	
One or several events older than 5000 years of similar size					0.5	33.3 %	
One or several events younger than 5000 years of similar size					1	33.3 %	
Comment: Uncertain if there exist earlier event with size compared to this scenario in the vicinity of the unstable area.							

Figure 8.9: Complete hazard assessment of scenario 4 (figure 4.39 and figure 4.40).

Hazard assessment of large unstable rock slopes in Norway							
Site name:	Tytefjell	Scenario:	5	Made by:	Øyvind Rem	Date:	06/05/2016
<b>Hazard classes</b>	<b>Probability</b>	<b>Cumulative prob.</b>	<b>Hazard score</b>		<b>Fitted normal distribution</b>		
Very low	0.0 %	0.0 %	Minimum	3.50	Mean $\mu$	5.6	
Low	27.5 %	27.5 %	Maximum	9.50	St. dev. $\sigma$	1.5	
Medium	54.6 %	82.1 %	Mode	4.50	Mean - $2\sigma$	2.6	
High	17.9 %	100.0 %	Mean	5.78	Mean + $2\sigma$	8.5	
Very high	0.0 %	100.0 %	5th percentile	3.75	Corr. coeff.	0.9984	
			95% percentile	7.98	K-S-test (max.)	6.5 %	
<b>1. Back-scarp</b>							
Not developed					Score	Norm. prob.	
Partly open over width of slide body (few cm to m)					0	0.0 %	
Fully open over width of slide body (few cm to m)					0.5	100.0 %	
Comment: Back scarp fully developed.					1	0.0 %	
<b>2. Potential sliding structures</b>							
No penetrative structures dip out of the slope					0	0.0 %	
Penetrative structures dip on average < 20 degree or steeper than the slope					0.5	100.0 %	
Penetrative structures dip on average > 20 degree and daylight with the slope					1	0.0 %	
Comment: Foliation dips parallell with slope angle. J4 dips out of slope, but is not penetrative. Back scarp follows J4.							
<b>3. Lateral release surfaces</b>							
Not developed					0	0.0 %	
Partly developed on 1 side					0.25	0.0 %	
Fully developed or free slope on 1 side or partly developed on 2 sides					0.5	0.0 %	
Fully developed or free slope on 1 side and partly developed on 1 side					0.75	100.0 %	
Fully developed or free slope on 2 sides					1	0.0 %	
Comment: Southern flank is fully developed. Northern flank partly developed.							
<b>4. Kinematic feasibility test</b>							
Kinematic feasibility test does not allow for planar sliding, wedge sliding or toppling					0	0.0 %	
Failure is partly kinematically possible (movement direction is more than $\pm 30^\circ$ to slope orientation)					0.5	0.0 %	
Failure is kinematically possible (movement direction is less than $\pm 30^\circ$ to slope orientation)					0.75	100.0 %	
Failure is partly kinematically possible on persistent discontinuities (movement direction is more than $\pm 30^\circ$ to slope orientation)					0.75	0.0 %	
Failure is kinematically possible on persistent discontinuities (movement direction is less than $\pm 30^\circ$ to slope orientation)					1	0.0 %	
Comment: Planar sliding is feasible along J4 within the $30^\circ$ limit. Wedge failure along J1 and the foliation partly feasible if friction angle is lowered.							
<b>5. Morphologic expression of the rupture surface</b>							
No indication on slope morphology					0	50.0 %	
Slope morphology suggests formation of a rupture surface (bulging, concavity-convexity, springs)					0.5	25.0 %	
Continuous rupture surface is suggested by slope morphology and can be mapped out					1	25.0 %	
Comment: Zone of deformation observed below this scenario. Is interpreted as a rupture surface.							
<b>6. Displacement rates</b>							
No significant movement					0	30.0 %	
0.2 - 0.5 cm/year					1	30.0 %	
0.5 - 1 cm/year					2	30.0 %	
1 - 4 cm/year					3	10.0 %	
4 - 10 cm/year					4	0.0 %	
> 10 cm/year					5	0.0 %	
Comment: No displacement measurements are ready until August 2016. It is believed that the unstable area moves less than 4cm/year.							
<b>7. Acceleration (if velocity is &gt;0.5 cm/yr and &lt;10 cm/yr)</b>							
No acceleration or change in displacement rates					0	50.0 %	
Increase in displacement rates					1	50.0 %	
Comment: This criterion is not possible to evaluate without displacement measurements. According to the instructions, equal probabilities are given to all conditions of this criteria.							
<b>8. Increase of rock fall activity</b>							
No increase of rock fall activity					1	0.0 %	
Increase of rock fall activity					0	100.0 %	
Comment: Irrequent rockfall from the frontal region.							
<b>9. Past events</b>							
No post-glacial events of similar size					0	33.3 %	
One or several events older than 5000 years of similar size					0.5	33.3 %	
One or several events younger than 5000 years of similar size					1	33.3 %	
Comment: Uncertain if there exist earlier event in the vicinity of the unstable area.							

Figure 8.10: Complete hazard assessment of scenario 5 (figure 4.39 and figure 4.40).



## Hazard assessment of large unstable rock slopes in Norway

Site name: Tytefjell Scenario: 6 Made by: Øyvind Rem Date: 06/05/2016

Hazard classes	Probability	Cumulative prob.	Hazard score		Fitted normal distribution	
Very low	0.0 %	0.0 %	Minimum	3.8	Mean $\mu$	5.4
Low	40.0 %	40.0 %	Maximum	8.8	St. dev. $\sigma$	1.4
Medium	41.7 %	81.7 %	Mode	4.8	Mean - $2\sigma$	2.6
High	18.3 %	100.0 %	Mean	5.7	Mean + $2\sigma$	8.3
Very high	0.0 %	100.0 %	5th percentile	3.8	Corr. coeff.	0.9977
			95% percentile	7.7	K-S-test (max.)	8.9 %

1. Back-scarp		Score	Norm. prob.
Not developed		0	0.0 %
Partly open over width of slide body (few cm to m)		0.5	100.0 %
Fully open over width of slide body (few cm to m)		1	0.0 %
Comment: Back scarp partly developed.			

2. Potential sliding structures		Score	Norm. prob.
No penetrative structures dip out of the slope		0	0.0 %
Penetrative structures dip on average < 20 degree or steeper than the slope		0.5	100.0 %
Penetrative structures dip on average > 20 degree and daylight with the slope		1	0.0 %
Comment: Foliation dips parallell with slope. J4 dips out of slope angle, but is not penetrative.			

3. Lateral release surfaces		Score	Norm. prob.
Not developed		0	0.0 %
Partly developed on 1 side		0.25	0.0 %
Fully developed or free slope on 1 side or partly developed on 2 sides		0.5	100.0 %
Fully developed or free slope on 1 side and partly developed on 1 side		0.75	0.0 %
Fully developed or free slope on 2 sides		1	0.0 %
Comment: Both flanks are partly developed			

4. Kinematic feasibility test		Score	Norm. prob.
Kinematic feasibility test does not allow for planar sliding, wedge sliding or toppling		0	0.0 %
Failure is partly kinematically possible (movement direction is more than $\pm 30^\circ$ to slope orientation)		0.5	0.0 %
Failure is kinematically possible (movement direction is less than $\pm 30^\circ$ to slope orientation)		0.75	100.0 %
Failure is partly kinematically possible on persistent discontinuities (movement direction is more than $\pm 30^\circ$ to slope orientation)		0.75	0.0 %
Failure is kinematically possible on persistent discontinuities (movement direction is less than $\pm 30^\circ$ to slope orientation)		1	0.0 %
Comment: Planar sliding is feasible along J4 within the $30^\circ$ limit. Wedge failure along J1 and the foliation partly feasible if friction angle is lowered.			

5. Morphologic expression of the rupture surface		Score	Norm. prob.
No indication on slope morphology		0	0.0 %
Slope morphology suggests formation of a rupture surface (bulging, concavity-convexity, springs)		0.5	100.0 %
Continuous rupture surface is suggested by slope morphology and can be mapped out		1	0.0 %
Comment: No clear rupture surface. The morphology suggest a rupture surface below the block.			

6. Displacement rates		Score	Norm. prob.
No significant movement		0	30.0 %
0.2 - 0.5 cm/year		1	30.0 %
0.5 - 1 cm/year		2	30.0 %
1 - 4 cm/year		3	10.0 %
4 - 10 cm/year		4	0.0 %
> 10 cm/year		5	0.0 %
Comment: No displacement measurements are ready until August 2016. It is believed that the unstable area moves less than 4cm/year.			

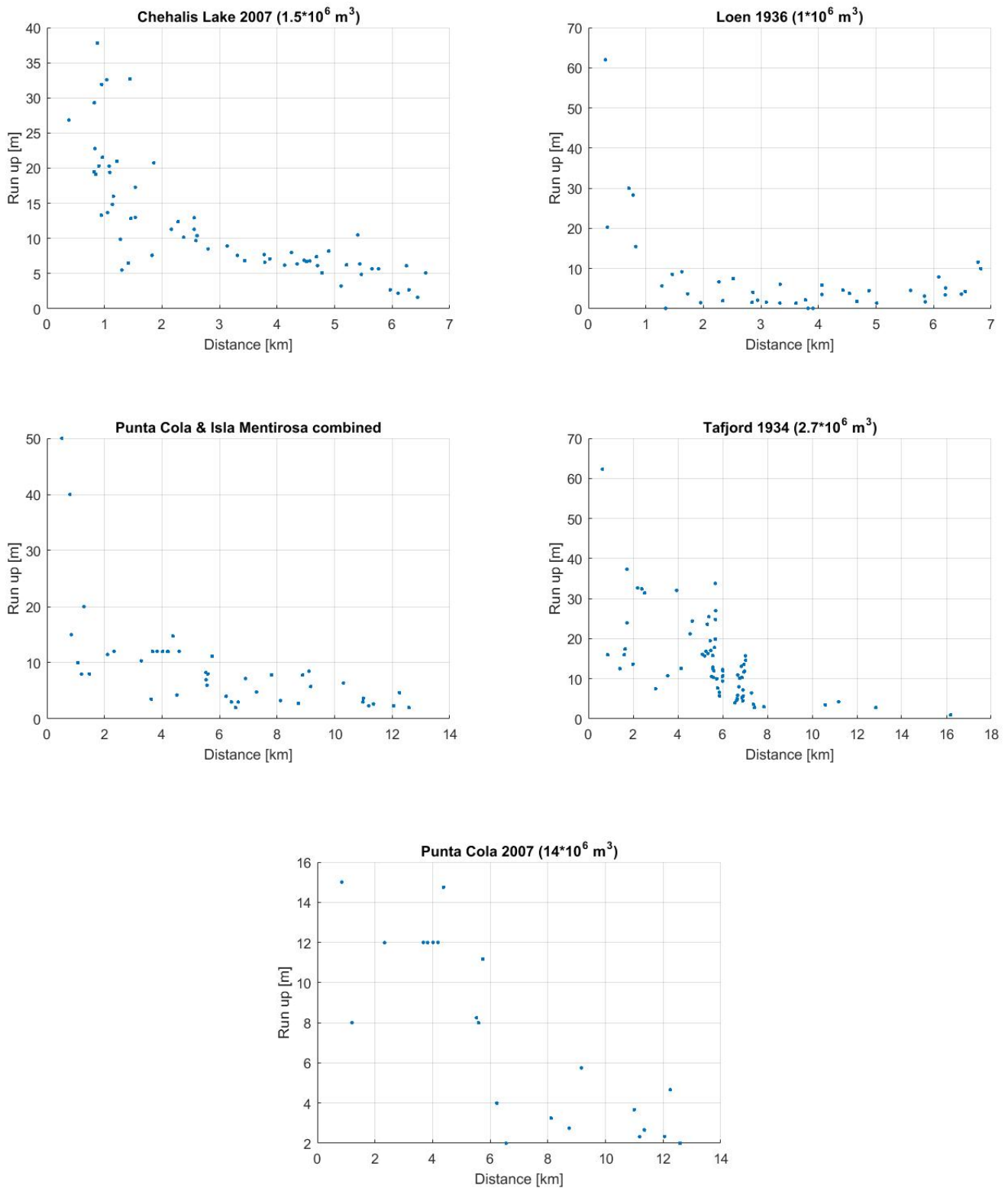
7. Acceleration (if velocity is >0.5 cm/yr and <10 cm/yr)		Score	Norm. prob.
No acceleration or change in displacement rates		0	50.0 %
Increase in displacement rates		1	50.0 %
Comment: This criterion is not possible to evaluate without displacement measurements. According to the instructions, equal probabilities are given to all			

8. Increase of rock fall activity		Score	Norm. prob.
No increase of rock fall activity		0	0.0 %
Increase of rock fall activity		1	100.0 %
Comment: Several rockfall event from the frontal limit is recorded the last 20 years. Frequent rockfall from the frontal limit is observed by locals during rainfall.			

9. Past events		Score	Norm. prob.
No post-glacial events of similar size		0	33.3 %
One or several events older than 5000 years of similar size		0.5	33.3 %
One or several events younger than 5000 years of similar size		1	33.3 %
Comment: Events with this volume have almost certain occurred in the vicinity of the unstable area.			

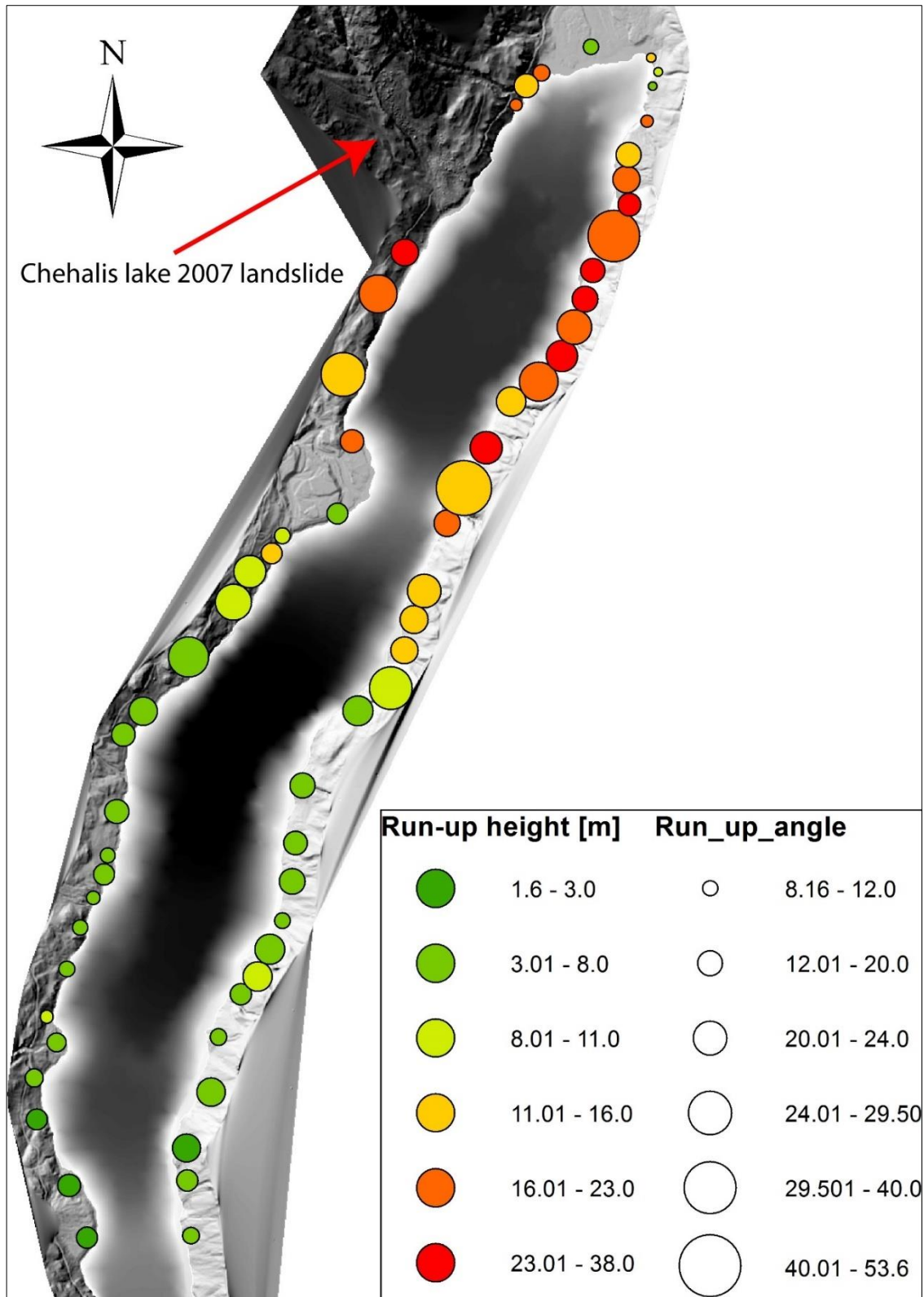
Figure 8.11: Complete hazard assessment of scenario 6 (figure 4.39 and figure 4.40).

## G. Empirical analysis of displacement wave parameters

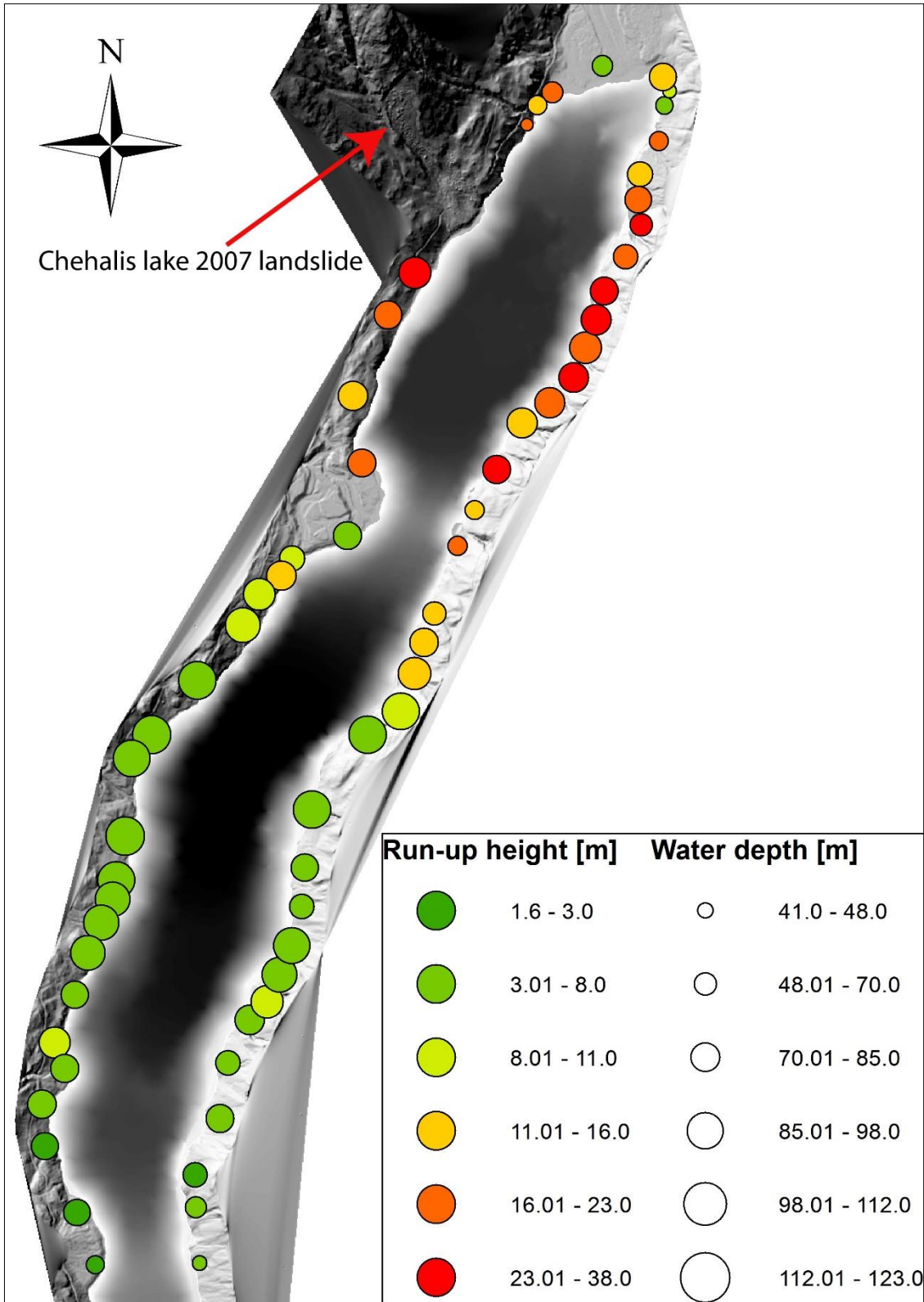


**Figure 8.12:** The four plots at the top are showing the landslide events with a good fit  $R^2 > 0.6$  between run-up and distance. The Punta Cola and Isla Mentirosa events do not show a good fit separately and are therefore combined into one plot. Also the Punta Cola dataset in the lowermost plot does not show a clear decrease of run-up with distance.

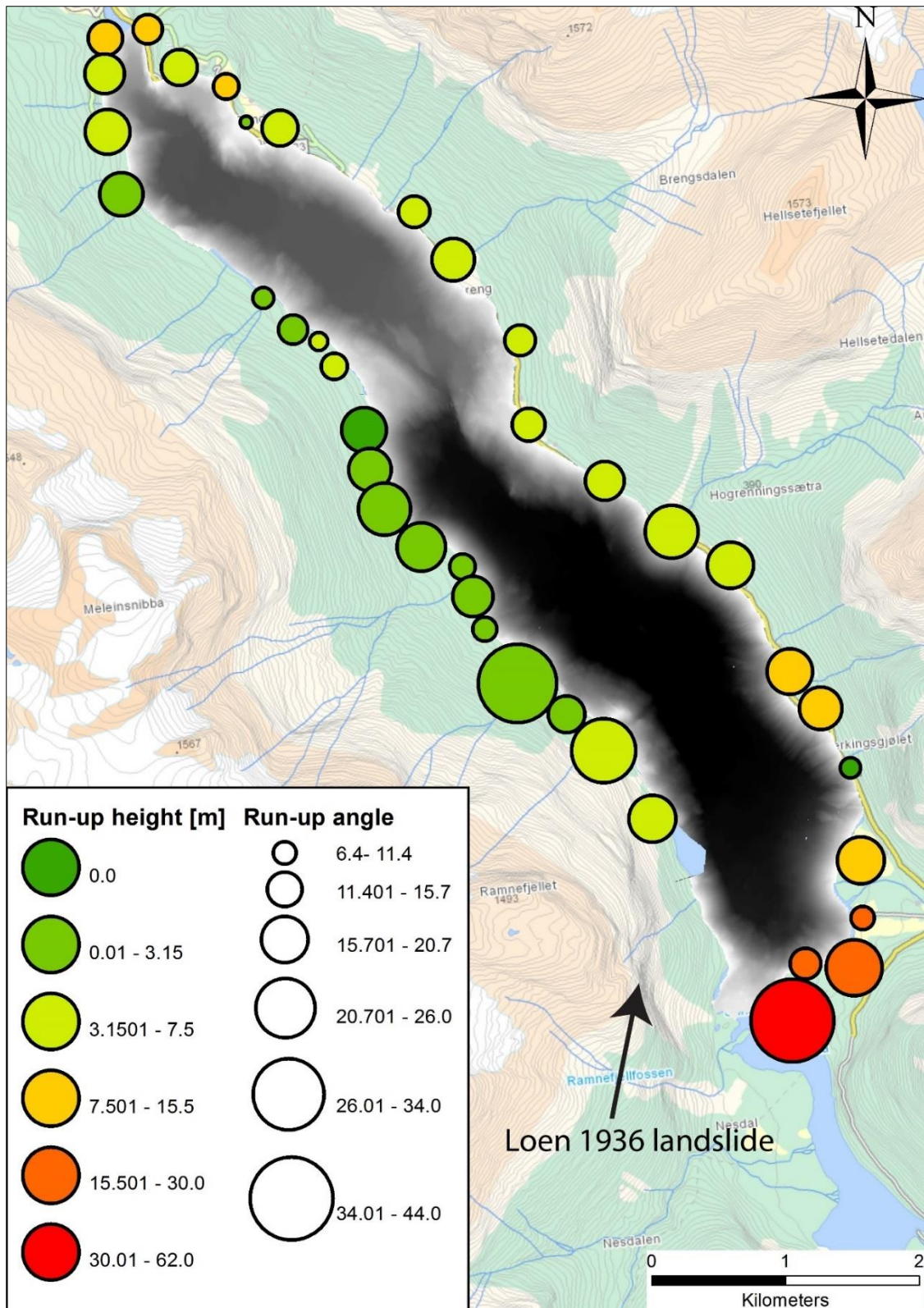
**H. Maps displaying wave height and run-up slope angle or water depth for historical rock slope failures with existing bathymetry**



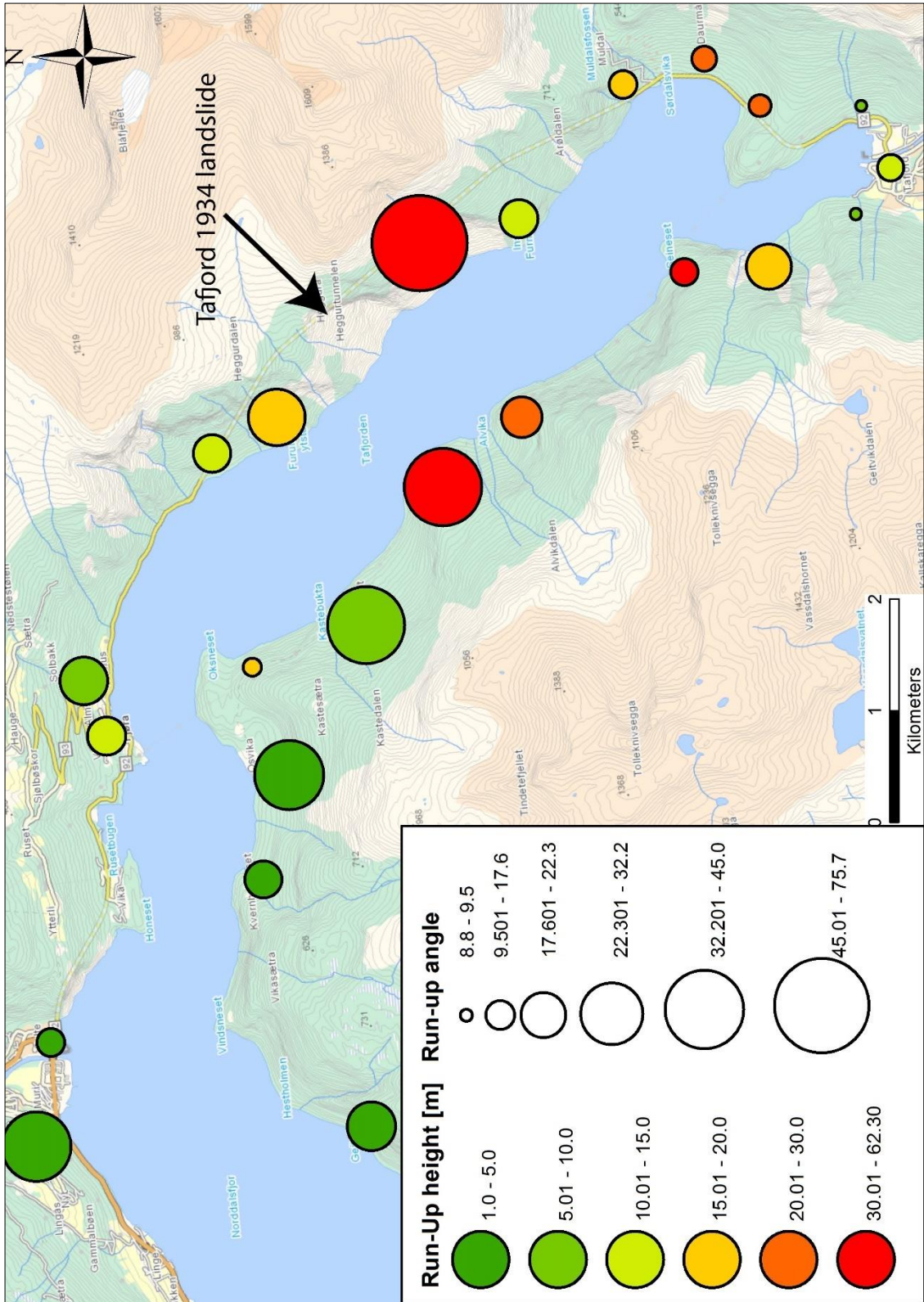
**Figure 8.13:** Map displaying run-up height and run-up slope angle along Chehalis lake. The location of the landslide is indicated on the figure.



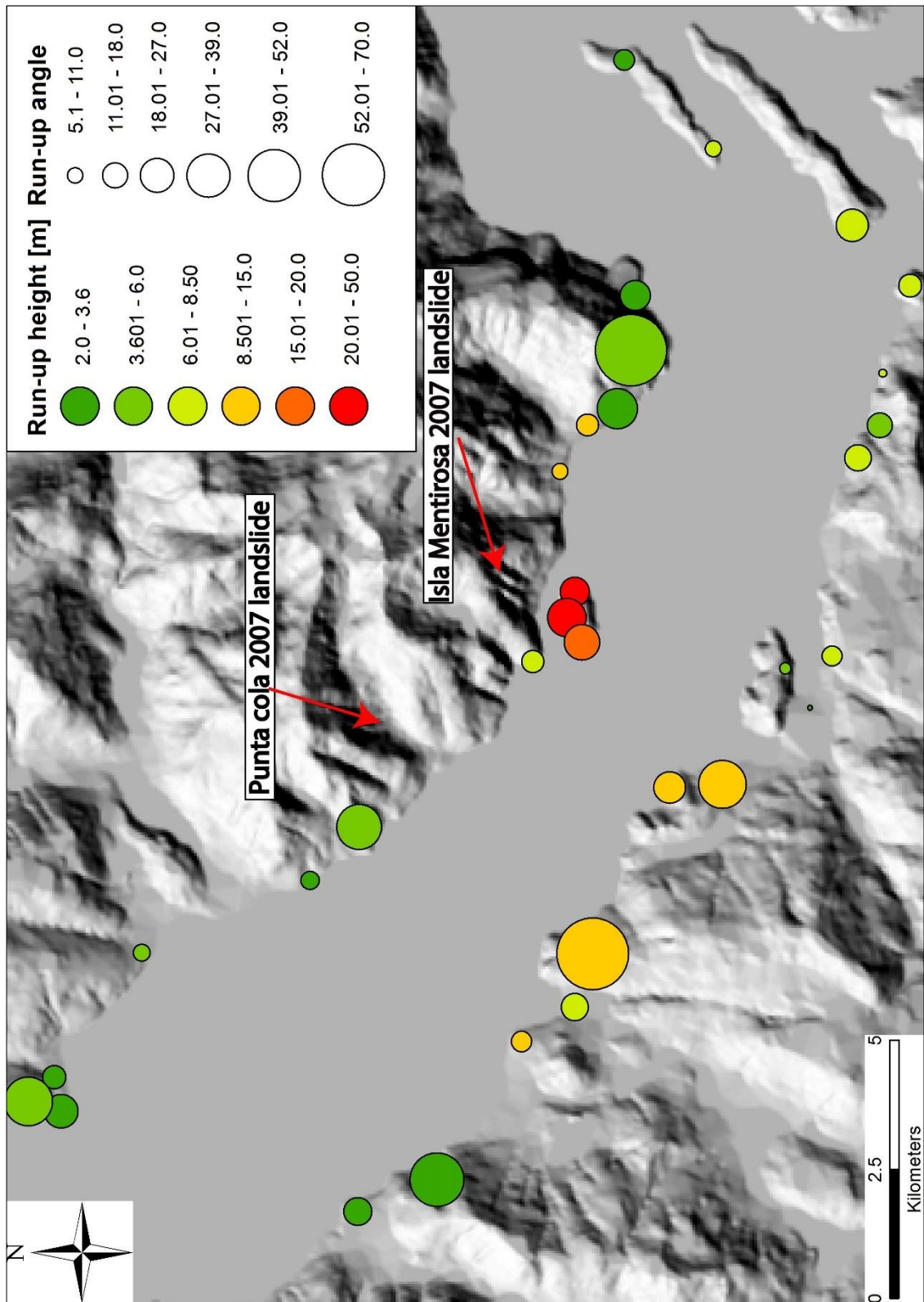
**Figure 8.14:** Map displaying run-up height and water depth along Chehalis lake. The location of the landslide is indicated on the figure.



**Figure 8.15:** Map displaying run-up height and run-up angle along the Loen lake from the 1936 event. The location of the landslide is indicated on the figure.



**Figure 8.16:** Map displaying run-up height and run-up angle along Tafjord from the 1936 event. The location of the landslide is indicated on the figure.



**Figure 8.17:** Run-up height and run-up angle displayed along the Aysén Fjord. The location of the two landslides is indicated on the figure.